STRUCTURAL STUDY AND THERMOELECTRIC PROPERTIES OF SOME GROUP 9 TERNARY METAL CHALCOGENIDES

by

Gerard Garcia i Sobany BSc, MSc

A thesis submitted for the degree of

Doctor of Philosophy

Heriot-Watt University

Department of Chemistry

October 2009

Abstract

The crystal structure and thermoelectric properties of the anion-substituted ternary skutterudites $MQ_{1.5}Y_{1.5}$ (M = Co, Rh, Ir; Q = Ge, Sn; Y = S, Te) have been investigated. A group theoretical analysis based on powder neutron diffraction data of $CoGe_{1.5}Te_{1.5}$ is presented, revealing new symmetry elements overlooked in previous studies of similar compounds. The new model obtained was applied in a subsequent neutron diffraction study of the sulphides $MGe_{1.5}S_{1.5}$ (M = Co, Rh, Ir). A resonant scattering synchrotron experiment has also been performed on the tellurides $MQ_{1.5}Te_{1.5}$ (M = Co, Rh, Ir; Q = Ge, Sn) in order to assess the extent of anion disorder. The thermoelectric properties of all the compounds under study were measured and put into context with both state-of-the-art and new thermoelectric materials.

The synthesis of the fully filled skutterudite $LaFe_3CoGe_6Te_6$ has also been attempted. The results as well as the theoretical background have been presented in a separate results chapter.

An attempted synthesis of the ternary skutterudite $RhGe_{1.5}Te_{1.5}$ led to the unexpected preparation of the equiatomic RhGeTe phase. Replacement of the transition metal atom by other group 9 elements resulted in the synthesis of the phase CoGeTe. The crystal structure of these materials has been investigated using single-crystal and powder X-ray diffraction. These results have been complemented with a study of both their magnetic and electrical properties. Finally, a thermal conductivity measurement provides an assessment of these materials in terms of their thermoelectric properties up to 350 K.

During the course of a study of the Co-Sn-S ternary phase diagram, the ternary phase $Co_3Sn_2S_2$ was synthesized, instead of the sought $CoSn_{1.5}S_{1.5}$ phase. It had been reported that such compound presented a break in the resistivity *vs*. temperature plot around 150 K and was ascribed to a likely phase transition, possibly magnetic. As a result of that, a powder neutron diffraction experiment was undertaken in order to shed some light on the origin of such anomaly. Moreover, transport property and magnetic measurements were carried out to obtain a further insight into the electronic nature of $Co_3Sn_2S_2$. The results obtained support those of the diffraction experiment and form the last results chapter within this thesis.

Dedicat als meus pares, Antoni i Trinitat,
i a la meva germana Laia

The most difficult barriers to overcome
are those built by yourself

Personal motto

Acknowledgements

Some persons, institutions and even places have made important contributions to this thesis. Without them, my PhD would have been much harder or even impossible. For this reason, they deserve to be acknowledged accordingly.

I would like to thank my first supervisor Dr Paz Vaqueiro Rodríguez and my second supervisor Professor Anthony V. Powell for their assistance, support and many helpful discussions and also for the opportunity they have given me of going through a life-changing experience.

Alan Barton and Paul Allan
Whose technical skills and sympathy are simply amazing.

Dr Kevin Knight and Dr Irene Margiolaki
For their help during the neutron and synchrotron scattering experiments, respectively.

Heriot-Watt University

The solid state group

Marion, the most exceptional person I have ever met.

Patricia, con quien tantas risas y secretos he compartido. Trabajar con ella siempre significó diversión. Mi doctorado no hubiera sido lo mismo sin ella.

Je voudrais remercier Anne-Sophie pour les deux plus heureuses années de ma vie et sa famille pour m'avoir accueilli et traité comme un des leurs.

María de St Andrews, cuyo doctorado y amistad han sido referencias inestimables a lo largo de todos estos años.

Mrs Thomson and the F&A Fowkes Trust for great and affordable accommodation.

The GR-11, GR-20 and TMB, natural beauty in its pure state.

Mario, Manuel, Gine, Andy and Zsolt for so many great moments.

My flatmates Alex and Amalia, my sister Laia and Cineworld for making my writing-up so enjoyable.

Table of contents

Abstract ..... *ii*

Acknowledgements ..... *iv*

Table of contents ..... *v*

1. CHAPTER 1: INTRODUCTION **1**

1.1 Thermoelectrics 2

1.1.1 Overview and applications 2

1.1.2 Thermoelectric figure of merit and limiting value 4

1.1.3 Materials for thermoelectric energy conversion 9

1.2 Skutterudites 13

1.2.1 Structure 13

1.2.2 Ternary skutterudites 16

1.2.3 Filled skutterudites 17

1.2.4 Thermoelectric properties of binary, ternary and filled skutterudites 22

1.2.5 Anomalous phenomena in filled skutterudites 24

1.3 Equiatomic ternary phases 26

1.3.1 ZrSiS-type 26

1.3.2 Anion-anion pair-forming phases 28

FeS_2 pyrite archetype 29

NiSbS ullmannite 30

CoAsS cobaltite 31

FeAsS asenopyrite 33

α-$NiAs_2$-type 36

1.4 Shandites 38

1.4.1 Metal-rich chalcogenides 38

1.4.2 Shandite structure 41

1.4.3 Parkerite structure 44

1.4.4 Structural relation between parkerite and shandite 45

1.4.5 Bonding in shandites 46

1.4.6 Electronic transport in shandites and parkerites 46

1.4.7 Half-metallicity and spintronics 48

2. CHAPTER 2: EXPERIMENTAL TECHNIQUES 50

2.1 Synthetic methods 51

2.1.1 Solid state reaction 51

2.1.2 Chemical vapour transport 51

2.2 Structural characterization 54

2.2.1 Laboratory powder X-ray diffraction 54

2.2.2 Single Crystal X-ray diffraction 56

2.2.3 Synchrotron X-ray diffraction 57

2.2.4 Anomalous scattering or resonant diffraction 59

2.2.5 Time-of-flight neutron diffraction 60

2.2.6 Group-theoretical analysis 63

2.2.7 Single crystal *vs*. powder 63

2.2.8 Integral method 66

2.2.9 Rietveld Method 68

2.2.10 Goodness of fit 69

2.3 Analytical techniques 72

2.3.1 Thermogravimetric analysis (TGA) 72

2.3.2 Electron-probe microanalysis (EPMA) 72

2.4 Physical property measurements 72

2.4.1 SQUID magnetometry 72

2.4.2 Electrical resistivity 77

2.4.3 Seebeck coefficient 79

2.4.4 Thermal conductivity 84

3. CHAPTER 3: TERNARY SKUTTERUDITES $MY_{1.5}Q_{1.5}$ (M = Co, Rh; Y = Ge, Sn; Q = S, Te) 87

3.1 Introduction 88

3.1.1 Synthesis 88

3.2 Thermogravimetric analysis 90

3.3 EPMA analysis 92

3.4 Neutron diffraction study of $CoGe_{1.5}Te_{1.5}$ 93

3.5 Neutron diffraction study of $MGe_{1.5}S_{1.5}$ (M = Co, Rh, Ir) 108

3.6 Synchrotron diffraction study of $MQ_{1.5}Te_{1.5}$ (M = Co, Rh, Ir; Q = Ge, Sn) . 118

3.7 Electrical resistivity 134

3.8 Seebeck coefficient 146

3.9 Thermal conductivity 151
3.10 Power factors 153

4. CHAPTER 4: FILLED TERNARY SKUTTERUDITES 157
4.1 Introduction 158
4.2 Synthetic approach 158
4.3 Powder X-ray diffraction 166

5. CHAPTER 5: EQUIATOMIC TERNARY PHASES MGeTe (M = Co, Rh) 170
5.1 Introduction 171
5.2 Synthesis 171
5.3 Structural characterization of MGeTe (M = Co, Rh) 172
5.4 Electrical resistivity 185
5.5 Seebeck coefficient 193
5.6 Magnetic susceptibility 196
5.7 Thermal conductivity and power factors 198

6. CHAPTER 6: $Co_3Sn_2S_2$ SHANDITE 201
6.1 Introduction 202
6.2 Synthesis 202
6.3 Thermogravimetric analysis 202
6.4 Powder neutron diffraction 203
6.5 Magnetic measurements 212
6.6 Electrical Resistivity 217
6.7 Seebeck coefficient 219

7. CONCLUSIONS 221
7.1 Anion-substituted ternary skutterudites 222
7.2 Filled ternary skutterudites 227
7.3 Equiatomic ternary phases MGeTe (M = Co, Rh) 227
7.4 $Co_3Sn_2S_2$ shandite 233
7.5 Summary 235
7.6 Further work 236

References 237

Publications in support of this thesis

Paz Vaqueiro, Gerard G. Sobany, A. V. Powell, A synchrotron powder X-ray diffraction study of the skutterudite-related phases $AB_{1.5}Te_{1.5}$ (A = Co, Rh, Ir; B = Ge, Sn), *Dalton Trans*., *xxx* (2010). Accepted.

P. Vaqueiro, Gerard G. Sobany, F. Guinet, P. Leyva-Bailen, Synthesis and characterisation of the anion-ordered tellurides MGeTe (M = Co, Rh), *Solid State Sci*., **11**(6), 1077-1082 (2009).

Paz Vaqueiro, Gerard G. Sobany, A powder neutron diffraction study of the metallic ferromagnet $Co_3Sn_2S_2$, *Solid State Sci*., **11**(2), 513-518 (2009).

Paz Vaqueiro, Gerard G. Sobany, Martin Stindl, Structure and electrical transport properties of the ordered skutterudites $MGe_{1.5}S_{1.5}$ (M = Co, Rh, Ir), *J. Solid State Chem*., **181**, 768-776 (2008).

Paz Vaqueiro and Gerard G. Sobany, Ternary skutterudites: Anion ordering and thermoelectric properties, *8th Symposium on Thermoelectric Power Generation MRS Fall Meeting*, **1044**, 185-190 (2008).

Paz Vaqueiro, Gerard G. Sobany, A. V. Powell, Kevin S. Knight, Structure and thermoelectric properties of the ordered skutterudite $CoGe_{1.5}Te_{1.5}$, *J. Solid State Chem*., **179**, 2047-2053 (2006).

Chapter 1

Introduction

1.1 Thermoelectrics

1.1.1 Overview and applications

Currently, there exist three main methods of refrigeration: The Stirling cycle, thermionic emission and thermoelectricity. The traditional and more widely used method is the Stirling cycle. It takes place in a Stirling engine in which there is a closed gas that acts as a working fluid and a piston. The latter compresses and lets the gas expand in continuous cycles releasing and absorbing heat in the process. It is fundamentally different from the cycle used in commercial refrigerators in which a phase change of the working fluid takes place (Rankine cycle). Overall, the Stirling cycle possesses the highest obtainable efficiency among any other cooling method.

Thermionic emission is a well-known effect that has been used traditionally for power generation until recently, when its applications for refrigeration purposes have been studied [1]. The basic principle underlying this effect is that electrons emitted from a hot cathode have enough energy to overcome the energy barrier between anode and cathode in a vacuum. Such kinetic energy can be transformed into potential energy at the colder anode, which can be used for powering any device. Thus, the working fluid in this case is an electron gas that receives heat at high temperatures and rejects heat at lower temperatures, delivering useful electrical work in the process. It has been shown that thermionic refrigeration is only possible at high temperatures and presents several advantages in environments where cold water is not available, such as rockets or satellites.

Thermoelectric phenomena are applied to refrigeration taking advantage of the fact that charge carriers are able to carry heat as well as electric charge in conductors acting as an effective working fluid in thermoelectric devices. Broadly speaking, such devices convert thermal energy heat into electricity using solid-state technology based on the Seebeck effect and present many advantages. They can work as electric generators or as refrigeration devices that use electricity to pump heat from cold to hot sides, both without any moving parts or bulk fluids that may be toxic or dangerous for the environment, namely chlorofluorocarbons (CFCs) or hydrochlorofluorocarbons (HCFCs). Moreover, thermoelectric devices are small, lightweight and ideal for small-scale refrigeration, and are less prone to failure because there are no moving parts.

Application of thermoelectric technology has been limited due to its relatively low heat to electricity conversion efficiency. It is normally expressed as a function of the Carnot efficiency, which is the maximum achievable and is dictated by the thermodynamic laws. At present, thermoelectric devices operate at about 10% of Carnot efficiency, whereas that of a conventional refrigerator approaches a 30% and the largest air conditioners for big buildings operate even near a 90% efficiency [2]. Comparative studies carried out between a thermoelectric module and a small compressor clearly show that nowadays they are still far away from replacing compressors for the range of a few hundred watts of cooling [3]. The prospects of large-scale power generation by thermoelectric means are also poor. However, assets such as high reliability, low maintenance and a long life make them very attractive for several applications. The most appealing one is enhancing the overall efficiency of conventional power plants by waste heat recovery from turbines as well as from automobiles. The latter example is especially interesting because it involves the automobile industry and the vast amounts of investment it can attract. The waste heat represents a 70% of the energy provided by the gasoline; being only 30% of the energy is converted into driving force [4]. Power generation in hostile environments is another important application, as seen in radioisotope thermoelectric generators (RTGs) used in deep-space probes, where the hot source consists of a radioisotope, usually $^{238}PuO_2$, which disintegrates releasing heat in the process. On the whole, there exist three major flaws that hamper the wide application of such devices:

- Compared to traditional compressors, they reach a 25% of their efficiency, resulting in four times the operation costs and the need of larger heat exchangers [5].
- The costs are at least double the cost of competitive systems.
- To date, there have not been simulation tools capable of optimising thermoelectric system designs for cost, efficiency, size and other important parameters.

Cooling power wise, thermoelectric devices find important applications in the field of electronics and biology for powers ranging from a few milliWatts up to two or three tens of Watts because the above-mentioned advantages clearly outweigh the efficiency consideration. Interesting uses applied to biology have been put into practice in the direct cooling of personnel, the so-called man-portable microclimate systems. Temperature stabilization purposes also fit the capabilities of thermoelectric devices when small cooling and heating powers are required. They are of enormous utility in biological sciences where often it is critical to maintain a constant temperature to within

a tenth of degree, particularly for medication and food. Besides, hot/cold stimulators, microtome stage coolers, portable mini cool boxes for insulin and cold plates for dental cement are everyday biological uses where thermoelectric technology has proved to outperform any other cooling technology. Nonetheless, of much more importance is the electronic application. They are of paramount importance in the field of photoelectric detectors, given that their sensitivity as well as their signal-to-noise ratio are highly dependant on the temperature. Likewise, they play a leading rôle in microprocessor technology. The performance enhancement that microprocessors undergo when they can be conveniently and reliably cooled is outstanding. Hence, it is possible to use thermoelectric coolers to gain speed. For instance, most microprocessors currently operate at approximately 100 °C. By cooling them down to approximately 0 °C, their speed may increase by a factor of 2 and their reliability by as much as two orders of magnitude. However, requirements such as the price of the starting materials and the environmentally friendliness are also important factors that may prevent domestic applications of thermoelectric devices from becoming widespread.

1.1.2 Thermoelectric figure of merit and limiting value

Pioneering work developing the theory of thermoelectric cooling was carried out by Altenkirch [6] as early as 1911 and thermodynamic expressions for the principal parameters of a thermoelectric refrigerator were derived. Later on, in 1957, A. F. Ioffe developed those concepts and showed their applicability to build practical thermoelectric devices [7].

A thermoelectric couple consists of two semiconducting legs, having opposite charge carrier signs, connected electrically in series and thermally in parallel (Figure 1-1). Let us assume a model of thermoelectric couple that will allow us to find reasonably simple expressions for its performance. In such a model, the problem of the heat transfer between the heating and the cooling medium will not be considered. It will be assumed that the junction resistance is negligible with respect to the bulk resistance of the arms whose cross-sectional area along their length is uniform. Moreover, the thermal conductivity, the Seebeck coefficient and the electrical conductivity are considered independent of the temperature (which is true for small variations of temperature). For more realistic models and the expressions of their performances the reader is referred to [8].

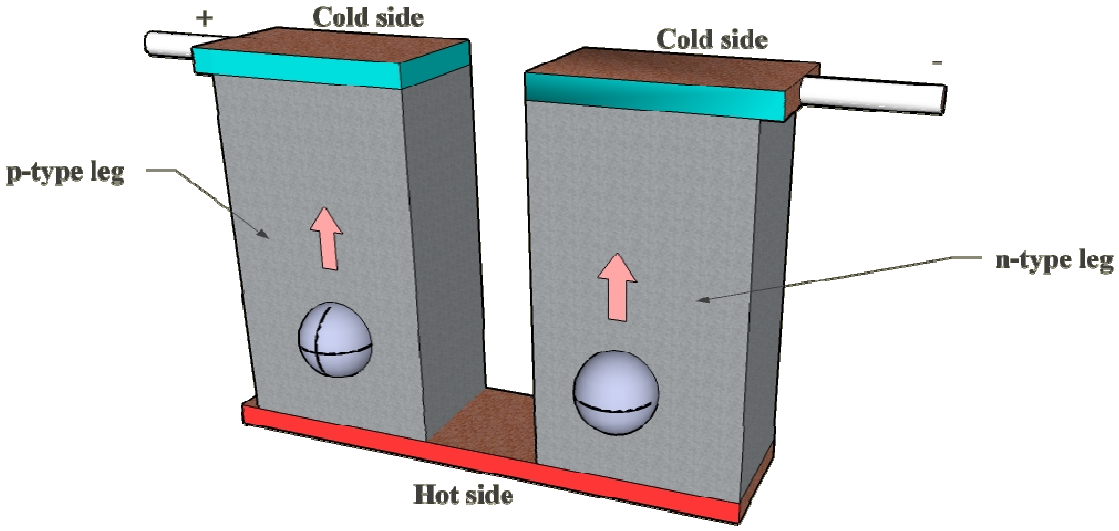

Figure 1-1 Schematic of a thermoelectric generator with its semiconducting legs thermally in parallel and electrically in series.

Hence, its efficiency working as a power generator (γ) or as a refrigerator (φ) can be calculated taking into account effects such as the Peltier heat that will be absorbed at the hot junction, the Joule heat generated in the elements and the heat transmitted through the elements away from the hot junction. Thus, an expression for both may readily be obtained [9]:

$$\gamma = \frac{\Delta T}{T_H}\left[\frac{(1+Z\overline{T})^{1/2}-1}{(1+Z\overline{T})^{1/2}+(T_C/T_H)}\right] \qquad \textbf{(1-1)}$$

$$\varphi = \frac{T_C}{\Delta T}\left[\frac{(1+Z\overline{T})^{1/2}-T_H/T_C}{(1+Z\overline{T})^{1/2}+1}\right] \qquad \textbf{(1-2)}$$

Where T_C and T_H are the temperatures at cold and hot sides respectively; $\overline{T}$ is the arithmetic mean of both temperatures and Z is the figure of merit of the couple.

It is worth noticing the fact that both efficiencies are limited by the Carnot efficiency reduced by a factor (square bracketed) depending on the thermoelectric figure of merit Z. The first term tells us about the maximum efficiency achievable dictated by thermodynamics, whereas the second term includes structural and physical properties of the couple gathered in the variable Z, which is defined as:

$$Z = \frac{(S_p - S_n)^2}{\left[(\rho_p \kappa_p)^{1/2} + (\rho_n \kappa_n)^{1/2}\right]^2} \qquad \textbf{(1-3)}$$

Where S (in μVK^{-1}), ρ (in Ωcm) and κ (in $Wcm^{-1}K^{-1}$) correspond to the Seebeck coefficient, the electrical resistivity and the thermal conductivity of the *p*-type leg (*p*) or the *n*-type leg (*n*), respectively. The definition of these three transport properties, alongside the Peltier heat and the Thomson relation is given in section 2.4. Z has units of K^{-1} and contains information about the transport properties of the materials from which the thermocouple is made and their effect on its global performance. Z is a function of temperature as well as the variables that define it. However, it is a rather cumbersome expression and implies that materials have to be tested in pairs to assess their suitability for thermoelectric purposes. This problem can be solved if we assume a hypothetical thermocouple made of exactly the same materials but having both legs identical Seebeck coefficient of opposite sign. The resulting expression is:

$$Z = \frac{S^2}{\rho\kappa} \qquad \textbf{(1-4)}$$

This formula is equivalent to the figure of merit of a couple, although concerning a single material. Likewise, an equivalent expression can be written considering the reciprocal relation between the electrical conductivity and the electrical resistivity:

$$Z = \frac{S^2\sigma}{\kappa} \qquad \textbf{(1-5)}$$

The numerator $S^2\sigma$ is the so-called power factor ($\mu Wcm^{-1}K^{-2}$) and tells us about the assets of a certain material regarding only electronic properties. It can be shown that if the *n* and *p* legs are made of materials with similar electrical and thermal properties, then Z of the couple can be maximized if both Z_p and Z_n are maximized independently of each other [10]. The maximum Z_{Couple} results when an *n*-type material with the highest Z_n value at a certain temperature is used with a *p*-type material with the highest Z_p value.

The three transport properties Z depends on can be measured independently and substituted into equation (1-5). Nevertheless, Harman has developed a method to calculate the value of Z in one single measurement as a much faster means of assessing thermoelectric materials. A measurement of the potential drop between ends is needed for a constant current (V_T) and an alternating current (V_{ac}) in order to separate the ohmic and thermoelectric contributions. Then, taking into account the relation between the Seebeck coefficient and the thermal conductivity at steady state:

$$SIT = \kappa \Delta T(A/L) \qquad \textbf{(1-6)}$$

Where T is the absolute temperature, I the electric current, ΔT is the temperature difference between ends and A and L correspond to the cross-sectional area and the sample length, respectively. The thermoelectric figure of merit is now given by [11]:

$$Z = \frac{V_T - V_{ac}}{V_{ac} T} \qquad \textbf{(1-7)}$$

Such a method, however, is very sensitive to small heat losses and great care has to be taken when mounting the sample, giving rise to large inaccuracies otherwise. Further, it has been shown that is possible to express the thermoelectric figure of merit Z in terms of parameters that depend directly on the band structure of the material as well as the scattering processes that take place between charge carriers and the lattice; which ultimately determine the value of each transport property. Such a relation is useful to assign trends in the temperature dependence plots of the transport coefficients to specific variations in the electronic structure and the scattering mechanisms governing them. Chasmar and Stratton showed that the dimensionless quantity ZT for an extrinsic semiconductor can be expressed in terms of three other dimensionless quantities, namely, the reduced Fermi energy, E_F^*, a scattering parameter r and a material parameter, β, as follows [12]:

$$ZT = \frac{[E_F^* - (r + \frac{5}{2})]^2}{(\beta e^{E_F^*})^{-1} + (r + \frac{5}{2})} \qquad \textbf{(1-8)}$$

The Fermi energy corresponds to the energy of the highest occupied electronic energy level at 0 K, and the reduced Fermi energy is that relative to the thermal energy $k_B T$, (being k_B the Boltzmann constant) defined as:

$$E_F^* = E_F / k_B T \qquad \textbf{(1-9)}$$

The scattering parameter r is the exponent the temperature is powered to in the temperature dependence plot of the charge carrier mobility. Different values of r correspond to different charge carrier scattering mechanisms [13]. Finally, β is the so-called material factor and is proportional to the carrier mobility. It is worthwhile noticing that three assumptions have been made in deriving expression (1-6):

- The semiconductor is non-degenerate, *i.e*. charge carriers obey classical statistics and the probability of finding occupied electronic states as a function of their energy follows a Maxwell-Boltzmann distribution.
- The conduction mechanism is dominated by one type of charge carrier (either hole or electron) in one band solely (either valence or conduction band).
- The phonon-drag effect does not contribute to the thermopower. This assumption is realistic given the fact that phonon drag effects are rarely observed other than at low temperatures and it is unlikely that it enhances Z values [14].

To sum up, in order for a thermoelectric couple to achieve the maximum efficiency, *i.e*. either maximum γ or maximum φ, two conditions can be readily inferred from equations (1-1) and (1-2): a large or a small temperature gradient, respectively, to maximize the Carnot efficiency and a Z value as large as possible. As a matter of fact, it is clear that for a thermoelectric couple running either as a power generator or as a cooling device, the value of Z is crucial to improve dramatically its efficiency at a given temperature gradient. Therefore, according to the definition of Z, large Seebeck and electrical conductivity values as well as low thermal conductivity values are sought. From expression (1-6) it is also inferred that a large scattering parameter *r*, high carrier mobilities and an appropriate reduced Fermi energy are desirable features in a potential material for thermoelectric applications. Nonetheless, the feasibility of unlimitedly large Z values may be questioned. It has been calculated that with a ZT = 4, the efficiency of thermoelectric cooling devices would be equal to that of compressor-based home refrigerators reaching a 55% of the Carnot efficiency [15]. A value of ZT = 3 would make thermoelectric home refrigerators economically competitive.

It has been shown by means of irreversible process thermodynamics that the upper bound of the thermoelectric figure of merit is infinity [16]. The Seebeck coefficient is a monotonically growing function of the reduced Fermi energy; which, in turn, depends on the size of the band gap [7]. So is the conductivity of the charge carrier concentration. If the lattice thermal conductivity could be reduced to the minimum, then no apparent upper limit is expected. Other studies have shown, however, that there exist relationships among the various physical quantities that determine the transport properties; namely, band gap, material factor and scattering parameter, that are not taken into account in the above treatment [17]. Larger band gaps do not always lead to an increase of ZT, but the maximum value of ZT tends to level off. It has been demonstrated that band gaps larger than ten times k_BT are not effective in improving the

figure of merit [18]. Further, it has also been demonstrated that the adjustability of the Fermi energy is limited because of dopant solubility limitations, leading to an upper bound on ZT of approximately 10 [19].

1.1.3 Materials for thermoelectric energy conversion

Very few materials are suitable for thermoelectric energy conversion. Insulators have large Seebeck coefficients (~ 1 mVK^{-1}), but extremely poor electric conductivity. Conversely, metals have small Seebeck coefficients (~ 5 μVK^{-1}) and good electrical conductivity. Semiconductors, however, possess a moderately large Seebeck coefficient (~ 200 μVK^{-1}) and worse electrical conductivity than metals but better than that of insulators. Therefore the ideal material should be a semiconductor whose thermoelectric properties can be optimized to maximize its thermoelectric figure of merit Z. Equation (1-5) is based entirely on measurable transport properties, from which it can be inferred that the following features are highly desirable in a good thermoelectric material:

- High thermoelectric power S. To produce high voltage in the circuit when a temperature gradient is applied.
- Large electrical conductivity σ. To minimize losses caused by Joule heating.
- Small thermal conductivity κ. To retain as much heat as possible at the hot side and minimize the losses down the arms of the couple towards the cold side.

Bond theory tells us that semiconductors composed of elements covalently bonded will have high conductivity owing to the larger orbital overlapping present throughout the covalently bonded network. Moreover, if these elements are heavy and are found in large numbers within the unit cell, the thermal conductivity of the material will be low as phonon scattering processes will occur to a greater extent. Therefore, thermoelectric materials that fit in this description will be narrow-gap semiconductors that have been doped to maximize their electronic properties [20]. Elements from the lower right corner of the periodic table comply with these characteristics, being reflected in the current use of bismuth telluride Bi_2Te_3 or Bi_2Te_3-Sb_2Te_3 alloys for refrigeration applications and Si-Ge alloys for power generation purposes at high temperature. The best commercial thermoelectric materials are $Bi_2Te_{2.7}Se_{0.3}$ and $Bi_{0.5}Sb_{1.5}Te_3$ with a ZT ~ 1 at 300 K as well as $Si_{0.7}Ge_{0.3}$ with a ZT ~ 0.6-0.7 at 1200 K. Another classical bulk binary semiconductor used in mid-temperature thermoelectric applications is PbTe, which reaches a ZT ~ 0.7 at 700 K [14]. It is also possible to obtain a ZT value larger

than unity at 700 K in solid solutions of $AgSbTe_2$ (80%) and GeTe (20%), the so-called TAGS (Te-Ag-Ge-Sb), however, stability problems at this temperature prevents them from being used in commercial thermoelectric devices.

The quest for finding higher-performance thermoelectric materials has opened new ideas as to the features that good thermoelectric materials must possess. There is general agreement in the fact that it must be a narrow-gap semiconductor, *i.e*. possessing a band gap of approximately 10 k_BT, having large charge carrier mobility. In the early nineties the advent of new promising materials based on an entirely different approach, such as semiconductors with 'rattling' atoms or molecules, correlated metals or semiconductors and superlattices, opened a new field that seemed exhausted ten years before [21]. New complex inorganic structures based on ternary and quaternary chalcogenides containing heavy atoms and possessing low dimensional structures have recently attracted the attention of researchers. Among them, it is noteworthy the compound $CsBi_4Te_6$ possessing a layered structure made of $(Bi_4Te_6)^{1-}$ slabs intercalated with layers of Cs^+ ions. $CsBi_4Te_6$ reaches a ZT of 0.8 at 225 K, which is the highest value ever reported below room temperature [22]. Thallium-containing compounds Tl_9BiTe_6 and Tl_2SnTe_5 are also both ternary chalcogenides with very low thermal conductivity (~0.39 and 0.5 $Wm^{-1}K^{-1}$, respectively) which attain ZT values of 1.2 and 1 at 500 and 300 K, respectively [23]. Recently, a high ZT (~ 0.95 at 1275 K) has been discovered in the compound $Yb_{14}MnSb_{11}$, outperforming state-of-the-art high-temperature thermoelectric materials [24]. Its structure is composed of isolated anion units, *i.e*. $(MnSb_4)^{9-}$ tetrahedra, polyatomic $(Sb_3)^{7-}$ anions and isolated Sb^{3-} anions, where electrons are donated by the Yb^{2+} cations. β–Zn_4Sb_3 is one of the most efficient thermoelectric materials known, as it reaches a ZT of 1.3 at 670 K, which falls within the mid-temperature range and outperforms existing PbTe and TAGS materials. Its structure can also be described in a similar fashion as the above compounds, *i.e*. Sb_2^{4-} dumbbells and isolated Sb^{3-} units, where electrons are donated by Zn^{2+} cations. The disorder of the Zn^{2+} cations confers this structure one of the lowest thermal conductivity values known for a crystalline material, a truly glass-like value (0.6 $Wm^{-1}K^{-1}$ at 400 K) (Figure 1-2, right) [25]. All these compounds, along with skutterudites (section 1.2.1), can be included within a wider group of Zintl phases with interesting thermoelectric applications. Zintl phases are composed of electropositive atoms that donate their electrons to an electronegative anion framework in order to satisfy the octet rule. Cations in Zintl phases allow alloying and doping to vary electron concentration as well

as increase phonon scattering. Thus, by understanding the Zintl chemistry, the properties can be engineered and tuned to optimize thermoelectric performance [26].

Layered cobalt oxides also attracted the interest of the scientific community since a high Seebeck coefficient was reported in $NaCo_2O_4$ single crystals [27]. This structure is composed of CdI_2-type CoO_6 edge-sharing octahedra layers and the Na layers are located in between along the *c*-axis, which may be partially occupied. The Na layers are strongly disordered, which causes important phonon scattering, and are also prone to chemical substitution by other species. The CoO_6 blocks are responsible for the electronic properties and play a rôle of charge confinement within the sodium cobaltite structure. Thus, a ZT of 0.83 at 973 K has been measured for the compound $(Ca_2CoO_3)_{0.7}CoO_2$ [28].

Research on the pentatellurides $HfTe_5$ and $ZrTe_5$ has been boosted given the dearth of suitable thermoelectric materials for low-temperature applications. These materials exhibit a high Seebeck in the low temperature range (~ 100 μVK^{-1}), which makes them very interesting. They are low-dimensional structures comprised of MTe_3 (M = Hf or Zr) chains which are subsequently bridged into large two-dimensional sheets by tellurium atoms. These sheets are weakly bound one another by van der Waals interactions [29]. Adequately doped with selenium, these materials have been reported to have a power factor exceeding that of bismuth telluride at low temperature [29].

Recently, the lead-based chalcogenide compounds $AgPb_mSbTe_{m+2}$, the so-called LAST-*m* (Pb-Sb-Ag-Te) materials, have shown optimal thermoelectric performance with ZT values ranging from 1.2 (LAST-10) to 1.7 (LAST-18) at 700 K [30]. They possess the rocksalt structure and a glass-like thermal conductivity (~0.45 $Wm^{-1}K^{-1}$ at 700 K), which is thought to be accounted for endotaxially dispersed quantum dots embedded in a matrix [23].

A complete new approach to the problem of increasing Z has been given by Dresselhaus *et al*. predicting that it may be possible by preparing materials in the form of multilayered superlattices. The layering would then enhance the phonon scattering, thereby increasing Z even further [31,32]. There are two factors responsible for such an increase over the bulk value [33]:

- The separation of the two bands (electrons and holes) and the transformation of the material in an effective one-band system.
- The two-dimensional nature of the density of states (DOS).

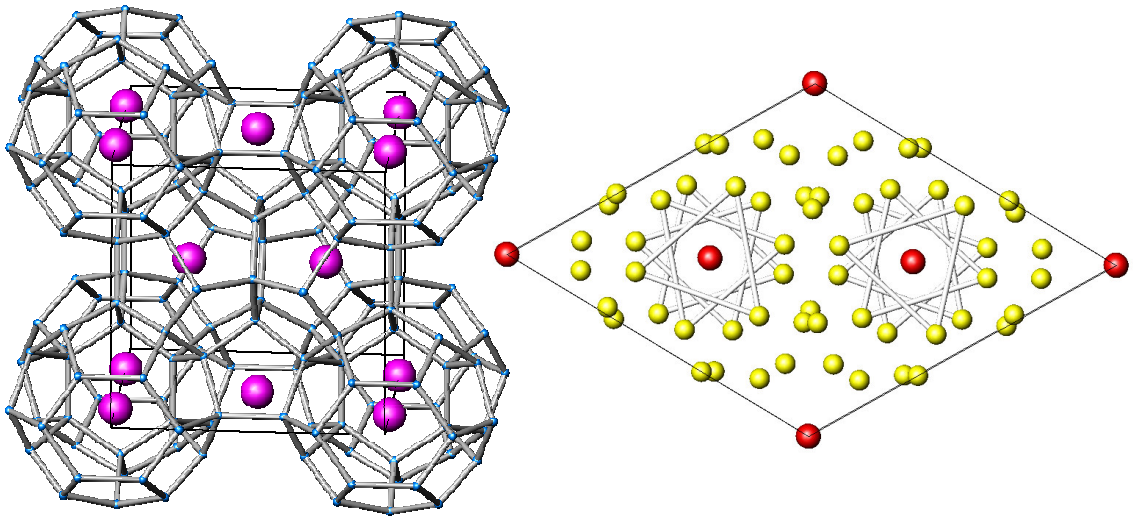

Figure 1-2 Left: Clathrate type I where the rattling atoms are highlighted (in purple). Right: Unit cell of the β-Zn_4Sb_3. Key: Sb in red, Zn in yellow.

Thus, it has been calculated that a Bi_2Te_3 quantum-well structure has the potential to increase ZT 13 times over the bulk value [31]. This prediction has been confirmed by Venkatasubramanian who measured a ZT of 2.4 for *p*-type superlattices at room temperature and a ZT of 1.2 for *n*-type superlattices synthesized by depositing thin films (1 to 4 nm) of Bi_2Te_3 and Sb_2Te_3, alternatively [34].

In 1993 G. A. Slack suggested that the best thermoelectric material should possess the electron properties of a crystalline material as well as the thermal properties of an amorphous or glass-like material, the so-called PGEC (Phonon-Glass-Electron-Crystal) approach [35]. Since then, several PGEC materials fulfilling both constraints have started new research lines. Materials whose thermal conductivity is reduced by the 'rattling' motion of a guest species fall within this group. The most important examples of such compounds are the filled skutterudites and the clathrates. Skutterudites are cubic structures that possess a void surrounded by a cluster of MX_6 octahedra (M = Co, Rh, Ir; X = P, As, Sb) that may be filled with species such as lanthanides, actinides, alkali and alkaline earths, *etc*. Their structure is comprehensively described in the next section. Clathrates are also PGEC materials containing up to eight cavities in their unit cell. They form a framework of cages that contain small alkali or alkaline earth that are strong phonon scatterers (Figure 1-2, left). Type I clathrates possess glass-like thermal conductivity and high thermopower, which make them suitable for thermoelectric applications after they have been heavily doped. ZT values as high as 0.7 at 700 K and 0.87 at 870 K have been reported for $Ba_8Ga_{16}Ge_{30}$ and $Ba_8Ga_{16}Si_{30}$ [36].

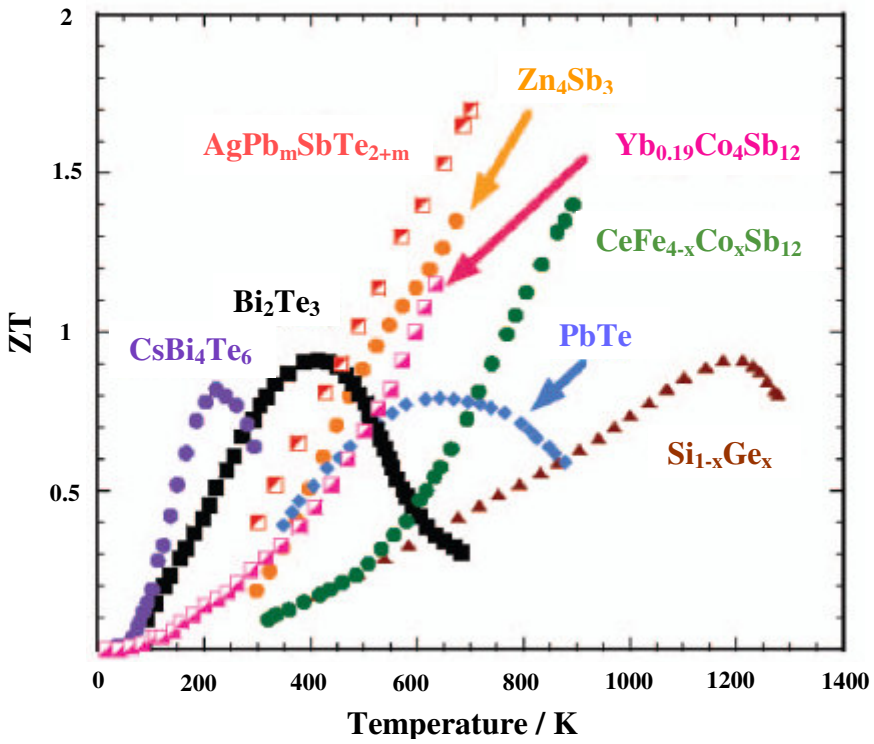

Figure 1-3 Dimensionless thermoelectric figure of merit of several state-of-the-art and new thermoelectric materials. Extracted from reference [37].

An overall picture of the dimensionless figures of merit for the most relevant state-of-the-art and new thermoelectric materials is shown in Figure 1-3.

1.2 Skutterudites

1.2.1 Structure

The name Skutterudite comes from the Norwegian town where the $CoAs_3$ mineral ore was extracted and the mineral structure was first studied. Its general formula is MX_3 where A corresponds to elements from group 9 (Co, Rh, Ir) and X to elements from group 15 (P, As, Sb). The binary skutterudite structure crystallizes in the body-centred cubic space group $Im\bar{3}$ [38]. The crystallographic unit cell consists of 32 atoms (M_8X_{24}) where the metallic atoms occupy the Wyckoff *c* positions and group 15 atoms (also known as pnictogen atoms) the *g* positions. It can be regarded as a distortion of the more symmetric structure of the cubic perovskite-related ReO_3. In skutterudites, the ReO_3-like octahedra are tilted and share corners forming an infinite network [39]. This tilt gives rise to a rather peculiar disposition of the pnictogen atoms forming nearly perfect square four-membered rings of X atoms. These planar X_4 rings are opposed perpendicularly running along the three crystallographic axes and were first studied by

Oftedal who stated that in order to be perfect squared rings their y and z coordinates should comply with $y + z = ½$, the so-called Oftedal relation [40]. Also, it is shown that one can completely determine the skutterudite structure by specifying the exact position of the pnictogen atoms and the lattice constant. However, more precise subsequent studies indicated that the Oftedal relation is rarely accomplished [41]. As a matter of fact, the exact values of y and z depend on the particular compound and reflect the fact that the rings are not perfect squares, but distorted and forming rectangles. Moreover, in order to satisfy the relation, a much longer side length would be necessary between pnictogen atoms, thereby weakening the covalent interaction.

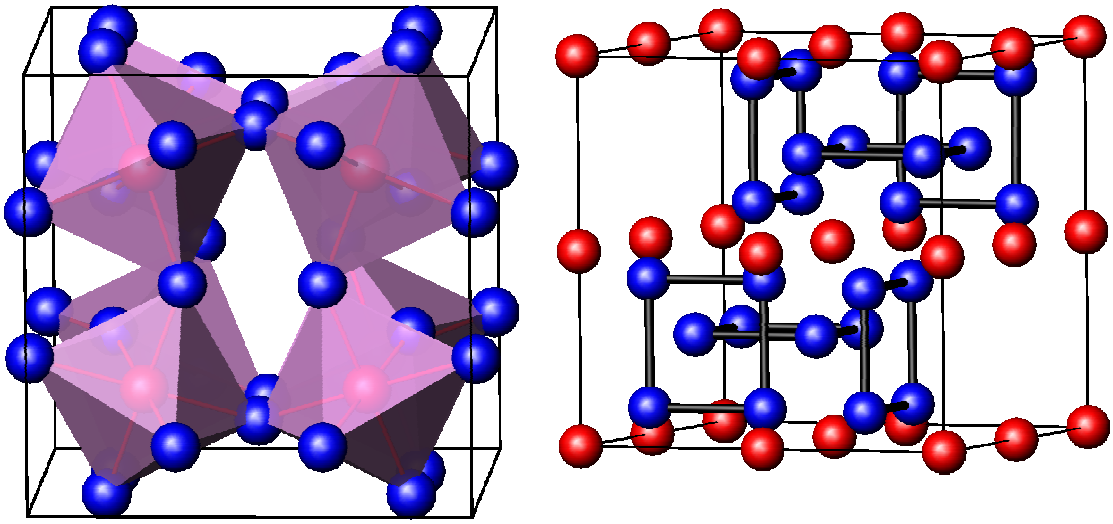

Figure 1-4 Left: Polyhedral representation of a binary skutterudite; view of the central icosahedral cavity surrounded by 12 pnictogen atoms. Right: $CoSb_3$ $Im\bar{3}$ unit cell where the pnictogen Sb_4^{4-} rings have been highlighted. Key: Sb in blue, Co in red.

Had the skutterudite octahedra been undistorted, the highly symmetric ReO_3 ($Pm\bar{3}m$) structure would form instead [42]. Therefore, in order to maintain the skutterudite phase, the MX_6 octahedra undergo a slight trigonal antiprismatic distortion while the pnictogen rings assume a rectangular rather than square shape as a means of achieving stronger and more covalent bonding; whereby the electric properties are enhanced. Another important consequence of the octahedral tilting is the existence of two voids within the unit cell. The unit cell can be described as composed of 8 cubes 6 of them having a pnictogen ring located in its centre. The other two remain empty at opposite corners within the unit cell. Each of these voids is surrounded by 12 pnictogen atoms forming an icosahedral cage with a volume that varies depending on the skutterudite (Figure 1-4).

As far as electrons are concerned, the reason why only elements from the group 9 and 15 form skutterudites is not casual. Each metallic atom is at the centre of an octahedron surrounded by 6 pnictogen atoms. We know that each pnictogen atom is bonded to two more of its kind to form the X_4 rings and to two metallic atoms; that leaves three electrons per pnictogen atom to interact with two metallic atoms. That results in 9 overall electrons for each group 9 atom: $(3 \times 6) / 2$. It turns out that if we add these to the 9 electrons already owned by the M atoms (d^7s^2 configuration) the metallic atom acquires the 18-electron rare-gas configuration, giving rise to diamagnetism and semiconducting behaviour [43]. As far as the pnictogen atoms are concerned, they also acquire the closed-shell configuration if we assume a 3+ oxidation state for the M atom. To their s^2p^3 configuration we have to add two electrons supplied by the other two X atoms they are attached covalently to and half an electron supplied by each of the two M atoms. This would leave the M atom in a d^6 configuration within an octahedral site. The crystal field splitting into a ground state triplet (t_{2g}) and an excited state doublet (e_g) would let the 6 electrons occupy a low-spin state, leaving the t_{2g} orbitals (that hybridise with the s and p states of the X atoms to form the *dps* orbital complex, which provides the M-X bonding) completely full and with no net magnetic moment and a diamagnetic behaviour [44]. Thus, we obtain a total valence electron count (VEC) of 144 electrons for the whole M_8X_{24} unit cell (9 from each M atom and 3 from each X atom).

The semiconducting skutterudite structure will not form unless the above number of electrons is available. This is the fundament for the synthesis of ternary skutterudites in which the VEC is maintained. Nevertheless, there are exceptions to this bonding scheme. NiP_3 and PdP_3 are the only binary skutterudite phases formed by non-group 9 metals. They are metastable phases that should not form *a priori*. As expected, they possess metallic conductivity and paramagnetism [45,46]. VECs lower than 72 will inevitably lead to unfilled bands and metallic conductivity thereof. Filling is a known method of synthesizing ternary compounds with the skutterudite structure, where the guest atoms occupy the icosahedral voids within the unit cell. Such atoms are electropositive and donate their electrons to the M-X cage-forming structure, thereby stabilizing it and allowing group 8 atoms to incorporate in the M-X framework (Table 1-2). Filled-skutterudite VECs obtained vary between 71 and 72 depending on the filling fraction, the oxidation state of the filler atom and the presence of mixed valency [47,48]. Recently, the new skutterudite $BaPt_4Ge_{12}$ with a VEC of 66 has been synthesized based entirely on a germanium framework. The filler atom, however,

strongly stabilizes the structure and there is no evidence of the 'rattling' motion observed in other filled skutterudites (section 1.2.3) [49].

1.2.2 Ternary skutterudites

Ternary skutterudites are another known family of unfilled skutterudites, although there is little information about their electrical and thermal properties. They are formed by isoelectronic substitution either on the cation or anion sites keeping the VEC constant, *i.e*. equal to 72 per formula unit or 144 per unit cell, thus they all are diamagnetic semiconductors. M, M' and M'' correspond to group 9, 8 and 10 metals, respectively; whereas X, X' and X'' correspond to group 15, 14 and 16 elements, respectively. Their reported thermoelectric properties are summarized in (Table 1-4) and they can be classified according to four different substitution patterns.

The last three columns are anion-substituted skutterudites, whereas the second column shows cation-substituted skutterudites (Table 1-1). On average, the lattice parameter increases by 0.7%, 1.1% and 0.6% when substitution occurs either on the transition metal site, the pnictogen site or both sides simultaneously, respectively [50].

Table 1-1 Known ternary skutterudites. The nine binary skutterudites have been included for the sake of completeness. Stoichiometry as per half of the unit cell [51,52].

M_4X_{12}	$M'_2M''_2X_{12}$	$M_4X'_6X''_6$	$M'_4X_8X'_4$	$M''_4X_8X'_4$
Co_4P_{12}	$Fe_2Ni_2Sb_{12}$	$Co_4Ge_6Te_6$	$Fe_4Sb_8Se_4$	$Ni_4P_8Ge_4$
Co_4As_{12}	$Fe_2Ni_2As_{12}$	$Co_4Sn_6Se_6$	$Fe_4Sb_8Te_4$	$Ni_4Bi_8Ge_4$
Co_4Sb_{12}	$Fe_2Pd_2Sb_{12}$	$Co_4Sn_6Te_6$	$Ru_4Sb_8Se_4$	$Pt_4Sb_{7.2}Sn_{4.8}$
Rh_4P_{12}	$Fe_2Pt_2Sb_{12}$	$Co_4Ge_6S_6$	$Ru_4Sb_8Te_4$	$Ni_4Sb_8Sn_4$
Rh_4As_{12}	$Ru_2Ni_2Sb_{12}$	$Co_4Ge_6Se_6$	$Os_4Sb_8Te_4$	$Ni_4Sb_9Sn_3$
Rh_4Sb_{12}	$Ru_2Pd_2Sb_{12}$	$Rh_4Ge_6S_6$		$Ni_4As_8Ge_4$
Ir_4P_{12}	$Ru_2Pt_2Sb_{12}$	$Ir_4Ge_6S_6$		$Ni_4As_{9.1}Ge_{2.9}$
Ir_4As_{12}		$Ir_4Ge_6Se_6$		
Ir_4Sb_{12}		$Ir_4Ge_6S_6$		
		$Ir_4Sn_6S_6$[a]		
		$Ir_4Sn_6Se_6$		
		$Ir_4Sn_6Te_6$		

[a] **Synthesized at high pressure (40 kbar) [53].**

Cation substitution does not lower the cubic $Im\overline{3}$ symmetry of the parent binary compound, given that both cations remain disordered within the 8*c* Wyckoff position [54]. Reported crystallographic studies on mixed substitution, *i.e*. substitution in both the cation and anion site keeping the VEC constant (columns four and five in Table

1-1), in $Ni_4Sb_9Sn_3$ show that the archetype binary skutterudite structure ($Im\bar{3}$) is also maintained [52]. On the contrary, if the substitution takes place on the anion site, distortion of the square rings may occur. Such distortion has been previously studied by Partik *et al*. who carried out a single crystal study on twinned crystals of $CoGe_{1.5}Q_{1.5}$ (Q = S, Se), showing that the Ge and Q atoms exhibit long-range ordering, which results in a lowering of the symmetry from cubic ($Im\bar{3}$) to rhombohedral ($R3$) [55]. This evidence has been confirmed by infra-red spectra analysis, where the large number of lattice vibrations obtained in the compounds $CoGe_{1.5}S_{1.5}$, $CoGe_{1.5}Se_{1.5}$, $IrGe_{1.5}Se_{1.5}$ and $IrGe_{1.5}S_{1.5}$ demonstrates the ordering in the non-metal lattice [56].

Two structural studies of ternary skutterudites of the type $M_4X'_6X''_6$, *i.e.* $IrSn_{1.5}Te_{1.5}$ and $CoSn_{1.5}Te_{1.5}$, have been recently carried out using the structural model determined in this thesis, which is described in chapter 3 and has been published in [57,58]. They both confirm the conclusions obtained within this thesis as to anion ordering. It is also noteworthy that the new filled ternary skutterudites $A_xCo_4Ge_6Te_6$ (A = La, Yb) and $A_xCo_4Ge_6Se_6$ (A = Ce, Yb, Eu) with $0 \leq x \leq 0.3$ have been recently reported by the groups of Navratil *et al*. and Lin *et al*. [59].

1.2.3 Filled skutterudites

The first filled skutterudite reported was $LaFe_4P_{12}$ in 1977 by Jeitschko *et al*. [42]. They are synthesized by filling the empty cavities existing within the skutterudite unit cell, which can be expressed as $\square_2T_8X_{24}$, where the two cavities per unit cell are represented as a void $\square$. In this case, T stands for a group 8 instead of a group 9 metal seen in binary skutterudites (Figure 1-5). The electropositive ion supplies the missing electron of the iron group in order to fulfil the electron requirements and neutralize the structure. Hence, a general formula to describe a filled skutterudite is RT_4X_{12} or $R^{4+}[T_4X_{12}]^{4-}$ if charge balance is to be indicated, where each rare-earth atom is located at the centre of a distorted icosahedron formed by 12 pnictogen atoms. The size of this icosahedral cage formed by the pnictogen atoms increases as the pnictogen atom changes down the group.

Moreover, the atomic displacement parameters of the rare earths are unusually large, indicating a strong interaction between the lattice phonons and the atom within the cage, giving rise to an important reduction of the lattice thermal conductivity [60].

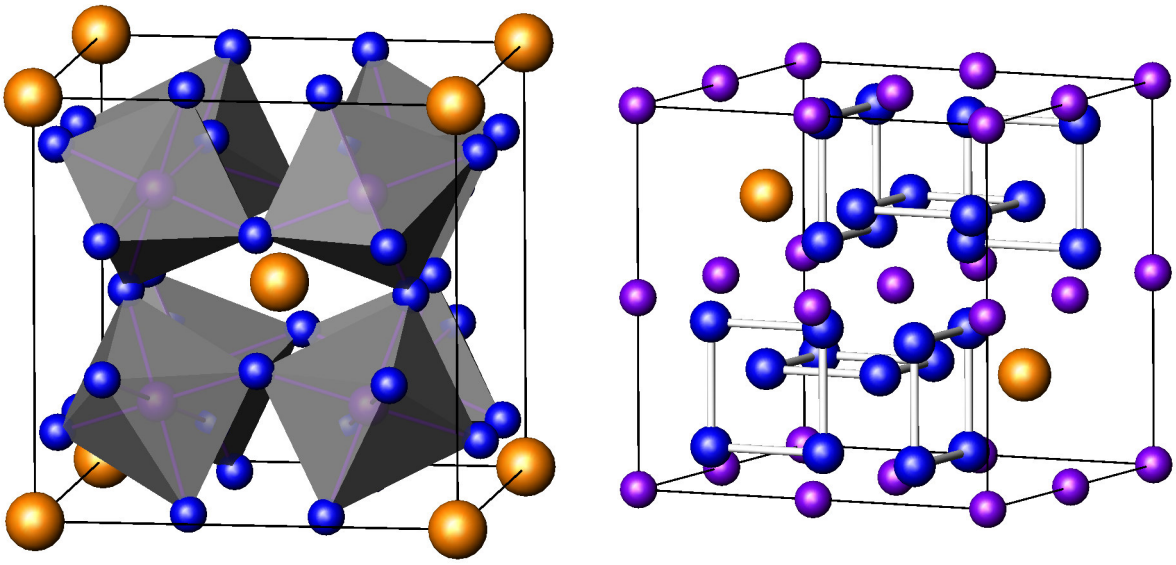

Figure 1-5 Left: Polyhedral representation of the $LaFe_4Sb_{12}$ filled skutterudite; view of the filled central icosahedral cavity. Right: $LaFe_4Sb_{12}$ unit cell where the pnictogen Sb_4^{4-} rings along with the filled voids are recognizable. Key: Fe in purple, Sb in blue, La in golden.

The kind of movement undergone by the filler atom has been described with the term 'rattling', used for the first time by Braun and Jeitschko in 1980 [61]. It is seen in Table 1-2 that not all the rare earth elements are present. Filled skutterudites containing the lightest and the heaviest filler atoms do not exist. This is not surprising as the $[T_4X_{12}]^{4-}$ framework is rather rigid and cations with small radius cannot fulfil the optimal bonding distances within the cage. Binary phases become then more stable than the filled skutterudite phase.

The VEC in these compounds, however, will be reflected in their conductivity properties. Those with a filler ion with an oxidation state 4+ will achieve 72 electrons per RT_4X_{12} unit and semiconducting properties will arise, as it is indeed observed in $CeFe_4P_{12}$, UFe_4P_{12} and $CeFe_4As_{12}$ [62,63]; whereas lower oxidation states will lead to metallic conductivity, as in $CeFe_4Sb_{12}$ [64]. In order to take the filled skutterudite phase back to a semiconducting state, charge compensation may be applied. This can be done by partially replacing the pnictogen atoms, as in $LaIr_4Ge_3Sb_9$ [65] or, alternatively, by replacing some of the metal atoms to form compounds such as $CeFe_{4-x}Co_xSb_{12}$ [66], $LaFe_{4-x}Co_xSb_{12}$ [67] or even $CeFe_{4-x}Ni_xSb_{12}$ [68]. Nevertheless, it is important to realize that full occupancy of the voids may not be achieved even by charge compensation. It has been observed that the Ce occupancy in $CeFe_{4-x}Co_xSb_{12}$ is controlled by the fraction of Co in the sample.

While all voids are occupied in $CeFe_4Sb_{12}$ no more than 10% are occupied in pure $CoSb_3$ [66]. According to Bauer *et al.*, filled skutterudites can be divided into two subgroups [51]:

- Compounds formed simply by filling the 2*a* Wyckoff position in the framework formed by the already known binary skutterudites.
- Electronically promoted filled skutterudites, where the electrons provided by the filler atom stabilize the structure when the VEC is lower than 72.

Filled skutterudites in Table 1-2 belong to the second group as well as those formed by charge compensation, such as $LaFe_3CoSb_{12}$ and $CeFe_4Sb_{11}Te$.

Table 1-2 Known stable filled ternary skutterudites of the type RT_4X_{12} (R = filler atom; T = group 8 metal; X = pnictogen) [69].

	P	As	Sb
Fe	$LaFe_4P_{12}$ $CeFe_4P_{12}$ $PrFe_4P_{12}$ $YbFe_4P_{12}$ $NdFe_4P_{12}$ $SmFe_4P_{12}$ $EuFe_4P_{12}$ $GdFe_4P_{12}$ $ThFe_4P_{12}$ UFe_4P_{12}	$LaFe_4As_{12}$ $CeFe_4As_{12}$ $PrFe_4As_{12}$	$PrFe_4Sb_{12}$ $NdFe_4Sb_{12}$ $YbFe_4Sb_{12}$ $CaFe_4Sb_{12}$ $SrFe_4Sb_{12}$ $BaFe_4Sb_{12}$ $LaFe_4Sb_{12}$ $CeFe_4Sb_{12}$
Ru	$LaRu_4P_{12}$ $CeRu_4P_{12}$ $PrRu_4P_{12}$ $NdRu_4P_{12}$ $EuRu_4P_{12}$ $ThRu_4P_{12}$	$LaRu_4As_{12}$ $CeRu_4As_{12}$ $PrRu_4As_{12}$	$LaRu_4Sb_{12}$ $CeRu_4Sb_{12}$ $PrRu_4Sb_{12}$ $NdRu_4Sb_{12}$ $EuRu_4Sb_{12}$ $SrRu_4Sb_{12}$ $BaRu_4Sb_{12}$
Os	$LaOs_4P_{12}$ $CeOs_4P_{12}$ $PrOs_4P_{12}$ $NdOs_4P_{12}$	$LaOs_4As_{12}$ $CeOs_4As_{12}$ $PrOs_4As_{12}$ $NdOs_4As_{12}$ $ThOs_4As_{12}$	$LaOs_4Sb_{12}$ $CeOs_4Sb_{12}$ $PrOs_4Sb_{12}$ $NdOs_4Sb_{12}$ $SmOs_4Sb_{12}$ $EuOs_4Sb_{12}$ $SrOs_4Sb_{12}$ $BaOs_4Sb_{12}$

***A new filled skutterudite, $BaPt_4Ge_{12}$, based entirely on a Ge framework with a VEC of 66 has been recently synthesized [49].**

Other charge-compensated filled skutterudites such as $CeCo_4Ge_3Sb_9$, $REIr_4Ge_3Sb_9$ (RE = La, Sm, Nd) and $RERh_4Ge_3Sb_9$ (RE = La, Ce, Pr, Nd) have also recently been synthesized with the new Ge-substituted skutterudite framework [49,65,70,71,72]. Hitherto, $Ce_{0.9}Fe_3CoSb_{12}$ is the charge-compensated filled skutterudite with the highest ZT value ever measured for a similar system, *i.e.* 1.4 at 800 K [73].

Filled skutterudites belonging to the first group have recently attracted a lot of interest, especially the Co_4Sb_{12}-based compounds of the type $M_xCo_4Sb_{12}$ (where M is a guest species and $0 \leq x \leq 1$), owing to their excellent thermoelectric properties [74]. As a matter of fact, it has been shown that partial void filling causes a greater reduction in the lattice thermal conductivity than complete filling, owing to the onset of point-defect phonon scattering.

Moreover, multi-filling (partial filling with different types of atoms) has proven effective to decrease even further the thermal conductivity. The stability of such multi-filled skutterudites strongly depends on chemical and physical features, such as ionic radius and electronegativity, between the filler elements.

Likewise, heavier smaller filling atoms also cause a greater decrease in the thermal conductivity than lighter and bigger atoms [75,76]. The lowest thermal conductivity is found at a filling fraction of approximately 30-40% [77]. Further, partial filling has been observed to enhance carrier mobilities, thereby increasing Z [77]. Nevertheless, these compounds are difficult, if not impossible, to synthesize by traditional solid state methods, as it has been demonstrated by Morelli *et al*. for cerium-filled Co_4Sb_{12}-based skutterudites [78]. Thus, by means of alternative synthetic as well as high-pressure techniques, both the amount and the variety of guest species that can be accommodated in the Co_4Sb_{12} voids are increased resulting in metastable phases. A list of the reported known Co_4Sb_{12}-based filled skutterudites is provided without including the multi-filled skutterudites (Table 1-3). It is noteworthy that more filler atoms have been reported, however these require charge compensation to some extent in order to enter the Co_4Sb_{12} framework as seen in, for instance, uranium-filled skutterudites [79].

The filling fraction limit (FFL) is greatly influenced by the ionic radius to the cage radius ratio and the valence state of the filler elements. For Co_4Sb_{12}-based filled skutterudites, stability ranges of the r_{ion} / r_{cage} ratio are found between 0.6 and 0.9. The filling fraction increases with increasing the ionic radius and with decreasing the ionic valence of the fillers. It has been shown that atoms with a lower oxidation state enter

more easily inside the cavities because they donate fewer electrons to the structure. An entirely empirical relation based on the r_{ion} / r_{cage} ratio and the filler atom oxidation state n has been inferred to predict the maximum filling fraction [80]:

$$y_{max} = r_{ion} / r_{cage} - 0.086n - 0.24 \qquad \textbf{(1-10)}$$

Nonetheless, detailed studies of the difference between barium and cerium filling in systems such as $Ba(Ce)_yFe_xCo_{4-x}Sb_{12}$ show that there is no direct correlation between the oxidation state and the filling fraction; therefore such relation is still under investigation [81]. As regards the structural response to filling, some studies on filled skutterudite systems show common trends in all of them as the filling fraction increases, such as the increase in the unit cell, the shape change of the four-membered rings towards a more square form and the decrease of the filler atomic displacement parameter [82,83].

Table 1-3 Known Co_4Sb_{12}-based filled skutterudites. Those with the highest filling fraction (%) are shown, excluding multi-filled skutterudites.

Filler atom	Materials	filling fraction	Reference
La	$La_{0.42}Co_4Sb_{12}$†	42	[84]
	$LaCo_4Sb_{12}$†	100	[85]
Ce	$Ce_{0.10}Co_4Sb_{12}$	10	[78]
	$CeCo_4Sb_{12}$†	100	[85]
Nd	$Nd_{0.13}Co_4Sb_{12}$	13	[86]
Eu	$Eu_{0.2}Co_4Sb_{12}$	20	[87]
Gd	$Gd_{0.15}Co_4Sb_{12}$†	15	[84]
Yb	$Yb_{0.19}Co_4Sb_{12}$	19	[88]
Lu	$Lu_{0.14}Co_4Sb_{12}$†	14	[84]
Li	$Li_xCo_4Sb_{12}$	-	[89]
Na	$Na_xCo_4Sb_{12}$	-	[89]
K	$K_{0.45}Co_4Sb_{12}$	45	[90]
Cs	$Cs_xCo_4Sb_{12}$	-	[89]
Ca	$Ca_{0.2}Co_4Sb_{12.46}$	20	[91]
Sr	$Sr_{0.40}Co_4Sb_{12}$	40	[92]
Ba	$Ba_{0.44}Co_4Sb_{12}$	44	[93]
Hf	$Hf_{0.13}Co_4Sb_{12}$†	13	[84]
In	$In_{0.2}Co_4Sb_{12}$	20	[94]
Tl	$Tl_{0.22}Co_4Sb_{12}$	22	[95]
Ge	$Ge_{0.25}Co_4Sb_{12}$*	25	[96]
Sn	$SnCo_4Sb_{12}$*	100	[97]
Pb	$Pb_{0.25}Co_4Sb_{12}$†	25	[84]

*** Synthesized under pressure**
† Non-metallurgical synthesis method
- Not available

Rare-earth elements such as Ce, La, Pr, Nd, Yb, Eu; the alkaline earths Ca, Sr and Ba; the alkali earths Na, K and the main group elements Tl and In have all been inserted into

Co_4Sb_{12}-based skutterudites without charge compensation and by traditional solid state methods up to a filling fraction limit (FFL) of 44%, *i.e.* $0 \leq x \leq 0.44$ in $M_xCo_4Sb_{12}$ [90]. By means of controlled crystallization of elementally modulated reactants, Gd, Lu, La, Pb and Hf-filled Co_4Sb_{12}-based skutterudites were synthesized with a maximum filling fraction of 42% for $La_{0.42}Co_4Sb_{12}$ [84]. Y, Si, Ge, Sn and Pb can also be inserted by high-pressure techniques, being $SnCo_4Sb_{12}$ fully filled [97,98]. By using a thin-film technique, the completely filled compounds $LaCo_4Sb_{12}$ and $CeCo_4Sb_{12}$ have also been successfully synthesized [85]. Other binary skutterudite-based systems have also been studied, although less thoroughly, given the poorer thermoelectric performance obtained. Zemni *et al*. inserted La, Ce, Pr, Nd and Yb into a CoP_3 framework using a molten tin solvent, obtaining FFLs ranging between 20-25% [99]. The Co_4Sb_{12}-based filled skutterudite with the highest ZT value reported hitherto is $Ba_{0.30}Ni_{0.05}Co_{3.95}Sb_{12}$, which has been doped with a 1.25 % of Ni in the cobalt 8*c* site to enhance the electronic properties. The measured value is 1.25 at 900 K [100].

1.2.4 Thermoelectric properties of binary, ternary and filled skutterudites

The $CoSb_3$ skutterudite attracted a great deal of attention as a thermoelectric material in the early nineties given the exceptionally high value of the Hall mobility (3445 $cm^2\ V^{-1}\ s^{-1}$) measured in a *p*-type $CoSb_3$ single crystal [101]. Low electrical resistivity values combined with the highest Seebeck among the binary skutterudites also targeted this compound (Table 1-4). The only drawback is the high thermal conductivity; however, this may be overcome given the open structure of the skutterudite and the possibility of atom insertion. The power factor, which gathers the electronic properties of skutterudites, can be optimized by means of doping either at the cation or the anion site. Chemically close elements may be used for such purpose such as Fe and Ni for the cation site, as well as Te and Sn for the anion site. The extra electron in Ni, Te atoms will turn them into electron donors, whereas Fe, Sn atoms will act as electron acceptors given the one-electron deficiency when compared to cobalt.

This fact will also be reflected in positive and negative Seebeck coefficients, respectively; since the electric charge will be driven by electrons in $Co_{1-x}Ni_xSb_3$ and $Co_{1-x}Sb_{3-x}Te_x$ or holes in $Co_{1-x}Fe_xSb_3$ and $Co_{1-x}Sb_{3-x}Sn_x$. Doping has two immediate effects as to the electronic transport properties at concentrations as low as 1%, *i.e*. an important reduction in the electrical resistivity and also a decrease in the Seebeck coefficient owing to the direct relation of both properties with the charge carrier density

[102,103,104,105]. Considering the thermal conductivity, the binary skutterudites CoX_3 (X = P, As, Sb) follow the expected trend that heavy elements scatter phonons more efficiently, *i.e.* CoP_3 > $CoAs_3$ > $CoSb_3$ (Table 1-4). Moreover, the lattice thermal conductivity represents the most important contribution to the overall value, being the carrier contribution approximately constant even if doping occurs [102]. Anion-substituted ternary skutterudites show large values of the electrical resistivity as well as the Seebeck coefficient, consistent with a low charge carrier density.

Table 1-4 Reported lattice parameter and thermoelectric properties at room temperature of ternary skutterudites. Binary skutterudites have been included for comparison purposes.

Ternary Skutterudite	*a* / Å	Ref.	ρ / mΩcm	Ref.	S / μVK^{-1}	Ref.	κ W/mK	Ref.
$CoGe_{1.5}S_{1.5}$	8.017	[106]	-		-		-	
$CoGe_{1.5}Se_{1.5}$*	8.299	[106]	1000	[107]	-580	[107]	5	[107]
$CoGe_{1.5}Te_{1.5}$**	8.7270	[50]	120	[108]	-500	[108]	-	
$CoSn_{1.5}Te_{1.5}$	9.1284	[109]	67	[109]	-440	[109]	4	[109]
$CoSn_{1.5}Se_{1.5}$	8.7959	[50]	-		-		-	
$RhGe_{1.5}S_{1.5}$	8.2746	[53]	8000	[110]	100	[110]	-	
$IrGe_{1.5}S_{1.5}$	8.297	[53]	15000	[53]	-		-	
$IrGe_{1.5}Se_{1.5}$	8.5591	[53]	4000	[53]	-		-	
$IrSn_{1.5}S_{1.5}$+	8.7059	[53]	-		-		-	
$IrSn_{1.5}Te_{1.5}$	9.3320	[50]	60	[57]	140	[57]	-	
$IrSn_{1.5}Se_{1.5}$	8.9674	[50]	-		-		3	[50]
$Fe_{0.5}Ni_{0.5}Sb_3$	9.0904	[111]	-		50	[50]	3.5	[50]
$Fe_{0.5}Ni_{0.5}As_3$	8.256	[112]	-		-		-	
$PtSn_{1.2}Sb_{1.8}$	9.39	[113]	-		-		-	
$Ru_{0.5}Pd_{0.5}Sb_3$	9.2960	[54]	0.57	[54]	10	[50]	2	[50]
$Fe_{0.5}Ni_{0.5}As_3$	8.2560	[56]	-		-		-	
$PtSn_{1.2}Sb_{1.8}$	9.3900	[113]	-		-		-	
$Fe_{0.5}Pd_{0.5}Sb_3$	9.2060	[50]	-		-		-	
$Fe_{0.5}Pt_{0.5}Sb_3$	9.1950	[50]	-		-		-	
$Ru_{0.5}Ni_{0.5}Sb_3$	9.1780	[50]	-		-		-	
$Ru_{0.5}Pt_{0.5}Sb_3$	-	[50]	-		-		-	
$FeSb_2Se$	-	[50]	-		-		-	
$FeSb_2Te$	9.1120	[50]	-		80	[50]	2.3	[50]
$RuSb_2Se$	9.2570	[114]	-		-		-	
$RuSb_2Te$	9.2680	[50]	-		140	[50]	2.8	[50]
$OsSb_2Te$	9.2980	[50]	-		-		2.3	[50]
$NiGeP_2$	7.9040	[50]	-		-		-	
$NiGeBi_2$	9.4400	[50]	-		-		-	
CoP_3	7.7073	[50]	0.47	[115]	30	[115]	25.8	[115]
$CoAs_3$	8.2043	[50]	8.40	[115]	26	[115]	12.5	[115]
$CoSb_3$	9.0385	[50]	0.44	[116]	108	[116]	10	[116]
RhP_3	7.9951	[50]	1.4	[117]	32	[117]	-	
$RhAs_3$	8.4427	[50]	4.5	[112]	-		-	
$RhSb_3$	9.2322	[50]	50	[118]	80	[118]	10.7	[118]
IrP_3	8.0151	[50]	-		-		-	
$IrAs_3$	8.4673	[50]	-		-		-	
$IrSb_3$	9.2533	[50]	0.43	[116]	72	[116]	16	[116]
NiP_3	7.8190	[50]	metallic		-		-	
PdP_3	7.705	[50]	metallic		-		-	

***Exact composition determined by EPMA: $CoGe_{1.452}Se_{1.379}$**
****Exact composition determined by EPMA: $CoGe_{1.7}Te_{1.47}$**
+Subjected to 600 °C, 40 Kbars for 1 hour after reaction.

Such deleterious effect becomes readily evident in Table 1-4; however this fact is offset by an increase in the Seebeck coefficient and a remarked decrease in the thermal conductivity.

Compounds formed by heavier anions show smaller electrical resistivities than those formed by lighter elements, consistent with the less ionic character of the elements at the bottom of the group. All ternary skutterudites presented in Table 1-4 also show a marked reduction in thermal conductivity. The relation between the latter effect and the symmetry loss explained in section 1.2.1 is comprehensively treated in section 3.9. Nevertheless, in some cation-substituted skutterudites, namely $Ru_{0.5}Pd_{0.5}Sb_3$, such decrease cannot be explained on the grounds of symmetry changes, as the resulting skutterudite retains the parent binary cubic symmetry, or due to mass or volume fluctuations because they are simply not large enough. It has been postulated that it has its origin in a different phonon scattering mechanism caused by valence fluctuations in the metal lattice [119]. Very few doping studies have been carried out on ternary skutterudites. Cation-site Ni and Ru doping resulting in lowering of both the electrical resistivity and the Seebeck has been reported for $CoSn_{1.5}Te_{1.5}$ [109]. Ni-doped $CoGe_{1.5}S_{1.5}$ was also successfully synthesized in our group with similar results [110]. Anion-site In and Sb doping has also been carried out on $IrSn_{1.5}Te_{1.5}$ [57]. It is worth noticing that in all the previous studies, doping always led to an overall power factor enhancement. However, the reported dimensionless figures of merit are low. For $Ru_{0.5}Pd_{0.5}Sb_3$, ZT reaches 0.02 at 800 K, whereas the only reported value for anion substituted skutterudites in $CoGe_{1.5}Se_{1.5}$ does not go beyond 0.0005 at 300 K [54,107].

With regard to the effect of filling on the transport properties, it was already mentioned the drastic decrease in the lattice thermal conductivity they caused (section 1.2.3). Moreover, introducing extra electropositive atoms also dopes the structure and increases the charge carrier concentration typically to values between 10^{20} and 10^{22} cm^{-3}. This also drives the structure to *n*-type conduction with negative Seebeck coefficients. The Seebeck coefficient also remains high and, in some cases, filling produces an optimal effect both in the electronic and thermal transport properties [77].

1.2.5 Anomalous phenomena in filled skutterudites

Strong hybridisation between 4f electrons from the lanthanide ions and conduction electrons leads to a variety of ground states and electron correlation phenomena that are

manifested by atypical properties in filled skutterudite compounds. Phenomena such as Kondo insulator and non-Fermi liquid behaviours, ferromagnetism, valence fluctuation phenomena, heavy Fermion behaviour, superconductivity and metal-insulator transitions have all been observed in these systems [120].

Hybridization between localized f electrons and conduction electron states can lead to a semiconducting behaviour with a small energy gap (~ 10^{-3}-10^{-1} eV) possessing a large density of states near the Fermi energy level leading to an enhancement of the Seebeck coefficient. Rare earths and actinide compounds that exhibit this behaviour are referred to as "hybridisation gap" semiconductors or "Kondo insulators". This behaviour was first observed in SmS and SmB_6 [121] and the first examples of filled skutterudites where it was found are $CeFe_4P_{12}$ and UFe_4P_{12}.

Valence fluctuation and heavy Fermion behaviour can be found in compounds such as $CeFe_4Sb_{12}$ and $YbFe_4Sb_{12}$. Valence fluctuation phenomena occur in rare-earth compounds in which the proximity of the 4f level to the Fermi energy leads to instabilities of the charge configuration (valence) and/or the magnetic moment. The term "heavy Fermion" is used in condensed matter physics to describe metallic materials having very large electronic mass enhancement arising from an antiferromagnetic interaction between conduction electrons and local magnetic moments (d- or f-electron type) located in a sublattice of atoms in the metal. The rapid decrease of $\rho(T)$ below 150 K gives away the onset of the highly correlated heavy Fermion ground state. Recently, heavy Fermion behaviour was observed in the Pr compounds $PrFe_4P_{12}$ [122] and $PrOs_4Sb_{12}$ [123].

A Fermi liquid is a generic term for a quantum mechanical liquid of fermions that arises under certain physical conditions at low temperatures. An example of such systems is electrons in a metal. However, in heavy-fermion systems where there exist large effective electron masses the Fermi liquid approximation looses its validity. Non-Fermi liquid (NFL) behaviour in f-electron materials is manifested as weak power law and logarithmic divergences in temperature in the physical properties at low temperatures. It has been reported that $CeRu_4Sb_{12}$ exhibits strongly correlated electron behaviour with NFL dependences at low temperatures [123]. Heavy Fermion superconductivity has been found for the first time in a Pr-based compound in $PrOs_4Sb_{12}$ [124] and also in $LaRu_4As_{12}$ and $PrRu_4As_{12}$ [125]. Unlike normal superconductivity, it cannot be

explained by the Bardeen-Cooper-Schrieffer (BCS) theory. The anomalies that give away the presence of such a phenomenon are the large values of the electronic specific heat coefficient (C_p / T) at T_c (critical temperature) indicating that electrons with large effective mass (approximately 200 times the free electron mass) participate in the superconducting pairing of the BCS theory. Meisner emphasized the importance of the four-membered pnictogen rings for thermoelectricity as well as for superconductivity with the discovery of the latter effect in the ternary phosphides LaM_4P_{12} (M = Fe, Ru, Os) [126]. Band structure calculations performed on skutterudite-type phosphides confirm that the highest-occupied band has a larger contribution from the phosphorous atoms than the M atom. Since superconductivity is associated to electrons near the Fermi level, such phenomenon is linked in these compounds to electrons from the phosphorous sublattice [127,128]. Superconductivity has also been found in the arsenides $LaRu_4As_{12}$ and $PrRu_4As_{12}$ as well as in the antimonide $LaRu_4Sb_{12}$. Property measurements on these materials indicate that they all are type II superconductors [125,129].

1.3 Equiatomic ternary phases

By and large, ternary equiatomic compounds can be grouped, regarding their crystallization structure, into three main categories: those adopting the ZrSiS, the CoAsS cobaltite and the FeAsS arsenopyrite structure. The α–$NiAs_2$ structure is included as a subgroup owing to its direct relation with the results obtained.

1.3.1 ZrSiS-type

There exist over 200 compounds crystallizing under this structure type. ZrSiS-type compounds usually contain 2D square nets of transition metals that often show different degrees of distortion, originating interesting physical properties. ZrSiS-type structures are frequently named with other synonyms, namely PbFCl, Fe_2As, Cu_2As or BiOCl, sharing all of them the same features described below. The difference lies mainly in the degree of anion-anion bonding in the structure, ranging from highly electronegative anions, as in PbFCl where the distance between anions is equal or larger than the van der Waals non-bonding distance, to covalency and electron delocalization between anions, as seein in Fe_2As, and even chain-shaped distortions of the 2D anion lattice in GdPS [130,131,132].

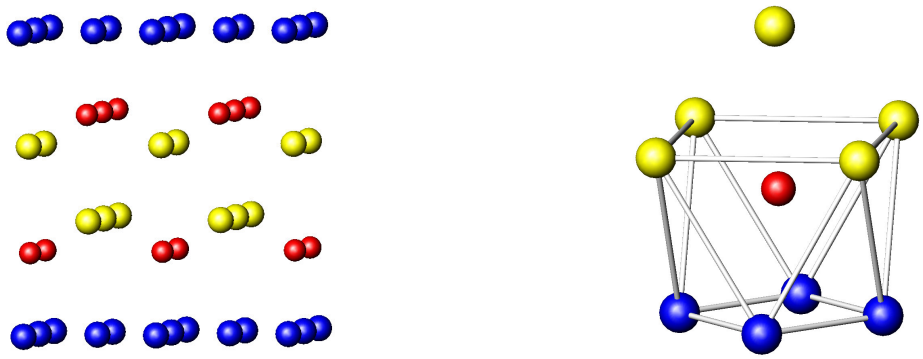

Figure 1-6 ZrSiS structure. Left: general view of the Si-Zr-S-S-Zr layers. Right: Zr coordination sphere. Key: Zr in red, sulphur in yellow and Si in blue.

Table 1-5 MXY compounds with the ZrSiS structure (*P4/nnm*). c/a ratios as well as electron deficiency, Δ, are shown.

Compound	c/a	Δ	ref	Compound	c/a	Δ	ref
ZrSiS	2.273	2	[133]	ThPS	2.213	1	[134]
ZrSiSe	2.309	2	[133]	ThPSe	2.029	1	[134]
ZrSiTe	2.573	2	[133]	ThAsS	2.110	1	[134]
ZrGeSb	2.245	3	[135]	ThAsSe	2.098	1	[134]
ZrGeS	2.212	2	[133]	ThAsTe	2.068	1	[134]
ZrGeSe	2.232	2	[133]	ThSbSe	2.083	1	[134]
ZrGeTe	2.224	2	[133]	ThSbTe	2.094	1	[134]
ZrSnTe	2.148	2	[134]	ThBiTe	2.053	1	[134]
ZrSbTe	2.228	2	[134]	USiS	2.200	0	[136]
HfSiS	2.273	2	[134]	UGeS	2.179	0	[134]
HfSiSe	2.292	2	[134]	USnTe	2.144	0	[134]
HfSiTe	2.651	2	[134]	UPS	2.093	1	[137]
HfGeS	2.199	2	[134]	UPSe	2.072	1	[134]
HfGeSe	2.222	2	[134]	UAsS	2.106	1	[134]
HfGeTe	2.196	2	[134]	UAsSe	2.103	1	[134]
NbSiAs	2.263	3	[138]	UAsTe	2.103	1	[134]
NbGeAs	2.238	3	[138]	USbS	2.162	1	[134]
NbSiSb	2.247	3	[138]	USbSe	2.108	1	[134]
NbGeSb	2.218	3	[138]	USbTe	2.097	1	[134]
LaSbTe	2.133	2	[134]	UBiTe	2.065	1	[134]
CeSbTe	2.165	2	[139]	NpAsS	2.153	-	[134]
PrSbTe	2.163	2	[134]	NpAsSe	2.158	-	[134]
NdSbTe	2.173	2	[134]	NpAsTe	2.152	-	[134]
SmSbTe	2.171	2	[134]	NpSbTe	2.121	-	[134]
GdSbTe	2.172	2	[134]	AmSbTe	2.124	-	[134]
GdPS	3.098	2	[132]	PuSbTe	2.124	-	[134]
GdAsSe	2.198	2	[132]	EuSnP	2.048	*	[140]
UOTe	1.871	0	[135]	PbClF	1.763	0	[131]

- Data not available
*** Not considered a Zintl compound**

Accordingly, insulating, semiconducting and metallic behaviour can be observed across the family of compounds, being the most interesting properties among those containing elements from groups 14, 15 and 16; excluding the elements of the second period. Main group elements from group 13 are too metallic, forming a new class of materials on their own, and those from group 17 and the second period are too electronegative, giving rise to wide band gaps, thereby loosing chemical interest. The Zr coordination sphere consists of a monocapped square antiprism. The basal square is made of Si atoms, whereas the S atoms form a larger square rotated 45° relative to the Si square, which is capped by a fifth S atom. If the capping atom is named "head", then the structure can be described as an arrangement of such antiprisms oriented head-to-head and tail-to-tail. It can also be regarded as a layered structure composed of square nets following the sequence Si-Zr-S-S-Zr in which the Si nets are twice as dense as those of Zr or S [135]. Thus, the main difference when compared to the PbFCl structure is the presence of Si-Si bonding, both intra and between layers (Figure 1-6). These compounds can be, in turn, classified considering their *c/a* ratio, which is a useful indicator of a characteristic transition from a layered to a three dimensional structure that occurs when isoelectronic substitutions take place.

Thus, interlayer bonding exists in ZrSiS, but it completely disappears in ZrSiTe, becoming a purely layered compound. It is seen that *c/a* ratios between 2.0 and 2.3 correspond to 3D structures, whilst larger ratios are indicative of layered (2D) arrangements [135]. Further, *c/a* ratios are also indicative of PbFCl-type structures when they are lower than 2 and ZrSiS-type structures for larger values. Therefore, a *c/a* ratio of 2 is a boundary value between non-metallic and metallic phases, respectively. Such deficiency is also indicative of anion-anion bonding necessary to offset the electrons that cannot be supplied by the metal. A more comprehensive list of ZrSiS-type phases can be found elsewhere [141]. A list of the most relevant compounds is presented in Table 1-5, along with their *c/a* ratios and their electronic deficiencies, Δ, with respect to the octet rule.

1.3.2 Anion-anion pair-forming phases

There exists a family of closely related compounds whose main characteristics are the formation of anion pairs and the octahedral and tetrahedral coordination environments around the metal and non-metal atoms, respectively. Among them, FeS_2 pyrite, FeS_2

marcasite, FeAsS arsenopyrite, CoAsS cobaltite and NiSbS ullmannite are the most frequent structure archetypes. For the sake of clarity, a brief description of all of them is included.

FeS_2 pyrite archetype

Pyrite is the most abundant sulphide in the Earth´s crust. FeS_2 consists of S_2^{2-} molecular ions and Fe^{2+} cations, and its structure can be derived from that of the NaCl rocksalt. The Na^+ cations are replaced by Fe^{2+} and Cl^- anions by S_2^{2-}, respectively, where the centre of the diatomic molecule occupies the former Cl^- crystallographic position. Each iron is octahedrally coordinated by sulphur and each sulphur is tetrahedrally coordinated by three Fe and one S. Its crystals are cubic with four formula units per unit cell. The FeS_6 octahedron shares corners with neighbouring octahedra, being the metal-metal distance too long for bonding interactions (3.84 Å). Further, it can also be regarded as derived from the CaC_2 structure in which the C_2 dimers oriented along the [001] crystallographic direction have been replaced and tilted.

Transition metal dichalcogenides having the pyrite-type structure are frequent in the 3d series, namely MnS_2, $MnSe_2$, $MnTe_2$, FeS_2, CoS_2, $CoSe_2$, NiS_2, $PtAs_2$, $PtSb_2$, $AuSb_2$ and $NiSe_2$, although there exist others, such as CuS_2, $CuSe_2$, $CuTe_2$, $NiTe_2$, $CoTe_2$, $FeSe_2$ and $FeTe_2$, obtained by using high-pressure synthesis [142]. Pyrite compounds display a wide variety of electronic properties, ranging from antiferromagnetism in d^5 high-spin Mn^{2+} insulating compounds and semiconducting behaviour for d^6 systems, to metallic strongly correlated electron systems in CoS_2 and NiS_2, and metallic weakly correlated itinerant electrons as seen in CuS_2. These properties have been rationalized by a one-electron band model proposed by Goodenough [143]. In this model, it can be seen that for $d \geq 6$ metals the cation t_{2g} orbitals (octahedral coodination) are completely filled, thereby semiconducting properties are observed for d^6 metals and metallic conductivity for those with higher electron counts. Progressive occupation of antibonding states will eventually lead to a weaker bonding and longer bond distances. The same conclusion can be arrived at taking into account that pyrite-like structures are well-behaved valence compounds (they possess two-centre two-electron bonds) and follow the 8-N rule, *i.e.* equation (1-11). By assigning charges, a description of the pyrite as $Fe^{2+}S_2^{2-}$ fills up the s-p valence shell of both sulphurs, and semiconducting properties are expected. From the cation point of view, the 18-electron rare-gas configuration is also achieved as follows: the Fe neutral atom possesses 8 electrons, being bonded to six sulphurs which,

in turn, are bonded to two other Fe atoms and one S atom. Therefore, only five out of the six S valence electrons are available for the metal atom. This adds up to thirty electrons available in the six sulphurs coordinating the iron in an octahedral environment, leaving ten electrons to complete the metal outer shell per metal atom. A more detailed discussion on the pyrite-like compounds and their properties in relation to their band structure can be found elsewhere [142].

NiSbS ullmannite

The NiSbS ullmannite structure is derived from the substitution of one S by one group 15 element in the pyrite structure. During the process, the centre of inversion is lost and an ordered distribution of the elements of the groups 15 and 16 takes place. Sb and S atoms are ordered and occupy different crystallographic sites having the same multiplicity, *i.e*. four. All the atoms in the crystal structure occupy special positions on one of the four existing three-fold axes, and each set of atoms is allowed to move along them. Thus, the initial pyrite octahedral hole occupied by the cation can be now regarded as trigonal antiprismatic, where Sb and S atoms occupy opposite triangular faces. The cobalt atoms are shifted along their axis towards the smaller S atoms and away from the Sb atoms [144]. Owing to the fact that the ullmannite and the pyrite structures are closely related, the same band structure model to explain its properties can be used. Thus, NiSbS possesses one electron more than FeS_2 (VEC 20 e^- *vs*. 21 e^-), which has to occupy antibonding states; giving rise to metallic conduction as it is observed in other ullmannite-type compounds (cf. Table 1-8).

Table 1-6 Comparison of the atomic coordinates in pyrite, ullmannite and cobaltite structures [145].

		x	y	z
FeS_2-*p*	$Pa\bar{3}$ (No. 205)			
Fe	4*a*	0	0	0
S	8*c*	0.384	0.384	0.384
NiSbS	$P2_13$ (No. 198)			
Ni	4*a*	0.976	0.976	0.976
Sb	4*a*	0.625	0.625	0.625
S	4*a*	0.390	0.390	0.390
CoAsS	$Pbc2_1$ (No. 29)*			
Co	4*a*	0.260	0.995	0
As	4*a*	0.869	0.619	0.617
S	4*a*	0.631	0.384	0.381

*** The non-standard setting *Pbc*2_1 has been chosen for the sake of clarity.**

Table 1-7 Bond distances and most relevant angles in MXY pyrite, ullmannite and cobaltite structures [146].

	Pyrite*	Ullmannite	Cobaltite
M-X	2.27 Å	2.38 Å	2.30 Å
M-Y	2.27 Å	2.55 Å	2.36 Å
Y-M-Y	94.26°	95°	87-96°
Y-M-X	85.74 °	85°	85-95°
X-M-X	94.26°	95°	83-93°

***Both X and Y refer to sulphur in the pyrite.**

An ionic charge description given by the formula $Ni^{3+}[PS]^{3-}$ accounts for the fulfilment of the octet rule for the anions, leaving the Ni atom with a d^7 configuration with seven available electrons. Six of them participate in the bonding with three Sb and three S and the last electron is, again, accountable for the metallic behaviour.

CoAsS cobaltite

Despite having an orthorhombic space group ($Pca2_1$), the CoAsS cobaltite unit cell is metrically cubic, showing a close relation with its parent structure, FeS_2 pyrite ($Pa\bar{3}$) as well as with the cubic NiSbS ullmannite ($P2_13$). It can also be derived from the pyrite structure by substitution of one S atom by another of the main groups 15 or 16.
The Co, As and S atoms also occupy three different crystallographic sites each of them having multiplicity four; however, in this case, they are allowed to move off the three-fold axes and not only along them. The same displacement trend is observed in the Co atoms towards the smaller S anions. Further, bond angles and bond distances are approximately the same as in the ullmannite (Table 1-6 and Table 1-7) [146].

Therefore, once more, the pyrite band model is still useful to understand the properties of cobaltite-like compounds. CoAsS possesses the same number of electrons as the FeS_2 pyrite and a formal charge formula $Co^{3+}[AsS]^{3-}$ can be assigned. This description fulfils the octet rule for the anions and also the 18-electron rule for the cation, leaving the Co atom in a d^6 configuration that leads to semiconducting properties, as it is indeed observed in other cobaltite-type compounds (Table 1-8) [147].

Table 1-8 MXY compounds with the CoAsS cobaltite structure ($Pca2_1$, VEC 20 e^-), and the ullmannite NiSbS structure ($P2_13$, VEC 21 e^-) [148].

Electron count: 20 e^-		Electron count: 21 e^-	
Compound	***a* / Å**	**Compound**	***a* / Å**
CoPS	5.422	NiPS	5.544
CoAsS	5.578	NiAsS	5.688
		NiSbS	5.933
RhPS	5.640		
RhAsS	5.780	NiAsSe	5.845
RhSbS	6.027	NiSbSe	6.090
RhBiS	6.138	NiBiSe	6.214
RhPSe	5.795	PdAsS	5.949
RhAsSe	5.934	PdSbS	6.185
RhSbSe	6.176		
RhBiSe	6.283		
RhAsTe	6.165	PdAsSe	6.092
RhSbTe	6.392	PdSbSe	6.323
RhBiTe	6.504	PdBiSe	6.432
IrPS	5.650	PdSbTe	6.533
IrAsS	5.791	PtAsS	5.929
IrSbS	6.036	PtSbS	6.174
IrBiS	6.143		
IrPSe	5.798		
IrAsSe	5.940		
IrSbSe	6.184	PtSbSe	6.33
IrBiSe	6.290	PtBiSe	6.42
IrAsTe	6.164		
IrSbTe	6.397	PtSbTe	6.48
IrBiTe	6.500	PtBiTe	6.50

A comparison of the pyrite, ullmannite and cobaltite octahedral environments is illustrated in Figure 1-7. The question as to why some compounds adopt the ullmannite structure, whereas others crystallize in the cobaltite structure has been treated extensively by Bayliss [146]. If one looks at the possible arrangements of two distinct anions in the pyrite structure, it turns out that only four arrangements are possible. That of highest symmetry corresponds to the ullmannite structure and the second one to the cobaltite [149]. Bayliss proposes a simple electronic theory where compounds within the cobaltite subgroup are semiconductors with a d^6 electronic configuration, whereas those within the ullmannite subgroup are metallic with a d^7 electronic configuration.

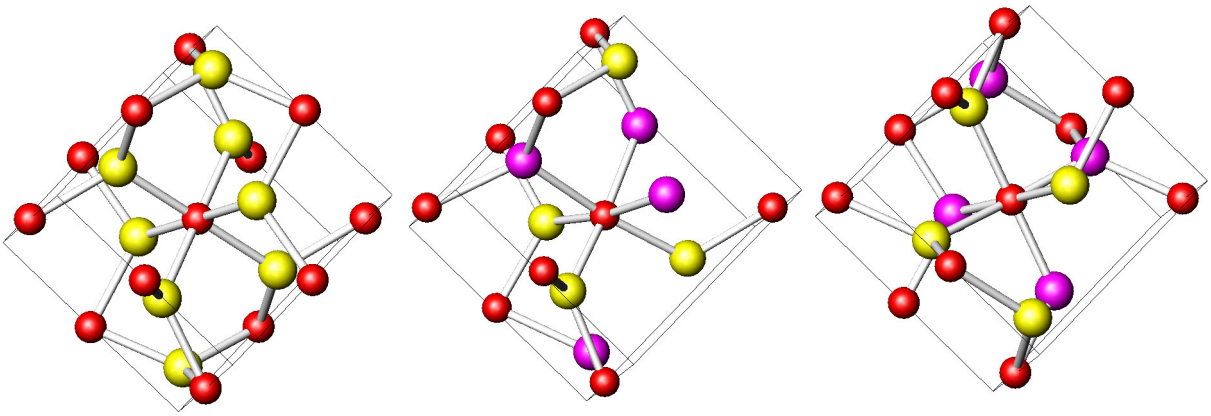

Figure 1-7 From left to right: FeS_2 pyrite, NiSbS ullmannite and CoAsS cobaltite octahedral coordination spheres. Key: metal atoms in red, sulphur in yellow and pnictogen atom in pink.

Both CoAsS and NiAsS undergo a phase transformation at 850 °C and 600 °C, respectively into the pyrite $Pa\overline{3}$ space group; evidencing the fact that high temperatures reverse the anion ordering towards the parent space group.

FeAsS asenopyrite

FeAsS arsenopyrite possesses monoclinic symmetry ($P2_1c$), although it is metrically orthorhombic, and is isotypic with $CoSb_2$. Besides belonging to the same family of compounds as the pyrite, possessing anion-anion pairs, arsenopyrite-type structures are characterized by having metal-metal pairs as well. Each Fe atom is surrounded by a distorted octahedral coordination sphere formed by two types of anions, *i.e.* As and S, grouped in two sets of three. Unlike the pyrite structure, these octahedra share both corners and edges, as in the FeS_2 marcasite structure, being the Fe atoms shifted off the octahedron centre to fulfil the metal-metal bonding interaction. These metal-metal pairs are approximately parallel to the [101] direction [150]. Each anion has, in turn, a tetrahedral coordination environment formed by another anion from a different set and three metal atoms. The interatomic distance between As-S pairs (2.35 Å) is consistent with already reported As-S single bond distances (2.12 Å) [151] and the Fe-Fe shortest distance (2.92 Å) is close to that of the metal (2.87 Å). This distance is regarded as a strong bonding interaction when compared with the other metal-metal distance (3.63 Å), and it is understood in terms of a compromise between the structure stability and the metal closed-shell requirements.

The arsenopyrite structure is closely related to that of the FeS_2 marcasite (*Pnnm,* also orthorhombic) (Figure 1-8). Pyrite contains a metal sublattice consisting of a set of face-centred square planar nets parallel to the (100) plane and separated from one another by a_0 / 2. Similar nets exists in marcasite parallel to the (101) lattice plane, but are face-centred rectangular rather than face-centred square [152]. The key difference, however, between pyrite and marcasite is that each FeS_6 octahedron shares corners with twelve more in the pyrite, whereas they share corners and edges with ten others in the marcasite. The edge-sharing allows for linear cation chains which, in marcasite, are of equal length, whereas short and long distances alternate in arsenopyrite.

Despite the large amount of existent compounds with the pyrite and marcasite structures, only metals from the Co group and pnictogens form binary phases with the $CoSb_2$ structure. Ternary phases formed by isoelectronic substitution of one anion by a chalcogen and one cation by a Fe group atom also lead to the arsenopyrite (Table 1-9). Nevertheless, a relation between structure type, structural deformation and electron count can be drawn. Compounds of the form TX_2, where T is a transition metal and X a pnictogen or a chalcogen, with the marcasite structure and a metal d^6 configuration, such as $NiAs_2$, have their metal atom already in a closed-shell configuration. Therefore, there is no bonding between them due to the repulsion caused by the filled non-bonding t_{2g} levels. When the metal atom is found in a d^5 configuration, the two singly occupied d levels of neighbouring cations in a hypothetical low-spin marcasite split up into a filled bonding and an unfilled antibonding level, giving rise to cation pairing in the arsenopyrite structure. For this reason, it is regarded as a distortion of the marcasite structure [153].

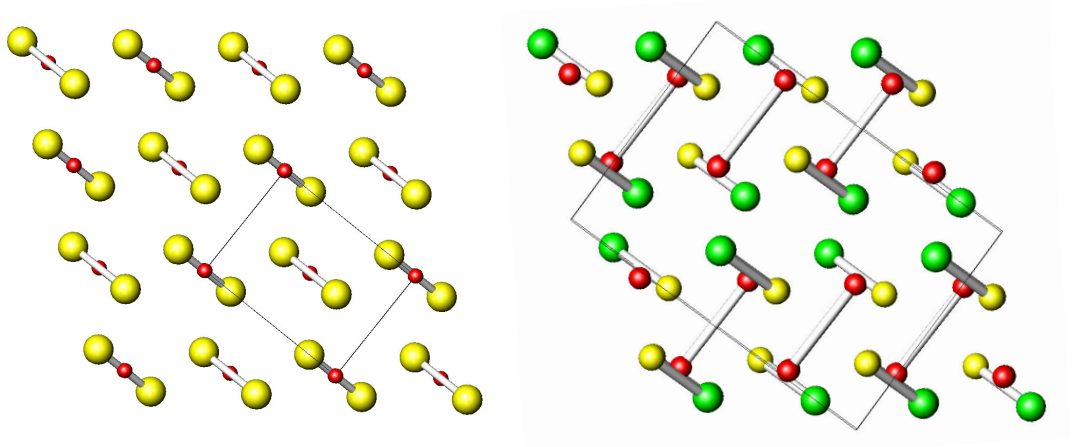

Figure 1-8 Differences between the FeS_2 marcasite (P*nnm*, left) and the FeAsS arsenopyrite ($P12_1/c$, right) structures. The distortion caused by the metal-metal bonding becomes readily evident. Key: Fe in red, S in yellow and As in green.

The phenomenon of pairing can also be understood in terms of a Peierls distortion of a Co linear chain with half-filled band; being the long metal-metal distances interpreted as half-bonds in the localized-bond model, *i.e.* containing only one electron, and thereby fulfilling the 8-N rule. The appearance of a band gap is inherent to such distortion [154]. Again it is seen that the metal atom complies with the 18-electron rule following a covalent electron count, in which anions are not able to provide all their valence electrons but one less given the single bond existent between them (section 5.3) [155]:

Fe in $FeAs_{3/3}S_{3/3}$ neutral atom:	8 e^-
3/3 As atoms in $AsFe_3S$ units: 3/3 x 4	4 e^-
3/3 S atoms in SFe_3As units: 3/3 x 5	5 e^-
1 Fe-Fe bond:	1 e^-
Total:	18 e^-

If formal oxidation states are assigned, the formula $Fe^{3+}[As\text{-}S]^{3-}$ reveals the anion filled shells as well as five electrons on the cation to form three Fe-As and three Fe-S covalent bonds as well as a Fe-Fe bond. As a consequence, all binary and ternary $CoSb_2$ / arsenopyrite-type compounds have been reported as non-metallic [156,157].

Finally, for marcasites with a d^4 configuration, namely $FeAs_2$, all the metal-metal distances are short, where each metal atom obtains one electron from each neighbouring metal interaction to complete their closed shell. As a result of these configurations the octahedral and tetrahedral environments become distorted insofar as the metal atom approaches the ideal bond length. From the point of view of the distortion existing in the pyrite, marcasite and arsenopyrite structures as to the ideal octahedral geometry, it is seen that pyrite is the less distorted structure, allowing for different metal electronic configurations. High-spin d^5, low-spin d^6, metallic d^7 ($d^6 + 1$) and high spin d^8 are found in pyrite, whereas configurations prone to Jahn-Teller distortions are observed in the more distorted marcasite structure, namely, high spin d^2 and low-spin d^4, where the degeneracy of the t_{2g} orbitals is broken [147]. A further insight into the relation between structure and electron count is given in terms of band structure calculations elsewhere [158].

Table 1-9 MXY compounds with the FeAsS arsenopyrite structure ($P2_1c$). Band gap values are included for some of them conditioned to data availability [157].

Compound	ΔE / eV	Compound	ΔE / eV
RuPS	> 1.4	OsPS	> 1.4
RuAsS	~ 1.2	OsAsS	~ 1.3
RuSbS	-	OsSbS	1.2
RuPSe	0.9	OsPSe	~ 1.4
RuAsSe	-	OsAsSe	-
RuSbSe	-		
RuAsTe	-	OsAsTe	-
RuSbTe	0.5		
RhAsSb	-	IrAsSb	-

α-$NiAs_2$-type

By and large, the α–$NiAs_2$ structure is regarded as intermediate between the FeS_2 pyrite and the FeS_2 marcasite, possessing their characteristic anion-anion pairs. It crystallizes in the orthorhombic space group *Pbca* and forms a small group within the TX_2 compounds family with very few structures reported hitherto (Table 1-10). The metal and the two anions occupy three different sites with the same Wyckoff multiplicity (8*c*). As regards the orientation of the anion-anion pairs and their packing, one anion set maintains a tetrahedral coordination environment similar to that of the pyrite, whereas the other resembles that of the marcasite [159]. Within the pyrite structure, the anion pairs are alternatively oriented parallel to the [110] and $[\bar{1}10]$ lattice directions, whereas in the marcasite all pairs are oriented parallel to $[\bar{1}10]$. In the α–$NiAs_2$ structure both configurations alternate. There are two pyrite-like layers of anions oriented along the $[01\bar{1}]$ and $[0\bar{1}\,\bar{1}]$ directions, respectively; and one more marcasite-like layer oriented along $[0\bar{1}\,\bar{1}]$, forming a stacking sequence of the type pyrite / marcasite / pyrite (Figure 1-9) [160].

With respect to the linkage among octahedra, the same conclusion can be drawn. In the pyrite, each octahedron shares corners with two other octahedra, *i.e*. twelve octahedra, whereas in the marcasite both corners and edges are shared with 10 other octahedra. The edge-sharing is also useful to emphasize the differences between the three structures. In the pyrite structure, each edge is linked to that of a neighbouring octahedron via a 5-membered ring formed by three X and two metal atoms. In the marcasite, only eight

edges are linked in this way. The octahedra are arranged so that two edges parallel to the (001) plane are shared with adjacent octahedra.

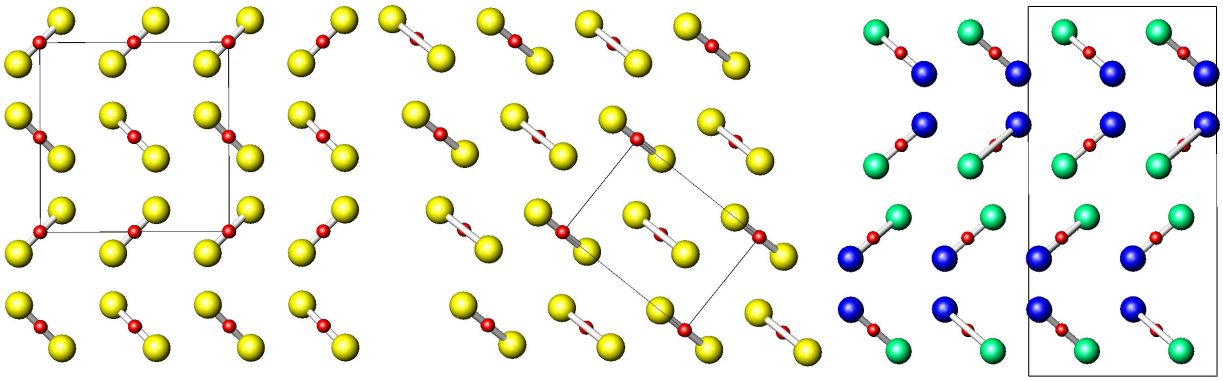

Figure 1-9 Comparison of the anion pair layout in the pyrite FeS_2 (left), marcasite FeS_2 (centre) and α-$NiAs_2$ (right) structures.

The other two edges are perpendicular to the (001) plane and are linked to neighbouring octahedra via a 6-membered ring formed by four X and two metal atoms. In the $NiAs_2$ structure, 10 edges are linked as in the pyrite, one edge is shared and the other is linked as in the marcasite [161]. Despite the edge sharing, the Ni-Ni distance (3.53 Å) cannot be considered bonding, although a metal-metal bonding distance has been observed in PtSiSb (2.86 Å), resulting in an extra distortion of the structure [162].

A formal oxidation state description, such as $Ni^{4+}(As\text{-}As)^{4-}$ accounts for both the anion full shells and the 6 octahedral cation-anion bonds along with the remaining d^6 unshared electrons. The Ni atom also acquires the rare-gas 18-electron configuration, leading to a non-metallic behaviour observed across the series of compounds shown in Table 1-10. PdSnTe and PtSiSb have been reported to be semimetals or strongly degenerated semiconductors owing to their large resistivities and the increasing resistivity with temperature [162,163,164].

Table 1-10 Lattice parameters of reported MXY compounds crystallizing in the α-$NiAs_2$ structure (*Pbca*).

Compound	*a*	*b*	*c*	ref
α-$NiAs_2$	5.7718(5)	5.8342(6)	11.421(1)	[159]
PdSnTe	6.5687(2)	6.6028(2)	12.8849(4)	[164]
PtSiTe	6.3128(8)	6.3347(8)	11.395(1)	[165]
PtSiSb	6.119(2)	6.200(2)	12.379(4)	[162]
CoAsSe	5.7285(8)	5.7741(7)	11.366(2)	[166]
CoPSe	5.5475(6)	5.6588(7)	11.185(1)	[166]
CoSbS	5.764(3)	5.952(3)	11.635(4)	[167]
$PtBi_2$	6.732(2)	6.794(2)	13.346(2)	[168]
IrPTe	6.03	6.131	12.132	[169]

The fact that all the compounds shown in Table 1-10 share the same crystal structure, allows us to compare them in terms of fulfilment of the octet rule, as most of them behave as normal valence compounds following the Zintl-Klemm concept [170]. If the transition metal M provides enough electrons for the anion to satisfy the octet rule, no anion-anion bonding is necessary and the anions are found isolated. Conversely, as the number of electrons supplied by the metal is insufficient, anion-anion and even cation-cation bonding becomes the only means to fulfil the rule. The octet (8-N) rule is expressed as follows:

$$\frac{n_e + b_A - b_C}{n_A} = 8 \qquad \textbf{(1-11)}$$

Where n_e is the total number of electrons per formula unit, n_A is the number of anions, b_A is the number of electrons involved in forming anion-anion bonds and b_C is the number of electrons involved in forming cation-cation bonds, including any unshared valence electrons on the cation. Thus, in the α–$NiAs_2$ structure n_e = (10 + 5 + 5), n_A = 2, and b_A = 2. Each of the Ni atoms share four electrons, as indicated in the previous ionic formula, and six electrons remain unshared in the d orbitals, therefore b_C = 6 and the octet rule is fulfilled. Consequently, semiconducting properties are observed in α–$NiAs_2$ [147].

1.4 Shandites

1.4.1 Metal-rich chalcogenides

They form their own class within the metal chalcogenides due to their peculiarities regarding bonding and physical properties. They comprise those compounds having a metal to chalcogen ratio greater than one. This reduction implies that metal atoms become closer; thereby metal-metal bonding is expected as well as transition metals with an oxidation state lower than expected. Most of the research on this type of chemistry has been carried out by the groups of J. Corbett and A. Simon, giving an insight into the understanding of the origin of many interesting properties based on metal-metal interactions. For instance, compounds such as Ag_8MCh_6 (M = Si, Ge, Sn) are particularly interesting because of their photosensitivity as semiconductors, high ionic conductivity and phase transitions [171]. Also, it is known that nickel-chalcogenide cluster complexes are important in biological routes because they take part in many cellular processes as active centres of many enzymes [172].

They exhibit a wide range of structural motifs, from isolated clusters in Ni_9S_8 [173] and one-dimensional metal chains in Ti_5Te_4 [174] to two-dimensional metal sheets in Sc_9Te_2 (the metal richest compound known to date) [175] and even three-dimensional networks in Sc_6MTe_2 (M = Mn, Fe, Co, Ni) [176] when high levels of reduction are present. However, the electron-counting rules governing these structures are not as clear as those involved in main group elements, where number of skeletal electrons and cluster shape are directly correlated. Within the same condensed metal clusters different types of bonding may occur, namely edge-localized bonds (electron-precise) or delocalized bonding (electron-poor or electron-rich). Little or no relation at all may exist with the number of cluster edges, unlike transition metal clusters found in solution complying with the valence electron count rule [177,178]:

$$N_e = 18n - 2E \qquad \textbf{(1-12)}$$

Where n is the number of atoms in the cluster skeleton and E is the number of edges of the cluster ring or polyhedron. In addition to this, it should be noted that sometimes no general relation exists between bond order and bond length, contrarily to what is a generally accepted concept [179].

Studies on the correlation between metal-metal bonding in metal-rich chalcogenides and that in metals have shown that the empirical relation between bond distance and bond order, *i.e.* equation (1-13), holds well for compounds in which the metal to non-metal ratio is greater than two and that the metal-richest compounds possess bond orders comparable to those of the metals, *i.e*. one, as it would be expected [180].

$$D_n = D_1 - 0.60 \log n \qquad \textbf{(1-13)}$$

Where n is the bond order, D_n is the interatomic distance for a given bond order n and D_1 is the interatomic distance within the metal. Nevertheless, in phases such as Sc_8Te_3 and Y_8Te_3, some M-M bonding distances are considerably larger than the non-bonding distances. The metal atoms are held together by electrostatic and covalent interactions with the neighbouring tellurium atoms instead of by bonding electrons in what is known as a cooperative matrix effect, giving as a result biased bond orders [181]. There are simply not enough electrons in the electron-poorest transition metals to account for all the bonding metal-metal distances.

Considering the large variety of structures encountered in the metal-rich chalcogenide family, some factors governing the structure formation can be clearly inferred:

- The valence electron concentration
- The metal to non-metal ratio
- The radii differences between metal and non-metal atoms

Comprehensive correlation studies between the VEC and the metal to non-metal ratio have been carried out for the family of the transition metal halides, whose results can also be extrapolated to the metal chalcogen family. It is shown that the fewer valence electrons the more prone the system is to cluster condensation as it is seen for the halides $NbCl_5$, Nb_2I_8 and Nb_3I_8 where isolated Nb atoms, Nb_2 pairs and Nb_3 clusters are found, respectively [182].

It is also observed that the metal to non-metal criterion outweighs the latter. The lack of non-metal atoms to coordinate the increasing cluster size when increasing the metal to non-metal ratio becomes the limiting factor. Thus, compounds such as Nb_6F_{15}, Ta_6Cl_{15} and $CsNb_4Cl_{11}$, despite having the same VEC only the latter forms Nb_4 clusters.
Finally, the non-metal atom radius is a determinant factor as to the intracluster variations of metal-metal distances owing to the above-mentioned matrix effect, as observed in Nb_3Cl_8, Nb_3Br_8 and Nb_3I_8 where the Nb-Nb distance is 2.81, 2.88 and 3.00 Å respectively [183]. Furthermore, metal condensation in solid state does not take place in random aggregates but under a unified principle, pointed out by Simon. Isolated clusters increase their size up to M_6X_{12} or M_6Ch_8 units for metal to non-metal ratios of 0.5 and 0.75, respectively. Beyond these ratios, different types of condensation between clusters occur (vertex-linked, edge-linked, face-sharing clusters, *etc*.) giving rise to the already mentioned rich diversity of structures.

Ternary metal-rich chalcogenides are formed by adding a second metal: an alkali, alkaline-earth, transition, rare-earth or main group metal. Alkali or alkaline earth metal-rich chalcogens with condensed or large metal clusters should be difficult to find due to the extra supply of electrons provided by the most electropositive metal, with which it would be feasible to fulfil the two centre-two electron covalent bond demand. As a matter of fact, they do not exist, excepting the family of compounds with the formula $A_xM_yCh_z$ (A = group 1 or 2 metals; M = group 12 metals); however this compound forms open-framework structures with cluster sizes of only 3 or 4 atoms [184].

The structural distortions caused by the addition of alkali or alkaline earth metals are more "predictable" owing to their large electropositivity. They can be intercalated and deintercalated easily from layered binary chalcogenides, and they also originate Zintl phases, in which the alkali or alkaline earth metal transfers all the valence electrons to a transition metal-chalcogen framework [185]. Such frameworks are bonded covalently by traditional two-centre-two-electron bonds, changing their linkage to accommodate the extra electrons in order to fulfil the electron-counting rules. This behaviour renders a decrease in dimensionality as the alkali/alkaline metal proportion increases. For instance, the structures of ZnS and the polychalcogenides $Na_2Zn_3S_4$, Na_2ZnS_2 and Na_6ZnS_4 show respectively a 3D (dimensional), 2D, 1D and 0D character [186].

Transition metal atoms play a more important rôle in terms of bonding, creating new types of structures. The unusually strong bonding existing between early and late transition metals, reported for the first time by Brewer and Wengert [187], gives rise to nine different formula types which, in turn, can be classified depending on whether their building blocks are tricapped trigonal prisms, square antiprisms or face-sharing trigonal prisms [188]. Furthermore, rare-earth metals share many common features with early transition metals originating a similar type of chemistry when combined with late transition metals. Ternary compounds having main group metals, however, remain quite unexplored. The best known of this kind are the families of the antimony transition metal chalcogenides [189] and those with the formula $T_3M_2Ch_2$ (T = Co, Ni, Rh, Pd; M = In, Tl, Sn, Pb, Bi) belonging to the parkerite (M = Bi) or the shandite structure. Exploratory efforts on the Ni-Sn-S system have uncovered several new members of this family, namely Ni_6SnS_2, $Ni_9Sn_2S_2$ and $Ni_{7-\delta}SnQ_2$ (Q = Se, Te) [190,191].

1.4.2 Shandite structure

The mineral $Ni_3Pb_2S_2$, also known as shandite (in honour of Professor S. J. Shand, 1882-1957), is the archetype of a family of compounds with the general formula $M_3A_2Ch_2$ (M = Co, Ni, Rh and Pd; A = In, Pb, Sn and Tl; Ch = S or Se). Its structure was first reported by Peacock *et al*. in 1950 [192].

The large resemblance between the powder pattern of $Ni_3Pb_2S_2$ and that of a closely-related compound, $Ni_3Bi_2S_2$, known as parkerite with a pseudocubic structure, led to the initial assignment of an F-centred cubic unit cell containing 4 formula units.

Table 1-11 Ternary chalcogenides with the shandite structure [193].

Se \ S	In	Pb	Sn	Tl
Ni	$Ni_3In_2S_2$ $Ni_3In_2Se_2$	$Ni_3Pb_2S_2$ $Ni_3Pb_2Se_2$	$Ni_3Sn_2S_2$	$Ni_3Tl_2S_2$
Co	$Co_3In_2S_2$		$Co_3Sn_2S_2$	
Rh		$Rh_3Pb_2S_2$ $Rh_3Pb_2Se_2$		$Rh_3Tl_2S_2$
Pd		$Pd_3Pb_2Se_2$		$Pd_3Tl_2S_2$ $Pd_3Tl_2Se_2$

However, it was rapidly assumed that a primitive rhombohedral unit cell was a more appropriate symmetry, according to the extra reflections observed that destroyed the cubic symmetry, despite having a metrically cubic unit cell [194]. $Ni_3Pb_2S_2$ crystallizes in the space group $R\bar{3}m$ where the Ni atoms occupy 9*d* Wyckoff positions, S atoms 6*c* positions and Pb atoms are split between two positions: Pb(1) in 3*a* and Pb(2) in 3*b*. Therefore, the structure of the known shandites (Table 1-11) is described by substituting the Ni and Pb atoms with the appropriate atoms.

The Ni atoms form a planar metallic array so-called Kagomé lattice formed by corner-sharing Ni hexagons. In the middle of each hexagon lies a Pb(2) atom configuring the centre of a hexagonal bipyramid along with two sulphur atoms. The Pb(1) atoms are found between the Ni layers in a trigonal antiprismatic environment of Ni atoms. The sulphur atoms are capping equilateral triangles of Ni atoms formed between adjacent Ni hexagons at one side, and are bonded to Pb(2) atoms at the opposite side.

The shandite structure can also be regarded as build from face-sharing octahedra formed by the coordination of each Ni atom by two Pb(1), two Pb(2) and two sulphur atoms forming layers of distorted face-sharing octahedra. Some of the vertices of such octahedra lie on 3-fold axes perpendicular to the layers, so that they are related by 120° rotations forming triangular arrays within each layer, the Kagomé lattices.

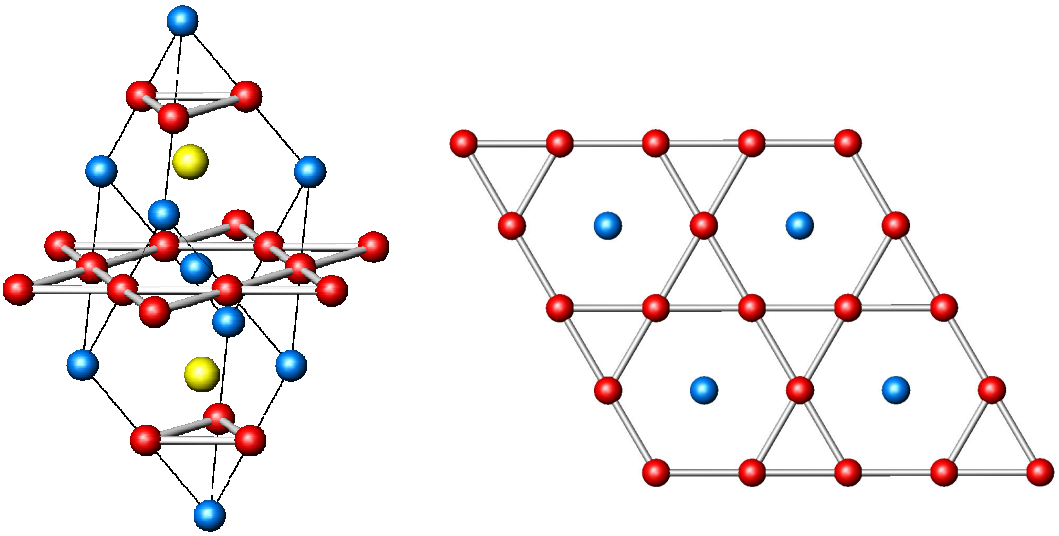

Figure 1-10 Left: $Ni_3Pb_2S_2$ shandite rhombohedral unit cell. Right: Ni Kagomé lattice. Key: Ni in red, Pb in blue and S in yellow.

All the atoms are fixed by symmetry excepting the *z* coordinate of the sulphur atom (Table 1-12), which varies between different compounds. The *z* coordinate shows the displacement of the sulphur atoms along the hexagonal *c* axis and determines the metal-sulphur distances. The structure of the $Co_3Sn_2S_2$ shandite (Figure 1-10) was determined by single crystal diffraction showing the characteristic Kagomé lattice of Cobalt atoms with short Co-Co distances (2.68 Å), slightly longer than those found in Co metal (2.50 Å), and is analogue to that of $Ni_3Pb_2S_2$ (Figure 1-10). A value of 0.2828 was found for the sulphur z coordinate giving rise to remarkably short Co-S distances (2.18 Å) compared to other Co-S bonds in other binary or ternary sulphides [195].

Table 1-12 Atom positions in the shandite structure. Space group $R\bar{3}m$. Hexagonal setting.

Atom	Site	*x*	*y*	*z*
A(1)	3*a*	0	0	0
A(2)	3*b*	0	0	1/2
M	9*d*	1/2	0	1/2
Ch	6*c*	0	0	*z*

1.4.3 Parkerite structure

The mineral $Ni_3Bi_2S_2$ was named Parkerite by Scholtz in 1936 [196]. Despite having the same stoichiometry as the shandite, $Ni_3Bi_2S_2$ crystallizes in a different structure, albeit related. It was indexed on the basis of a cubic body centred unit cell containing two formula units by comparison with other cubic patterns, however the splitting observed in many reflections led first to the assignment of an orthorhombic unit cell (*Pmam*) [197] and shortly after to the true monoclinic unit cell (*C*2/*m*) [194].

Range *et al*. found a model to explain the relation between shandite and parkerite based on the ordering of the Ni atoms [193]. $Ni_3Bi_2S_2$ possesses three Ni crystallographic independent positions corresponding to the 4*g*, 4*e* and 4*i* Wyckoff positions. Bismuth and sulphur atoms occupy two 4*i* and one 8*j* positions respectively. Sulphur atoms lie in a distorted octahedral environment formed by three distinct Ni atoms, two Bi atoms and one S atom. Also, Ni atoms are in the centre of face-sharing octahedra made of four Bi atoms and two S atoms, sharing four faces allowing short Ni-Ni distances (2.7 Å) and the formation of Ni walls within the unit cell. Bismuth atoms are coordinated to six Ni atoms and two S atoms at one side, and none at the other. This fact suggests the presence of a stereochemically active lone pair, being pointed out as the reason why the shandite structure does not form when Bismuth is present [198].

The only known parkerite-like compounds are $M_3Bi_2S_2$ (M = Rh, Ni, Pd) and $Pd_3Bi_2Ch_2$ (Ch = S, Se). $Pd_3Bi_2S_2$, however, is the only parkerite phase that does not crystallize in a monoclinic unit cell, but in the cubic system [199]. $Pd_3Bi_2S_2$ belongs to the space group $I2_13$ and is isopuntal (they share the same space group and occupation of the Wyckoff positions but they have different unit cell ratios and different atom coordination) to the corderotite $Hg_3S_2Cl_2$. The Pd atoms are coordinated by four Bi atoms, two S and four Pd atoms, whereas the S atoms are surrounded by three Pd atoms arranged in a triangular configuration and four Bi atoms. Each Bi atom is, in turn, bonded to three Pd atoms and four S atoms. Yet, the $Pd_3Bi_2S_2$ structure is closely related to that of parkerite, differing only in the occupation of one Pd position, which is, in turn, related to that of the shandite. The relation existing between the shandite, monoclinic parkerite and cubic parkerite structures has been comprehensively studied by R. Weihrich *et al*. showing that the three structure types can be derived from a simple ordering scheme [198].

1.4.4 Structural relation between parkerite and shandite

Both are phases with pseudocubic unit cells in which it is possible to find a CsCl-type cube made of A atoms centred by chalcogen atoms and the M atoms centring the faces of such cubes. The different occupation schemes of the M atoms as well as the off-centring of the chalcogen atoms eventually determine the space group and the type of shandite or parkerite (Figure 1-12).

Range *et al*. were the first to point out the group-subgroup relation existing between the antiperovskite structure, as in that found in the superconductor Ni_3MgC ($Pm\bar{3}m$) and the $M_3A_2Ch_2$ shandite-$Ni_3Bi_2S_2$ parkerite phases; thereby its primitive unit cell can be extracted from a superstructure made of 8 cubelets in which only half of the Ni sites are occupied following a certain ordering scheme [200]. Weihrich *et al*. realized the type-antitype relation existing between the shandite structure and that of the potassium oxostannate (II) $K_2Sn_2O_3$ as well as the existence of a cubic $K_2Sn_2O_3$ phase in full analogy with the cubic parkerite phase, emphasizing the consistency of nature.

They also extended Range´s model to include the cubic parkerite $Pd_3Sn_2S_2$ stating the occupation rules of half of the Ni sites that govern the formation of the shandite, parkerite and cubic parkerite phases [198]. Thus, a corner-sharing scheme leads to a shandite $R\bar{3}m$ phase, whereas edge sharing schemes to $C2/m$ and $I2_13$ parkerite phases (Figure 1-12).

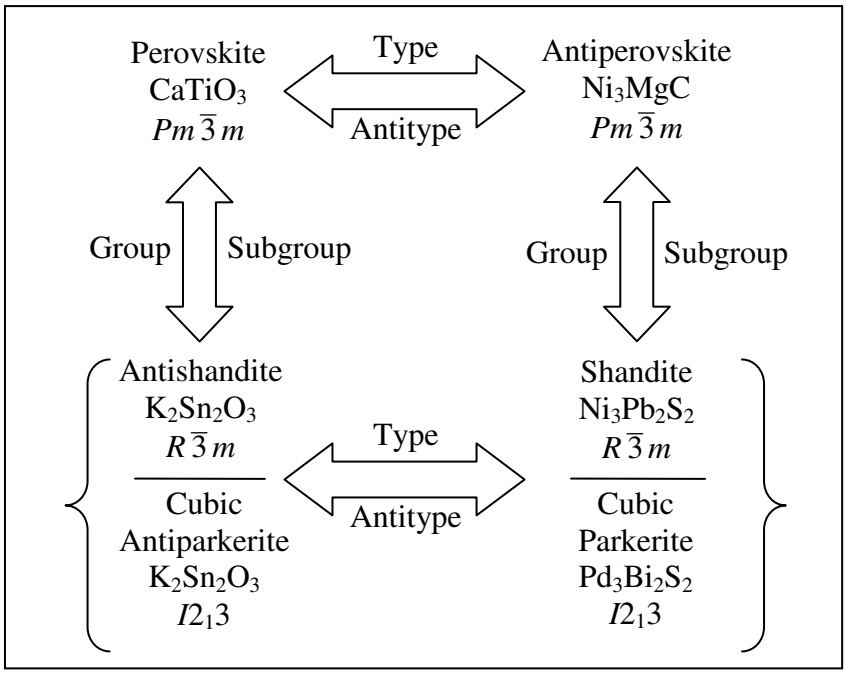

Figure 1-11 Chart depicting the distinct relation types among shandites, parkerites and perovskites, as described by Weihrich *et al*. [201].

Given the ordered half occupancy of the Ni sites and the group-subgroup relations showed in Figure 1-11, shandites and parkerites have been included in a wider group of compounds called half antiperovskites (HAP), with the general formula $M_{3/2}ACh$ (A = Tl, Pb, Bi; Ch = S, Se) [198].

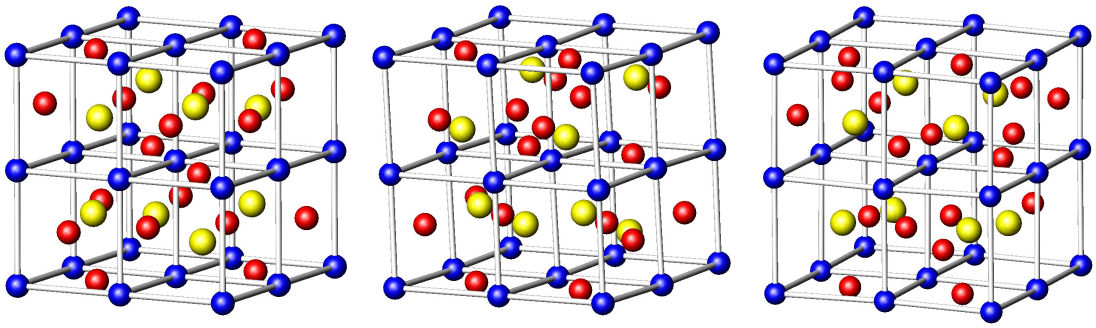

Figure 1-12 Three ordering schemes leading to the shandite *R* $\bar{3}$ *m* (left), the parkerite *C*2/*m* (centre) and the cubic parkerite *I*2$_1$3 (right). Key: sulphur atoms in yellow, M atoms in red, A atoms in blue, $M_3A_2S_2$.

1.4.5 Bonding in shandites

The value of the *z*(S) coordinate measures the extent of the deviation from the ideal body-centred cubic structure, *i.e.* 1/4 (Figure 1-10). The off-centering along the *c* axis of the S atoms brings about the shortening of some A-S distances and the enlengthening of others in a definite 1 + 3 + 3 +1 pattern. A small but steady increase of the z(S) value is observed as the atomic number of the A atom increases, from 0.279 in $Ni_3In_2S_2$ to 0.285 in $Rh_3Pb_2S_2$. The most prominent feature in shandites is the Kagomé layer of transition metal atoms allowing short metal-metal distances. They are slightly longer than in the metal (~ 0.2 Å), forming a covalent network as seen in the metal, after the Ni^0 oxidation state in $Ni_3Sn_2S_2$ was confirmed by Mössbauer spectroscopy [200]. Moreover, band calculations confirm, in the same study, that the d bands in Ni atoms are full.

1.4.6 Electronic transport in shandites and parkerites

As regards their electrical properties, most of the metal-rich compounds are metallic as it would be expected. However, the existence of extended metal-metal bonding systems does not guarantee such property. Spatial orbital delocalization is a *sine qua non* condition for metal-like conductivity. A clear example of this is the compound Y_2Cl_3. Despite possessing a 1D chain of Y atoms as a result of octahedral cluster condensation, all the Y_2Cl_3-type compounds are semiconductors. It has been found that the lack of

orbital overlapping between adjacent octahedral units is accountable for [202]. Unfortunately that is something that cannot be forecast *a priori.*

Hitherto, all resistivity measurements carried out on shandites and parkerites show metallic behaviour, *i.e*. an increase in the resistivity as the temperature rises, as it would be expected for metal-rich chalcogenides and also taking into account the short metal-metal distances. The first data on nickel parkerites and shandites were reported by Michelet *et al*. and complemented later on by Natarajan *et al*. [203,204]. The absolute resistivity values are small (between 10^{-4} and 10^{-6} Ωcm) throughout the whole temperature range for all the measured compounds, consistent with metal-like conductivity (Table 1-13).

Mitchelet *et al*. also noticed an anomaly in the resistivity *vs*. temperature plot for the lead shandites $Ni_3Pb_2S_2$ and $Ni_3Pb_2Se_2$, consisting of a slope change approximately at 100 K. A similar discontinuity was found by Natarajan *et al*. for the shandite $Co_3Sn_2S_2$ around 150 K and was initially ascribed to a magnetic phase transition.

Superconductivity has never been reported in shandite phases, whereas three superconducting compounds have been found in the parkerite family, namely $Rh_3Bi_2Se_2$, $Ni_3Bi_2S_2$ and $Ni_3Bi_2Se_2$, with critical temperatures of approximately 0.7 K [205,206].

Table 1-13 Resistivity (ρ) and Seebeck coefficient (S) values, in Ωcm x 10^{-4} and μVK^{-1} respectively, for some shandite and parkerite phases at 300 K.

Compound	ρ[a]	S[b]	Compound	ρ[b]	S[b]
$Ni_3Bi_2S_2$	1.2	-1.2	$Rh_3Bi_2S_2$	5.6	-2.0
$Ni_3In_2S_2$	1.5	-	$Co_3Sn_2S_2$	9.0	-44.5
$Pd_3Bi_2S_2$	0.6[b]	1.5	$Co_3In_2S_2$	4.5	-6.5
$Pd_3Bi_2Se_2$	1.3[b]	-	$Rh_3In_2S_2$	1.6	0.8
$Ni_3Sn_2S_2$	0.4	-	$Rh_3Pb_2S_2$	4.0	-4.3
$Ni_3Pb_2S_2$	0.8	-	$Rh_3Pb_2Se_2$	2.0	-13.2
$Ni_3Pb_2Se_2$	1.1	-	$Pd_3Pb_2Se_2$	9.0	-

[a] **Extracted from reference [203].**
[b] **Extracted from reference [204].**

Seebeck coefficient measurements were also carried out on some phases showing small values for metallic conductors, as expected. However, the abnormally high value for $Co_3Sn_2S_2$ has been object of further study and it is dealt with further on within this thesis (chapter 6) [195]. It is also worthwhile noticing the influence of the metallic network of M atoms as to the sign of the Seebeck coefficient.

While nearly all shandites possess *n*-type charge carriers, in parkerites the type of metal may invert the value of the thermopower (Table 1-13). As regards their magnetic behaviour, Michelet *et al*. measured the magnetic susceptibility as a function of temperature for the Ni shandites and Ni parkerites in Table 1-13. A typical temperature independent susceptibility curve was observed characteristic of Pauli paramagnetism. They established that Ni d electrons are weakly correlated and that such behaviour is linked to the close Ni-Ni distances within the Kagomé lattice [203].

1.4.7 Half-metallicity and spintronics

The term half-metal has been coined by de Groot to name materials in which only majority-spin electrons with a specific value of the quantum number m_S (either ↑ or ↓) participate in the conduction process, while minority-spin electrons with opposite m_S lie in filled bands typical of semiconducting states [207]. These materials are characterized by having an integral magnetic moment at 0 K; however, experimental methods to determine spin polarization such as photoemission, tunnelling magnetoresistance, Andréev reflection and the Tedrow-Merservey method present an uncertainty that is not negligible. Thus, the best way of identifying half-metals is by means of band structure calculations [208]. According to Coey *et al*., there are four categories of half-metals: Type I_A (IB) only has majority (minority) spin electrons at the Fermi energy. In type II, electrons are confined and localized in a narrow band and conduction takes place via electron hopping (sections 3.7 and 5.4) between spin-polarized sites. Type III have localized ↑ electrons and delocalized ↓ electrons or *vice versa*. Finally, type IV half-metals are semimetallic with a large effective mass difference between electrons and holes [209]. Their conduction characteristics are presented in Table 1-14.

The first half-metallic ferromagnet was predicted by de Groot in the Heusler alloy NiMnSb, as it was confirmed experimentally [210]. Likewise, half-metallic ferromagnetism has been found in CrO_2 with a spin polarization of 100% [211]. This

property has also been recently considered as optimum for the development of spintronic technology, which uses half-metallic ferromagnets for sophisticated electronic devices. Among them, we can find spin transistors, spin filters, spin valves or magnetic tunnel junction devices [208,212,213,214].

Table 1-14 Conductivity features of half-metals. Extracted from reference [208].

Type	DOS	Conductivity	$\uparrow e^-$ at E_F	$\downarrow e^-$ at E_F
$\mathbf{I_A}$	Half-metal	Metallic	Itinerant	None
$\mathbf{I_B}$	Half-metal	Metallic	None	Itinerant
$\mathbf{II_A}$	Half-metal	Non-metallic	Localized	None
$\mathbf{II_B}$	Half-metal	Non-metallic	None	Localized
$\mathbf{III_A}$	Metal	Metallic	Itinerant	Localized
$\mathbf{III_B}$	Metal	Metallic	Localized	Itinerant
$\mathbf{IV_A}$	Semimetal	Metallic	Itinerant	Localized
$\mathbf{IV_B}$	Semimetal	Metallic	Localized	Itinerant

Chapter 2

Experimental techniques

2.1 Synthetic methods

2.1.1 Solid state reaction

This method is applied at much lower temperature than the melting point of the reactants. The limiting factor is the diffusion rate and the reaction timescale ranges from a few days onwards. Hence, the elements must be intimely blended together prior to the reaction in order to obtain the correct stoichiometry throughout the reaction mixture. This step is determinant as to avoid local deviations from the initial stoichiometry and the formation of unwanted impurities thereof.

Stoichiometric quantities of the starting elements are mixed in an agate mortar before being put into a carbon-coated silica tube and sealed under vacuum (10^{-4} torr). Carbon coating is produced by the pyrolysis of acetone. The inner walls are soaked with acetone and heat is applied by means of a blow torch from the outer side. The process is repeated three times to ensure a uniform and homogeneous layer. The silica tube, approximately 13 cm long and 1 cm internal diameter, is then placed in a furnace and heated up to high temperature (typically between 600-1200 °C) during two-three days (Figure 2-1). Heating and cooling rates are controlled when necessary. Afterwards, the tube is opened, its contents ground in an agate mortar and analysed by powder X-ray diffraction to monitor the reaction progress. This process is repeated until reaction completeness.

2.1.2 Chemical vapour transport

This method is based on the concept of chemical transport reactions, which was first introduced by Schäfer [215] and is routinely used to synthesize single crystals from a mixture of elements. Instead of vaporising a solid directly at high temperatures it may be vaporized at much lower temperatures by forming highly volatile chemical intermediates. Then, the reaction mixture in gas phase can be controlled by using the temperature dependence of the chemical equilibrium involved. The surprising feature of this method is that only small amounts of the transporter agent are needed to convert unlimited amounts of solid into the gas phase. The transporter set free after the crystallization, diffuses back to react with more solid following a closed cycle. The chemical reaction involved in the transport is:

$$A_s + B_g = AB_g \qquad \textbf{(2-1)}$$

And the amount of transported material, n_{AB}, can be quantified by the expression:

$$n_{AB} = (Dqt / sRT)(P_{AB(2)} - P_{AB(1)}) \qquad \textbf{(2-2)}$$

Where n_{AB} are the number of mols of AB diffused, D is the diffusion coefficient, q is the tube cross section, s is the length of the diffusion path, t is the reaction time, R is the gas constant, T is the absolute temperature of the diffusion path and $P_{AB(i)}$ is the partial pressure of AB at the location with temperature T_i.

Whether the reaction takes place from the hot to the cold end or *vice versa* is determined by the sign of the heat of reaction ΔH in the temperature dependence expression of the equilibrium constant:

$$\frac{d\ln K}{dT} = \frac{\Delta H}{RT^2} \qquad \textbf{(2-3)}$$

In the transport reactions in which the material is the same at both sides of the reaction tube, the driving force for the transport is simply the concentration gradient caused by the temperature dependence of the heterogeneous equilibrium. The choice of such reactions has to meet the following criteria:

- Chemical transport is only possible when only gases participate in the reaction.
- The reaction must be reversible. This is achieved at high temperature because of the volatility of the reactants.
- The equilibrium position of the reaction must not be extreme, *i.e*. must not be displaced towards the reactant or the product side. Otherwise, the concentration gradient is not large enough for the transport to occur.
- The transport efficiency is maximum if the concentration gradient (ΔP_{AB}) is maximum. In this case, the Gibbs enthalpy of the transport reaction is close to zero, although this condition is not critical.

Chemical vapour transport can be applied in fields such as the preparation of epitaxial layers, crystal-growing, compensation of tungsten vaporization in a filament lamp, detection of new gaseous compounds and determination of thermodynamic data. Transport reactions are usually carried out in sealed cylindrical tubes made of silica. The reactants and the transporting agent are sealed under vacuum if the latter is not volatile at room temperature, namely NH_4Cl or S. If iodine is used the tube needs to be cooled prior to sealing. If the transporting agent is gaseous at room temperature, namely

Cl_2, HCl or HBr, then the tube is flushed with the gas and then sealed off. The most important transporting agents are the following:

- F_2, Cl_2, Br_2, I_2
- HF, HCl, HBr, HI
- O_2, S, H_2O, CO, CO_2
- $HgCl_2$, $AlCl_3$, $SiCl_4$, $NbCl_5$

Stoichiometric amounts of the elements are ground together in an agate mortar and placed directly into a silica tube. Approximately 100 mg of I_2 are added as a transporter agent and the tube is kept under a liquid nitrogen bath until the vacuum reaches 10^{-4} torr to avoid sublimation of the iodine. Once sealed, the tube is placed into a zone tube furnace where a temperature gradient is set and controlled. The timescale for this method ranges from one week onwards depending on the quantity and size of the desired crystals. The temperature gradient necessary for the crystal growth to take place is reaction dependent. A systematic approach to the optimized conditions needs to be carried out. Larger or smaller gradients can lead from no crystal growth at all to growth of crystals with unexpected stoichiometries. During this process, it was found that very small temperature gradients are needed for the crystal growth of CoGeTe. Examples in the literature emphasizing the different temperature gradients needed for each type of reaction can be found elsewhere [216].

Figure 2-1 Left: high-temperature furnaces used for both synthesis in powder form and crystal growth. Right: typical sealed silica tube containing the reaction mixture.

2.2 Structural characterization

2.2.1 Laboratory powder X-ray diffraction

X-rays were discovered by Wilhem Röntgen in 1895. They are an electromagnetic radiation with a wavelength in the range between 0.1 and 100 Å, which is the order of magnitude of interatomic distances and therefore can be used to explore them. The production of X-rays involves the acceleration of electrons by means of high voltages and their collision against a metallic target from which the radiation is released (Figure 2-3). As the voltage is increased, white radiation emerges from the target until a certain threshold is reached (typically 20-50 kV) at which the ionisation of the 1s electrons (*K* shell) takes place and two very intense wavelengths are emitted superimposed to the white radiation: the corresponding to the 2p → 1s transition (K_α) and the 3p → 1s transition (K_β) (Figure 2-2).

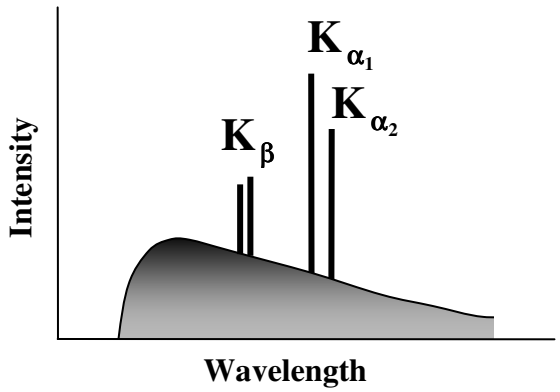

Figure 2-2 Typical X-ray emission spectrum of a metal.

The frequencies of the K_α and K_β lines are very characteristic of the target metal. The K_α lines corresponding to several metals are displayed in Table 2-1.

Table 2-1 Most common metal targets and their characteristic X-ray wavelength.

Metal	K_α wavelength / Å
Cr	2.29
Fe	1.94
Cu	1.54
Mo	0.71
W	0.21

Chromium radiation is too soft for crystallographic purposes, whereas wolframium radiation is too hard to be used in conventional X-ray diffractometers because the

instrumental resolution is not good enough to take advantage of its properties. The target metal most commonly used is copper both for being cheap and with an intermediate wavelength. Molybdenum is the most common target for single crystal X-ray diffraction, given that its shorter wavelength radiation produces diffraction spots that are closer together. This is ideal for area detectors that allow entire datasets to be collected in one single position.

In the field of crystallography, monochromatic radiation is highly desirable and the K_β radiation is eliminated by means of monochromators or nickel filters before passing through the sample. The diffracted radiation pattern is then recorded and analyzed. Depending on whether this pattern has been reflected from the sample or has gone through it, the diffraction geometries can be classified as Bragg-Brentano (flat plate geometry) or Debye-Scherrer (transmission geometry), respectively.

X-ray radiation is diffracted by crystalline solid structures giving rise to a very definite pattern that acts as a characteristic fingerprint. Diffraction takes place only if the incident and diffracted beams fulfil a relationship known as the Bragg's law:

$$2d_{hkl}\sin\theta = n\lambda \qquad \textbf{(2-4)}$$

This law establishes that a diffractive event will occur for a radiation of wavelength λ at an angle 2θ between the incident and diffracted beams (Figure 2-4), caused by the atoms lying in the (*hkl*) planes that are at a distance *d* from each other, being *n* the reflection order.

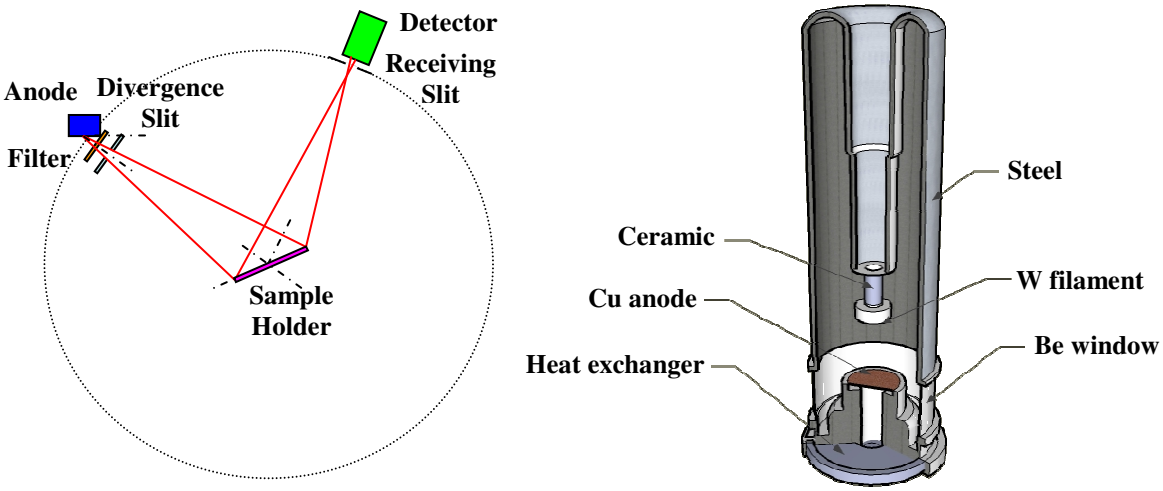

Figure 2-3 Left: Bragg-Brentano geometry diffractometer. Right: Typical laboratory X-ray tube.

The intensity of the reflected beams is collected in an automated X-ray diffractometer and plotted as a function of the 2θ angle. A proportional relation to the square of the structure factor F_{hkl} relates such intensities to the crystalline structure of a material, as it was pointed out in section 2.2.8, by means of equation (2-16).

Laboratory powder X-ray diffraction patterns shown in chapter 6 were collected on a Philips PA2000 diffractomer with nickel-filtered Cu K_α radiation ($\lambda = 1.5418$ Å) between 10-80 2θ° in 0.02 2θ° steps. The patterns show in chapter 4 were collected using a Bruker D8 Advance powder diffractometer, operating with monochromated germanium Cu $K\alpha_1$ radiation ($\lambda = 1.5405$ Å) and fitted with a Bruker LynxEye linear detector. Data were collected between 10-120 2θ° in 0.014 2θ° angular increments.

2.2.2 Single Crystal X-ray diffraction

The same principles used in powder laboratory X-ray diffraction can be applied in single crystal X-ray diffraction as to the generation of X-rays and the law governing the diffractive events (Figure 2-4). The most common target metal for single-crystal X-ray sources is molybdenum instead of copper.

Selected crystals were collected (typically 0.1 x 0.1 x 0.1 mm), mounted on a glass fibre and placed under the X-ray beam of a Bruker Nonius X8 Apex diffractometer with Mo-K_α ($\lambda = 0.71073$ Å). Data collection was carried out by Ms Patricia Leyva-Bailén. An initial quick data collection was performed in each of the crystals to determine the unit cell using the software package Apex-2 [217]. Following full data collection, a list of reflections was obtained, the observed structure factors, $F_{0,}$ and their standard deviations, which were used to determine the space group of the crystal by the Apex software. Direct methods were used to solve the structure by means of the SIR-92 software [218], in which the most important reflections are used to obtain an initial guess of the crystal structure. Further refinement of the structure was carried out using the CRYSTALS program suite [219] by creating a Fourier difference map between the observed structure factors $|F_o|$ and those calculated using the initial guess $|F_c|$. The peaks and valleys found in the map are used to find out what atoms need to be changed, added or subtracted, along with the chemical knowledge. The completeness of the model is expressed by the value of the residual *R* factor, which is to be minimized:

$$R = \frac{\sum \left| |F_o| - |F_C| \right|}{\sum |F_o|} \qquad \textbf{(2-5)}$$

The value of *R* is typically between 0.02 and 0.07 for a correct model. The refined parameters that enter into the model are the atomic positions and their thermal parameters, adding up to nine refined parameters for each independent atom. For some larger crystals a correction for X-ray extinction is needed to account for the loss of transmitted beam intensity.

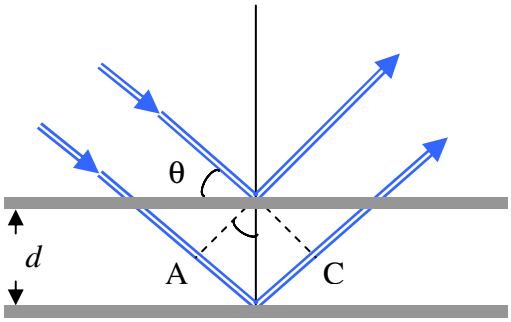

Figure 2-4 Schematic representation of a diffractive event.

2.2.3 Synchrotron X-ray diffraction

The experiments were carried out at the European Synchrotron Radiation Facility (ESRF), beam line ID31, formerly known as BM16 (high-resolution powder diffraction) situated at Grenoble (France). The ESRF is a third-generation synchrotron light source with 844 m of storage ring circumference, 40 beam lines and 6 GeV of maximum electron energy. ID31 can accept 4 mrad of white X-ray radiation in the horizontal plane from the insertion device, which is collimated on a curved mirror to obtain a residual vertical divergence around 12 μrad at FWHM (Full Width at Half Maximum) [220]. This implies a beam thickness of 0.3 mm at 25 m from the source.

Synchrotron light was first observed at General Electric (USA) in 1946 [221] and, initially, it was considered as a nuisance in particle accelerators for the study of high-energy particle collisions. It caused a costly energy loss, that had to be offset with more electrical power, as well as heating of the walls and ion desorption thereof, which interfered with the particle beam and reduced its lifetime. It was not until 1981 that the world's first dedicated synchrotron light source was built at Daresbury (UK). Nowadays there are around 50 synchrotron facilities throughout the world with circumference ranging from 10 m to 1.3 km. Synchrotrons are particle accelerators, generally

electrons, with a circular shape that are optimised for long-term containment of particle beams at ultrahigh vacuum (10^{-9} mbar). They possess radiofrequency cavities and other magnetic devices whereby the particles are forced to bend following a circular orbit and accelerated to velocities close to the speed of light *c*. Electrons are produced in a linear accelerator (LINAC) and then introduced into the storage ring where they are accelerated up to 6 GeV.

The principle behind synchrotron radiation is the emission of photons by charged particles whenever these are accelerated in a magnetic or electric field. Such emission has a dipole pattern which changes to a very narrow strip of radiation when the particles are accelerated to *c*. Thus, the angle between the photon and the direction of motion ϑ, for the worst-case scenario (*i.e.* 90°) is reduced following the expression:

$$\vartheta = \frac{mc^2}{E} \qquad \textbf{(2-6)}$$

Where *m* is the electron mass, *c* is the speed of light and *E* is the energy of the ring in GeV. Therefore the radiation emitted tangentially will have a vertical divergence dictated by equation (2-6).

Intrinsic collimation in the vertical direction and a highly polarized and intense beam allow synchrotron X-ray radiation to provide high resolution with good counting rates. Moreover ID31 possesses a white (continuous) spectral distribution permitting the selection of any wavelength between 2.48 Å and 0.21 Å (5-60 keV) with very little absorption along the beam path. Only beryllium windows isolate the ultrahigh vacuum of the storage ring from the chamber where the experiment takes place. The beam is monochromated via a water-cooled double crystal of Si [111] before being sent to the sample. The diffractometer can accept either a spinning capillary or flat-plate specimens. The diffracted beam analyzer consists of 9 scintillation detectors, which are preceded by 9 Ge [111] crystals mounted on a single rotation stage, allowing a clear signal when changing wavelength with just one single adjustment.
Data were collected by Dr Paz Vaqueiro and Dr Irene Margiolaki. The samples were loaded into a borosilicate glass capillary, mounted on the axis of the diffractometer and spun at 50 Hz during measurements in order to improve powder randomisation. Appropriate wavelengths were selected and data were collected in a continuous scan mode up to 30°.

2.2.4 Anomalous scattering or resonant diffraction

The atomic scattering factor of an atom, f_a, is defined as the ratio of the amplitude of the wave scattered by the atom to the amplitude of the wave scattered by a free electron. It is a complex expression given by:

$$f_a = f_a^0 + f_a^{'} + if_a^{''} \qquad \textbf{(2-7)}$$

The first term on the right is the most frequently quoted and is wavelength independent. Mathematically it is defined as the Fourier transform of the electronic density $\rho_a(r)$ in the atom. It is measured in number of free electrons, is angle dependent and tends to the atomic number Z_a of the element as the Bragg angle 2θ does to zero.

The complex part of the atomic scattering factor, is the resonant scattering factor, which is sensitive to the X-ray photons that are absorbed, when their energy is close to an electronic resonance, by electrons from inner shells (K, L,...). Its value is negligible far away from an absorption edge, but it becomes important close to it and has no dependence with the scattering angle [222]. The resulting scattering factor, if the experiment is performed near the absorption edge, can be between 2 and 8 electrons lower than the free atom. Moreover, it is known that oxidation states, local symmetry and chemical effects can have a marked influence of f' and f'' [223].

This fact can be exploited to perform experiments that distinguish equal atoms with different oxidation states (valence contrast experiments) or atoms with similar scattering factors (neighbouring element contrast experiment) and to solve complicated structures by varying the scattering power of an atom in order to determine the phase of the structure factor. The value of $f_a^{''}$ can be readily determined experimentally by measuring the X-ray absorption as a function of the radiation energy, following the optical theorem [224]:

$$f_a^{''}(\omega) = (\omega/4\pi r_e c)\sigma(\omega) \qquad \textbf{(2-8)}$$

Where ω is the radiation frequency, r_e is the classical radius of the electron and σ is the absorption cross section. $f_a^{'}$ is then calculated by the Kramers-Kronig integral, whereby both components of the anomalous scattering are related:

$$f_a^{'}(\omega_i) = (2/\pi)\int_0^{\infty} \omega f_a^{''}(\omega)/(\omega^2 - \omega_i^2)\mathrm{d}\omega \qquad \textbf{(2-9)}$$

2.2.5 Time-of-flight neutron diffraction

Neutrons are subatomic particles with no net charge and a mass very close to the proton mass, 1.67495 x 10^{-27} kg. They possess a nuclear magnetic moment and a half-life of 11.2 min. X-rays and neutrons are scattered by completely different mechanisms. X-rays are scattered by electrons, meaning that elements with high atomic number will be better scatterers than elements from the top of the periodic table, with fewer electrons.

Moreover, electrons surrounding the atom cause interference phenomena, which originates an angle-dependent decay of the scattered intensity. Conversely, neutrons are scattered by nuclei. Such mechanism implies that there is no direct relation between the scattering intensity and the atomic number; therefore the scattering cross section must be determined experimentally. It changes between different nuclei and also between different isotopes of the same element and it is not angle dependent. The nuclei size is very small compared to the surrounding electron cloud; therefore there is no need to introduce a form factor to account for the interference with other nuclei, hence originating an angle-independent scattering.

The coherent scattering cross section of deuterium is three times larger than hydrogen and the isotope ^{14}N is a 550 times better coherent scatterer than ^{51}V, whose coherent scattering cross section is almost negligible, although the ^{51}V scattering is almost entirely incoherent. Furthermore, the small size of the nucleus in relation to the atom allows neutrons to penetrate deep into matter without being affected. This obliges to use larger amounts of sample than in X-rays (typically 2-3 grams), although this fact is offset by the lower absorption of neutrons by elements across the periodic table, which is 4 orders of magnitude smaller than X-rays.

Yet, neutrons also interact with the electronic spin causing an extra scattering mechanism when long-range magnetic ordering occurs. The neutron nuclear magnetic moment is responsible for such interaction revealing that it is not a fundamental particle. The main applications of neutron diffraction experiments are the study of cation distribution, hydrogen location, structure determination and solution of magnetic structures.

There exist two main methods of producing neutrons for crystallographic purposes, namely, constant-wavelength nuclear reactors and by spallation. In both methods, fast neutrons are produced that must be slowed down to thermal energies in order to obtain a neutron wavelength in the order of magnitude of interatomic distances, *i.e.* $\lambda \sim 1.55$ Å.

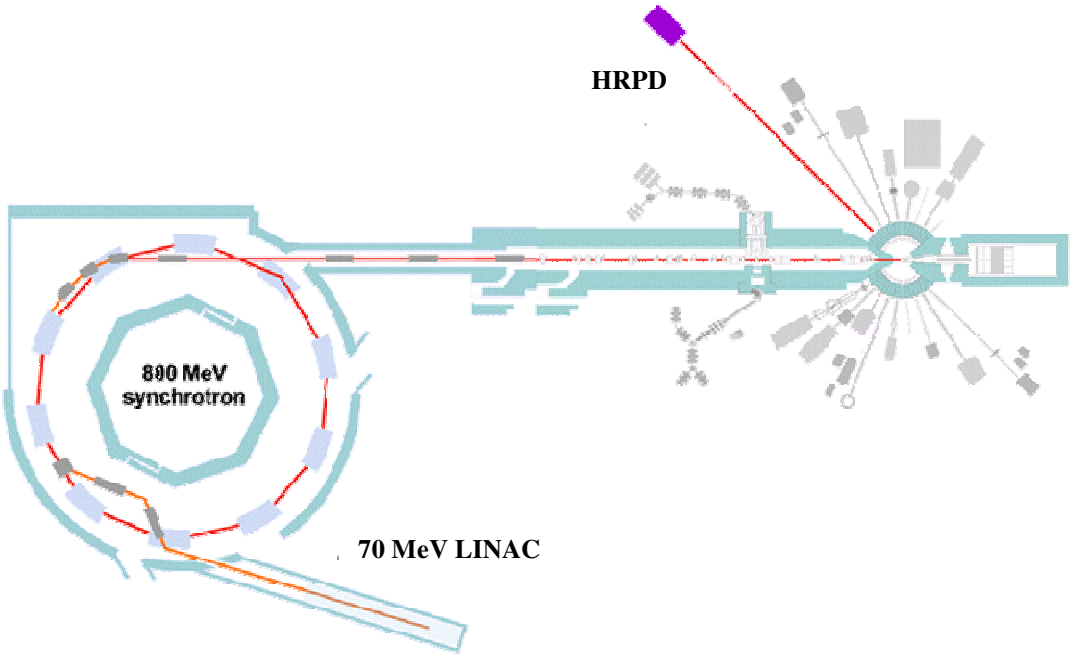

Figure 2-5 Layout of the ISIS spallation source. The HRPD diffractometer has been highlighted for clarity [225].

Since 1945, controlled nuclear fission is available through the disintegration of the isotopes ^{235}U and ^{239}Pu giving rise to neutrons that can be taken advantage of. To be operative, these sources require a fuel package (enriched ^{238}U), control rods made of any neutron absorbing material (typically boron-enriched steel or nickel), a neutron moderator to slow neutrons (usually light and / or heavy water) and a shielding material to cover the reaction chamber. Nuclear reactors offer a neutron flux of approximately 10^{15} n $s^{-1}cm^{-2}$. Neutrons arising from the moderator are in thermal equilibrium and their spectrum follows a typical Maxwell-Boltzmann distribution.

In the spallation method, a pulsed source replaces the continuous source from a steady-state reactor. The interaction of a high-energy proton beam (> 500 MeV) with a heavy metal target (W or ^{238}U) causes "bursts" of neutrons by the spallation process (spalling, or chipping of the target nucleus) that, in turn, must be slowed down to produce a pulsed beam. At the ISIS facility, high-energy protons (> 20 MeV) are produced and accelerated to nearly the speed of light in a proton synchrotron to strike a tantalum target producing a 0.4 μs wide pulse 50 times per second allowing very intense narrow neutron pulses, whereby enabling high-resolution time-of-flight (TOF) experiments.

Fast neutrons are cooled down by a liquid methane moderator covered in a strong scatterer of neutrons (either nickel or beryllium) yielding neutron fluxes greater than 10^{17} n $s^{-1}cm^{-2}$. These "bursts" of neutrons possess a pulsed time structure comprised of

many wavelengths. Then, neutrons sort themselves according to their velocities (wavelengths) so that the time of flight T from the moderator to an instrument detector is proportional to the wavelength λ and is given by:

$$T = \frac{\lambda L m}{h} \qquad \textbf{(2-10)}$$

Where L, m and h are the total flight path, the mass and the Planck constant, respectively. It is worth mentioning that the time spectrum of neutrons in spallation sources depends on the type of moderator (water, liquid methane or liquid hydrogen), offering the possibility of tailoring the wavelength distribution in time. The relation of the time of flight to the d-spacing is quadratic, following the expression:

$$T = Cd + Ad^2 + Z \qquad \textbf{(2-11)}$$

Where C, A and Z are constants characteristic of a given detector and may be refined. Time-of-flight neutron diffraction data were collected on the HRPD diffractometer at ISIS, Rutherford Appleton Laboratory (Figure 2-5). It belongs to the first generation of neutron diffractometers capable of achieving a resolution (Δd / d) lower than 0.001 at the backscattering bank. The flight path is approximately 100 metres long, achieving a resolution of 8 x 10^{-4} at the backscattering bank, which is effectively constant over the wide range of d-spacing available (0.2-5 Å). The flight path consists of a curved section from 6 to 60 metres with an 18 km radius optimised for a 50 Hz source with no direct line of sight to the sample and no neutrons transmitted below 0.48 Å. A straight section, from 60 to 90 metres, to eliminate beam irregularities and a sample holder at 95 m from the source [226]. Detection of the scattered beam takes place at the backscattering, 90° and low angle (30°) banks. The low angle detector is made up of a ^{3}He gas tubes array, which detects neutrons by inducing a nuclear reaction with the highly absorbing helium isotope ^{3}He and detecting the resulting γ radiation, following the nuclear reaction:

$$^1\text{n} + {}^3\text{He} \rightarrow {}^1\text{H} + {}^3\text{H} + 0.77\ \text{MeV} \qquad \textbf{(2-12)}$$

The backscattering and 90° detectors are based on ^{6}Li-enriched scintillators that emit flashes of light when reaction products and an Ag-doped ZnS phospor come into contact. The nuclear reaction in this case is:

$$^1\text{n} + {}^6\text{Li} \rightarrow {}^3\text{He} + {}^4\text{He} + 4.79\ \text{MeV} \qquad \textbf{(2-13)}$$

The light is then amplified and converted into an electric signal by a set of 64 photomultipliers [225]. The samples, in the form of friable powder, were loaded into thin-walled vanadium cans of approximately 5 cm length and the data manipulation and reduction was carried out using Genie [227]. When necessary, the sample was cooled down in a cryostat.

2.2.6 Group-theoretical analysis

Under certain conditions, many solids undergo phase transformations keeping the same chemical composition; this phenomenon is known as polymorphism. In those cases in which a profound internal atomic rearrangement does not occur, changes can be studied by symmetry relations. In order to determine the space group associated to the distortion occurring when anion substitution takes place, group-theoretical analysis was used implemented using the software package ISOTROPY [228]. This program displays information about space groups, irreducible representations, isotropy subgroups and phase transitions, making them more accessible. Mainly, three steps are involved in the space group determination of any given distortion [229]:

- The association of an irreducible representation (irrep) with any given distortion
- The listing of the isotropy subgroups associated to this irrep
- The identification of group-subgroup relationships

2.2.7 Single crystal *vs*. powder

By and large, any crystal structure can be regarded as ”determined” when its space group and lattice parameters are known as well as the positions of all the atoms contained within the unit cell. There exist common steps regardless the method used (either single crystal or powder diffraction) in order to obtain such information:

- Indexing of the diffraction pattern and determination of the crystal system (*e.g.* cubic, rhombohedral, *etc.*) and lattice parameters. This is a critical step, which consists of assigning *hkl* values to each of the observed reflections
- Identification of the space group. Once the crystal system has been determined, with the assistance of the International Tables for Crystallography the space group can be worked out by looking at the systematic absences and index relations among the *hkl* values.

- Solution of the phase problem and determination of an approximate structure by means of either the Patterson method or direct methods.
- Refinement of the structure.

With single crystal X-ray data these steps are carried out routinely by software packages such as Apex-2 [217] for the space group determination, SIR-92 [218] for the solution of the phase problem and Crystals [219] for refining and solving the structure.

With powder X-ray data, however, the difficulty in solving the structure roots on the overlapping and the crystal system. If the crystal system is cubic, indexing can be carried out by hand owing to the straightforward relationship between the lattice parameter, the *d*-spacing values and the sum of the squared *hkl* values:

$$\frac{1}{d_{hkl}} = \frac{1}{a^2}(h^2 + k^2 + l^2) \qquad \textbf{(2-14)}$$

However, for crystal systems of lower symmetry this relationship becomes rather cumbersome [230] and computational methods are required to automatically index reflections belonging to any system. The most wide-spread software package for such purpose is DICVOL91 [231]. The next step involves the obtention of the integrated intensities, and therefore the absolute values of the structure factors, $|F_k|$, from which a similar single crystal data treatment can be performed. Nevertheless, the most widely used method for solving structures in powder diffraction involves de last step, *i.e.* the structure refinement. A great many of the unknown crystal structures are simply derived from known parent structures in which either the elements and/or the stoichiometry have changed and the atomic positions of the model can readily be used for refining the atomic positions of the new compound. In section 2.2.9 this method will be reviewed in more detail.

The powder diffraction method using conventional X-ray sources was developed independently in 1916 by Debye and Scherrer in Germany and in 1917 by Hull in the United States. Traditionally, powder diffraction has been routinely used in phase identification, unit cell determination and the analysis of structural imperfections and from the seventies onwards for refining crystal structures from powder data.
A powder sample differs from a single crystal in that it is an ensemble of very small homogeneous particles, which can be regarded as elementary single crystals called crystallites (Figure 2-6). A common term used when dealing with powders is grain. It is

a physically differentiated entity from the rest of the bulk phase and has sizes typically ranging from a few micrometers to millimetres. A sample can be composed of only one or many crystallites, being a single crystal regarded as one unique crystallite. A powder is then an aggregate of crystallites that are randomly orientated across the powder sample.

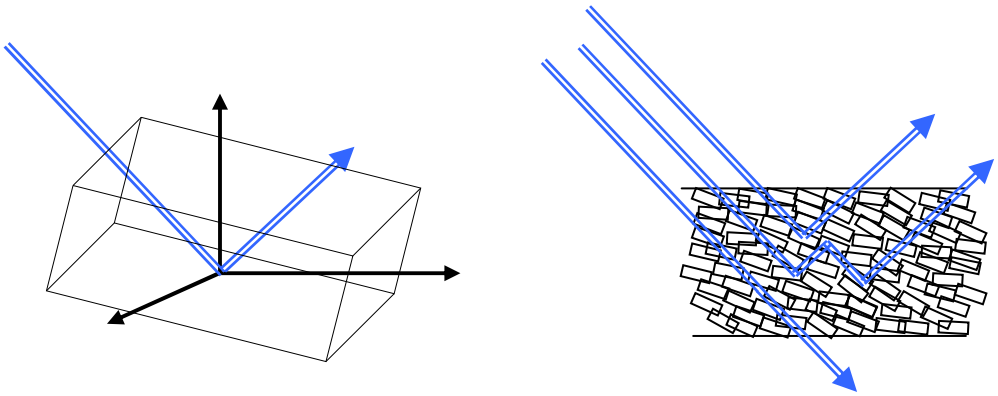

Figure 2-6 Different paths followed by X-rays when they go through a single crystal (left) or a sample in powder form (right). Paths are marked in blue.

Until the advent of the Rietveld method in 1969 [232] the usual procedure to solve structures of crystalline materials was to obtain a well-formed single crystal and analyse its single crystal diffraction pattern by means of either direct methods or the Patterson method, in order to obtain the atomic positions within the crystal. However, crystal growth is not a straightforward step.

Large single crystals are needed (typically 1-3 mm across) and cumbersome and expensive experimental set-ups are often necessary. Even if a large crystal is obtained, it may suffer from defects such as dislocations, faults and disorder and magnetic domain structures, which make the interpretation of the diffracted intensities unreliable; twinning of the crystal is also a common problem, which obliges to discard the crystal. All these effects may hinder the correct solution of the structure. Furthermore, a single crystal is not representative of the bulk; it may decompose during the data collection or it simply may have a too complicated structure.

Contrarily, many of these effects are just inexistent or become isotropic in the powder method being easier to model and determine. Nevertheless, there is an unavoidable loss of information when going from a three-dimension to a one-dimension X-ray pattern. The penalty to pay with powder techniques is the unavoidable large inaccuracy in the estimates of the intensity due to peak overlap, background and texture effects.

Moreover, the polycrystalline nature of the sample causes an extra loss as a result of the random orientation of the crystallites.

Until very recently, *ab initio* structure determination following the above-mentioned procedure was seldom possible. However, more sophisticated computational methods along with improvements in the resolution and power of the radiation sources have brought about that such determinations become feasible to a larger extent. The obtention of a starting model with which refine the unknown structure is the main purpose of the methods based on powder data, which can be summarized as follows:

- Identification of an isostructural material of known structure.
- Use of difference Fourier methods to investigate derivatives of known structures. Again, it is of paramount importance to obtain a unique set of integrated intensities to succeed in the structure determination.
- Trial and error methods, which can be very time consuming and frequently unrewarding.

Once the correct model has been obtained, it will need further refinement by fitting the calculated powder pattern to the experimental pattern, from which further information can be extracted. Thus, the success in determining the structure from a powder pattern will depend strongly on the reflection overlapping, and until 1969 the only known method was the use of the total integrated intensities (integral method) of separated groups of overlapping peaks; thereby allowing the structure determination of structures belonging solely to either cubic or hexagonal systems. Such a method overlooks the detailed profile, on top of the above-mentioned loss of information.

Rietveld's breakthrough consisted of considering each of the points of the pattern as an independent observation (Rietveld's method), whose intensity is the addition of intensities coming from all the overlapping reflections at that point of the pattern. Hence, it overcomes the underlying problem of peak overlapping and allows the extraction of the maximum amount of information contained in the powder diagram offering the possibility of solving the structures of low-symmetry materials. Both methods will be summarized hereafter.

2.2.8 Integral method

Few structures have been refined using this method, most of them of high-symmetry space groups where little overlapping occurs among reflections. If the peaks present in a

pattern are resolved, even if there exists overlapping to a small extent, the structural parameters can be determined by refinement directly from the integrated intensities of the separate peaks, as a proportional relation to the square of the structure factor, F_{hkl}, relates such intensities to the crystalline structure of a material:

$$I_k = \left|F_k\right|^2 A_k \qquad \textbf{(2-15)}$$

Where A_k comprises all those variables affecting the intensity of a reflection k. The structure factor F_k is determined by the atomic positions within the unit cell and is expressed as follows:

$$\mathrm{F_{hkl}} = \sum_{\mathrm{j}} \mathrm{N_j f_j} \exp(i2\pi[\mathrm{hx_j} + \mathrm{ky_j} + \mathrm{lz_j}]) \exp(-\mathrm{M_j}) \qquad \textbf{(2-16)}$$

Where hkl are the Miller indices of a given plane, x_i, y_j, z_j are the atomic positions of the atom j in the unit cell, f_j is the atomic scattering factor for the atom j, which depends on the number of electrons, and $\exp(-M_j)$ is a thermal vibration parameter known as Debye-Waller factor.

The calculated intensity of any point in the pattern y_i' is then described by the scale factor S, the structural term I_k and another term describing the profile at that point, Ω_{ik}, which in the case of neutrons will usually be a normalized Gaussian-type function, or in the case of X-rays a more complicated function (normally a convolution of a Gaussian and a Lorentzian functions) describing a more asymmetric peak shape:

$$y_i' = SI_k \Omega_{ik} \qquad \textbf{(2-17)}$$

If a single reflection is made of n profile points, then we will have a system of n equations with i values from i_0 to $i_0 + n - 1$ so that:

$$\left.\begin{aligned} y_{i_0}' &= SI_k \Omega_{i_0,k} \\ &\vdots \\ y_{i_0+n-1}' &= SI_k \Omega_{i_0+n-1,k} \end{aligned}\right\} \qquad \textbf{(2-18)}$$

If these equations are added up we obtain:

$$\sum_{j=0}^{n-1} y_{i_0+j}' = SI_k \sum_{j=0}^{n-1} \Omega_{i_0+j,k} \qquad \textbf{(2-19)}$$

And provided that n is large enough, the right hand-side sumatory will be nearly one; therefore we can write:

$$\sum_{j=0}^{n-1} y'_{i_0+j} = SI_k \qquad \textbf{(2-20)}$$

Which is the equation used for a conventional integrated intensity refinement. It shows that the peak area is directly proportional to the intensity, which, in turn, is proportional to the square of the structure factor for a given reflection. The refinement of the calculated intensities to the observed ones is carried out by a least-square procedure minimizing the residual M:

$$M = \sum_k w_k (\sum_j y_{j,k} - SI_k)^2 \qquad \textbf{(2-21)}$$

Where w_k is the weight given to the integrated observed intensity for a given reflection j, which is the sumatory over all the j points the reflection j is composed of.

2.2.9 Rietveld Method

By definition, the Rietveld method is a whole-pattern-fitting of calculated to observed powder patterns through least-squares refinement of model(s) for the structure(s), diffraction optics effects and instrumental factors. A key feature is the feedback during the refinement between improving knowledge of the structure and improving allocation of observed intensity to individual Bragg reflections [233].

Hence, there is no intermediate step of extracting structure factors and the main characteristics of the structure have to be known beforehand in order to calculate an initial value of the intensities. As in the integral method, it requires two input models:

- A structural model with an approximate value of the atoms positions and lattice parameters, from which the intensity of the reflections will be determined.
- A non-structural model that describes any other phenomena affecting the shape of the Bragg reflection as a function of the 2θ angle; namely, peak asymmetry, instrumental broadening, crystallite size and strain effects, microstructure *etc*.

The fitting to the experimental data will provide the physical information required. Unlike the integral method, each observed point in the pattern is considered as an independent observation and as such, a value of its intensity is then calculated taking

into account contributions of all the overlapping tails of other reflections. The algorithm used is:

$$y_i^{'} = y_{ib} + \sum_{\Phi=1}^{N_\Phi} S_\Phi \sum_k \left|F_{\Phi k}\right|^2 A_{\Phi k} \Omega_{i\Phi k} \qquad \textbf{(2-22)}$$

Where, in each point, the contribution of all the crystallographic phases Φ and the background y_{ib} are taken into account. As in the integral method, $\Omega_{\iota\Phi\kappa}$ describes the contribution of each phase and each experimental point to the peak shape of a given reflection *k*. S_Φ is the scale factor for each phase and $A_{\Phi\kappa}$ are all the other contributions to the intensity of a reflection from a given phase Φ. Such contributions are summarized in the following section. The fitting to the experimental data is carried out by a least-square minimization procedure in which, unlike the integral method, the square of the quantity to be minimized is the difference between every single experimental point and its calculated counterpart.

$$M = \sum_i w_i (y_i - y_i^{'})^2 \qquad \textbf{(2-23)}$$

A weighing scheme w_i is introduced to account for the fact that not all the points have the same importance. Those y_i with low uncertainties should weigh more than those with high uncertainties in the minimization process. This is done by setting $w_i = 1 / \sigma_i^2$ where σ_i^2 is the variance of the observed y_i. In the counting Poisson statistics the variance of an independent variable amounts to the number of counts, therefore the statistical weight associated to each measured point will be $w_i = 1 / y_i$.

2.2.10 Goodness of fit

There exist several quantities known as *R*-factors and χ^2 that tell us about how well our model is fitting the experimental data. In order to obtain a good fit, not only the correct structural model is needed, but also good counting statistics, a correct collection strategy and a thoughtful experimental set-up. Anomalous values can be indicative of problems in any of the areas just mentioned, being a proper understanding of their meaning mandatory. Thus, we have:

- **Weighted profile *R*-factor**:

$$R_{wp} = \sqrt{\left(\sum_{i=1}^{N} w_i (y_i - y_i^{'})^2 \right) \Big/ \left(\sum_{i=1}^{N} w_i y_i^2 \right)} \qquad \textbf{(2-24)}$$

Is the statistically most meaningful indicator of the overall fit in the sense that its numerator is the residual that is minimized in the least-squares procedure. However, R_{wp} is inflated both by contributions from the background statistics and by differences in peak shapes. It would be possible to obtain very low values with high well-fitted backgrounds with poor counting statistics. For this reason it is preferable to use the background subtracted quantities as more accurate profile descriptors to rely on.

- **Expected *R*-factor**:

$$R_E = \sqrt{(N - P + C) \Big/ \left(\sum_{i=1}^{N} w_i y_i^2 \right)} \qquad \textbf{(2-25)}$$

Where N is the number of independent observations y_i, P is the number of refined parameters and C is the number of constraints set between parameters. It can be regarded as the statistically best R_{wp} factor, and is the value towards which tends to when only statistical fluctuations affect the observed points and these do not contain any systematic contribution. Since N is generally much larger than either P or C, the expected profile R-factor can be rewritten as $R_E = 1 / \sqrt{<y>}$. Thus, a small R_E means that the average number of counts in a profile is large, bearing no relationship with the quality of the fit. In this case, weak peaks on top of a high background can also lead to a very low expected R-factor, being a background-subtracted R_E again a much more realistic value. Such subtraction does not affect the numerator where the background terms of both the observed and calculated intensities cancel each other out. Hence, the squared experimental points of the denominator in both background-subtracted weighted profile $R_{(bs)wp}$ and the expected $R_{(bs)E}$ R-factors take the form $(y_i - b_i)^2$.

- **Profile *R*-factor**:

$$R_P = \sqrt{\left(\sum_{i=1}^{N} (y_i - y_i^{'})^2 \right) \Big/ \left(\sum_{i=1}^{N} y_i^2 \right)} \qquad \textbf{(2-26)}$$

It is the least important of all the *R*-factors as it can be regarded as the unweighed R_{wp} factor. It gives an idea of how the pattern is fitted as a whole, without weighing schemes. This causes that its value depends on non-structural effects, *i.e*. the higher the background the better the profile fit.

- **Bragg *R*-factor**:

$$R_B = \sqrt{\left(\sum_{k=1}^{N_{ref}} (I_k^{obs} - I_k^{calc})^2\right) \Big/ \left(\sum_{i=1}^{N} (I_k^{obs})^2\right)} \qquad \textbf{(2-27)}$$

It is also known as R_{F^2} or R_F and it has no statistical basis. It is based on the intensities of the reflections rather than the observed points and it is equivalent to the single crystal *R*-factor. R_B is not affected by peak shape problems and is little affected by background statistics. This is because the area of the peak, *i.e*. the integrated intensity, assigned to each *hkl* reflection is what truly affects the crystal structure results, unlike the oscillations under a peak in the difference plot, which eventually add up to zero. As in the single crystal case, a good R_B value < 5% can be considered acceptable.

Last but not least, an important goodness-of-fit indicator is Chi-square, χ^2:

$$\chi^2 = \sum_{i=1}^{N} (y_i - y_i^{'})^2 /(N - P + C) = (R_{wP} / R_E)^2 = (R_{(bs)wP} / R_{(bs)E})^2 \qquad \textbf{(2-28)}$$

χ^2 is a good measure of how well the data are fitted and is simply the square of the ratio of R_{wp} and its best statistical value R_E. Hence, a flawless refinement should have a χ^2 value tending to one. Lower values mean that there is a problem in the collection strategy, whereas larger values point at a misfit of the calculated data.

As a concluding remark, it is worthwhile mentioning that good quality data and good fittings do not mean exclusively low *R*-factor values. An overall picture of the refinement is needed as well as of all the factors describing the goodness of fit. Any important deviation should be accounted for in relation to collection strategies, counting statistics or instrumental techniques before writing off the refinement as too bad or flawed by an incorrect model.

2.3 Analytical techniques

2.3.1 Thermogravimetric analysis (TGA)

This analytical technique relies on the weight change of samples to determine the amount of volatile elements in a sample, absorbed moisture, decomposition temperatures and the amount of organic and inorganic compounds in a material. It is composed of a high-precision balance and an electrically heated oven containing a thermocouple to accurately measure the temperature inside the oven [234].
In order to determine the sulphur content, a Du Pont 951 thermal analyser was used. Finely ground powder was placed in a quartz crucible suspended from the balance arm by a platinum wire under a 60 cm^3 min^{-1} O_2 flow. The temperature was raised at a rate of 5 °C min^{-1} up to 1000 °C and the weight change *vs*. time as well as the initial and final were recorded.

2.3.2 Electron-probe microanalysis (EPMA)

Analytical electron microscopy was performed using a Philips XL30CP scannning microscope, equipped with an EDAX PGT Spirit detection system. EPMA is also known as energy dispersive X-ray spectroscopy (EDX), it is a routinely used analytical technique for elemental analysis or chemical characterization of samples. During an EPMA analysis, the sample is bombarded with an electron beam capable of ionizing inner-shell electrons of the atoms forming the sample. Outer-shell electrons may then occupy the vacant holes by emitting radiation, whose wavelength is within the electromagnetic spectrum of X-rays and amounts to the binding energy difference between both electrons. This energy is characteristic of each atom in the periodic table and allows to identify as well as quantify the elements present in a given sample by an energy dispersive spectrometer [235].

2.4 Physical property measurements

2.4.1 SQUID magnetometry

SQUID stands for Superconducting Quantum Interference Device. Commercially available SQUID systems are the most sensitive magnetometers ever created, since they can detect magnetic field changes as small as one ten thousand millionth of the Earth's magnetic field [236]. The key component of such devices is a superconducting ring in which two constrictions or weak junctions are built, the so-called Josephson weak links.

When this ring is cooled down to helium liquid temperature (4.2 K) it becomes superconducting, *i.e*. electric currents can flow indefinitely as any electrical resistance disappears. Therefore, all magnetic field lines are expelled from the metal and those already present inside the ring become trapped (Meissner effect). Should the ring be of uniform thickness, it would remain in such state forever. However, the presence of the weak links allows some magnetic field lines to escape and enter the ring. Thus, any change in the magnetic flux will cause a variation in the magnetic flux within the ring, which will generate a voltage that can be measured (Faraday's law). As a matter of fact, the surperconducting ring is so sensitive that it is capable of detecting variations of one quantum of magnetic flux. The variation in the magnetic flux is caused by the magnetic moment of the sample being moved up and down the core of a superconducting magnet.

Materials can be classified depending on their magnetic behaviour into five categories: diamagnetic, paramagnetic, ferromagnetic, antiferromagnetic and ferrimagnetic. The trend of the bulk magnetic susceptibility *vs*. the applied field determines which category a certain material falls in. The magnetic susceptibility χ is defined as the magnetization M (the magnetic moment per unit of volume) per unit of applied field H:

$$\chi = \frac{M}{H} \qquad \textbf{(2-29)}$$

The magnetic susceptibility can be related to the number of paired-unpaired electrons that atoms possess within a crystal structure and the type of interaction existing among them. Thus, magnetic materials can be:

- *Diamagnetic*: the magnetic susceptibility shows small and temperature independent negative values (~ -10^{-5} emu). All the electrons are paired and tend to offset the applied field. Superconductors are included within this type, however the diamagnetism originates from macroscopic currents circulating in the material which oppose to the applied field, instead of changes in the orbital motion of closely bound electrons.
- *Paramagnetic*: the magnetic susceptibility is small and positive (~ 10^{-4} emu). Characteristic of materials with unpaired electrons in which there is no interaction among them. Electrons behave as independent magnetic moments that align themselves under a magnetic field. The magnetic susceptibility follows an inverse proportional relation with the temperature known as the Curie law:

$$\chi = \frac{C}{T} \qquad \textbf{(2-30)}$$

Where *C* is the proportionality constant, so-called Curie constant. As a matter of fact, the Curie law is included in a more general expression known as the Curie-Weiss law, when $\theta = 0$:

$$\chi = \frac{C}{T - \theta} \qquad \textbf{(2-31)}$$

This equation was designed for explaining the behaviour of ferromagnetic materials in their paramagnetic state. When the material is ferromagnetic the Weiss constant θ is positive and its value amounts to the transition temperature between the ferromagnetic and the paramagnetic state T_C (Curie temperature).

Conversely, if the material is antiferromagnetic θ is negative and equals to the transition temperature between the antiferromagnetic and the paramagnetic state T_N (Néel temperature). It should be born in mind that positive or negative values of θ do not imply exclusively long-range magnetic ordering, but may just indicate that there exists ferromagnetic or antiferromagnetic correlations between neighbouring atoms.

- *Ferromagnetic*: the magnetic susceptibility is large and positive (~ 50-10000 emu). They possess unpaired electrons that interact one another in a long-range ordered manner, so that the individual magnetic moments become aligned in a parallel fashion.
- *Antiferromagnetic*: They are very similar to ferromagnetic materials with the exception that the interaction between the unpaired electrons has opposite sign and tends to align the magnetic moments in an antiparallel fashion.
- *Ferrimagnetic*: It is only observed in more complex crystal structures where there exist sublattices with opposite types of interaction between the magnetic moments, giving rise to a behaviour very similar to ferromagnetism, but with lower values of the susceptibility.
- *Helimagnets*: These are magnetic structures that arise when nearest- and next-nearest-neighbour interactions play a fundamental rôle. In the base plane, the moments are all aligned ferromagnetically, however successive base planes have their moments at an angle ϕ to the moments in the next base plane. This configuration originates a helical magnetic structure.

- *Superparamagnets*: They are composed of very small crystallites that can flip under the Néel / Curie temperature due to thermal fluctuations. The material is not magnetized unless a magnetic field is applied. Thus, their name originates from their paramagnetic properties beyond the Néel / Curie temperature.

The magnetization of a sample in related to its saturation magnetization M_S:

$$M = M_S B_J(y) \qquad \textbf{(2-32)}$$

Where $B_J\ (y)$ is the Brillouin function, defined as a function of the total angular momentum quantum number J and the variable y defined as in equation (2-33). $B_J\ (y)$ can take values between –1 and 1.

$$y = g_J \mu_B JB / k_B T \qquad \textbf{(2-33)}$$

The magnetic moment of the sample acquires its largest value when all the atomic magnetic moments of the sample become aligned under a strong magnetic field; hence its value amounts to:

$$\mu_{sat} = n g_J \mu_B J \qquad \textbf{(2-34)}$$

Being n the number of magnetic ions per unit of volume and g_J the Landé constant, defined as:

$$g_J = \frac{3}{2} + \frac{S(S+1) - L(L+1)}{2J(J+1)} \qquad \textbf{(2-35)}$$

S and L represent the total spin and orbital angular momentum. It can be shown that for low magnetic fields and substituting equation (2-32) into equation (2-29) the Curie law can be deduced [237]:

$$\chi = \frac{n\mu_0 \mu_{eff}^2}{3k_B T} \qquad \textbf{(2-36)}$$

Where the Curie constant is broken down into its components and an effective magnetic moment μ_{eff} can be extracted, which can be readily compared with its theoretical value:

$$\mu_{eff} = g_J \mu_B \sqrt{J(J+1)} \qquad \textbf{(2-37)}$$

As shown in equation (2-34), the effective and the saturation magnetic moment will differ, unless *J* can take any orientation, *i.e.* in the classical limit.

SQUID measurements have been performed at Edinburgh University using a Quantum Design MPMS system. Samples between 10 and 50 mg were weighed out and loaded into pre-weighed gelatine capsules, which were placed in the middle of a plastic straw and then placed at the end of the sample stick before being introduced into the SQUID. Measurements as a function of temperature were carried at two different field strengths, namely 100 G and 1000 G. Two different cooling conditions for each field strength were used: zero-field cooling and field cooling. Measurements as a function of the field were also carried out at 5 K after cooling the sample under zero-field conditions. The SQUID output is given as raw magnetization, which has to be corrected for the negative magnetization produced by the diamagnetic gelatine capsule:

$$M_{cap} = 3.188 \text{ x } 10^{-10} \text{ x mass of the capsule(mg) x magnetic field (G)} \qquad \textbf{(2-38)}$$

And the corrected magnetization is given by:

$$M_{corr} = M_{raw} - M_{cap} \qquad \textbf{(2-39)}$$

From which the molar magnetic susceptibility can be obtained:

$$\chi_{mol} = \frac{M_{corr}}{nH} \qquad \textbf{(2-40)}$$

Where *H* is the field strength and *n* is the number of mols. If the material possesses a paramagnetic region, then magnetic susceptibility data will follow the Curie-Weiss law that can be reordered to fit a straight line:

$$\frac{1}{\chi_{mol}} = \frac{T}{C} - \frac{\theta}{C} \qquad \textbf{(2-41)}$$

Where the Curie and Weiss constants are readily obtained from the slope and the interception with the ordinate axis, respectively. An effective magnetic moment, which will depend on the local environment of the magnetic ions, can be extracted from the Curie constant using the expression:

$$\mu_{eff} = \sqrt{\frac{8C}{n}} \qquad \textbf{(2-42)}$$

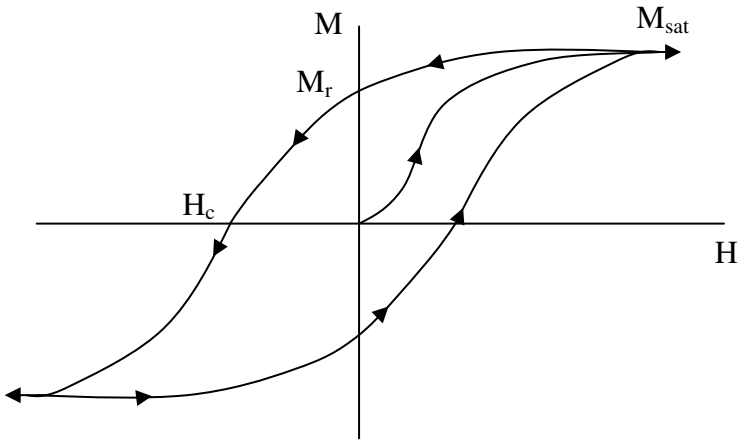

Figure 2-7 Typical hysteresis loop where the characteristic points have been highlighted, namely the saturation magnetization, M_{sat}, the residual magnetization or remanence, M_r, and the reverse field required to demagnetize the material or coercivity, H_c.

The saturation magnetization was determined by plotting the value of the magnetic moment as a function of the field (Figure 2-7). Then, the curve was extrapolated up to infinite field. The magnetic moment per magnetic ion was determined at each field strength in Bohr magnetons units by means of the expression:

$$M_{sat} = \frac{M_{corr}}{mnN_A\mu_B} \qquad \textbf{(2-43)}$$

Where *m* is the number of mols, *n* the number of magnetic ions per formula unit, N_A is the Avogadro's number and μ_B corresponds to the Bohr magneton expressed in adequate units [237].

2.4.2 Electrical resistivity

In order to understand the physical meaning of the electrical resistivity, it is easier to deal with electrical conductivity, rather than resistivity. Given the reciprocal relation between them, *i.e.* $\sigma = 1 / \rho$., the electrical conductivity can be expressed as:

$$\sigma = nq\mu \qquad \textbf{(2-44)}$$

Being proportional to the number of charge carriers, *n*, their charge, *q*, and their mobility, μ. The mobility of charged carriers is the averaged drift velocity acquired in the direction of an applied electric field of one volt per centimetre and is expressed in centimetres per second per volt per centimetre. The mobility is, in turn, directly proportional to the mean free path ($\mu \propto l_m$) of the charged carriers, which is the average

distance that it takes for the charge carriers to be scattered. The scattering mechanisms are those due to the thermal vibrations of the crystal lattice and to the effect of impurity atoms. However, when dealing with semiconductors, the impurity atoms are not always ionised and the scattering by neutral impurity atoms must also be accounted for.

From a band structure point of view, the electrical conductivity is proportional to the density of states near the Fermi energy. The DOS is a measure of the number of available states at a given energy. The conduction mechanism involves electrons of the outer atomic shells changing constantly from one state to another. Therefore, the availability of quantum states within the energy range in which the particles involved in the conduction process are found is of paramount importance.

Further, high-temperature resistivity *vs*. temperature data can be used to estimate the size of the band gap in semiconductors by fitting to an Arrhenius-type law:

$$\rho = \rho_0 e^{\frac{E_a}{k_B T}} = \rho_0 e^{\frac{\Delta E_g}{2k_B T}} \qquad \textbf{(2-45)}$$

Where E_a is the activation energy, E_g the band gap, ρ_0 the resistivity at $T \rightarrow \infty$ and k_B the Boltzmann constant. When the conduction mechanism is dominated by intrinsic conduction at high temperature, electrons from the valence band possess enough energy to jump to the conduction band leaving holes behind. Both charge carrier types contribute then to the conduction process and the Fermi level is located halfway between the valence and the conduction band. Only when this occurs, the band gap amounts to twice the Fermi level.

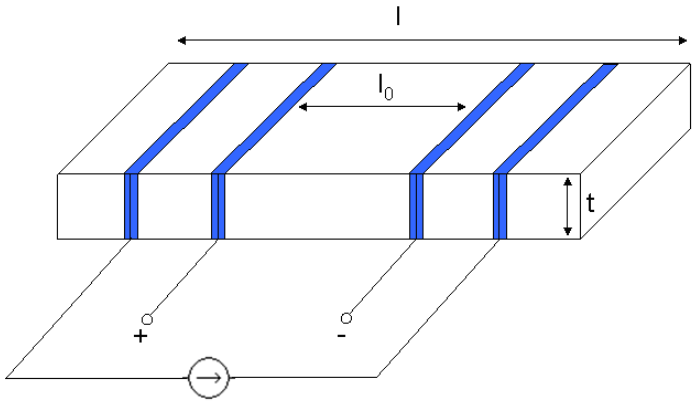

Figure 2-8 Schematic diagram of a pellet in a typical setup for a resistivity measurement.

Samples are cold pressed into pellets of approximately 13 mm diameter and 2 mm thickness. The disc-shaped pellets are sealed under vacuum (10^{-4} torr) and sintered for a period of 24 hours at the synthesis temperature.

The electrical resistance of the samples was measured using the four-probe DC technique. An ingot of rectangular shape is cut from a sintered pellet on top of which four 50 μm silver wires are attached using colloidal silver paint. Connections are made to a HP34401A multimeter as shown in Figure 2-8. The sample is mounted in an Oxford Instruments CF1200 cryostat connected to an ITC502 temperature controller. The uncertainty in the resistivity assuming rectangular shape is given by the following expression:

$$\frac{\delta\rho}{\rho} = \frac{\delta R}{R} + \frac{\delta t}{t} + \frac{\delta w}{w} + \frac{\delta l}{l} \qquad \textbf{(2-46)}$$

Where R is the resistance, w the sample width, l the length and t the thickness. The length l of the sample is measured under the microscope and the value of the resistance uncertainty is given by the technical specifications of the multimeter. The total error is estimated to be within ± 1%.

There exist several sources of error when measuring the electrical resistivity of a sample, especially if it is of semiconducting nature, that are taken into account during the measurement set-up and the sample preparation through sintering at high temperature. These are:

- Contact potentials
- Seebeck emf's and Peltier heat
- Sample shape
- Position of the voltage leads
- Grain boundaries

2.4.3 Seebeck coefficient

The variation of the Seebeck coefficient, S, as a function of temperature is of paramount importance for studying semiconductors, as it gives an insight into their electronic properties and band structure. From a thermodynamic point of view, it is better understood if it is related to the Peltier effect, formulated by equation (2-48). When an electric current, I, goes through a junction of two dissimilar metals, a certain amount of

heat, Q, is absorbed or released reversibly per Coulomb of charge. Such amount will determine the value of the Peltier coefficient, Π, possessing therefore units of heat (energy) divided by electric charge, *i.e*. Volts.

$$Q = \Pi I \qquad \textbf{(2-47)}$$

Thus, the value of the Seebeck coefficient obtained under no-current conditions and under a temperature gradient is essentially a measure of the entropy (reversible) transported per Coulomb of charge with units of Volts per Kelvin [238]. The relation between both coefficients being given by:

$$\Pi = ST \qquad \textbf{(2-48)}$$

From an electronic point of view, however, the picture is rather different. If we think of a conductor in terms of a lattice surrounded by free electrons, when a temperature gradient is applied a diffusion process will take place. Electrons from the hot end will diffuse towards the cold end until enough negative charge is accumulated at the cold end to create an electric field strong enough to offset the diffusion process. If the lattice-electron interactions are overlooked, then the value of the Seebeck coefficient would simply be a linear function of the temperature gradient, but this is not the case. Electrons interact with the lattice to different extents depending on the conductor, giving rise to differences in the diffusion process.

A comprehensive treaty on all the possible scattering processes that affect the electronic contribution to the thermopower can be found elsewhere [239]. However, the value of the Seebeck coefficient cannot be explained just in terms of diffusion throughout the whole temperature range in many metals and semiconductors. It has been observed [240] that there exists an additional mechanism that enhances the diffusion process involving the lattice vibration and electron interactions. Such a phenomenon has been named as the phonon-drag effect (being phonon the quantic name of a lattice vibration) contribution to the thermopower. At certain temperatures the lattice phonons will "sweep" electrons causing a dragging effect that will add up to the existing diffusion process. The extent of the phonon-electron interaction or coupling will be different depending on the temperature and the solid. By and large, it is hardly existent at very low temperatures, *i.e.* ~ 0-10 K, where the lattice vibrations are extremely damped; it becomes important in the range ~ 10-100 K and becomes weaker as the temperature

increases owing to the overcoming of the phonon-electron interactions by the phonon-phonon interactions.

Yet, a band structure interpretation can be extracted out of a Seebeck measurement. A completely theoretical expression can be derived from first principles. The thermoelectric power is known to be proportional to the derivative of the electrical conductivity, σ, with respect to the energy, E, at the Fermi level E_F [241]:

$$S \propto \frac{1}{\sigma(E)}\left(\frac{d\sigma(E)}{dE}\right)_{E=E_F} \qquad \textbf{(2-49)}$$

This equation shows that the thermopower is maximized for materials that present a rapid variation (large derivative) of $\sigma(E)$ close to the Fermi energy. Because the electrical conductivity is dependent on the DOS (section 2.4.2), the variation in the density of states near the Fermi energy is important as to the magnitude of the thermoelectric power. Hence, bandwise, a steep band edge close the Fermi energy would be favourable to a large value of the Seebeck coefficient.

There exist two well established methods for measuring the Seebeck coefficient, differing between them in the magnitude of the temperature gradient applied:

- **Integral method**

  In this method large thermal gradients are employed. The Seebeck coefficient at a certain temperature can be obtained from the slope of the Seebeck voltage *versus* temperature at a given temperature, T:

  $$S = \left(\frac{dV}{dT}\right)_T \qquad \textbf{(2-50)}$$

  The problem of spurious voltages in this method is overcome by the fact that large values of the Seebeck coefficient are generated by large temperature gradients and, therefore, this method is preferred for materials used for high-temperature energy conversion. Measurements of the Seebeck coefficient using the integral method have been reported elsewhere [20].

- **Differential method**

  In this method a small thermal gradient (between 1-10 K) is applied across the sample that gives rise to a Seebeck voltage with which the Seebeck coefficient can be calculated:

$$S = \frac{\Delta V}{\Delta T} \qquad \textbf{(2-51)}$$

  In order to avoid the effect of spurious voltages the Seebeck voltage is plotted against several incremental values of ΔT and the Seebeck coefficient is obtained from the slope of the linear region, overcoming the inconvenient that the linear plot does not go through the origin. In order to ensure that the measured Seebeck coefficient falls within the linear range, the temperature difference ΔT should not exceed a few percents of the absolute sample temperature. This method is often applied for semiconductor specimens and it is widely used at any temperature for its versatility and set-up simplicity. Burkov describes thoroughly the experimental set-up for measurements between 100-1300 K using this method with an accuracy of $\pm (0.5\ \mu VK^{-1} + 4\%)$ [242].

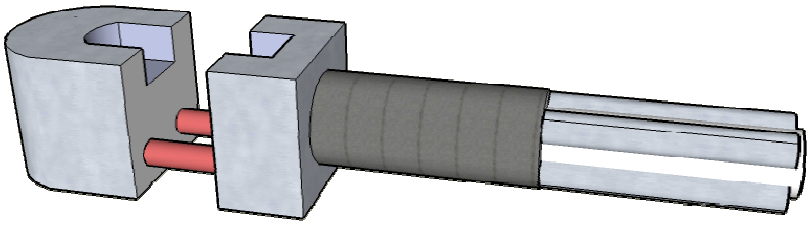

Figure 2-9 Detailed view of the sample stick showing the sample groove and the heater isolated from the main body by two ceramic bars.

Samples are cold pressed into pellets of approximately 13 mm diameter and 2 mm thickness. The disc-shaped pellets are sealed under vacuum (10^{-4} torr) and sintered for a period of 24 hours at the synthesis temperature.

The measurement of the Seebeck coefficient is based on the differential method. The samples were mounted in an in-house built sample stick, which includes a small heater located close to one end of the sample that provides the temperature gradient necessary for the measurement (Figure 2-9). A maximum temperature gradient of *ca*. 5 K was used.Two chromel-Au / 0.07% Fe thermocouples were also placed on top of each copper wire (Figure 2-10).

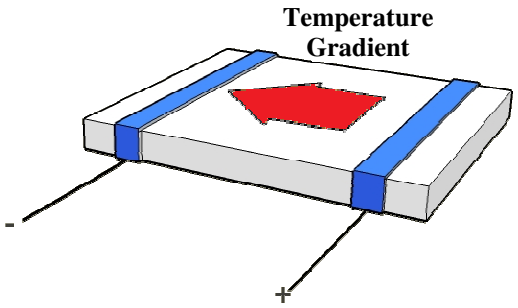

Figure 2-10 Schematic diagram of a pellet in a typical setup for a Seebeck measurement.

In order to calculate the Seebeck coefficient of the sample without any other contribution, the electromotive forces (EMFs) involved in the measurement must be considered. As a result of the temperature gradient between the two probes, a thermoelectric voltage arises $\Delta V_{TE} = V_{Hot} - V_{Cold}$. Such Seebeck voltage is measured with the aid of two copper wires attached using colloidal silver paint, which are subjected to a temperature gradient alike. The wires attached to the hot and cold ends have their other end connected to the nanovoltmeter at room temperature, originating two more EMFs ΔV_{Hot} and ΔV_{Cold}. Thus, the voltage measured at the terminals of the nanovoltmeter will be given by:

$$\Delta V = \Delta V_{TE} + \Delta V_{Hot} + \Delta V_{Cold} \qquad \textbf{(2-52)}$$

It is known that the temperature of the nanovoltmeter leads does not affect the final reading. Thus, taking into account the definition of the Seebeck coefficient in equation (2-51) we obtain:

$$\Delta V_{Hot} + \Delta V_{Cold} = S_{Cu}(T_{Cold} - T_{Hot}) \qquad \textbf{(2-53)}$$

Where S_{Cu} is the Seebeck coefficient of copper. Therefore the voltage at the nanovoltmeter leads will be:

$$\Delta V = \Delta V_{TE} + S_{Cu}(T_{Cold} - T_{Hot}) \qquad \textbf{(2-54)}$$

Being interested just in the Seebeck coefficient of the sample, using expression (2-49) it can be obtained straightforwardly:

$$S = \frac{\Delta V_{TE}}{\Delta T} = \frac{\Delta V}{T_{Cold} - T_{Hot}} - S_{Cu} \qquad \textbf{(2-55)}$$

Thus, the value of the Seebeck coefficient obtained is relative to that of copper. However, it does not affect greatly the measurements due to the fact that the copper contribution is less than 1%, *i.e.* 1.94 μVK^{-1} at 300 K, when measuring semiconductors and therefore is negligible [243]. The most common sources of error in Seebeck measurements can be summarized in two:

- Thermopower sign
- Temperature gradient determination

2.4.4 Thermal conductivity

Heat conduction through a solid takes place by means of vibrational modes of the lattice as well as electrons. These modes are quantum entities, the so-called phonons. Analogously to the electrical conduction mechanism, a mean free path for phonons can be defined as well as different scattering mechanisms that reduce such path, thereby lowering the thermal conductivity. Different scattering mechanisms will predominate depending on the temperature:

- *Phonon-Phonon scattering*: the main mechanism at high temperatures.
- *Point-defect scattering*: including both lattice imperfections and alloying.
- *Phonon-electron scattering*: important in metals. It predominates at low temperatures where the energies of both entities are comparable.
- *Boundary scattering*: only relevant when the phonon wavelength is of the same order of magnitude as the grain size.

Electrons also participate actively in the heat transport in those cases in which either there are many free electrons present (metals) or the lattice thermal conductivity is very low (thermoelectric materials). The amount of heat transported by electrons in a solid is governed by the Wiedemann-Franz-Lorenz law, which establishes a linear relation between the heat transported by electrons and the electrical conductivity:

$$\kappa_e = L_0 \sigma T \qquad \textbf{(2-56)}$$

The constant of proportionality L_0 is the Lorenz number, and has the numerical value 2.45 x 10^{-8} $W\Omega K^{-2}$. Such relation was derived for metals, in which most part of the heat

flow is carried by electrons; therefore the validity of the formula will depend upon how close the solid is to this ideal situation. The ratio $\kappa / \sigma T$ gives an idea of the validity of the approximation when compared to the ideal value of the Lorenz number. Therefore, the overall thermal conductivity will have a contribution from both the lattice, κ_l, and the electrons, κ_e, being the latter determined by equation (2-56). Heat will be mostly carried by electrons (or holes) in those materials with high density of free charge carriers, whereas heat conduction through the lattice will become more relevant insofar as the charge carrier density diminishes. In semiconductors, the lattice thermal conductivity already plays an important rôle and in insulators the lattice conduction is the main heat transport mechanism. Comprehensive treaties have been written on the complex problem of thermal conductivity and its measuring methods, to which the reader is referred [244].

Data collection was carried out by Dr Vaqueiro and Mr Fabien Guinet. Samples are cold pressed into pellets of approximately 13 mm diameter and 2 mm thickness. The disc-shaped pellets are sealed under vacuum (10^{-4} torr), sintered for a period of 24 hours at the synthesis temperature and subsequently carbon coated.

The laser-flash thermal diffusivity method is used to determine the thermal conductivity by means of a commercial module from Anter Corporation (Anter Flashline FL-3000). It is a method of great simplicity, applicable to high temperatures and is free of most of the radiation loss problems given its inherent short duration.

A flash of thermal energy is supplied to a sample surface (by means of a Xe lamp) in the form of a disc placed inside a graphite furnace, within a time interval that is short (millisecond) compared to the time it takes for the heat to propagate through the whole sample thickness. The temperature of the opposite face is monitored by an IR sensor and the temperature *vs*. time curve is recorded. The method, which uses the sigma-shaped curve obtained, is a modification based on that developed by Parker *et al*. [245]. From the time required to reach half of the limiting temperature, $t_{1/2}$, the value of the thermal diffusivity is obtained as follows:

$$\delta = 0.13879 \frac{L^2}{t_{1/2}} \qquad \textbf{(2-57)}$$

Where L is the sample thickness. Nevertheless, the sample specific heat as well as its density must be known so as to determine the thermal conductivity κ. The former is determined by comparing the absorbed energy with a reference sample of known

density and specific heat (Pyroceram 9606). The relation between thermal diffusivity, δ, thermal conductivity, κ, specific heat, C_p, and density, ρ, is given by:

$$\kappa = \delta C_p \rho \qquad \textbf{(2-58)}$$

Thermal conductivity is by far the most difficult measurement to conduct due to the great many sources of error involved in the process:

- Low thermal conductivity of the samples
- Radiation losses
- Sample thickness
- Coating

Chapter 3

Ternary skutterudites

$MY_{1.5}Q_{1.5}$

M = Co, Rh, Ir

Y = Ge, Sn

Q = S, Te

3.1 Introduction

Despite the fact that a number of ternary skutterudites have been reported, there has been limited work to date on the structure and properties of these materials [50,54]. A neutron diffraction study as well as a group theoretical analysis were carried out on the ternary skutterudite $CoGe_{1.5}Te_{1.5}$. The results obtained were then applied to structurally characterize the sulphur-containing and tin-containing anion-substituted ternary skutterudites of the type $MGe_{1.5}S_{1.5}$ and $MSn_{1.5}Te_{1.5}$ (M = Co, Rh, Ir) by means of a neutron diffraction and a resonant scattering synchrotron experiment, respectively.
Furthermore, transport property measurements were carried out on all the ternary skutterudites under study, *i.e*. electrical resistivity, Seebeck coefficient and thermal conductivity, in order to assess their potential as thermoelectric materials. The results are then compared with other skutterudites and state-of-the-art thermoelectric materials.

3.1.1 Synthesis

Stoichiometric amounts of the elements cobalt (Aldrich, 99.9%), rhodium (99.9%), iridium (Aldrich 99.9%), germanium (Aldrich 99.99%), tin (J.M 99.8%), sulphur (Aldrich) and tellurium (Aldrich 99.997%) were mixed appropriately to obtain the following compounds: $CoGe_{1.5}Te_{1.5}$, $CoGe_{1.5}S_{1.5}$, $RhGe_{1.5}S_{1.5}$, $IrGe_{1.5}S_{1.5}$ $CoSn_{1.5}Te_{1.5}$, $RhSn_{1.5}Te_{1.5}$, $IrGe_{1.5}Te_{1.5}$ and $IrSn_{1.5}Te_{1.5}$. The synthesis of the ternary skutterudites $CoSn_{1.5}S_{1.5}$, $CoSi_{1.5}S_{1.5}$ and $RhGe_{1.5}Te_{1.5}$ was also attempted unsuccessfully.
Sulphur dried under vacuum and low-oxide tellurium was used for all the sulphur-containing and tellurium-containing compounds, respectively. The three-element mixture was then ground inside a glovebox in an agate mortar prior to sealing into an evacuated ($< 10^{-4}$ Torr) silica tube; which was, in turn, coated with pyrolitic carbon in order to avoid reactions with the inner walls. The tubes were then placed into a chamber furnace and given a thermal treatment at approximately 600 °C for a few days. The reaction progress was monitored by means of powder X-ray diffraction. The reaction product was ground in air and placed in an aluminium holder. Further firings were repeated until reaction completeness.

The data collection strategy consisted of 0.02° 2θ steps and a 5 s counting time per step over a 2θ angular range varying from 10° up to 100°. The samples containing tellurium were left for a period of between 1 and 2 days at a temperature between

400 °C and 430 °C to prevent tellurium from melting before reacting with the other elements (tellurium melting point is 450 °C).

The $CoGe_{1.5}Te_{1.5}$ sample was prepared by placing the silica tube directly into a hot furnace at 440 °C for one day and then heated slowly (1 °C min^{-1}) up to 600 °C, left at that temperature for another day more and let cool down to room temperature at natural rate. Following regrinding, the sample was placed into another silica tube and refired at 600 °C for one day before slowly (0.5 °C min^{-1}) cooling down to room temperature. The $IrGe_{1.5}Te_{1.5}$ was synthesized following the same procedure, except that the second firing lasted two days. The compound $RhGe_{1.5}Te_{1.5}$ did not form and a mixture of RhGeTe (chapter 5) and GeTe was obtained instead.

The $CoGe_{1.5}S_{1.5}$ sample was fired at 500 °C for two days, reground and refired at 700 °C for five days and cooled down to room temperature at 0.1 °C min^{-1}. The $RhGe_{1.5}S_{1.5}$ and $IrGe_{1.5}S_{1.5}$ samples were fired together. A three-step heating treatment was given in the first firing, consisting of placing the sample directly at 500 °C for 26 hours, heating up to 700 °C at 0.5 °C min^{-1}, left at this temperature for 24 hours and finally up to 800 °C at 0.5 °C min^{-1} for two days. After cooling at 0.5 °C min^{-1} to room temperature, the sample was ground, sealed into a second silica tube, heated up to 800 °C for two days and cooled down to room temperature at 0.5 °C min^{-1}.

An analogue firing-grinding-refiring procedure was followed for the tellurides. The $CoSn_{1.5}Te_{1.5}$ sample was fired four times, placing the sample at 430 °C for two days and then heating up to 580 °C for two more days the first time. The other consecutive firings consisted of heating the sample up to 580 °C for two days and cooling it down slowly (0.1 °C min^{-1}) in the last one. Exactly the same sequence was used for the $RhSn_{1.5}Te_{1.5,}$ $IrSn_{1.5}Te_{1.5}$, $CoGe_{1.5}Te_{1.5}$ and $IrGe_{1.5}Te_{1.5}$ samples, except that the first two were given three firings instead of four and the two last compounds were given only two firings, depending on the reaction completeness.

The $CoGe_{1.5}Te_{1.5}$ sample used in the neutron and synchrotron experiments was synthesized by Dr Vaqueiro, for the archetype structural study of the anion-substituted ternary skutterudites [246]. The sulphides used in the neutron experiments were synthesized *ad hoc* as large amounts of sample were needed, whereas the transport

property measurements and the synchrotron experiments for all the other tellurides were carried out in the same samples.

3.2 Thermogravimetric analysis

The sulphur content of the ternary skutterudites $MGe_{1.5}S_{1.5}$ (M = Co, Rh, Ir) was analyzed thermogravimetrically under a flow of O_2; the temperature was raised up to 1000 °C at a 5 °C min^{-1} rate. The products of the reaction were monitored by powder X-ray diffraction for phase identification. They consisted of transition metal oxides, *i.e.* CoO, RhO_2 and IrO_2 as well as GeO_2.

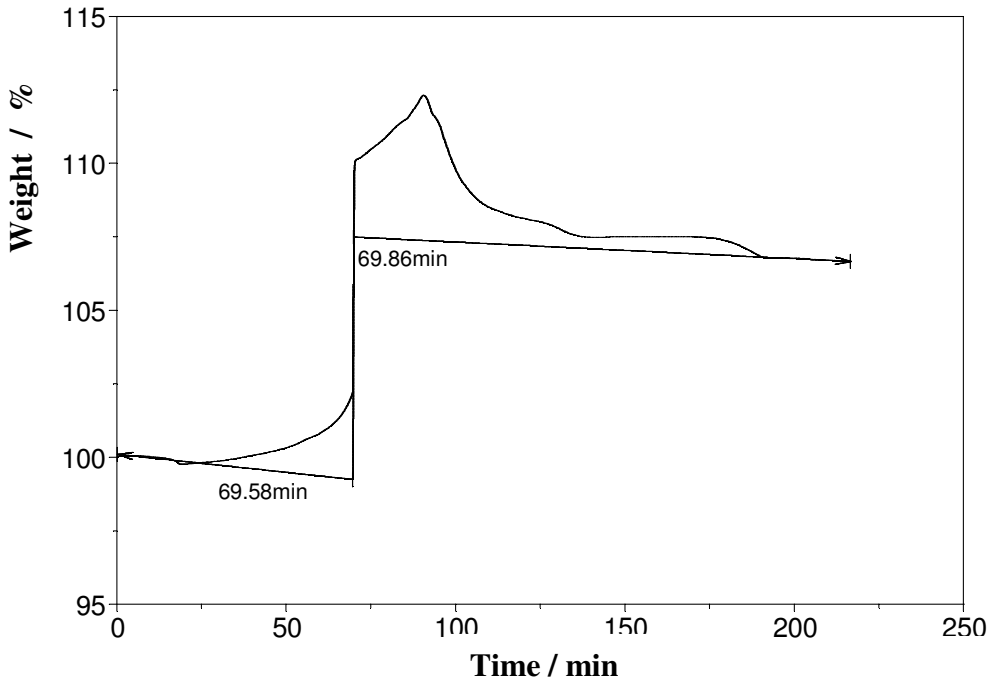

Figure 3-1 Weight change *vs*. time plot obtained from the thermogravimetric analysis of $CoGe_{1.5}S_{1.5}$.

The observed weight changes were all close to the nominal expected values (Table 3-1). Nevertheless, the $IrGe_{1.5}S_{1.5}$ sample shows a slightly higher sulphur content than the nominal value, which may be attributed to the fact that the weight *vs*. time plot has not reached yet a flat regime at the end of the measurement.

All patterns show a weight gain as the temperature raises consistent with the oxidation of the transition metal and the germanium to form their respective oxides (Figure 3-1 and Figure 3-2). The onset of weight loss corresponding to the sublimation of sulphur oxides is observed after 75 min, 75 and 150 minutes for $CoGe_{1.5}S_{1.5}$, $RhGe_{1.5}S_{1.5}$ and $IrGe_{1.5}S_{1.5}$, respectively.

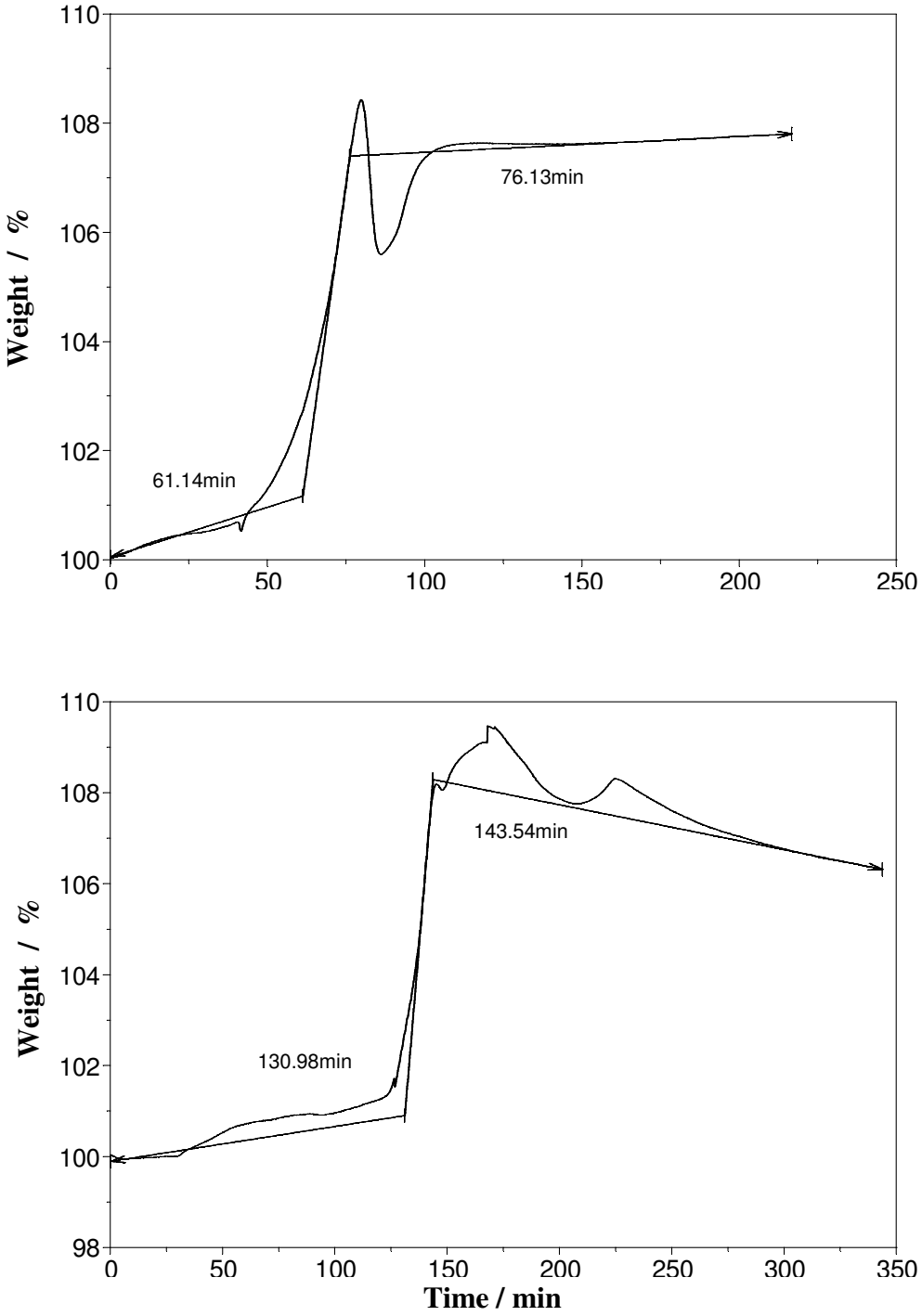

Figure 3-2 Weight change *vs*. time plot obtained from the thermogravimetric analysis of $RhGe_{1.5}S_{1.5}$ (top) and $IrGe_{1.5}S_{1.5}$ (bottom).

Table 3-1 Sulphur content determination by thermogravimetric analysis (%).

Nominal composition	Calculated weight change	Experimental weight change	Experimental composition
$CoGe_{1.5}S_{1.5}$	7.36	6.94	$CoGe_{1.5}S_{1.526(6)}$
$RhGe_{1.5}S_{1.5}$	8.17	7.75	$RhGe_{1.5}S_{1.533(9)}$
$IrGe_{1.5}S_{1.5}$	9.16	6.36	$IrGe_{1.5}S_{1.78(1)}$

3.3 EPMA analysis

The composition of the $MGe_{1.5}S_{1.5}$ (M = Co, Rh, Ir) sulphides was analysed by electron-probe microscopy. The final composition is an average over five measurements in the case of $CoGe_{1.5}S_{1.5}$ and $RhGe_{1.5}S_{1.5}$ and over four in $IrGe_{1.5}S_{1.5}$ (Table 3-2).

Table 3-2 Experimental stoichiometry obtained for each of the sulphides under study.

Nominal composition	Experimental composition
$CoGe_{1.5}S_{1.5}$	$CoGe_{1.16}S_{4.13}$
$RhGe_{1.5}S_{1.5}$	$RhGe_{0.35}S_{0.82}$
$IrGe_{1.5}S_{1.5}$	$IrGe_{1.36}S_{4.78}$

The experimental stoichiometries are clearly in disagreement with the nominal values and are not meaningful given the fact that samples with small grain sizes are troublesome in EPMA analysis (Figure 3-3). It is well known that samples consisting of small grains, *i.e.* < 5 μm, introduce large deviations in the relative intensities when analysing elements with significant differences in their atomic numbers [247]. This problem has been already reported in the partially filled ternary skutterudite $La_xCo_4Ge_6Te_6$ [248].

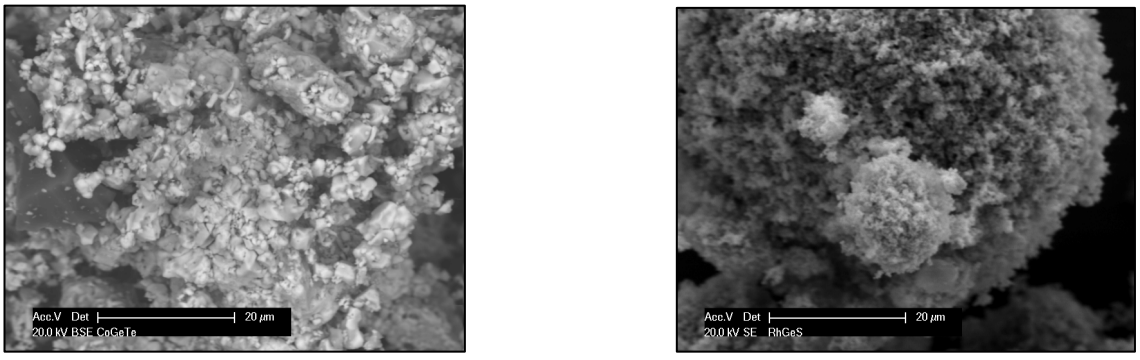

Figure 3-3 Microphotographs showing grain images for $CoGe_{1.5}S_{1.5}$ (left) and $RhGe_{1.5}S_{1.5}$ (right). The scale is 20 μm.

3.4 Neutron diffraction study of $CoGe_{1.5}Te_{1.5}$

A sample of $CoGe_{1.5}Te_{1.5}$ was sealed into a small silica tube (7 cm long, 0.5 cm diameter) to prevent contamination during the course of the experiment, given the poisonous nature of tellurium. Ultrahigh purity fused silica (Spectrosil®) was used to minimize background scattering. The tube was then placed into a vanadium can attached to the end of a long rod fitted to a vanadium-walled cryostat in order to perform low-temperature time-of-flight neutron scattering experiments. A dataset containing only the elements likely to cause background scattering, *i.e*. silica, vanadium can and cryostat walls, was collected to be subtracted from sample-containing datasets. Initial data manipulation and reduction was carried out using Genie spectrum manipulation software [249]. Neutron diffraction data from the highest resolution backscattering bank of detectors ($2\theta = 180°$) and from the mid-angle bank of detectors ($2\theta = 90°$) were summed and normalized for subsequent use in Rietveld refinements using the GSAS software package [250].

The background of all the datasets was modelled using a linear interpolation function with eight coefficients, taking advantage of the flatness obtained after data manipulation. Backscattering data was initially used in order to obtain an accurate estimate of the lattice parameters using the diffractometer constants determined with a standard sample for the highest resolution data bank. The 90° data was added after the lattice parameters obtained using the backscattering bank were fixed. The diffractometer constants for the second histogram were then refined to accommodate the value of the lattice parameters previously obtained. After the background and the lattice parameters, the atomic position parameters as well as the thermal parameters were refined. Finally, the peak-shape parameters were also refined using an exponential pseudo Voigt function. Least-square cycles were run until convergence was reached, *i.e*. until $\Sigma (\Delta x / \sigma_x) \leq 0.01$. The regions of the spectrum between 1.22-1.24 Å, 1.50-1.52 Å and 2.12-2.16 Å were excluded to eliminate small reflections originated from the vanadium can and the cryostat. The datasets show a small set of reflections attributed to the impurity phases $CoTe_2$ (*ca*. 4%) and GeO_2 (*ca*. 1%) (Figure 3-5 and Figure 3-6). Refined parameters as well as relevant bond distances and angles are presented in Table 3-3, Table 3-4 and Table 3-5.

Initial refinements using the skutterudite structure assuming a random anion distribution in the 24*g* site showed that most of the reflections can be indexed on the basis of a

primitive cubic unit cell, with the intense reflections corresponding to the skutterudite body-centred condition $h + k + l = 2n$. Nevertheless, this model also originates important intensity mismatches both at low and high *d*-spacings and there exist a number of weaker reflections that violate the body-centred condition of the skutterudite (Figure 3-4). The absence of peak splitting suggests that the cubic skutterudite unit cell is retained indicating the presence of pseudosymmetry (Figure 3-4). However, attempts to fit the data to other cubic space groups such as $Pm\bar{3}$ or $P23$ failed to reproduce adequately the correct intensities.

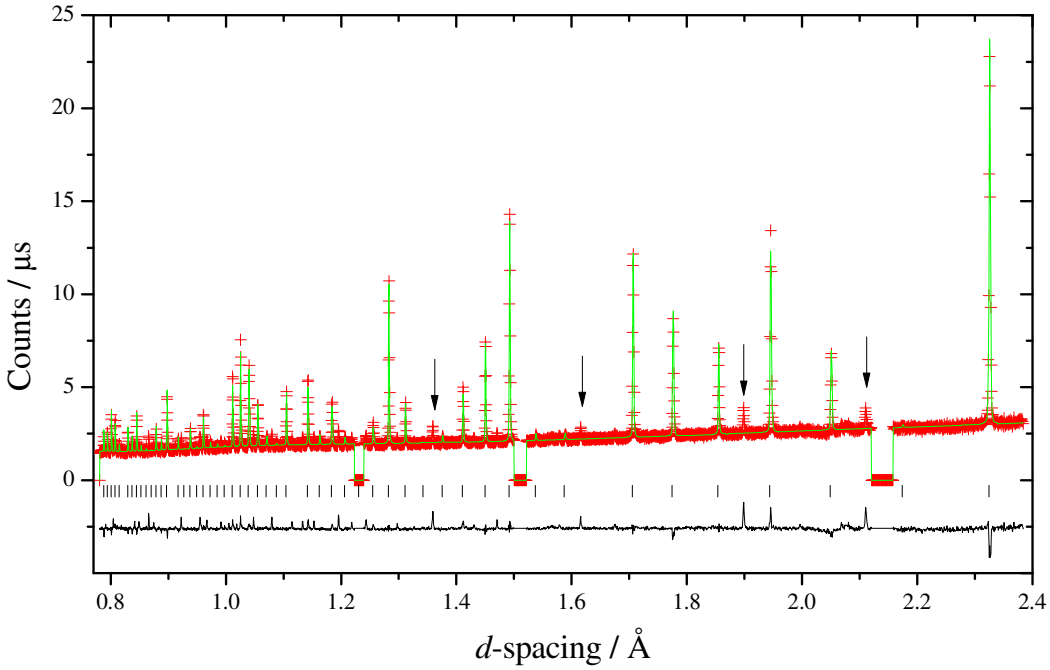

Figure 3-4 Rietveld refinement of the backscattering neutron data at 4.2 K in the skutterudite space group $Im\bar{3}$. Unindexed reflections have been marked with arrows. Key: experimental data (red crosses), fitted model (green line), difference curve (black line). Reflections positions are shown as black markers. R_{wp} = 5 %. χ^2 = 6.5.

Previous authors assigned the space group *R*3 to the anion-substituted skutterudites $CoGe_{1.5}Y_{1.5}$ (Y = S, Se) and also pointed out the existence of pseudosymmetry in the cobalt compounds [55,106]. Further, deviations of the 90° rhombohedral angle have been reported in ternary skutterudites containing heavier metals such as $RhGe_{1.5}S_{1.5}$ and $RhGe_{1.5}Se_{1.5}$ [56]. Data refinements in this space group resulted extremely unstable and did not reach convergence, although there was good agreement between the calculated and the experimental intensities. In order to determine the distortion occurring when anion substitution takes place, group theoretical analysis was used implemented using the software package ISOTROPY [228].

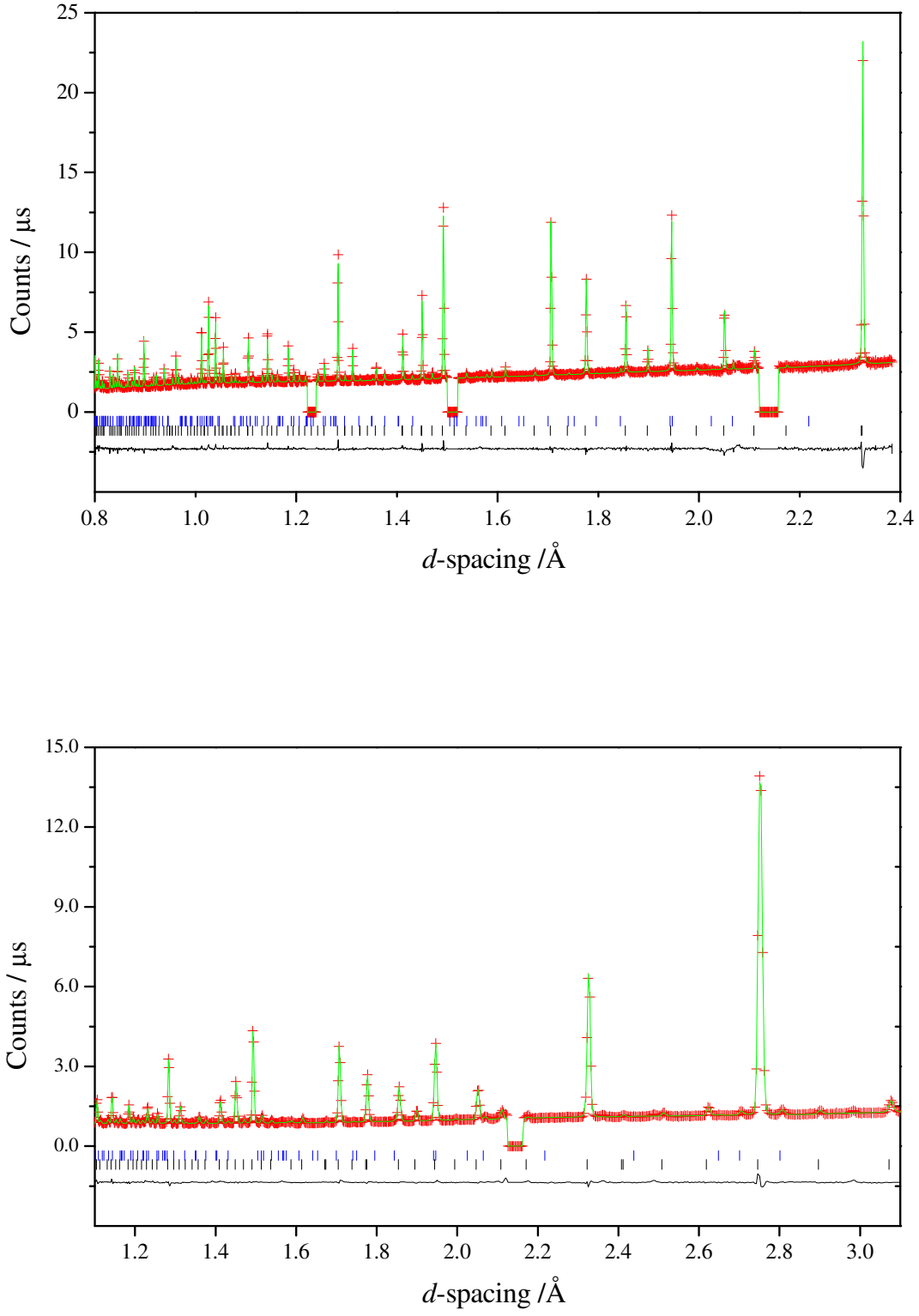

Figure 3-5 Rietveld refinement of neutron data at 4.2 K. Top: Backscattering bank. Bottom: 90° bank. Key: experimental data (red crosses), fitted model (green line), difference curve (black line). Reflections positions are shown as markers: the black markers refer to $CoGe_{1.5}Te_{1.5}$ ($R\bar{3}$) and the blue markers to $CoTe_2$.

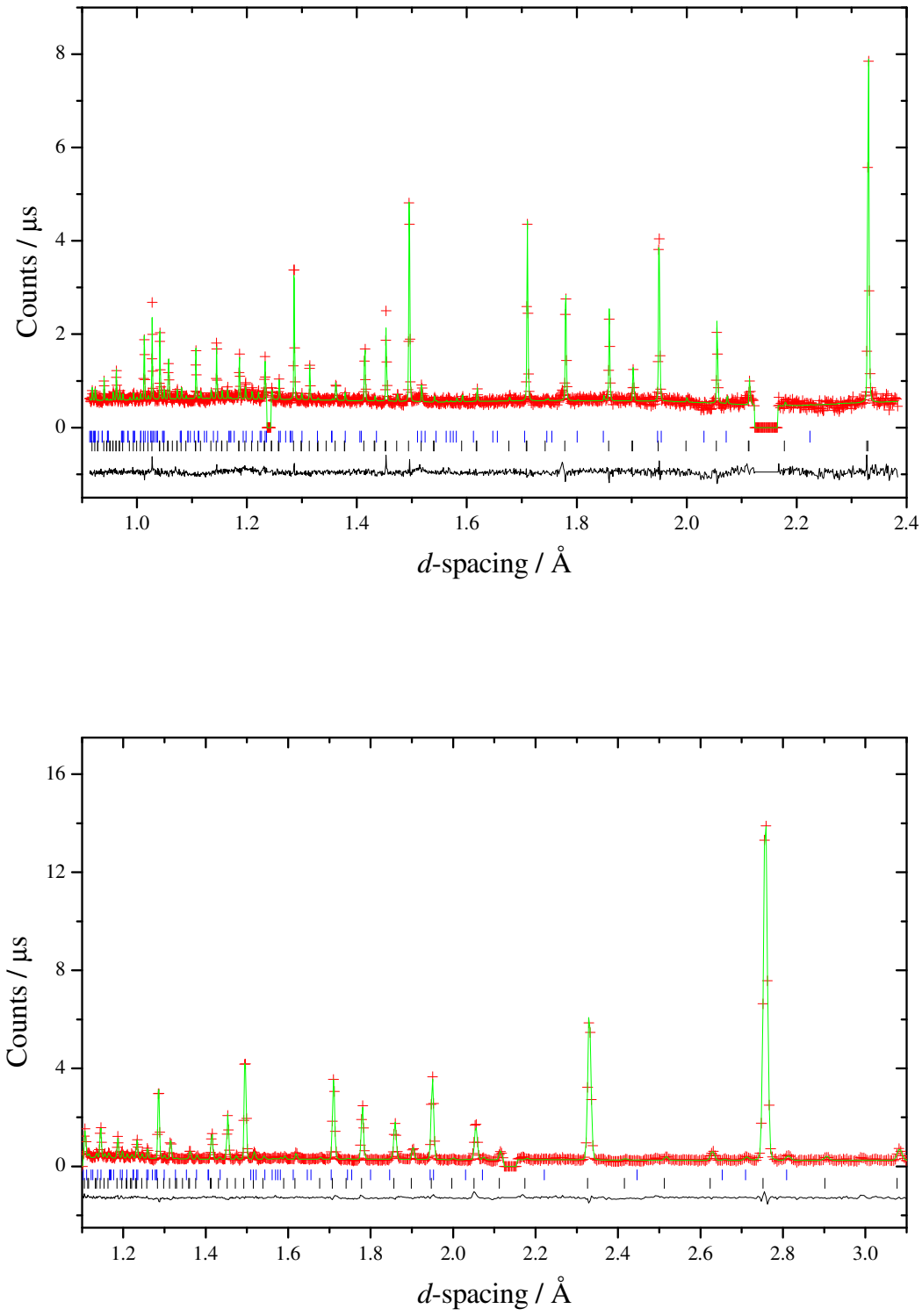

Figure 3-6 Rietveld refinement of neutron data at 293 K. Top: Backscattering bank. Bottom: 90° bank. Vanadium peaks have been excluded for simplicity. Key: experimental data (red crosses), fitted model (green line), difference curve (black line). Reflections positions are shown as markers: the black markers refer to $CoGe_{1.5}Te_{1.5}$ ($R\bar{3}$) and the blue markers to $CoTe_2$.

Table 3-3 Refined parameters for $CoGe_{1.5}Te_{1.5}$ determined from data collected at 4.2 and 293 K on HRPD, space group $R\bar{3}$ (hexagonal setting). A third column in which anion disorder has been modelled at 293 K is included and commented on in the text. (SOF: Structure Occupancy Factor).

		4.2 K	293 K	Disorder
a **(Å)**		12.32598(8)	12.3270(5)	12.3272(5)
c **(Å)**		15.1075(3)	15.102(1)	15.102(1)
a_R**(Å)**		8.71792(3)	8.7174(7)	8.7175(7)
α(°)		89.9715(7)	89.988(4)	89.989(4)
	B/Å^2	0.09(2)[a]	0.20(5)[a]	0.21(5)[a]
Co(1) 6*c*	*x*	0(-)	0(-)	0(-)
	y	0(-)	0(-)	0(-)
	z	0.247(6)	1/4(-)[b]	1/4(-)[b]
Co(2) 18*f*	*x*	0.668(6)	2/3(-)[b]	2/3(-)[b]
	y	0.832(4)	5/6(-)[b]	5/6(-)[b]
	z	0.581(2)	7/12(-)[b]	7/12(-)[b]
	SOF Ge	-	-	0.959(19)
	SOF Te	-	-	0.041(19)
Ge(1) 18*f*	*x*	0.835(1)	0.835(2)	0.836(2)
	y	0.9935(8)	0.993(1)	0.996(1)
	z	0.1599(8)	0.161(1)	0.162(1)
Ge(2) 18*f*	*x*	0.946(1)	0.946(2)	0.947(2)
	y	0.217(2)	0.217(2)	0.217(2)
	z	0.5550(5)	0.5557(8)	0.5553(9)
Te(1) 18*f*	*x*	0.934(1)	0.935(2)	0.935(2)
	y	0.213(2)	0.212(3)	0.211(2)
	z	0.0668(8)	0.065(1)	0.066(1)
Te(2) 18*f*	*x*	0.836(2)	0.837(3)	0.837(3)
	y	0.013(1)	0.014(2)	0.014(2)
	z	0.665(1)	0.667(2)	0.667(1)
$\mathbf{R_{wp}}$ **(%)**	180° bank	2.4	6.9	6.9
$\mathbf{R_{wp}}$ **(%)**	90° bank	1.9	6.1	6.0
χ^2		4.7	2.1	2.1

[a] **Atomic displacement parameters have been constrained to the same value.**

[b] **Non-refined variables.**

Table 3-4 Relevant interatomic distances (Å) in $CoGe_{1.5}Te_{1.5}$.

	4.2 K	293 K	Disorder	
Co(1)-Ge(1)	2.39(5)	2.40(2)	2.39(2)	x 3
Co(1)-Te(2)	2.48(5)	2.45(3)	2.44(3)	x 3
Co(2)-Ge(1)	2.31(5)	2.35(1)	2.35(2)	
Co(2)-Ge(2)	2.36(4)	2.39(2)	2.39(2)	
Co(2)-Ge(2)	2.39(4)	2.42(1)	2.42(1)	
Mean Co(2)-Ge(2)	2.35(4)	2.39(1)	2.39(1)	
Co(2)-Te(1)	2.52(4)	2.50(2)	2.50(2)	
Co(2)-Te(1)	2.53(4)	2.49(3)	2.49(2)	
Co(2)-Te(2)	2.49(4)	2.51(3)	2.52(3)	
Mean Co(2)-Te(1)	2.51(4)	2.50(2)	2.50(2)	

Table 3-5 Relevant bond angles (°) in $CoGe_{1.5}Te_{1.5}$.

	4.2 K	293 K	Disorder	
Ge(1)-Co(1)-Ge(1)	92.5(3)	91.8(7)	91.9(7)	x 3
Te(2)-Co(1)-Te(2)	94.2(3)	96.0(8)	96.1(7)	x 3
Ge(1)-Co(1)-Te(2)	90.3(6)	89.9(7)	89.8(7)	x 3
Ge(1)-Co(1)-Te(2)	83.2(4)	82.4(6)	82.3(7)	x 3
Ge(1)-Co(2)-Ge(2)	89.5(6)	88.9(5)	88.7(5)	
Ge(1)-Co(2)-Ge(2)	87.9(9)	86.7(4)	86.8(5)	
Ge(2)-Co(2)-Ge(2)	94.3(2)	92.9(8)	92.9(8)	
Te(1)-Co(2)-Te(1)	94.4(2)	94.9(1)	94.7(9)	
Te(1)-Co(2)-Te(2)	82.8(8)	83.8(8)	83.6(8)	
Te(1)-Co(2)-Te(2)	84.6(6)	85.6(6)	86.0(7)	
Ge(1)-Co(2)-Te(1)	97.1(2)	97.1(8)	97.2(7)	
Ge(1)-Co(2)-Te(1)	89.5(2)	89.5(6)	89.3(6)	
Te(1)-Co(2)-Ge(2)	89.0(8)	88.8(7)	89.2(7)	
Te(2)-Co(2)-Ge(2)	96.4(2)	83.5(7)	83.3(8)	
Te(2)-Co(2)-Ge(2)	94.3(2)	95.8(8)	95.9(7)	
Te(2)-Co(2)-Ge(2)	91.8(2)	92.3(7)	92.2(7)	

It is useful to track the distortion involved in the skutterudite formation from the parent ReO_3 structure as it will be a starting point to find out the distortion involved in the ternary skutterudites under study. ReO_3 possesses the ideal ABX_3 perovskite structure, space group $Pm\overline{3}m$, in which the A cation has been removed forming an infinite network of straight corner-sharing octahedra. The distortion involving the formation of the skutterudite unit cell consists of two steps, *i.e*. the doubling of the unit cell in the three crystallographic directions and the tilting of the octahedra.

Stokes *et al*. use this transformation as an example of the use of ISOTROPY in the tutorial of the program [251]. The distortion is associated to the irrep M3+ by inspection of the basis vectors and the tilting pattern and then the isotropy subgroups associated to this irrep are examined. It is seen that the skutterudite space group $Im\overline{3}$ shows up with a tilting pattern described as ($a^+a^+a^+$). This compact notation was introduced by Glazer. Different tilting magnitudes are indicated by different letters, the sense of the tilting by + - superscripts and the tilting around each crystallographic axis by a three-dimensional vector [252]. It has also been shown elsewhere that tilting of octahedra must necessarily reduce the symmetry of the parent space group $Pm\overline{3}m$ (tilt system $a^0a^0a^0$) and generate derivative subgroups of lower symmetry [253]. Two factors must be considered in order to shortlist the likely space groups involved in the distortion originated by anion substitution:

- After isoelectronic anion substitution, there is no change in the unit cell size as no extra reflections appear at large *d*-spacing (Figure 3-5 and Figure 3-6).
- Infrared spectroscopy studies suggest that the symmetry of the ternary skutterudites $MY_{1.5}Q_{1.5}$ is lower than cubic [56].

Group theoretical methods can only be applied to a specific case of polymorphism known as displacive phase transitions and also to order-disorder transformations. In the former case, the polyhedra undergo rotation only, and no bonds are broken. In this type of transformations, changes in the density and symmetry of the resulting material occur. Moreover, these transformations require little energy and are relatively fast. Order-disorder phase transitions can also be treated by group theoretical methods as long as the same conditions as in the displacive transformations are fulfilled. On the contrary, this methodology cannot be applied in a class of phase transitions known as transformations of first coordination. These include dilatational transformations, *e.g*. the conversion of a CsCl structure into a NaCl structure by a dilatation along a cube

diagonal, and also reconstructive transformations, in which the arrangement of the nearest neighbours is changed and the new structure has different coordination numbers.

Thus, displacive phase transitions can be readily studied by group theoretical methods implemented in the software package ISOTROPY, which makes the analysis of these transformations more accessible and user friendly. ISOTROPY operates as follows:
Every displacive phase transition can be associated to a unit distortion vector, namely $(\varphi_1, \varphi_2, \varphi_3 \cdots)$, whose dimensionality will depend on the type of distortion and describes it. For distortions involving atom displacements, it is a three dimensional vector whose components are the unit displacements along the three crystallographic axes. For those involving octahedra tilting, it is a six-component vector consisting of three components that describe the unit in-phase tilts and three components describing the unit out-of-phase tilting around the three crystallographic axes. Finally, for those involving cation or anion ordering, a one-, two- or a three-dimensional vector may be involved depending on whether the ordering occurs along a crystallographic axis, a *xy*, *yz*, or *xz* plane or a plane or any other configuration involving the three axes.

Then, a second vector, the order parameter, defines the magnitude of the distortion, namely $(\eta_1, \eta_2, \eta_3 \cdots)$ in the direction of the basis functions φ_i. This vector has, obviously, the same dimension as the distortion vector and has important implications within the Landau theory of phase transitions [254]. Such theory explains that the driving force of a phase transition is a non-zero free energy (Gibbs energy) expressed as a Taylor expansion in terms of the order parameter among others. Therefore, a phase transition can be characterized by the order parameter, which contains information on the extent of the deformation. Any displacement/distortion can then be described in terms of the distortion vector and the order parameter:

$$\varphi = \sum_i \varphi_i \eta_i \qquad \textbf{(3-1)}$$

The next step followed by ISOTROPY is to map all the symmetry elements, *g*, contained within the parent space group into matrices, D_{ij}, this means to apply all the symmetry elements to the distortion vector. This will generate another set of matrices some of which will keep the distortion vector invariant and others will not. If only those symmetry elements leaving the distortion vector invariant are selected, *i.e*. atoms become indistinguishable as such, it is seen that they fulfil the following equation:

$$g(\varphi_1, \varphi_2, \varphi_3 \cdots)\begin{pmatrix}\eta_1\\ \eta_2\\ \eta_3\\ \vdots\end{pmatrix} = (\varphi_1, \varphi_2, \varphi_3 \cdots)\mathrm{D}(g)\begin{pmatrix}\eta_1\\ \eta_2\\ \eta_3\\ \vdots\end{pmatrix} \qquad \textbf{(3-2)}$$

This equation can be simplified as the distortion vector is invariant. Therefore, those symmetry elements that leave the order parameter invariant have to fulfil the relation:

$$g\begin{pmatrix}\eta_1\\ \eta_2\\ \eta_3\\ \vdots\end{pmatrix} = \mathrm{D}(g)\begin{pmatrix}\eta_1\\ \eta_2\\ \eta_3\\ \vdots\end{pmatrix} \qquad \textbf{(3-3)}$$

These elements form a subgroup within the parent space group symmetry elements, which is called an isotropy subgroup of the parent space group. Therefore, each order parameter defines by itself an isotropy subgroup, whose total symmetry will be lower than that of the parent space group. This set of matrices constitutes by itself an irreducible representation (irrep) of which the parent space group is composed, as follows:

$$g\eta = \eta \qquad \textbf{(3-4)}$$

Where η is the order parameter. Each irreducible representation has a label, following the convention of Miller and Love [255]. Nevertheless, each irrep can transform as several distortion vectors. Therefore, in order to uniquely assign an isotropy subgroup to a certain distortion, it is necessary to find first the irrep that transforms as the distortion under study, by means of physical information such as diffraction data. Then, by inspection of the distortion order parameters, a unique isotropy space group is assigned.

The parent space group $Im\overline{3}$ (204) is assigned. It was previously mentioned that in the distortion, the size of the unit cell is maintained, as no extra reflections have been observed in the diffraction pattern at large *d*-spacing. This fact shortlists all the possible irreps to only those with the *k* vector (1,1,1), which corresponds to the irreps labelled as H (Figure 3-7). Based on our diffraction data, the isotropy subgroup that transforms as the ordering distortion under study can also be shortlisted. One-dimensional high-symmetry space groups are discarded, as extra reflections in the diffraction pattern reveal that the cubic symmetry of the parent space group is lost.

```
Isotropy, Version 6.4.2, August 2000
Harold T. Stokes and Dorian M. Hatch
Brigham Young University
Current setting is International (new ed.) with conventional basis vectors.
*VALUE PARENT 204
*SHOW KPOINT
*DISPLAY KPOINT
     k vector
GM   (0,0,0)
DT   (0,2a,0)
LD   (2a,2a,2a)
SM   (a,a,0)
H    (1,1,1)
N    (1/2,1/2,0)
P    (1/2,1/2,1/2)
D    (1/2,1/2,2a)
G    (a+1,-a+1,1)
C    (a+b,a+b,2a)
A    (-a+b,a+b,0)
GP   (b+c,a+c,a+b)
*_
```

Figure 3-7 ISOTROPY screenshot showing the k vectors and their labels

Distortions that originate low-symmetry space groups, such as monoclinic or orthorhombic are also discarded as the expected large splitting of the intense reflections at high *d*-spacing is not observed, should the symmetry be as low.

```
Isotropy, Version 6.4.2, August 2000
Harold T. Stokes and Dorian M. Hatch
Brigham Young University
Current setting is International (new ed.) with conventional basis vectors.
*VALUE PARENT 204
*VALUE KPOINT H
*SHOW DIRECTION VECTOR
*SHOW IRRE
*SHOW SUBGROUP
*DISPLAY ISOTROPY
Irrep (ML) Subgroup  Dir
H1+        200 Pm-3  P1  (a)
H2+H3+     47 Pmmm   C1  (a,b)
H4+        58 Pnnm   P1  (a,0,0)
H4+        148 R-3   P3  (a,a,a)
H4+        14 P2_1/c C1  (a,b,0)
H4+        2 P-1     S1  (a,b,c)
H1-        201 Pn-3  P1  (a)
H2-H3-     48 Pnnn   C1  (a,b)
H4-        59 Pmmn   P1  (a,0,0)
H4-        148 R-3   P3  (a,a,a)
H4-        11 P2_1/m C1  (a,b,0)
H4-        2 P-1     S1  (a,b,c)
*_
```

Figure 3-8 ISOTROPY screenshot showing all the distortion vectors with k point (1,1,1).

Therefore, the highest-symmetry non-cubic space group left is the rhombohedral $R\bar{3}$. This is consistent with a pseudocubic unit cell that is metrically cubic but of lower symmetry. Moreover, a broadening of the most intense reflection at high *d*-spacing is consistent with this evidence (Figure 3-5 and Figure 3-6).

However there are two irreps that originate a distortion whose final space group is $R\bar{3}$. These are H4+ and H4- (Figure 3-9). They both are three-dimensional distortions whose order parameter describes a distortion of the same magnitude along the three crystallographic axes. Their basis vectors correspond to the transformation matrix of a rhombohedral unit cell expressed in rhombohedral setting of exactly the same size as

the parent cubic cell into a hexagonal setting. The only difference is that H4- involves a change of origin, something that it is not sought. If the unit cell of the H4- distortion is looked at carefully, it is seen that all metal atoms occupy special positions, which may be linked to a ferroelectric phase transition [256]. H4+, however, maintains the same unit cell origin. Further, a Rietveld refinement using the atomic positions derived from the irrep H4- has been carried out, yielding larger goodness-of-fit parameters. Moreover, $R\bar{3}$ is the highest-symmetry space group that originates from the distortion and it possesses an extra symmetry element, the centre of inversion, missing in the previously reported $R3$ space group. The next step is then to determine how the Wyckoff positions of the parent space group transform into the distorted one.

```
Isotropy, Version 6.4.2, August 2000
Harold T. Stokes and Dorian M. Hatch
Brigham Young University
Current setting is International (new ed.) with conventional basis vectors.
*VALUE PARENT 204
*VALUE KPOINT H
*VALUE DIRECTION P3
*SHOW IRRE
*SHOW SUBGROUP
*SHOW ORIGIN
*SHOW BASIS
*DISPLAY ISOTROPY
Irrep (ML) Subgroup Basis Vectors              Origin
H4+        148 R-3  (1,-1,0),(0,1,-1),(1,1,1) (0,0,0)
H4-        148 R-3  (1,-1,0),(0,1,-1),(1,1,1) (1/4,1/4,1/4)
*_
```

Figure 3-9 ISOTROPY screenshot showing the shortlisted irreps.

The former Wyckoff 8*c* special position splits into another 6*c* special position and one 18f general position, whereas the former 24*g* general position splits into four 18*f* general positions and the relationship between them is given by ISOTROPY straightforwardly (Figure 3-10).

```
Isotropy, Version 6.4.2, August 2000
Harold T. Stokes and Dorian M. Hatch
Brigham Young University
Current setting is International (new ed.) with conventional basis vectors.
*VALUE PARENT 204
*VALUE IRRE H4+
*VALUE SUBGROUP 148
*SHOW WYCKOFF SUBGROUP
*VALUE WYCKOFF C G
*SHOW WYCKOFF VECTOR ALL
*DISPLAY ISOTROPY
Wyckoff New Wyckoff
c       c, z'=1/4
        f, x'=-1/3, y'=-1/6, z'=7/12
g       f, x'=-1/3y-1/3z, y'=1/3y-2/3z, z'=1/3y+1/3z
        f, x'=-1/3y+1/3z, y'=1/3y+2/3z, z'=1/3y-1/3z
        f, x'=-1/3y-1/3z, y'=1/3y-2/3z, z'=1/2+1/3y+1/3z
        f, x'=-1/3y+1/3z, y'=1/3y+2/3z, z'=1/2+1/3y-1/3z
*_
```

Figure 3-10 ISOTROPY screenshot showing the transformed Wyckoff positions.

In order to obtain the correct anion order in the new Wyckoff positions, the anions were permutated. Consecutive Rietveld refinements were carried out in each configuration (Ge-Ge-Te-Te, Te-Ge-Ge-Te, Te-Te-Ge-Ge, Ge-Te-Te-Ge) corresponding to the combination of four elements taken four at a time, and that with the lowest R_{wp} factor was chosen, matching the sequence Ge(1)-Te(1)-Te(2)-Ge(2). This experimentally determined anion configuration is also predicted theoretically by ISOTROPY for the H4+ distortion (Figure 3-11).

When anion substitution occurs we may expect anion ordering and/or tilting. ISOTROPY allows us to find out the type of distortion H4+ irrep belongs to. H4+ does not belong to the group of distortions involving tilting as no output is obtained from ISOTROPY, thereby retaining the $a^+a^+a^+$ original tilt system of the parent skutterudite structure. However, should an order-disorder microscopic distortion be modelled introducing ordering in the 24*g* site of the parent space group, we obtain an ordering pattern that agrees well with the experimental data (Figure 3-11). The coordinates on the left column correspond to the twenty four general positions of the *g* Wyckoff site in the skutterudite $Im\overline{3}$ space group and the right column shows the anion alternation by means of positive or negative signs. This pattern suits an octahedral anion configuration in which the two anions are occupying opposite capping faces of a trigonal antiprism (Figure 3-12). Further, the anions are ordered in layers perpendicular to the [111] direction of the skutterudite unit cell, which corresponds to the *c*-axis of the $R\overline{3}$ cell in the hexagonal setting (Figure 3-9 and Figure 3-14). Anion ordering can be described by a reciprocal lattice vector **k** = (1,1,1) that does not change the unit cell size and is also associated with the irrep H4+, as displayed by ISOTROPY.

```
Isotropy, Version 6.4.2, August 2000
Harold T. Stokes and Dorian M. Hatch
Brigham Young University
Current setting is International (new ed.) with conventional basis vectors.
*VALUE PARENT 204
*VAL IRRE H4+
*VALUE DIRECTION P3
*VALUE WYCKOFF G
*SHOW IRRE
*SHOW MICROSCOPIC SCALAR
*DISPLAY DISTORTION
Irrep (ML) Point                Mode Projected Order Functions
H4+        (0,y,z)              1    f
           (1/2,y+1/2,z+1/2)    1    -f
           (0,-y,-z)            1    f
           (1/2,-y+1/2,-z+1/2)  1    -f
           (0,y,-z)             1    -f
           (1/2,y+1/2,-z+1/2)   1    f
           (0,-y,z)             1    -f
           (1/2,-y+1/2,z+1/2)   1    f
           (y,z,0)              1    f
           (y+1/2,z+1/2,1/2)    1    -f
           (y,-z,0)             1    -f
           (y+1/2,-z+1/2,1/2)   1    f
           (-y,z,0)             1    -f
           (-y+1/2,z+1/2,1/2)   1    f
           (-y,-z,0)            1    f
           (-y+1/2,-z+1/2,1/2)  1    -f
           (z,0,y)              1    f
           (z+1/2,1/2,y+1/2)    1    -f
           (z,0,-y)             1    -f
           (z+1/2,1/2,-y+1/2)   1    f
           (-z,0,-y)            1    f
           (-z+1/2,1/2,-y+1/2)  1    -f
           (-z,0,y)             1    -f
           (-z+1/2,1/2,y+1/2)   1    f
```

Figure 3-11 ISOTROPY screenshot showing the H4+ ordering pattern in the 24*g* Wyckoff position.

The asymmetric octahedral anion environment causes the cobalt atoms to shift towards the germanium capping face of the trigonal antiprism (Table 3-4), thereby deviating slightly from the ideal positions. In the refinement at room temperature, these positions have been fixed given that a shorter collection time was employed (175 μA). At low temperature, however, a longer exposure time (425 μA) led to the precise determination of the cobalt atom positions. The overall effect is to distort slightly the 90° rhombohedral angle, accurately determined in the low-temperature refinement using a rhombohedral setting, *i.e*. a = 8.71792(3) Å, α = 89.9715(7) °.

A column named "disorder" has been introduced in an attempt to model possible anion disorder among the general *g* Wyckoff positions (Table 3-3). However, it is seen that the overall structure occupancy factor (SOF) of germanium in the place of tellurium atoms is not statistically significant and *vice versa*.

The most distinctive structural feature of anion substitution is the distortion of the nearly square Sb_4^{4-} rings of the parent skutterudite. In binary skutterudites, there is only one crystallographically distinct Sb_4^{4-} ring in which short and long distances alternate (Figure 3-13).

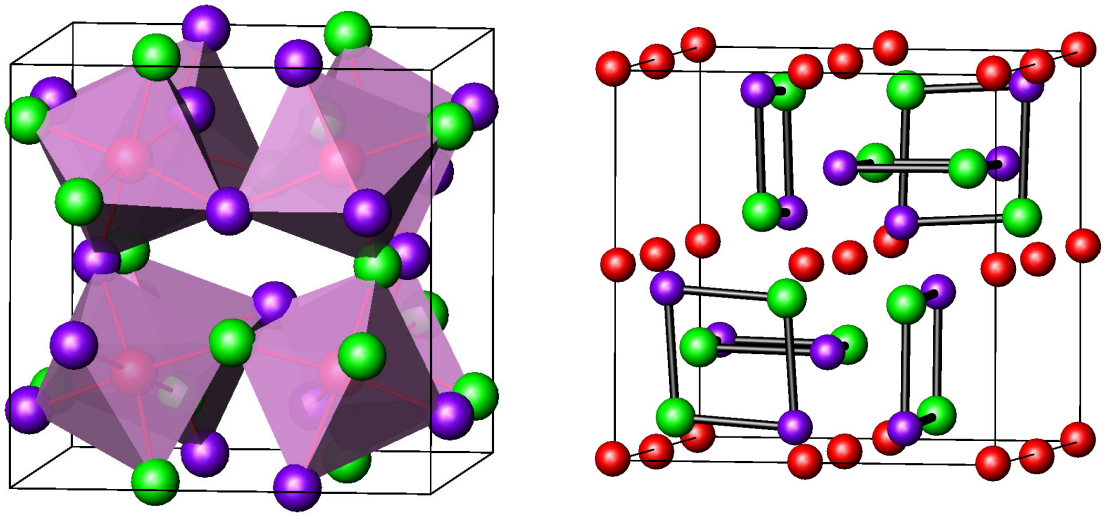

Figure 3-12 Left: Polyhedral representation of the ordered ternary skutterudite $CoGe_{1.5}Te_{1.5}$. Right: Refined unit cell emphasizing the distorted $[Ge_2Te_2]^{4-}$ rings. Key: germanium in green, tellurium in purple and cobalt in red.

Conversely, $CoGe_{1.5}Te_{1.5}$ possesses two crystallographically distinct four-membered rings with stoichiometry $[Ge_2Te_2]^{4-}$ in which germanium and tellurium are found in *trans* to each other (Figure 3-13). The Ge-Te intraring distances (2.72-2.92 Å) are similar to those of GeTe (2.89 Å), and the interring distance (~ 3.3 Å) is shorter than the sum of the van der Waals radii of the anions (~ 4 Å) [257]. Significant contributions of the anion sublattice to the density of states near the Fermi level have been calculated in binary skutterudites, being also of paramount importance as to the electron correlation phenomena observed in other filled ternary skutterudites, *e.g.* $LaFe_4P_{12}$ [127]. Should formal charges be assigned to the heterorings, the tellurium atoms fulfil the octet rule simply by forming two bonds, whereas the germanium atoms need also two negative charges each.

This asymmetric charge distribution may be accountable for the high electrical resistivity observed in anion substituted skutterudites (Figure 3-31), when compared to their binary counterparts (Table 1-4). Charge localization will inevitably have a deleterious effect on electron mobilities. Moreover, it has been already predicted that the skutterudite rings are a key factor as to the understanding of the lattice dynamics, given that they characterize the electronic states around the forbidden band gap [258].
The average Co-Ge distance (2.39 Å) is comparable to that observed in other binary cobalt germanides such as CoGe (2.37-2.58 Å). However, the Co-Te distance (2.50 Å) is slightly shorter when compared to other cobalt tellurides such as CoTe (2.61 Å) or $CoTe_2$ (2.58 Å).

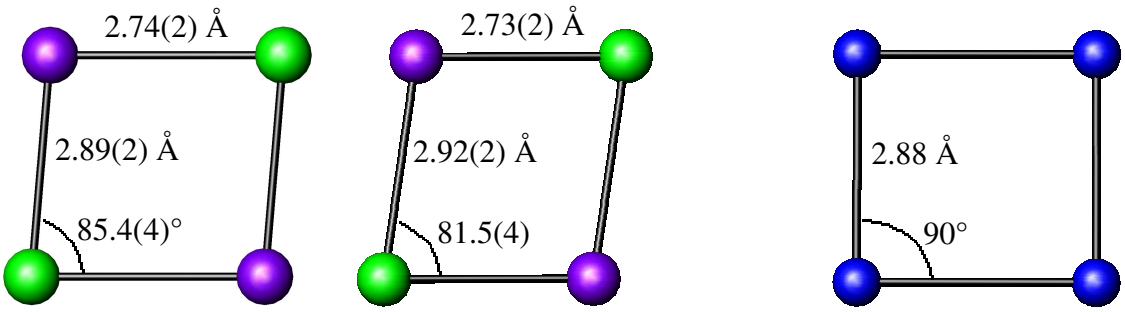

Figure 3-13 Left: The two crystallographically distinct four-membered rings in $CoGe_{1.5}Te_{1.5}$. Right: four-membered ring in $CoSb_3$ [259]. Key: germanium in green, tellurium in purple.

The formation of square heterorings with short Ge-Te distances causes the X-Co-X octahedral angles to distort, thereby deviating significantly from the ideal octahedral geometry, ranging between 82.4(6) ° and 97.1(8) ° (Table 3-5).

The tilt angle (ϕ) can be calculated from the Co-X-Co angle using the formula [260]:

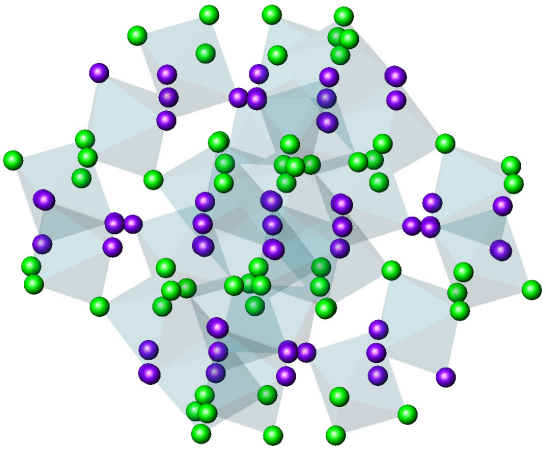

Figure 3-14 Anion ordering of the ternary skutterudite $CoGe_{1.5}Te_{1.5}$ along the [111] direction. Key: germanium in green and tellurium in purple.

$$cos(\text{Co - X - Co}) = 1 - \frac{2x^2}{9} \qquad \textbf{(3-5)}$$

$$x = 2\cos\phi + 1 \qquad \textbf{(3-6)}$$

The tilt angle obtained using and averaged Co-X-Co distance is 32.5°, very close to that observed in the parent $CoSb_3$ skutterudite, *i.e.* 32.8°. This indicates that the magnitude of the tilting around the three crystallographic axes is the same as in $CoSb_3$, supporting the previous statement as to the conservation of the tilt system when going from $CoSb_3$ to $CoGe_{1.5}Te_{1.5}$.

3.5 Neutron diffraction study of $MGe_{1.5}S_{1.5}$ (M = Co, Rh, Ir)

3 g samples were placed into a vanadium can attached to the end of a long rod fitting a vanadium-walled cryostat in order to perform low temperature neutron scattering experiments. A data treatment procedure similar to that of $CoGe_{1.5}Te_{1.5}$ was employed. The Genie spectrum manipulation software was used for initial data manipulation [249]. Data obtained from the backscattering and 90° detector banks were summed, normalised and used simultaneously in Rietveld refinements using the GSAS software package [250]. As part of the data processing / normalization, rhodium and iridium-containing sample datasets were also corrected for absorption given their large absorption cross sections, *i.e*. 144 and 425 barns, respectively. The backscattering bank data was initially used to determine accurately the lattice parameters of the present phases. These were fixed before adding the 90° bank data, whose diffractometer constants were refined to match the *d*-spacing–TOF relation of the backscattering bank and then fixed again to refine the lattice parameters. Subsequently, the structural parameters were refined, *i.e.* atom positions, occupancy fractions and atomic displacement parameters, followed by the variables accounting for peak shape. The atomic positions as well as the lattice parameters along with other details of the refinement are shown in Table 3-6.

The presence of small quantities of GeO_2 is observed despite efforts to reduce its content through five-hour heat treatments at 600 °C under a reducing (5/95 H_2/N_2) atmosphere (Figure 3-15 and Figure 3-17). The few CoS impurity reflections found in $CoGe_{1.5}S_{1.5}$ and both their small intensity and large overlapping caused a troublesome quantification as shown by the large calculated esds (Figure 3-15, Figure 3-16 and Table 3-6). Better defined and more intense impurity peaks lead to a more precise quantification of the RhS_2 impurity phase present in $RhGe_{1.5}S_{1.5}$ (Figure 3-17 and Table 3-6). The iridium sample, however, presents large impurity reflections corresponding to IrGe (~ 11%) and unreacted Ir (~ 3%) (Figure 3-19 and Table 3-6). Unexpectedly, no reflections of unreacted sulphur were observed, which may be ascribed to amorphous sulphur. This indicates a sample decomposition problem.

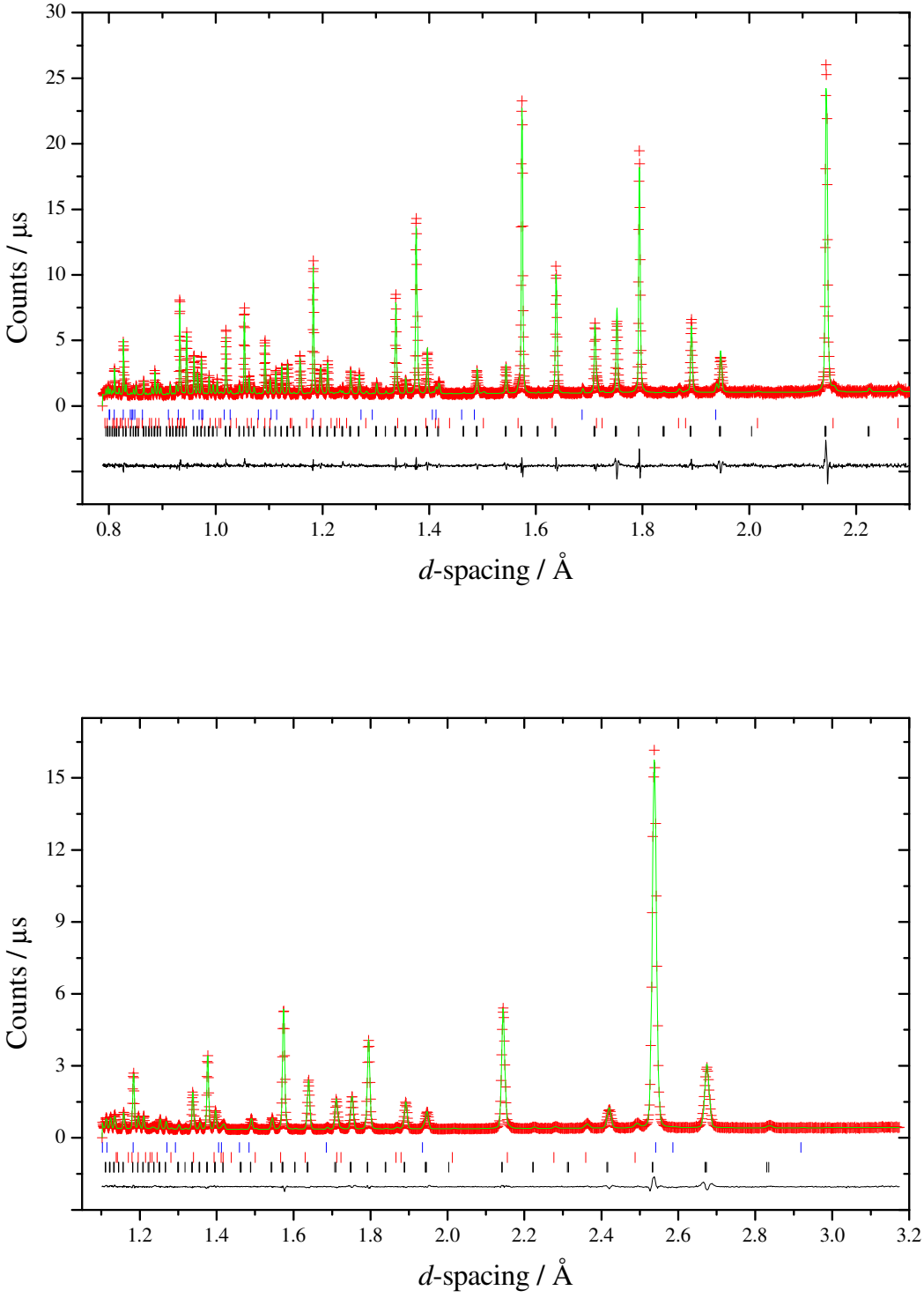

Figure 3-15 Powder neutron diffraction pattern of $CoGe_{1.5}S_{1.5}$ at 293 K. Top: Backscattering bank. Bottom: 90° bank. Key: experimental data (red crosses), fitted model (green line), difference curve (black line). Reflections positions are shown as markers: the black, red and blue markers refer to $CoGe_{1.5}S_{1.5}$ ($R\bar{3}$), GeO_2 and CoS, respectively.

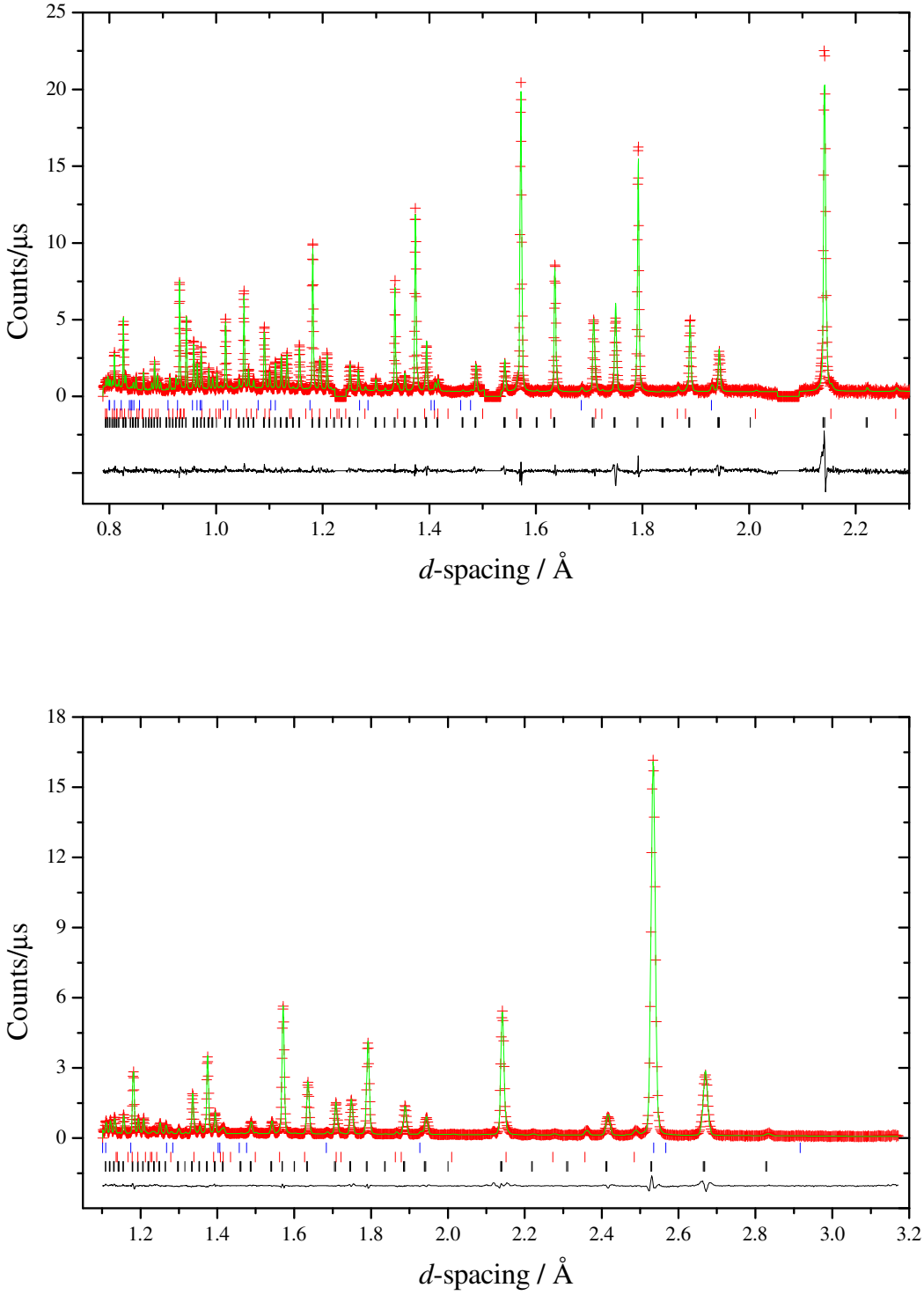

Figure 3-16 Powder neutron diffraction pattern of $CoGe_{1.5}S_{1.5}$ at 4.2 K. Top: Backscattering bank. Bottom: 90° bank. Key: experimental data (red crosses), fitted model (green line), difference curve (black line). Reflections positions are shown as markers: the black, red and blue markers refer to $CoGe_{1.5}S_{1.5}$ ($R\bar{3}$), GeO_2 and CoS, respectively.

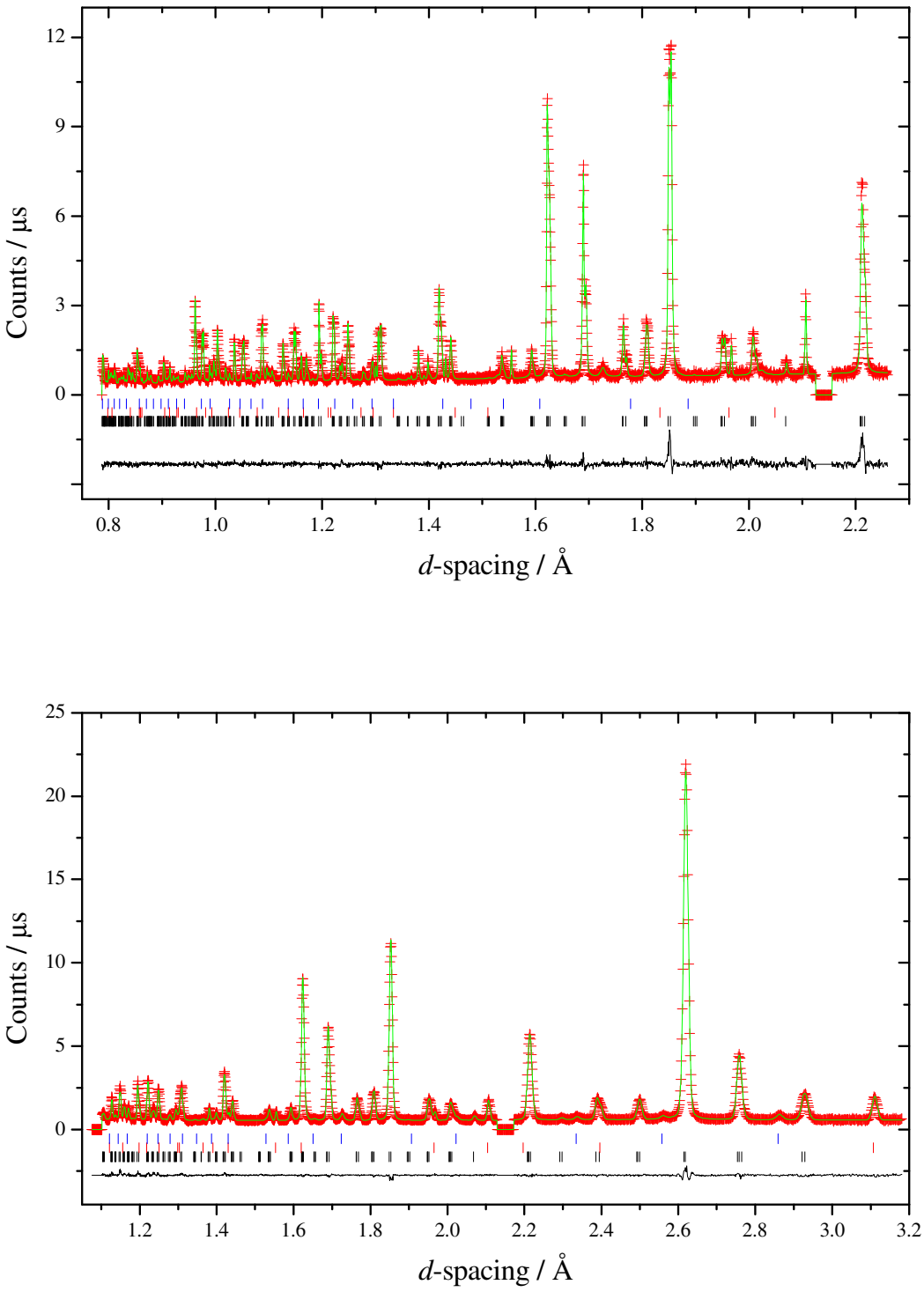

Figure 3-17 Powder neutron diffraction pattern of $RhGe_{1.5}S_{1.5}$ at 293 K. Top: Backscattering bank. Bottom: 90° bank. Vanadium peaks have been excluded for clarity. Key: experimental data (red crosses), fitted model (green line), difference curve (black line). Reflections positions are shown as markers: the black, red and blue markers refer to $RhGe_{1.5}S_{1.5}$ ($R\bar{3}$), GeO_2 and RhS_2, respectively.

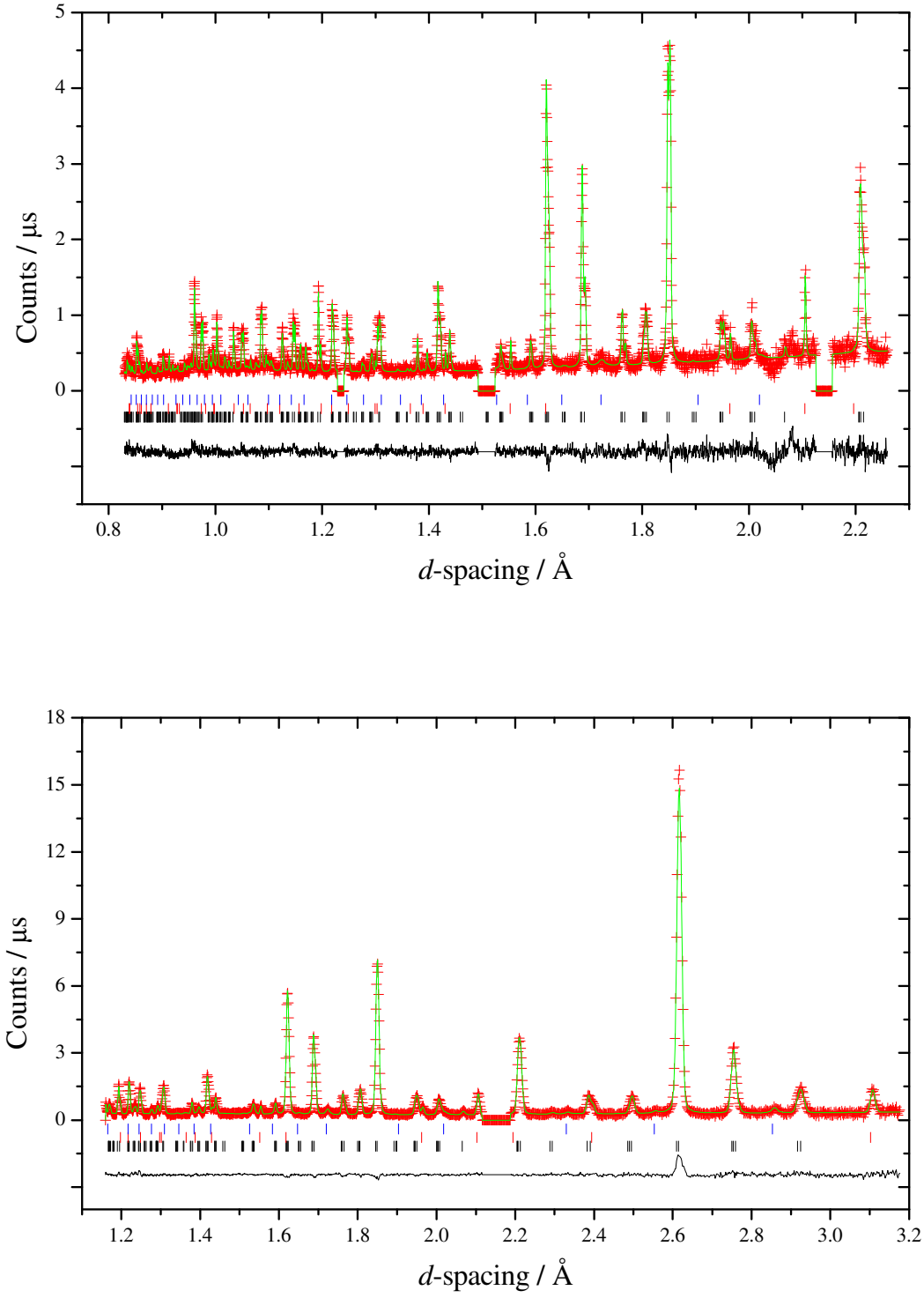

Figure 3-18 Powder neutron diffraction pattern of $RhGe_{1.5}S_{1.5}$ at 4.2 K. Top: Backscattering bank. Bottom: 90° bank. Vanadium peaks have been excluded for clarity. Key: experimental data (red crosses), fitted model (green line), difference curve (black line). Reflections positions are shown as markers: the black, red and blue markers refer to $RhGe_{1.5}S_{1.5}$ ($R\bar{3}$), GeO_2 and RhS_2, respectively.

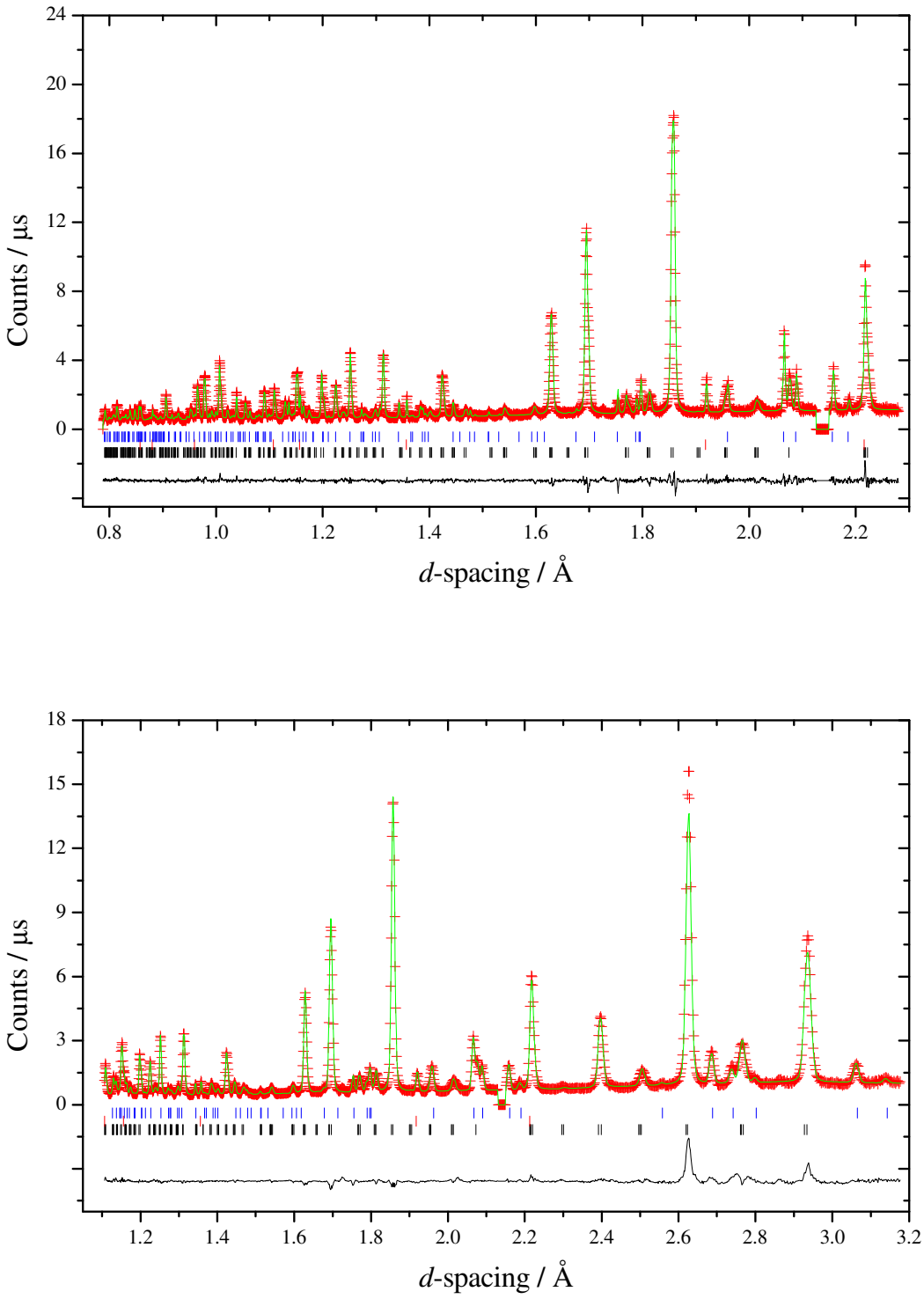

Figure 3-19 Powder neutron diffraction pattern of $IrGe_{1.5}S_{1.5}$ at 293 K. Top: Backscattering bank. Bottom: 90° bank. Vanadium peaks have been excluded for clarity. Key: experimental data (red crosses), fitted model (green line), difference curve (black line). Reflections positions are shown as markers: the black, red and blue markers refer to $IrGe_{1.5}S_{1.5}$ ($R\bar{3}$), Ir and IrGe, respectively.

Table 3-6 Refined parameters for the ordered skutterudites $MGe_{1.5}S_{1.5}$ (M = Co, Rh and Ir), Space group $R\bar{3}$ (hexagonal setting).

		$Co_2Ge_3S_3$		$Rh_2Ge_3S_3$		$Ir_2Ge_3S_3$
		4.2K	**293K**	**4.2 K**	**293 K**	**293 K**
***a* (Å)**		11.32286(6)	11.33907(7)	11.67833(9)	11.69422(5)	11.72726(9)
***c* (Å)**		13.8882(2)	13.9065(2)	14.3645(2)	14.3819(1)	14.4142(3)
a_R (Å)		8.01043(8)	8.02156(3)	8.266(1)	8.2805(1)	8.2994(1)
α(°)		89.943(1)	89.947(1)	89.8358(8)	89.840(2)	89.883(3)
M(1) 6*c*	*z*	0.259(1)	0.257(1)	0.2515(7)	0.2511(3)	0.2529(4)
	B[a] /Å^2	0.31(6)	0.62(4)	1.26(3)	0.85(2)	1.08(2)
M(2) 6*f*	*x*	0.672(3)	0.670(2)	0.666(1)	0.6681(5)	0.6673(7)
	y	0.838(1)	0.838(1)	0.8327(6)	0.8327(3)	0.8331(4)
	z	0.5886(4)	0.5895(4)	0.5863(3)	0.5865(1)	0.5857(2)
	B/Å^2	0.31(6)	0.62(4)	1.26(3)	0.85(2)	1.08(2)
Ge(1) 18*f*	SOF Ge	0.975(1)	0.975(1)	0.993(3)	0.993(1)	0.953(3)
	SOF S	0.025(1)	0.025(1)	0.007(3)	0.007(1)	0.047(3)
	x	0.8387(4)	0.8379(4)	0.8374(4)	0.8375(2)	0.8384(5)
	y	0.0127(3)	0.0123(3)	0.0170(3)	0.0174(2)	0.0164(4)
	z	0.1615(2)	0.1605(2)	0.1618(3)	0.1608(1)	0.1594(3)
	B[b]/Å^2	0.35(1)	0.68(1)	1.00(2)	0.89(1)	1.06(2)
Ge(2) 18*f*	SOF Ge	0.975(1)	0.975(1)	0.993(3)	0.993(1)	0.953(3)
	SOF S	0.025(1)	0.025(1)	0.007(3)	0.007(1)	0.047(3)
	x	0.9364(3)	0.9369(3)	0.9317(4)	0.9324(2)	0.9324(4)
	y	0.2111(4)	0.2110(4)	0.2095(5)	0.2092(2)	0.2077(5)
	z	0.5613(2)	0.5615(2)	0.5645(3)	0.5648(1)	0.5643(3)
	B/Å^2	0.35(1)	0.68(1)	1.00(2)	0.89(1)	1.06(2)
S(1) 18*f*	SOF Ge	0.025(1)	0.025(1)	0.007(3)	0.007(1)	0.047(3)
	SOF S	0.975(1)	0.975(1)	0.993(3)	0.993(1)	0.953(3)
	x	0.9334(9)	0.9354(9)	0.9299(9)	0.9298(5)	0.929(1)
	y	0.213(1)	0.213(1)	0.215(1)	0.2135(6)	0.210(1)
	z	0.0677(5)	0.0673(5)	0.0723(6)	0.0720(3)	0.0708(7)
	B/Å^2	0.35(1)	0.68(1)	1.00(2)	0.89(1)	1.06(2)
S(2) 18*f*	SOF Ge	0.025(1)	0.025(1)	0.007(3)	0.007(1)	0.047(3)
	SOF S	0.975(1)	0.975(1)	0.993(3)	0.993(1)	0.953(3)
	x	0.8410(9)	0.838(1)	0.836(1)	0.8380(6)	0.837(1)
	y	0.0203(7)	0.0197(8)	0.0246(9)	0.0261(5)	0.024(1)
	z	0.6656(6)	0.6654(6)	0.6669(9)	0.6658(4)	0.6655(8)
	B/Å^2	0.35(1)	0.68(1)	1.00(2)	0.89(1)	1.06(2)
Weight percentage (%)		1.64(7) GeO_2	1.79(7) GeO_2	2.52(4) GeO_2	2.43(2) GeO_2	3.17(4) Ir
Weight percentage (%)		9(2) CoS	8(1) CoS	4.0(1) RhS_2	4.70(7) RhS_2	11.1(1) IrGe
R_{wp} (%)	180° bank	7.7	5.3	9.7	5.8	5.6
R_{wp} (%)	90° bank	4.6	3.0	5.9	3.6	5.1
χ^2		4.7	2.4	1.8	1.3	3.9

[a] **Cation and anion atomic displacement parameters have been constrained to the same value, respectively**.

Table 3-7 Relevant bond distances (Å) and angles (°) for the $MGe_{1.5}S_{1.5}$ (M = Co, Rh, Ir) phases.

	$CoGe_{1.5}S_{1.5}$		$RhGe_{1.5}S_{1.5}$		$IrGe_{1.5}S_{1.5}$	
	4.2 K	**293 K**	**4.2 K**	**293 K**	**293 K**	
M(1)-Ge(1)	2.336(9)	2.337(9)	2.383(7)	2.3937(33)	2.410(6)	x 3
M(1)-S(2)	2.192(11)	2.237(12)	2.379(11)	2.385(6)	2.381(12)	x 3
Ge(1)-M(1)-Ge(1)	89.7(4)	90.3(4)	93.54(30)	93.32(14)	91.79(21)	x 3
Ge(1)-M(1)-S(2)	86.74(23)	86.62(23)	85.57(27)	86.23(13)	86.44(30)	x 3
	84.02(20)	84.10(19)	83.03(22)	83.31(11)	83.93(24)	x 3
S(2)-M(1)-S(2)	99.1(4)	98.7(5)	97.8(4)	97.09(20)	97.7(4)	x 3
M(2)-Ge(1)	2.351(13)	2.337(13)	2.373(9)	2.383(5)	2.372(7)	
M(2)-Ge(2)	2.285(10)	2.303(11)	2.387(7)	2.373(4)	2.392(6)	
	2.295(7)	2.316(9)	2.400(9)	2.4001(31)	2.387(5)	
M(2)-S(1)	2.271(10)	2.265(11)	2.398(11)	2.394(6)	2.396(10)	
	2.298(13)	2.264(14)	2.396(12)	2.423(6)	2.424(11)	
M(2)-S(2)	2.262(16)	2.252(16)	2.422(14)	2.423(7)	2.416(13)	
Ge(1)-M(2)-Ge(2)	84.22(26)	83.92(23)	84.88(19)	85.25(10)	85.98(19)	
	83.38(29)	83.54(24)	83.87(24)	84.09(11)	85.10(18)	
Ge(1)-M(2)-S(1)	94.5(6)	94.1(5)	97.8(4)	97.06(20)	96.15(34)	
	91.4(7)	91.8(7)	94.7(6)	93.64(26)	93.1(4)	
Ge(2)-M(2)-Ge(2)	92.0(4)	91.1(4)	92.74(33)	93.15(16)	92.55(26)	
Ge(2)-M(2)-S(1)	87.4(4)	87.36(34)	86.0(4)	86.83(18)	87.4(4)	
	83.21(28)	83.66(27)	82.10(27)	81.86(13)	83.45(28)	
Ge(2)-M(2)-S(2)	97.2(7)	97.0(7)	97.0(5)	97.53(24)	94.48(34)	
	95.1(5)	94.5(6)	94.9(4)	94.43(19)	96.6(4)	
S(1)-M(2)-S(1)	97.2(6)	97.7(6)	99.2(5)	98.18(27)	96.7(5)	
S(1)-M(2)-S(2)	87.0(4)	87.8(4)	84.4(4)	84.43(21)	84.3(4)	
	87.1(4)	87.1(4)	83.5(4)	83.48(21)	84.3(4)	
S(1)-Ge(1)	2.360(11)	2.358(11)	2.379(13)	2.362(6)	2.347(15)	
	2.540(10)	2.569(10)	2.494(14)	2.513(7)	2.583(14)	
S(1)-Ge(1)-S(1)	87.14(27)	87.72(27)	86.56(29)	86.78(16)	86.58(32)	
S(2)-Ge(2)	2.365(10)	2.370(10)	2.380(12)	2.357(6)	2.369(13)	
	2.556(10)	2.545(9)	2.502(12)	2.522(6)	2.555(13)	
S(2)-Ge(2)-S(2)	87.42(27)	87.03(26)	86.74(28)	83.47(16)	86.83(31)	

As regards the structure of the $MGe_{1.5}S_{1.5}$ (M = Co, Rh, Ir) phases, there have been several previously reported works. Korenstein *et al*. realized that the powder X-ray diffraction pattern of $CoGe_{1.5}S_{1.5}$ contained a few weak superstructure reflections that violated the condition $h + k + l = 2n$ followed by the main reflections. They described the structure in the trigonal crystal system and assigned the space group *R*3. However,

they were unable to solve the complete structure arguing lack of long-range ordering [106]. Lutz *et al.* indexed a series of $RhGe_{1.5}S_{1.5}$ Guinier photographs on the basis of a rhombohedral unit cell [56] and Partik *et al.* reported long-range ordering on twinned $CoGe_{1.5}Q_{1.5}$ (Q = S, Se) single crystals that were assigned, once more, the space group *R*3 [55].

The analysis of the crystallographic data from the ICSD service supplied by Korenstein [106] and Partik [55] with Platon/Addsym to identify missing symmetry elements clearly revealed that there is a centre of inversion missing and that the true space group is $R\bar{3}$ (Figure 3-10) [261,262]. Therefore, following the group theoretical analysis described in section 3.4, the same model was used, which resulted in a much better agreement than using the cubic space group $Im\bar{3}$.

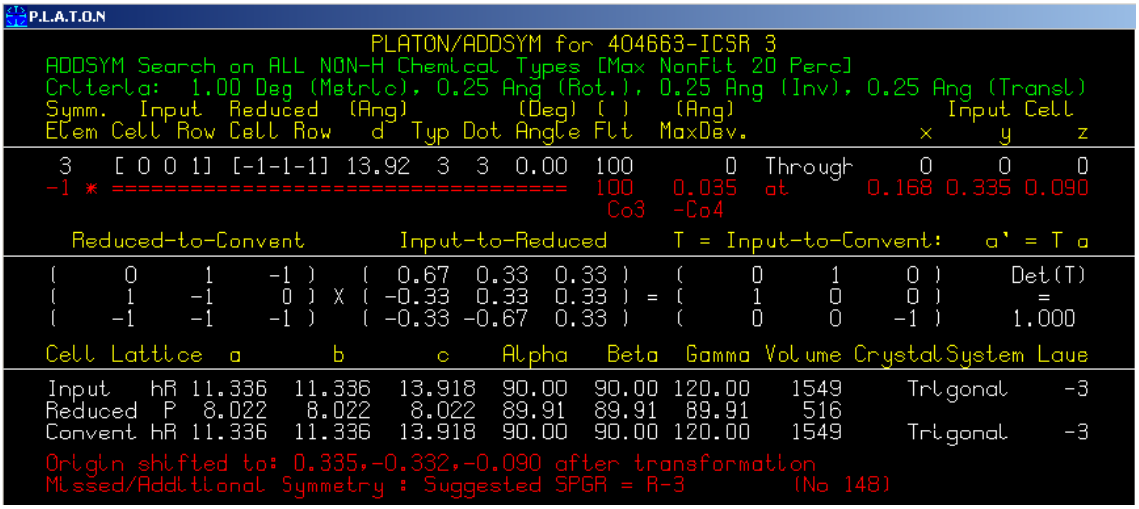

Figure 3-20 PLATON/ADDSYM screenshot showing the missing symmetry element and the suggested space group for the ICSD cif file of $CoGe_{1.5}S_{1.5}$ published by Partik *et al.* [55].

During the course of the refinement, it was noticed that the thermal parameters of the germanium atoms converged towards unusually large values, whereas those of the sulphur atoms converged towards small values.

This fact could be explained by the existence of disorder to some extent, as it had already been indicated by Korenstein *et al.* [106]. In order to model disorder, occupancy fractions of both anions were allowed to vary at each anion crystallographic site keeping both the site and the global stoichiometry constant. All the anion thermal parameters were constrained to have the same value as well as those of the cations. This practice is quite commonly found in powder refinements where data are limited and also used when strong correlations between thermal parameters and occupancy factors are present

[263]. The resulting goodness-of-fit parameters were lower by 15% in $CoGe_{1.5}S_{1.5}$, 12% in $RhGe_{1.5}S_{1.5}$ and 18% in $IrGe_{1.5}S_{1.5}$ at the 90° bank, corresponding to a sulphur to germanium occupancy fraction ratio at the germanium site (and *vice versa*) of 2.5 %, 0.7 % and 4.9 % , respectively.

According to the model, the tilt system ($a^+a^+a^+$) of the parent skutterudite is retained and anion ordering along the [111] direction also occurs. The M-Ge distances are similar to those found in other group 8 metal germanides, *i.e.* between 2.37 Å and 2.68 Å. The Ge-S distances are comparable to other germanium sulphides such as GeS (2.44 Å) or GeS_2 (2.21 Å); and the interring distance (~ 3.1 Å) is shorter than the van der Waal´s radius of the anions (3.80 Å), as it was also observed in $CoGe_{1.5}Te_{1.5}$. The Ge_2S_2 rectangular rings acquire a rhombus-like shape in which the chalcogen-germanium-chalcogen angles are more acute than the germanium-chalcogen-germanium angles (Table 3-7 and Figure 3-21). This fact has been rationalized by Partik *et al*. in terms of orbital interactions between the antiaromatic π-system of the four-membered ring and the fully occupied cobalt d orbitals within a more covalent picture of the bonding than the ionic $Co_4^{3+}(Ge_2S_2)_3^{4-}$ model [55,264]. The ring π antibonding orbital possesses four nodes, analogously to cyclobutadiene, but the larger electronegativity of the sulphur localizes the antibonding orbitals on the germanium atoms. The bonding interaction of the germanium empty π orbital with the cobalt atoms stretches the Ge_2S_2 rings along the Ge-Ge diagonal, thereby lowering the S-Ge-S angle value. Further, the difference between the side lengths varies between 0.15 Å and 0.24 Å, larger than that observed in binary skutterudites, *i.e.* 0.1 Å to 0.11 Å [111].

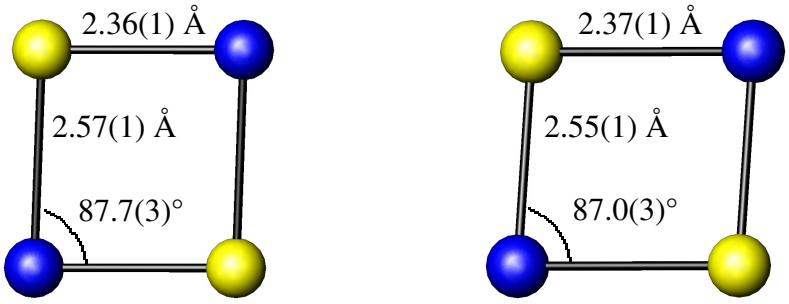

Figure 3-21 The two crystallographically distinct four-membered rings in $CoGe_{1.5}S_{1.5}$. Key: germanium in blue, sulphur in yellow.

The cause of such difference in the binary compounds has been attributed to anisotropic interactions arising from the non-metal sublattice [265], however the larger difference

found in anion-substituted skutterudites is ascribed to differences in covalency between the M-Ge and the M-S bonds [55]. Regarding the $CoGe_3S_3$ octahedra, the fact that the M-S distances are slightly shorter than the M-Ge distances shows the displacement of the metal atom towards the sulphur capping face of the trigonal antiprism, giving rise to distortions of the octahedral ideal geometry [266]. This displacement is explained by the much larger electronegativity of sulphur (2.5 *vs*. 1.8) and is responsible for the small deviations from the 90° rhombohedral angle (Table 3-6). The X-M-X angles vary between 87.54(24)° and 98.7(5)° in $CoGe_{1.5}S_{1.5}$, 84.09(11)° and 97.09(20)° in $RhGe_{1.5}S_{1.5}$ and between 85.10(18)° and 97.4(4)° in $IrGe_{1.5}S_{1.5}$; differing all of them from the ideal 90° value. The tilting of the octahedra can also be calculated with equation (3-5). The average value of all the M-S-M and M-Ge-M angles was used and a tilt angle value of 35.4°, 37.2° and 37.0° was found for M = Co, Rh and Ir, respectively. These values are similar to that found for $CoGe_{1.5}Te_{1.5}$, i.e. 32.5° (section 3.4) and also similar to those of the binary skutterudites MSb_3 M = Co, Rh and Ir, *i.e*. 32.8°, 34.8° and 34.3°, respectively. The observed increment of the tilt angle with the cation size for a given anion was already pointed out by O'Keefe *et al.* [260].

3.6 Synchrotron diffraction study of $MQ_{1.5}Te_{1.5}$ (M = Co, Rh, Ir; Q = Ge, Sn)

Synchrotron X-ray patterns of $CoGe_{1.5}Te_{1.5}$, $IrGe_{1.5}Te_{1.5}$, $CoSn_{1.5}Te_{1.5}$, $RhSn_{1.5}Te_{1.5}$ and $IrSn_{1.5}Te_{1.5}$ were collected at two different wavelengths for each sample, far from the absorption edge and close to it. The same wavelength was used in all the samples for the patterns collected away from the absorption edge, *i.e*. 0.42704(1) Å. Wavelengths of 0.38970(6) Å and 0.4249(1) Å close to the tellurium and tin K-edges were used for the germanium and tin-containing samples, respectively. The wavelengths were calibrated against the silicon standard NIST 640c, which has a certified cell parameter of a = 5.4311946(92) Å.

The atom anomalous scattering form factors must be found experimentally (section 2.2.4). In order to determine those of tin and tellurium, *i.e*. f' and f'', X-ray fluorescence spectra were collected near the K-edges of tin and tellurium, which were used as input for the program CHOOCH [267]. The program determines the X-ray energies and the anomalous scattering factor magnitudes at the points corresponding to f'' maximum and f' minimum. The peak values obtained for the tin and tellurium K-edges are f' = -9.3, f'' = 2.7 electron units at 0.42526 Å and f' = -8.6, f'' = 2.4 electron

units at 0.39025 Å, respectively. The exact values of f' and f'' at the wavelengths used for the experiments were determined graphically from the CHOOCH output data to be f' = -6.09, f'' = 3.79 (f' = -6.5, f'' = 0.56) electron units for tin and f' = -7.1, f'' = 4.26 (f' = -10.1, f'' = 0.57) electron units for tellurium (free atom values [268]).

By using a wavelength close to the absorption edge, we can change the X-ray scattering power of an atom and increase the scattering contrast between neighbouring atoms that, otherwise, would be impossible to distinguish by normal X-ray techniques (section 2.2.4). In this experiment, tin acquires the X-ray scattering properties of ruthenium and tellurium those of rhodium. In practice, this contrast is even higher, owing to the fact that the anomalous scattering factors show no dependence on the scattering angle. The scattering contrast between germanium and tellurium or between tin and tellurium can be defined as follows [269]:

$$2[(f_0 + f')_{Te} - (f_0 + f')_{Ge(Sn)}]/[(f_0 + f')_{Te} + (f_0 + f')_{Ge(Sn)}] \qquad \textbf{(3-7)}$$

The use of several datasets with different scattering contrasts reduces correlations between atomic displacement parameters and atomic occupancies, thereby being of great utility in the determination of site occupancies [270]. The wavelengths are selected typically at the low energy side of the K-edge so that the anomalous form factor f' is maximized without presenting possible problems with absorption and fluorescence [271]. In the germanium tellurides under study, the anomalous diffraction set of data does not represent an improvement as to the contrast between the two anions.

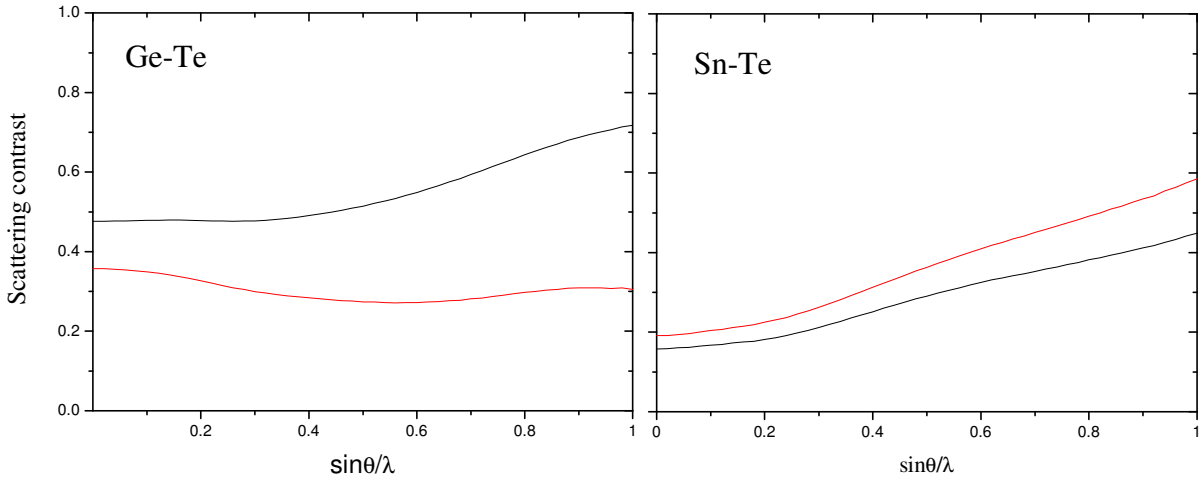

Figure 3-22 Variation of the scattering contrast as a function of sinθ / λ between germanium and tellurium (left) and between tin and tellurium (right). The red and black lines represent the scattering contrast with and without anomalous contribution, respectively.

However, given the proximity of tin and tellurium in the periodic table, the resonant scattering dataset is determinant to study the anion distribution in the 18*f* site and the likely disorder between tin and tellurium sites (Figure 3-22).

The refinement of the normal scattering data set was initially performed to determine accurately the lattice parameters. These were fixed when the anomalous scattering data set was added in order to determine the correct value of the diffractometer constant zero, and eventually were also refined. The anomalous scattering factors for the tin atom were also corrected in the normal scattering datasets, as $\lambda = 0.42704(2)$ Å lies above and very close to the tin experimentally determined K-edge, *i.e.* $\lambda = 0.42526$ Å.

A linear interpolation function with eight coefficients was used to model the background of both histograms. Subsequently, the structural parameters were refined, *i.e.* atom positions, occupancy fractions and thermal parameters.
Finally, the profile parameters were refined. A pseudo Voigt profile function taking into account axial divergence included within the GSAS software package has been used, which accounts for the larger misfits encountered at low angles when dealing with bright synchrotron radiation [272,273]. Given the strong correlation between both axial divergence parameters, they were refined independently and subsequently fixed, following the procedure indicated in reference [274]. It is worth noticing that the high instrumental resolution obtained with a synchrotron source along with highly collimated detectors make the peaks much sharper and it is more difficult to obtain a good fitting to the model. Absolute counts ranging between 8.4×10^4 and 1.3×10^6 are observed, causing any misfit to have a much larger influence on the goodness-of-fit parameters. Overall, this fact is reflected in poorer agreement indices than those of neutron or laboratory X-ray refinements [275,276,277]. The model used to fit the experimental data was also that obtained in the neutron diffraction study of $CoGe_{1.5}Te_{1.5}$ [246]. Rietveld refinement plots of both datasets for each of the five compounds under study are shown (Figure 3-23 to Figure 3-27) as well as the tabulated crystallographic information extracted from them (Table 3-8 and Table 3-9).

All the samples contain small amounts of impurities ranging between 0.7 and 5.3 weight %, except $RhSn_{1.5}Te_{1.5}$, which shows a large content of $RhTe_2$, *i.e.* 14% (Table 3-8). This can be linked to the electrical resistivity anomaly observed for this compound (section 3.7).

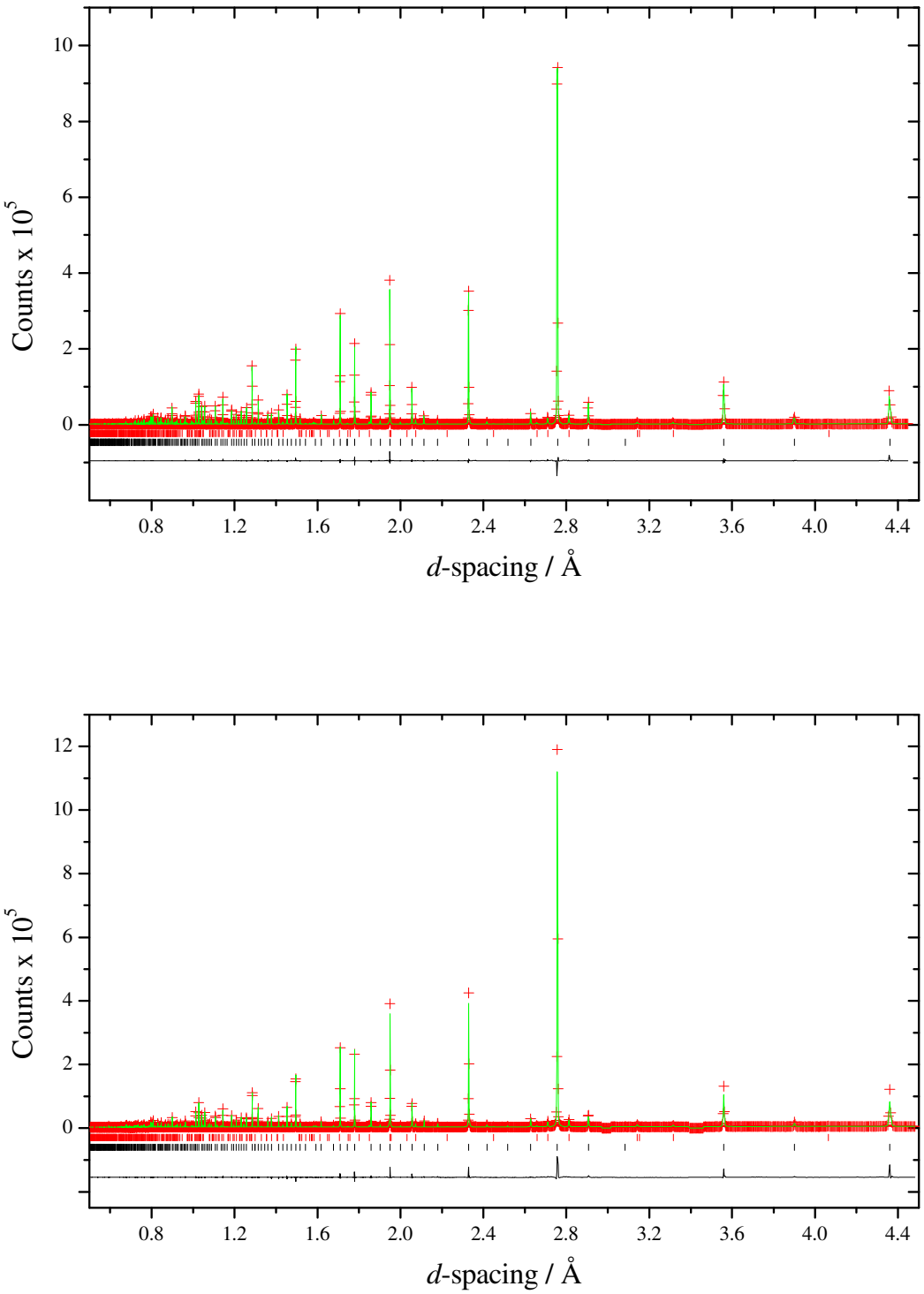

Figure 3-23 Synchrotron X-ray powder neutron diffraction pattern of $CoGe_{1.5}Te_{1.5}$ at 300 K. Top: normal scattering $\lambda = 0.42704(2)$ Å. Bottom: anomalous scattering near the Te K-edge, $\lambda = 0.38970(6)$ Å . GeTe and GeO_2 main reflections have been excluded for clarity. Key: experimental data (red crosses), fitted model (green line), difference curve (black line). Reflections positions are shown as markers: the black and red markers correspond to $CoGe_{1.5}Te_{1.5}$ ($R\bar{3}$), and $CoTe_2$, respectively.

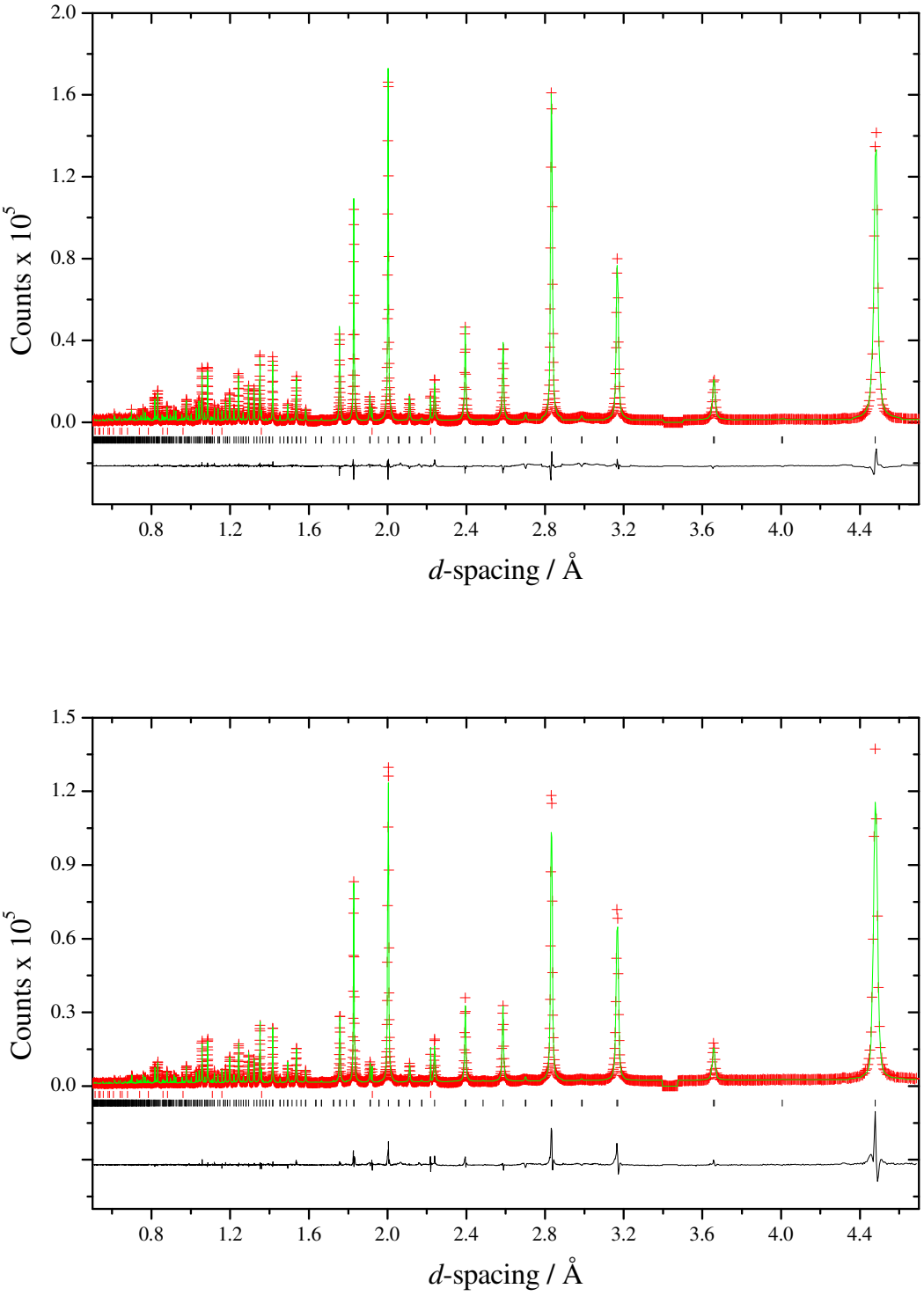

Figure 3-24 Synchrotron X-ray powder neutron diffraction pattern of $IrGe_{1.5}Te_{1.5}$ at 300 K. Top: normal scattering $\lambda = 0.42704(2)$ Å. Bottom: anomalous scattering near the Te K-edge, $\lambda = 0.38970(6)$ Å . GeO_2 main reflection has been excluded for clarity. Key: experimental data (red crosses), fitted model (green line), difference curve (black line). Reflections positions are shown as markers: the black and red markers correspond to $IrGe_{1.5}Te_{1.5}$ ($R\bar{3}$), and Ir, respectively.

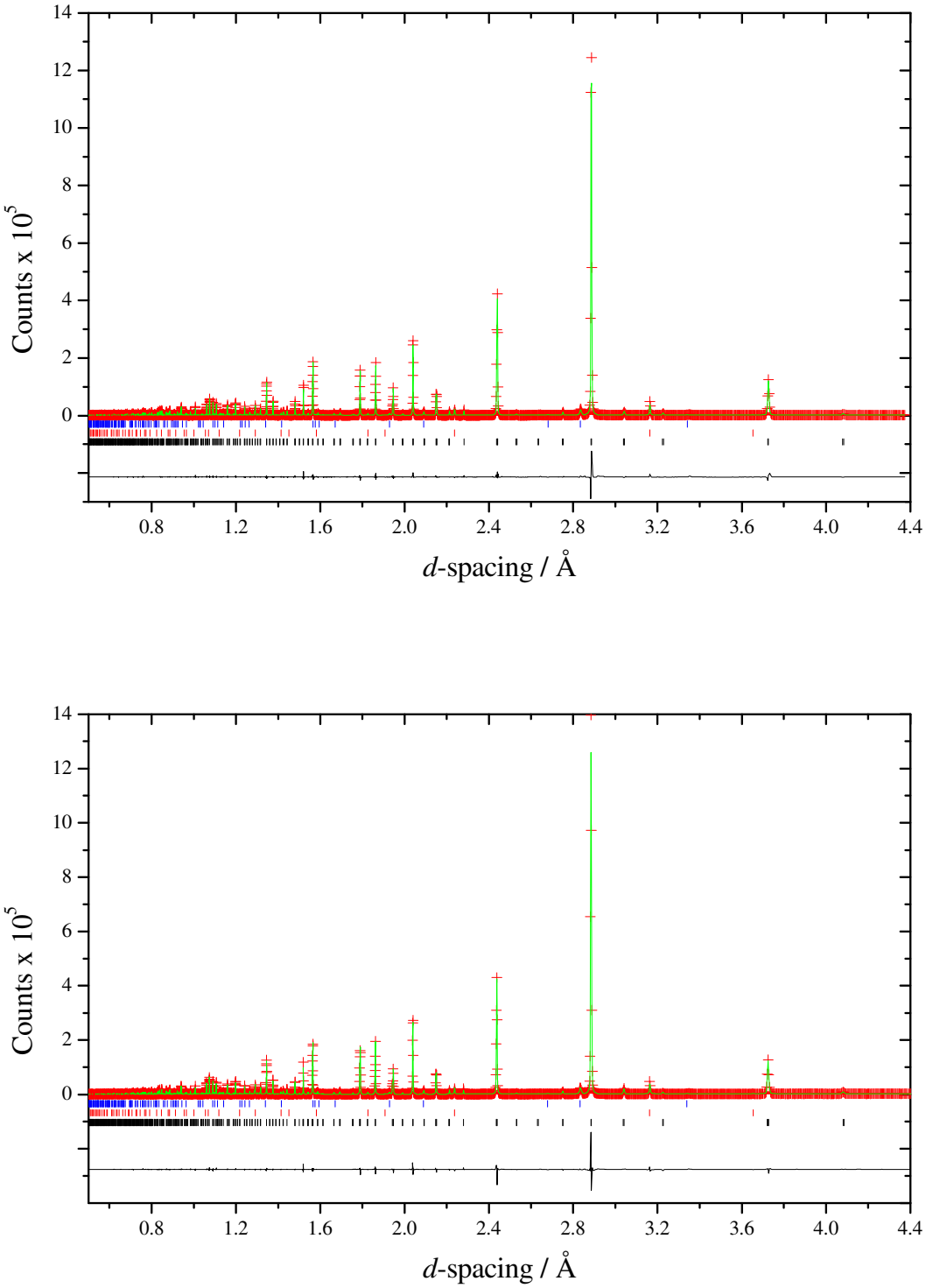

Figure 3-25 Synchrotron X-ray powder neutron diffraction pattern of $CoSn_{1.5}Te_{1.5}$ at 300 K. Top: normal scattering $\lambda = 0.42704(2)$ Å. Bottom: anomalous scattering near the Sn K-edge, $\lambda = 0.4249(1)$ Å . Key: experimental data (red crosses), fitted model (green line), difference curve (black line). Reflections positions are shown as markers: the black, red and blue markers correspond to $CoSn_{1.5}Te_{1.5}$ ($R\bar{3}$), SnTe and $Co_{0.63}Te$, respectively.

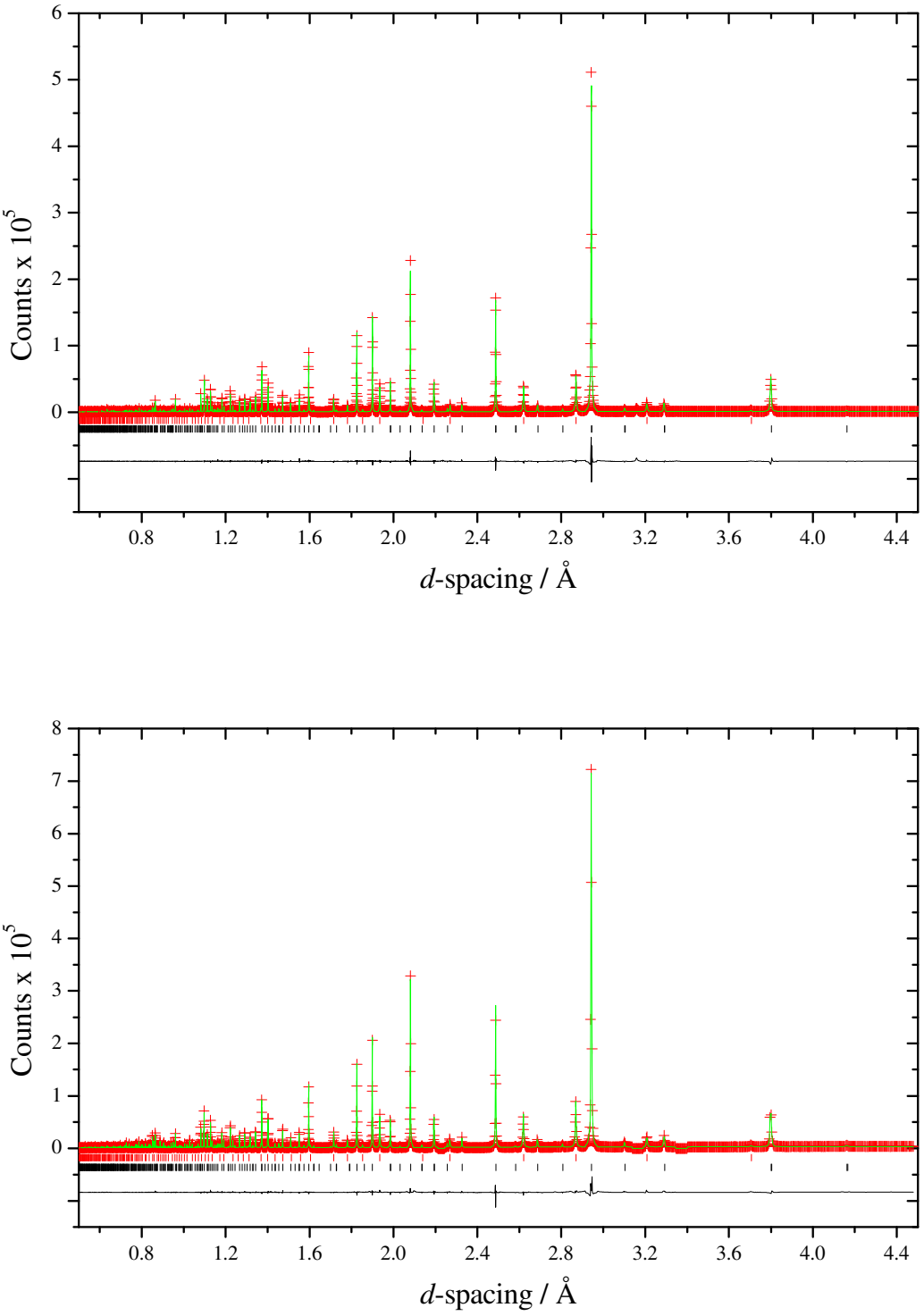

Figure 3-26 Synchrotron X-ray powder neutron diffraction pattern of $RhSn_{1.5}Te_{1.5}$ at 300 K. Top: normal scattering $\lambda = 0.42704(2)$ Å. Bottom: anomalous scattering near the Sn K-edge, $\lambda = 0.4249(1)$ Å . SnTe and SnO_2 main reflections have been excluded for clarity. Key: experimental data (red crosses), fitted model (green line), difference curve (black line). Reflections positions are shown as markers: the black and red markers correspond to $RhSn_{1.5}Te_{1.5}$ ($R\bar{3}$) and $RhTe_2$, respectively.

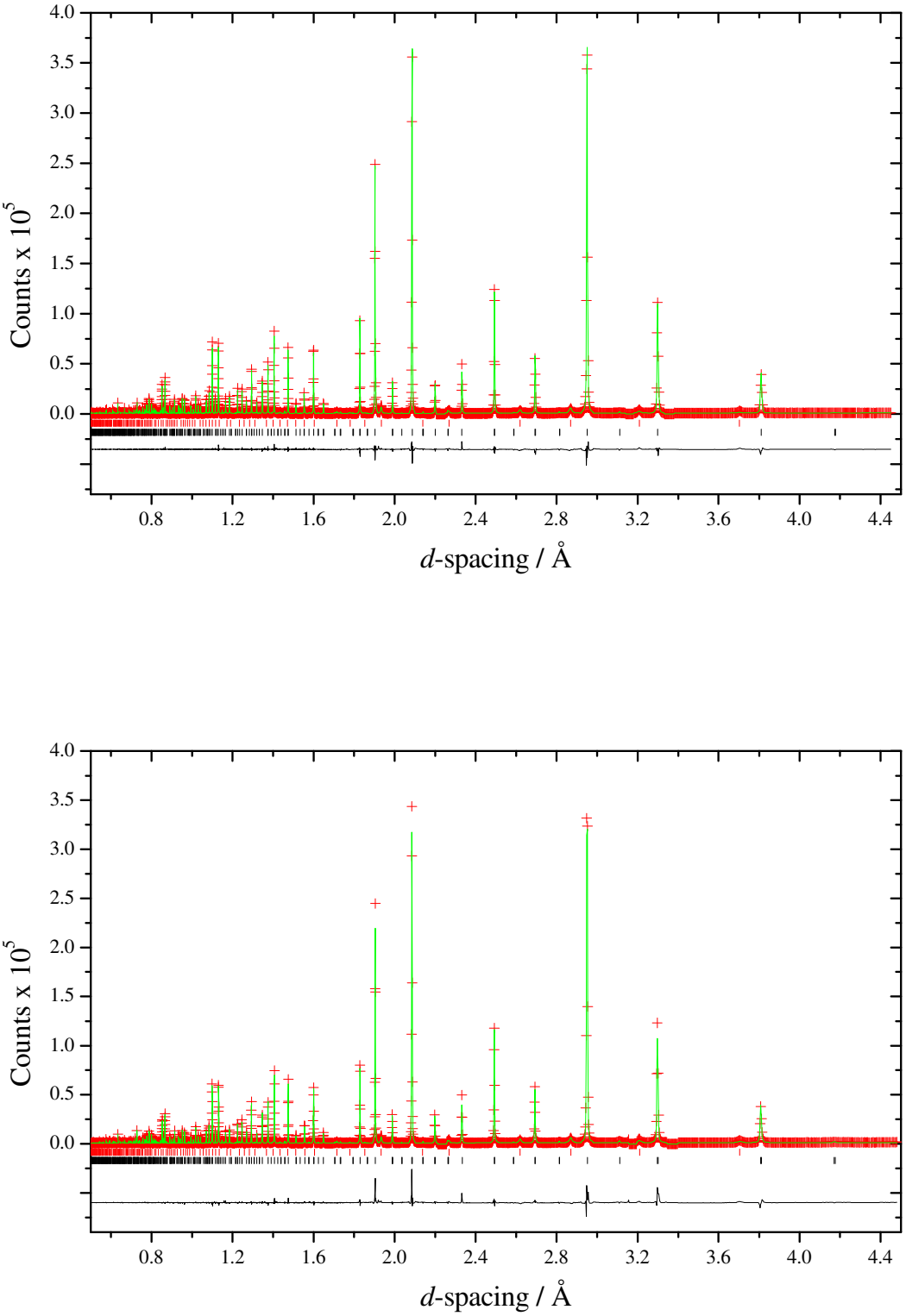

Figure 3-27 Synchrotron X-ray powder neutron diffraction pattern of $IrSn_{1.5}Te_{1.5}$ at 300 K. Top: normal scattering λ = 0.42704(2) Å. Bottom: anomalous scattering near the Sn K-edge, λ = 0.4249(1) Å . SnTe main reflections have been excluded for clarity. Key: experimental data (red crosses), fitted model (green line), difference curve (black line). Reflections positions are shown as markers: the black and red markers correspond to $IrSn_{1.5}Te_{1.5}$ ($R\bar{3}$) and Ir_3Te_8, respectively.

Table 3-8 Refined parameters for the ordered skutterudites $MGe_{1.5}Te_{1.5}$ and $MSn_{1.5}Te_{1.5}$ (M = Co, Rh and Ir), space group $R\bar{3}$ (hexagonal setting).

		$CoGe_{1.5}Te_{1.5}$	$IrGe_{1.5}Te_{1.5}$	$CoSn_{1.5}Te_{1.5}$	$RhSn_{1.5}Te_{1.5}$	$IrSn_{1.5}Te_{1.5}$
***a* (Å)**		12.33274(2)	12.6636(1)	12.90940(2)	13.16479(4)	13.19288(4)
***c* (Å)**		15.10425(5)	15.5194(3)	15.78619(4)	16.1268(1)	16.16815(8)
a_R (Å)		8.72052(2)	8.8029(2)	9.12361(3)	9.30955(6)	9.33075(5)
α (°)		90.0005(2)	88.968(1)	90.0593(1)	89.9922(3)	89.9758(3)
M(1) 6*c*	*z*	0.2460(8)	0.2531(5)	0.2520(3)	0.2511(4)	0.2505(3)
	B[a] /Å^2	0.247(9)	0.376(6)	0.22(1)	0.323(7)	0.287(4)
M(2) 18*f*	*x*	0.6680(8)	0.6664(7)	0.6679(5)	0.6691(4)	0.6664(3)
	y	0.8329(5)	0.8338(3)	0.8358(3)	0.8352(2)	0.8334(2)
	z	0.5813(3)	0.5853(2)	0.5872(1)	0.5854(2)	0.5845(1)
	B/Å^2	0.247(9)	0.376(6)	0.22(1)	0.323(7)	0.287(4)
Ge/Sn(1) 18*f*	SOF Ge/Sn	0.880(2)	0.341(7)	0.849(5)	0.817(7)	0.699(13)
	SOF Te	0.120(2)	0.659(7)	0.151(5)	0.183(7)	0.301(13)
	x	0.8357(3)	0.8366(7)	0.8373(2)	0.8379(5)	0.8364(5)
	y	0.9934(2)	0.0232(5)	0.9977(1)	0.0036(5)	0.0071(4)
	z	0.1608(2)	0.1649(5)	0.1605(1)	0.1597(3)	0.1625(3)
	B/Å^2	0.591(3)	0.67(1)	0.588(4)	0.600(5)	0.681(6)
Ge/Sn(2) 18*f*	SOF Ge/Sn	0.880(2)	0.341(7)	0.849(5)	0.817(7)	0.699(13)
	SOF Te	0.120(2)	0.659(7)	0.151(5)	0.183(7)	0.301(13)
	x	0.9452(2)	0.9338(5)	0.9475(2)	0.9440(4)	0.9436(4)
	y	0.2157(4)	0.2140(7)	0.2169(2)	0.2169(5)	0.2137(4)
	z	0.5562(1)	0.5652(2)	0.55284(8)	0.5556(3)	0.5563(2)
	B/Å^2	0.591(3)	0.67(1)	0.588(4)	0.600(5)	0.681(6)
Te(1) 18*f*	SOF Ge/Sn	0.120(2)	0.659(7)	0.151(5)	0.183(7)	0.301(13)
	SOF Te	0.880(2)	0.341(7)	0.849(5)	0.817(7)	0.699(13)
	x	0.9345(2)	0.9451(5)	0.9380(1)	0.9358(4)	0.9358(4)
	y	0.2138(3)	0.2148(6)	0.2167(2)	0.2162(4)	0.2155(4)
	z	0.0655(1)	0.0557(3)	0.06207(6)	0.0647(2)	0.0647(2)
	B/Å^2	0.591(3)	0.67(1)	0.588(4)	0.600(5)	0.681(6)
Te(2) 18*f*	SOF Ge/Sn	0.120(2)	0.659(7)	0.151(5)	0.183(7)	0.301(13)
	SOF Te	0.880(2)	0.341(7)	0.849(5)	0.817(7)	0.699(13)
	x	0.8383(2)	0.8360(9)	0.8375(1)	0.8360(4)	0.8362(4)
	y	0.0176(2)	0.0148(6)	0.0118(1)	0.0153(3)	0.0136(4)
	z	0.6656(2)	0.6625(5)	0.66621(8)	0.6665(3)	0.6648(3)
	B/Å^2	0.591(3)	0.67(1)	0.588(4)	0.600(5)	0.681(6)
Weight percentage (%)		4.44(3) $CoTe_2$	0.82(2) Ir	2.23(3) SnTe 2.8(5) $Co_{0.63}Te$	14.28(4) $RhTe_2$	5.29(4) Ir_3Te_8
R_{wp} (%)	H1	6.9	8.9	8.3	8.8	10.3
R_F^2 (%)	H1	3.3	6.5	3.5	4.5	5.5
R_{wp} (%)	H2	5.1	6.8	7.6	7.1	8.5
R_F^2 (%)	H2	7.0	6.7	5.7	4.8	5.3

[a] Cation and anion atomic displacement parameters have been constrained to the same value.

Table 3-9 Relevant bond distances (Å) and angles (°) for the ternary skutterudites $MGe_{1.5}Te_{1.5}$ and $MSn_{1.5}Te_{1.5}$ (M = Co, Rh and Ir).

	$CoGe_{1.5}Te_{1.5}$	$IrGe_{1.5}Te_{1.5}$	$CoSn_{1.5}Te_{1.5}$	$RhSn_{1.5}Te_{1.5}$	$IrSn_{1.5}Te_{1.5}$	
M(1)-α*	2.367(7)	2.617(7)	2.537(3)	2.614(6)	2.626(6)	x 3
M(1)-Te(2)	2.499(7)	2.540(9)	2.532(3)	2.627(5)	2.640(5)	x 3
α-M(1)-α	93.2(4)	95.15(28)	90.8(2)	91.28(22)	93.43(19)	x 3
α-M(1)-Te(2)	90.88(8)	85.96(19)	88.97(4)	88.02(14)	86.70(14)	x 3
	82.10(9)	83.09(21)	83.86(4)	83.93(14)	84.37(15)	x 3
Te(2)-M(1)-Te(2)	94.10(34)	95.82(30)	96.34(14)	96.69(21)	95.50(18)	x 3
M(2)-α	2.335(6)	2.631(8)	2.535(5)	2.604(7)	2.610(6)	
M(2)-β**	2.378(5)	2.581(8)	2.525(4)	2.578(6)	2.595(5)	
	2.399(6)	2.581(6)	2.540(3)	2.592(5)	2.603(4)	
M(2)-Te(1)	2.520(6)	2.460(7)	2.558(4)	2.638(5)	2.649(4)	
	2.517(5)	2.457(8)	2.535(3)	2.652(6)	2.649(5)	
M(2)-Te(2)	2.537(5)	2.526(9)	2.556(4)	2.636(5)	2.651(5)	
α-M(2)-β	90.02(11)	82.37(20)	86.27(8)	85.96(16)	85.97(13)	
	87.48(12)	84.09(19)	86.45(9)	86.70(17)	87.19(16)	
α-M(2)-Te(1)	96.75(29)	97.45(29)	95.26(16)	94.95(16)	96.03(15)	
	89.57(23)	90.92(23)	90.81(19)	91.45(18)	93.57(17)	
β-M(2)-β	94.02(28)	94.75(29)	90.68(16)	92.86(18)	91.72(16)	
β-M(2)-Te(1)	88.13(12)	88.08(21)	87.87(22)	87.96(17)	87.97(14)	
	83.53(12)	83.92(18)	85.49(21)	82.76(18)	83.95(14)	
β-M(2)-Te(2)	92.00(26)	95.11(25)	96.31(20)	97.79(18)	95.39(17)	
	96.39(25)	95.43(30)	91.85(15)	93.19(17)	92.06(15)	
Te(1)-M(2)-Te(1)	94.34(25)	93.22(27)	96.97(16)	96.48(16)	96.37(16)	
Te(1)-M(2)-Te(2)	83.56(11)	84.80(19)	86.47(9)	85.13(15)	84.74(15)	
	84.02(9)	89.85(22)	86.45(7)	84.81(14)	85.01(13)	
Te(1)-α	2.763(4)	2.705(10)	2.901(2)	2.869(6)	2.859(6)	
	2.942(4)	2.898(10)	3.087(3)	3.069(6)	3.009(6)	
Te(1)-α-Te(1)	81.99(9)	98.04(13)	84.98(5)	85.56(19)	87.10(14)	
Te(2)-β	2.685(4)	2.656(9)	2.910(2)	2.913(6)	2.884(6)	
	2.866(4)	2.805(9)	3.078(3)	3.032(6)	3.092(6)	
Te(2)-β-Te(2)	84.60(9)	90.58(16)	85.15(5)	85.08(18)	85.96(13)	
Tilt angle (ϕ)	32.8	38.0	32.0	33.4	33.7	

*** α = Ge/Sn(1)**

****β = Ge/Sn(2)**

$IrGe_{1.5}Te_{1.5}$ shows a small amount of unreacted iridium, which could be included in the refinement because there were a sufficient number of well-defined reflections. The main reflections of trace impurities such as SnTe, SnO_2 and GeO_2 located at 3.16 Å, 3.35 Å and 3.42 Å, respectively, have also been excluded from the refinements, as the presence of one or two small and broad reflections made their quantification unreliable and the refinement more unstable.

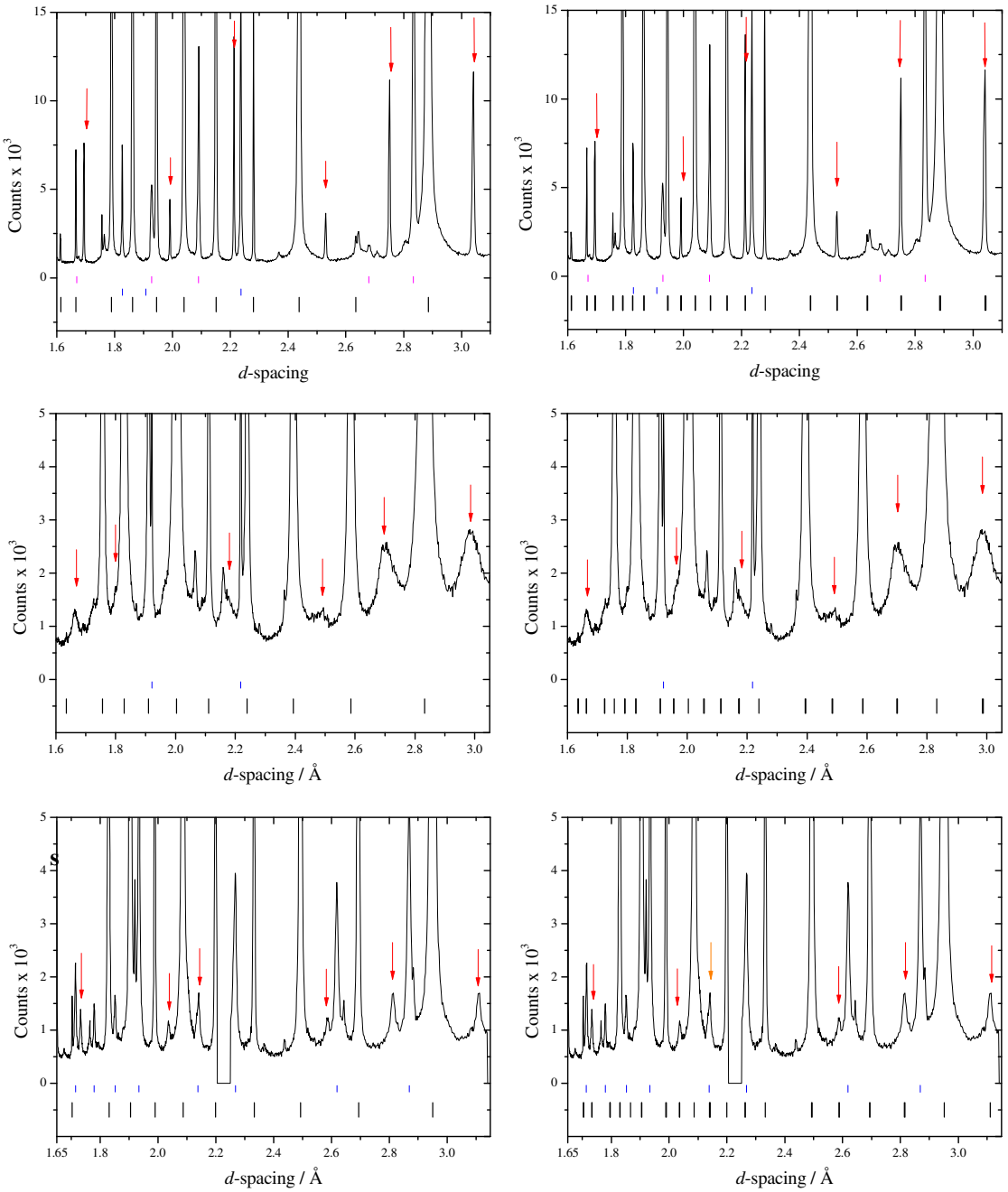

Figure 3-28 Left: $CoSn_{1.5}Te_{1.5}$ (top), $IrGe_{1.5}Te_{1.5}$ (middle) and $IrSn_{1.5}Te_{1.5}$ (bottom) synchrotron datasets along with *Im* $\bar{3}$ reflections. Right: Same data along with *R* $\bar{3}$ reflections. *R* $\bar{3}$ reflections are marked in both datasets with red arrows. Key: Experimental data (black line), skutterudite reflections (black markers), impurity reflections (either blue or pink markers).

As it was also observed during the course of the neutron data refinement, the atomic displacement parameters of the germanium/tin atoms was noticeably smaller than those of the tellurium atoms. This fact suggested the presence of some degree of disorder present in the anion 18*f* Wyckoff position. The disorder was modelled analogously to the neutron data, namely, allowing the exchange of both anion types in each of the four 18*f* sites, while keeping the site occupancy constant and equal to unity. The improvement in the goodness-of-fit parameters was much larger, *i.e*. between 1% and 2%, and it is, therefore, reflected in a larger disorder compared to that observed in the sulphides (Table 3-6). Within the tellurides family, the extent of the disorder is comparable for compounds with the same cation; however, there is a clear trend of disorder increase as the cation changes down the group.

This fact may be related to different-strength covalent interactions between the cation and both anions that would allow anion disorder inasmuch as the covalency difference decreases. The difference between M-Ge/Sn and M-Te bond lengths, although small, is smaller in the rhodium and iridium compounds than in the cobalt ones (Table 3-9). The different extent of disorder observed between the cobalt and iridium sulphides can also be explained in the same way, although the rhodium compound does not follow the expected trend (Table 3-6). The disorder observed in $IrGe_{1.5}Te_{1.5}$ shows that the fraction of tellurium present in the germanium sites is larger than the fraction of germanium itself, and *vice versa*. This implies that the alternating sequence of anion layers along the [111] direction is reversed. As a result, the expected trend in the tellurium-germanium-tellurium angle is also reversed (Table 3-9), being larger than 90°, consistent with the bonding interaction of the less electronegative anion of the $[Ge_2Te_2]^{4-}$ ring (Ge 1.8 *vs*. Te 2.1) and the filled cation d orbitals suggested by Partik *et al.* [55].

Nevertheless, for $IrSn_{1.5}Te_{1.5}$ and $IrGe_{1.5}Te_{1.5}$ the SOF approaches the random distribution or complete disorder value, *i.e*. 0.5 (Table 3-8). Therefore, it is fair to question whether the rhombohedral model accounts for any extra information present in the diffraction pattern for both compounds. A close inspection of the patterns reveals the presence of extra reflections that justify the use of a rhombohedral $R\bar{3}$ model instead of the cubic $Im\bar{3}$ in all five samples (Figure 3-28). The diffraction pattern of $CoSn_{1.5}Te_{1.5}$ has been included in Figure 3-28 for comparison purposes. $CoSn_{1.5}Te_{1.5}$ presents clearly defined sharp reflections that violate the skutterudite $Im\bar{3}$ body-centred

condition, *i.e.* $h + k + l = 2n$. Therefore, the use of the rhombohedral space group $R\bar{3}$ is fully justified and a large improvement is observed in the goodness-of-fit parameters when the latter model is used (Table 3-10). In the more anion-disordered compounds $IrGe_{1.5}Te_{1.5}$ and $IrSn_{1.5}Te_{1.5}$, the same reflections can still be observed, although slightly shifted towards smaller or larger *d*-spacings, respectively owing to the small difference in the lattice parameters (Table 3-8), possessing a much smaller intensity when compared to those of $CoSn_{1.5}Te_{1.5}$. Such decrease in intensity can be linked to the degree of disorder obtained from the synchrotron diffraction datasets (Table 3-10). This may be originated by the more isotropic covalent interaction cobalt atoms are engaged in when disorder is present in the sample. On the contrary, completely ordered skutterudites give rise to a larger covalency difference between metal-anion interactions, thereby distorting the cobalt lattice to a greater extent, becoming more suitably described by a rhombohedral $R\bar{3}$ model. Further, in order to emphasize the necessity of such model, a Rietveld refinement of the synchrotron data containing two different crystallographic phases, *i.e.* cubic and rhombohedral, of the same ternary skutterudite has been performed. The results are presented in Table 3-10. The fact that the lowest percentage of rhombohedral phase is found in the ternary skutterudite with the largest disorder supports the above-mentioned statement.

Table 3-10 Rietveld goodness-of-fit R_{wp} values for the normal scattering dataset using either a rhombohedral ($R\bar{3}$) or a cubic ($Im\bar{3}$) space group. Ge/Sn(1) SOFs are included. For the compounds shown in Figure 3-28 both crystallographic phases were included in the same refinement. The weight percentage obtained for each of them is shown in the two far-right columns.

Compound	$Im\bar{3}$	$R\bar{3}$	SOF	$Im\bar{3}$ (%)	$R\bar{3}$ (%)
$CoGe_{1.5}Te_{1.5}$	26.1	6.9	0.880		
$RhSn_{1.5}Te_{1.5}$	14.1	8.8	0.817		
$CoSn_{1.5}Te_{1.5}$	21.7	7.9	0.849	9.5(3)	85.0(5)
$IrSn_{1.5}Te_{1.5}$	12.4	10.3	0.699	56.8(5)	37.5(7)
$IrGe_{1.5}Te_{1.5}$	10.2	8.0	0.659*	64.1(4)	35.0(7)

* **Te(1) SOF**

Nevertheless, the difference in peak width between the $CoSn_{1.5}Te_{1.5}$, $IrGe_{1.5}Te_{1.5}$ and $IrSn_{1.5}Te_{1.5}$ reflections that justify the use of the rhombohedral model cannot be accounted for simply on the grounds of covalency. There exist other factors affecting the peak width, namely crystallite size, lattice distortion and structural faults.

Peak broadening has its origin in two main factors, *i.e.* instrumental broadening and diffraction effects caused by the sample. The total broadening may be regarded as a convolution of both contributions. The high brightness of synchrotron radiation along with the intrinsically narrow diffraction profile effectively deconvolute the angular dependence of the peak width and leave uncovered sample diffractions effects, which can be studied. Small particle size broadens all the diffraction peaks indistinctively, whereas distortions in the lattice and structural faults can be spotted by the broadening in specific reflections, a function of the *h*, *k* and *l* values. The full width at half maximum (FWHM) has been determined for a significant number of reflections of the main skutterudite phase as well as those impurity peaks that are not overlapped. A pseudoVoigt function has been used for this purpose of the form:

$$y = y_0 + A\left[\mu\frac{2}{\pi}\frac{FWHM}{4(x-x_c)^2 + FWHM^2} + (1-\mu)\frac{\sqrt{4\ln 2}}{\sqrt{\pi}FWHM}e^{\frac{4\ln 2}{FWHM^2}(x-x_C)^2}\right] \quad \textbf{(3-8)}$$

Where y_0, A, μ, x_c and $FWHM$ are all fitting parameters. This function is a convolution of a Lorentzian and a Gaussian functions determined by the mixing factor μ. Nevertheless, when peaks are not very intense and possess large widths the function that provides a better fit is a pure Gaussian of the form:

$$y = y_0 + \frac{A}{FWHM\sqrt{\pi/2}}e^{-2\frac{(x-x_c)^2}{FWHM^2}} \quad \textbf{(3-9)}$$

Where y_0, A, x_c and $FWHM$ are also fitting parameters. Values belonging to impurity peaks have been marked in different colours in Figure (Figure 3-28). Only well-defined peaks have been analysed, whereas those too small or too overlapped have been excluded. It can be seen that the FWHM as a function of the 2θ angle follow a different dependency compared to the main skutterudite phases. Regarding the absolute values, those at low angle are higher than values at high angle without exception. This is due to axial divergence, which is known to be a major contributor to the peak width at low scattering angles, especially in high-resolution synchrotron X-ray powder patterns, where the instrumental resolution may be only a few thousandths of a degree [273]. Further, the peak widths of $CoSn_{1.5}Te_{1.5}$ and $IrSn_{1.5}Te_{1.5}$ are comparable, whereas those of $IrGe_{1.5}Te_{1.5}$ are twice as large. This can be explained in connection with the low absolute counts and the broad peaks observable by the naked eye in the diffraction pattern as a smaller particle size in $IrGe_{1.5}Te_{1.5}$.

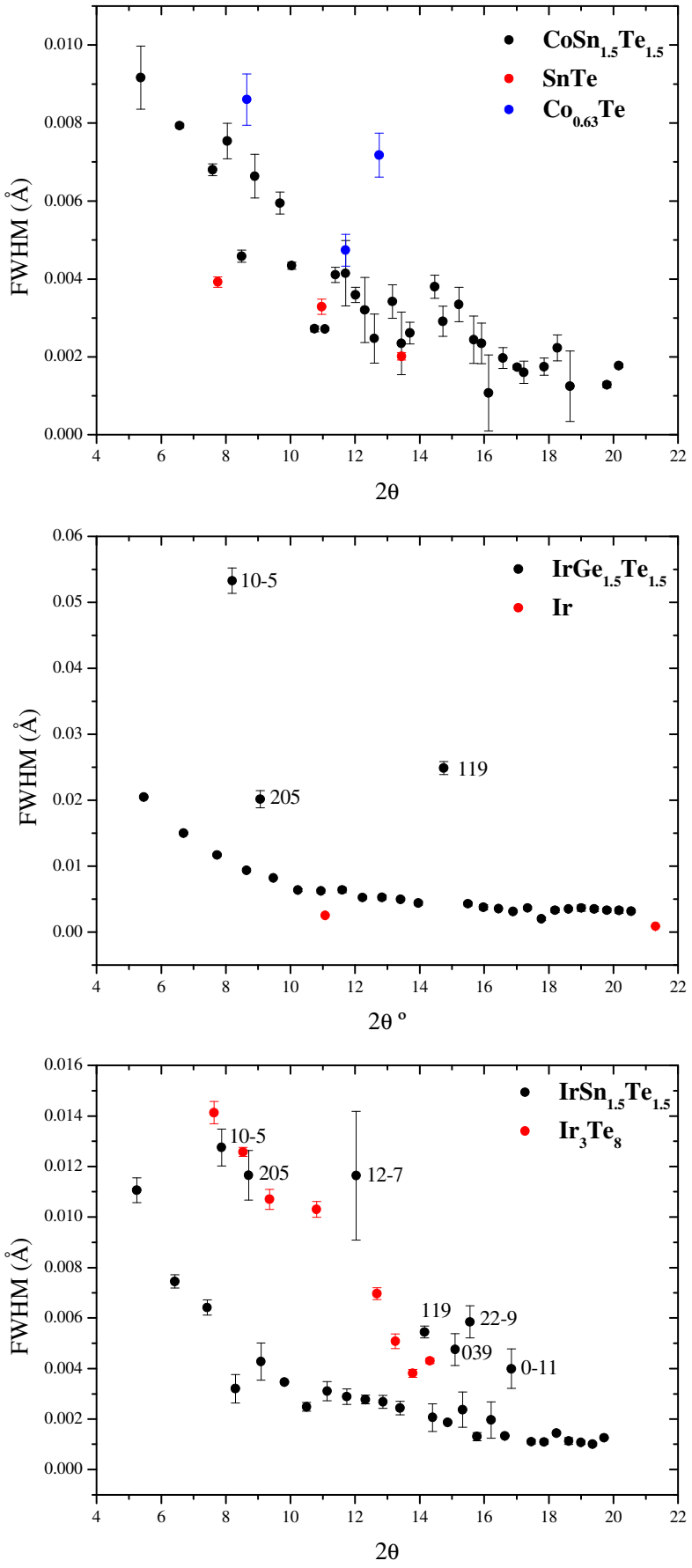

Figure 3-29 FWHM vs. 2θ for the three ternary skutterudites as well as the impurity phases shown in Figure 3-28. Error bars correspond to the fitting absolute error.

Yet, another peak broadening effect is observed in $IrGe_{1.5}Te_{1.5}$ and $IrSn_{1.5}Te_{1.5}$ that cannot be seen in $CoSn_{1.5}Te_{1.5}$, *i.e.* anisotropic broadening. Reflections fulfilling the relation *hk*5 and *hk*9 show a much larger peak width than expected. These reflections are also violating the body-centring condition and their width is related to anion ordering as it has been mentioned before. On the light of the anion mixing revealed by the SOFs, it may be argued that, instead of long-range ordering of anions with some degree of disorder, the actual situation consists of multiple ordered domains of short spatial extent. In $IrGe_{1.5}Te_{1.5}$, extra *hk*9 values cannot be shown because either they are overlapped or are too small and, therefore, difficult to distinguish from the background.

M-Te (M = Co, Rh and Ir) bond distances are comparable to those found in binary MTe_2 and MTe compounds, *i.e.* ranging between 2.5 Å and 2.7 Å, although the Ir(1)-Te distance is slightly shorter than its binary counterpart. Co-Ge and Ir-Ge distances are also within the range of other binary cobalt and iridium germanides, such as CoGe and IrGe. Likewise, M-Sn distances are similar to those of binary compounds such as MSn and MSn_2. As regards the anion rings, their behaviour as the metal changes down the group is similar to that found in the germanium sulphides. Both Te-Ge-Te and Te-Sn-Te angles increase, which can be related to the lesser metal-anion covalent interaction, owing to the larger polarizability of the metal atom (section 3.5). A decrease in the anion-anion bond distances within the rings is also observed thereof (Table 3-9). This trend can be ascribed to the link between the electron density within the anion rings and that existing between the metal and the anions. A depletion of electron density in the metal-anion bonding region will originate stronger covalent interactions in the anion-anion region, thereby shortening the anion-anion bond distances and *vice versa*. Such behaviour has already been observed in related structures, such as arsenopyrites, FeS_2 marcasite and FeS_2 pyrite [150].

Tiltwise, the skutterudite structure of the ternary tellurides also retains the ($a^+a^+a^+$) tilt system. The atomic positions are very similar to one another and, therefore, the anion ordering along the [111] direction is maintained. The octahedral tilting calculated using equation (3-5) and the averaged M-anion-M angles shows an increasing trend with cation size, as it was also observed in the ternary sulphides (section 3.5). Further, the neutron and synchrotron datasets collected on the same $CoGe_{1.5}Te_{1.5}$ sample offer an excellent opportunity to compare the results from both techniques. On the grounds of neutron scattering cross section, it is seen that neutrons is not the most indicated technique for the tin tellurides as their values differ little, *i.e.* 4.23 barn for tellurium and

4.87 barn for tin. This difference is much greater between sulphur and germanium, *i.e.* 1.02 and 8.42 barns, respectively. Thus, the difference between germanium and tellurium lies in between. The much higher collimation and intensity of the synchrotron source offers a larger precision in the determination of atom positions and lattice parameters, thereby smaller esds are obtained (Table 3-3 *vs*. Table 3-8). This allows, for instance, the refinement of both cobalt atom positions, which were fixed in the neutron dataset. In spite of the fact that the atom positions and bond distances are virtually the same in both datasets, they differ in the extent of the anion disorder. There is not a significant difference when disorder is modelled in the neutron dataset (Table 3-3), whereas an improvement of nearly 0.5% is obtained in the synchrotron source (Table 3-8). This may be attributed to the smaller correlation existing between occupancy and the atomic displacement parameters. Indeed, if the correlation matrix amongst the variables of both refinements is displayed, it is also seen that the thermal parameter constraint and the phase fraction are correlated by an 80.5% in the neutron refinement, whereas they only are by a 58.9% in the synchrotron refinement. Only pairs of variables from the correlation matrix with correlations larger than 50% are displayed.

3.7 Electrical resistivity

Rectangular-shaped ingots were cut from a cold pressed 13 mm diameter pellet and sintered for two days at synthesis temperature to minimize the grain boundary contribution to the overall resistivity. The electrical resistivity as a function of temperature was measured according to section 2.4.2 (Figure 3-30 and Figure 3-31). All the measured ternary skutterudites show a decreasing resistivity as the temperature rises, characteristic of semiconducting behaviour. The cobalt ternary skutterudites are by far the most resistive members in their respective families consistent with a larger ionic component in the bonding and lower electron mobility thereof. This ionic component originates a larger band gap, as it is indeed inferred from Arrhenius-type fits of high-temperature (up to 350 K) electrical resistivity data (Table 3-11) and agrees well with already known structure-property relations in semiconductors [278]. Should the charge to radius ratio be taken into account, *i.e.* 0.68 Å, 0.80 Å and 0.82 Å for Co^{3+}, Rh^{3+} and Ir^{3+} ionic radii in octahedral coordination respectively, the expected trend would be that of cobalt compounds being more resistive than rhodium compounds which, in turn, should be more resistive than iridium compounds. Such behaviour is followed by both the $MGe_{1.5}S_{1.5}$ and the $MGe_{1.5}Te_{1.5}$ family (M = Co, Rh, Ir), although the latter only up

to 225 K, temperature at which $IrGe_{1.5}Te_{1.5}$ is more resistive than $CoGe_{1.5}Te_{1.5}$ (Figure 3-30). As it was mentioned in the synthesis section (3.1.1), $RhGe_{1.5}Te_{1.5}$ does not form and the equiatomic phase RhGeTe is obtained instead.

$MSn_{1.5}Te_{1.5}$ compounds present and an anomaly consisting of $IrSn_{1.5}Te_{1.5}$ being more resistive than $RhSn_{1.5}Te_{1.5}$ throughout the whole temperature range. The X-ray synchrotron diffraction data of $RhSn_{1.5}Te_{1.5}$ sheds some light on the cause of such discrepancy. It reveals the existence of an impurity in a much higher proportion than other impurities found in the other ternary skutterudites under study (Table 3-8). The three orders of magnitude difference between $RhSn_{1.5}Te_{1.5}$ and $IrSn_{1.5}Te_{1.5}$ at low temperature may be explained by the existence of a less resistive impurity, namely $RhTe_2$ at a concentration of 14.3 weight percentage (Table 3-8). Considering the fact that the electrical resistivity in a sintered pellet may be affected by factors as different as grain size distribution, grain boundaries and even percolation, a simplified explanation consisting of the electric analogue of a circuit made of two resistances connected in parallel may account for such anomaly.

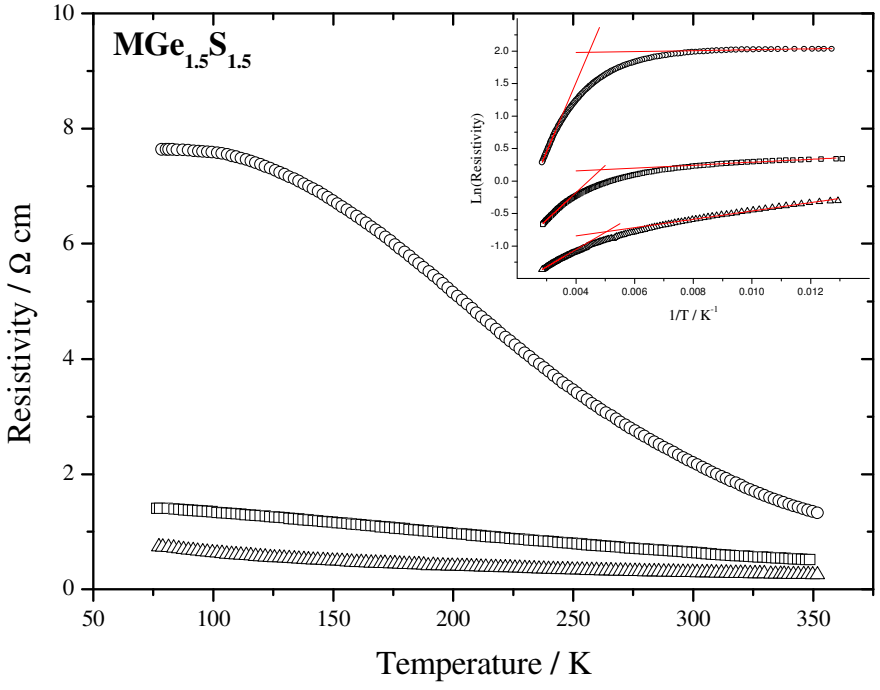

Figure 3-30 Electrical resistivity *vs*. temperature of the ternary skutterudites $MGe_{1.5}S_{1.5}$. M = Co (empty circles), Rh (empty squares) and Ir (empty triangles). Insets: Arrhenius-type fits at high and low temperature.

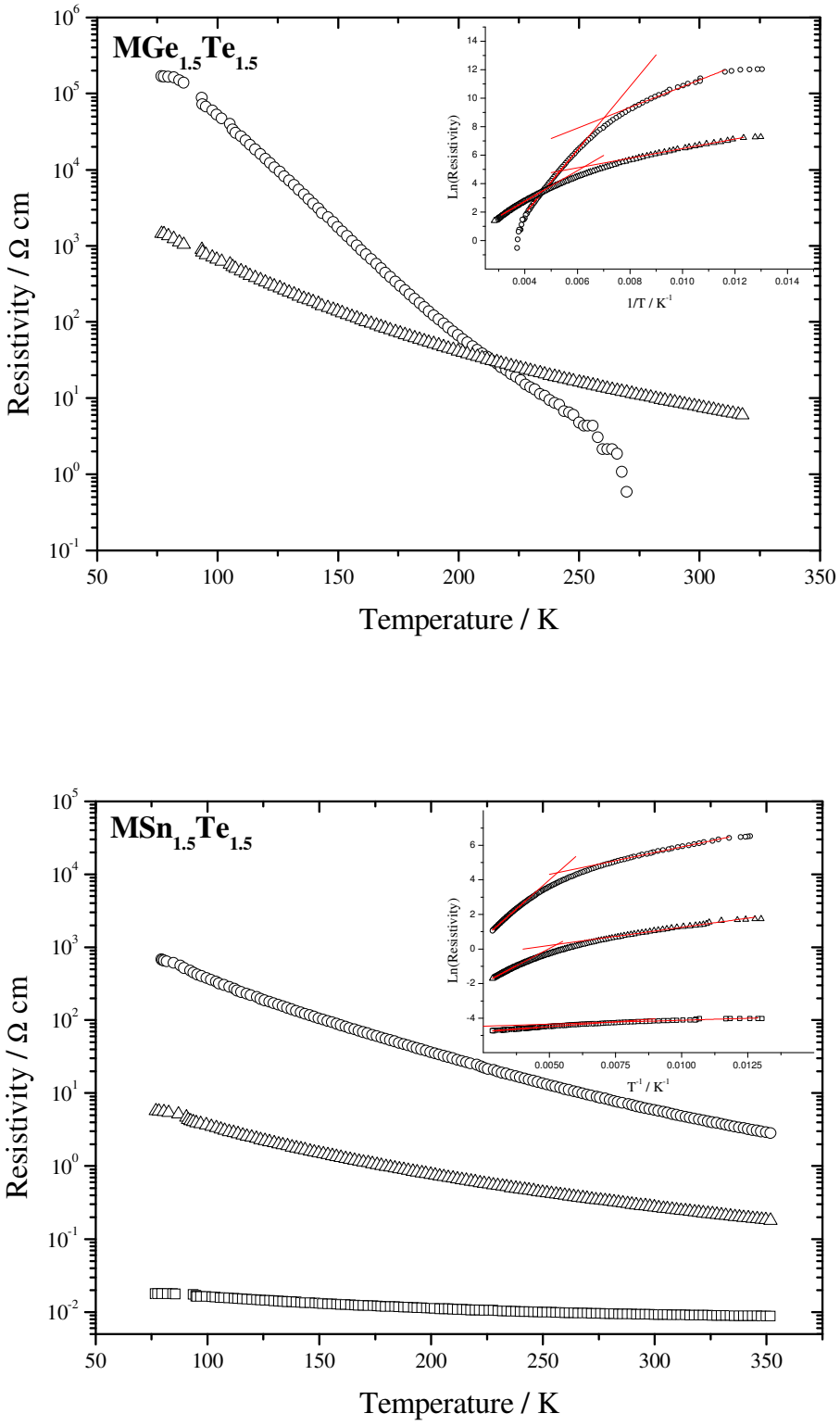

Figure 3-31 Electrical resistivity *vs*. temperature of the ternary skutterudite $MGe_{1.5}Te_{1.5}$ (top) and $MSn_{1.5}Te_{1.5}$ (bottom). M = Co (empty circles), Rh (empty squares) and Ir (empty triangles). Insets: Arrhenius-type fits at high and low temperature.

In this simple model, each resistance would correspond to one crystallographic phase and the overall resistance would be lower than that of the less resistive phase.

As regards the absolute resistivity values, the relatively low ones obtained for the $MGe_{1.5}S_{1.5}$ series (M = Co, Rh and Ir) are somewhat surprising, especially the $CoGe_{1.5}S_{1.5}$ sample. Small anions combined with larger electronegativity would give rise to scarce orbital overlapping resulting in low electron mobility and high electrical resistivity. A test measurement on a $CoGe_{1.5}S_{1.5}$ pellet before it was sintered shows values two orders of magnitude higher than those seen in Figure 3-30. Sintering was carried out in order to minimize grain boundary resistance; however, it may have decomposed the sample, giving rise to unreliable results. Another important issue involving these ternary sulphides I was not aware of by the time the measurement was done was their low stability. This implied that the time between sample preparation and sample measurement was also important to minimize spontaneous sample decomposition. As a result, this measurement could not be included in the publication on $MGe_{1.5}S_{1.5}$ skutterudites, and a more realistic value of the $CoGe_{1.5}S_{1.5}$ electrical resistivity in a sample synthesized and measured by Mr Martin Stindl was used instead [110].

The $IrGe_{1.5}S_{1.5}$ resistivity is also an order of magnitude lower than the literature value [53]. Neutron diffraction data also reveals that this sample contains a significant proportion of the impurity IrGe (Table 3-6). This fact makes the resistivity data unreliable for comparison purposes. The $RhGe_{1.5}S_{1.5}$ contains a small amount of RhS_2, less than 5 w%, which makes it the most reliable measurement among the ternary sulphides measured.

The values of the $CoGe_{1.5}Te_{1.5}$ sample agree very well with values reported by Dr Vaqueiro for a different sample of the same compound as well as with those of a sample with stoichiometry $CoGe_{1.7}Te_{1.47}$ analyzed by EPMA and reported by Navrátil *et al* [108,246]. A small amount, 4.44 w% of $CoTe_2$ (Figure 3-6), is present, which support the assumption that impurity levels below 5 w% do not affect significantly the conductivity properties. There are no previously reported values of the $IrGe_{1.5}Te_{1.5}$ resistivity. This sample possesses a small amount of unreacted iridium, which indicates that this measurement can be considered reliable.

For $CoSn_{1.5}Te_{1.5}$ there exists a reported value of the resistivity which, at room temperature, is one order of magnitude lower, *i.e.* 0.33 Ωcm [109]. The $CoSn_{1.5}Te_{1.5}$ sample measured has the highest resistivity of the tin telluride family. It also has a small amount of SnTe (2.4 w%) and $Co_{0.63}Te$ (3.19 w%), which, in principle, should not bias

significantly the measured resistivity, according to the evidence seen in $CoGe_{1.5}Te_{1.5}$. Therefore, this measurement is not regarded unreliable. the resistivity *vs*. temperature plot has also been fitted to two Arrhenius-type laws, although over a higher temperature range (300-800 K) (Figure 3-31) [109]. It is worth mentioning that the experimental density in all the measured pellets was rather low (~ 70 % theoretical density) and this is expected to give a high-biased value of the electrical resistivity, which may account for the high values obtained for $CoSn_{1.5}Te_{1.5}$. Other factors such as crystallinity, non-stoichiometry or impurities are also known to have a considerable influence on the electronic properties of a solid [279,280]. Comparing band gap values obtained with electrical resistivity measurements up to 350 K with those already reported [50], it is evident that extrinsic conduction is still occurring at this temperature.

The rhodium compound $RhSn_{1.5}Te_{1.5}$, however, has a very significant $RhTe_2$ impurity (14.3 w%), which eliminates the possibility of using the data for comparison purposes. Therefore, the fact that its resistivity is lower than that of $IrSn_{1.5}Te_{1.5}$ cannot be considered a genuine effect.

Finally, a resistivity measurement of $IrSn_{1.5}Te_{1.5}$ was reported during the course of this work, which was an order of magnitude lower than that shown in this thesis [57]. Bos *et al.* report an impurity Ir_3Te_8 concentration of 2 w% by means of laboratory X-ray data Rietveld analysis, whereas the same impurity is found at a concentration of 5.3 w% by means of synchrotron X-ray data. *A priori*, the sample with lower impurity is of better quality, however the determination of the impurity concentration is much more accurate using a highly collimated synchrotron source in terms of signal-to-noise ratio than laboratory X-rays. Further, it is also expected that low-density pellets originate larger values of the resistivity, as it has been seen in the $CoSn_{1.5}Te_{1.5}$ sample.

The observed two-slope resistivity *vs*. temperature plots are characteristic of semiconductors whose conduction mechanism is dominated by impurities at low temperatures (section 5.4), known as impurity semiconductors. In these systems, electrons occupying localized donor / acceptor levels also contribute to the overall electrical conductivity in a different way to the usual process of thermal excitation in normal intrinsic semiconductors. Depending on how localized the impurity states are, two possible conduction mechanisms at low temperature arise [280,281]:

- *Impurity band conduction*: in which there exists some degree of overlapping between electron wave functions in adjacent sites. Charge transport occurs then by tunneling.
- *Impurity hopping conduction:* in which electrons are more localized and there exists a potential barrier between adjacent sites. Charge transport occurs then by multiphonon excitation of the localized electrons over the potential barrier.

The pictorial view of this type of materials is drawn in Figure 3-32. Non-localized states are found above the conduction band edge, E_c, and below the valence band edge, E_v. Below E_c and above E_v there are more or less localized impurity states. As the temperature rises, the impurity levels (either donors or acceptors) become exhausted and the intrinsic regime takes over as the main conduction mechanism. At high temperature, the charge carriers are excited beyond the low-mobility impurity states into non-localized conduction bands, whereas at low temperature, these carriers do not possess enough energy to be excited into the conduction band, and conductivity takes place via tunneling or hopping around the Fermi level, depending on the width of the impurity levels [282]. A similar behaviour, *i.e*. two-slope lnρ vs. 1/T plot, has been observed in other narrow band gap semiconductors within this thesis (section 5.4) and also in the binary skutterudite $CoSb_3$ [283].

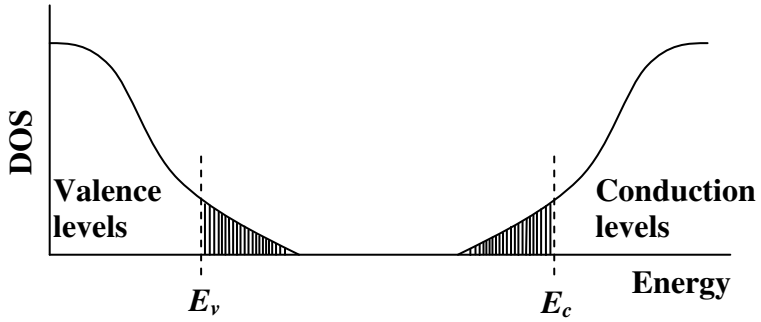

Figure 3-32 Density of states for an insulator with disordered structure. Shaded portions correspond to localized states. Extracted from reference [284].

The activation energies extracted from the Arrhenius-type fits to both the high and low temperature regions are shown in Table 3-11. The low temperature values represent the activation energy of extrinsic electrons, whereas those at high temperature indicate the activation energy of the charge carriers over the intrinsic energy gap. In Table 3-11, high temperature values are comparable to those of other ternary skutterudites found in the literature such as $IrGe_{1.5}S_{1.5}$ (110 meV) [53], $IrGe_{1.5}Se_{1.5}$ (76 meV) [53] and $CoGe_{1.5}Se_{1.5}$ (170 meV) [107] over comparable temperature ranges. The $CoGe_{1.5}Te_{1.5}$

activation energy determined by Dr Vaqueiro on one of her samples (160(10) meV) is comparable to the value obtained within this work [246]. The discrepancy found for $IrGe_{1.5}S_{1.5}$ is most likely due to sample degradation problems as it was pointed out earlier on, in spite of the fact that the literature author himself emphasizes that the intrinsic region has not been reached and measurements at high temperature are still necessary [53].

Additionally, materials possessing narrow band gaps in the vicinity of the Fermi energy are prone to electron-phonon coupling. Such interaction originates lattice distortions that move with electrons in the crystal lattice originating a mobility drop at low temperature [285]. The two-slope resistivity logarithm *vs*. inverse temperature plot (insets in Figure 3-30 and Figure 3-31) is also characteristic of systems with strong electron-phonon coupling in which transport at low temperature occurs by means of thermally activated jumps of polarons (instead of charge carriers) from site to site [286]. In the hopping process, the nearest-neighbour hopping probability is proportional to exp (a+b/T); whereas if available sites are randomly distributed, electrons hop a much larger distance the probability is proportional to exp(c/$T^{1/4}$) instead [287]. The conduction process at low temperature is then dominated by a variable-range-hopping (VRH) mechanism expressed by the equation [288]:

$$\rho = \rho_0 \left(\frac{T}{T_0} \right)^{\frac{1}{2}} \exp\left[\left(\frac{T_0}{T} \right)^{\upsilon} \right] \qquad \textbf{(3-10)}$$

Where the exponent υ is $\frac{1}{4}$ for a three dimensional conduction and $\frac{1}{3}$ for a two-dimensional conduction. Mott indicated that materials which are intrinsic semiconductors like the chalcogenide glasses, the valence and conduction bands will exist with a range of weakly localized states at the bottom, along with a tail of strongly localized states due to structural defects, which originate the impurity conduction mechanism at low temperature [289]. The problem of calculating the hopping probability between centres taking into account the random distribution of centres was solved by Miller and Abrahams [290]. Mott intuitively modified their work and applied such probability to describe the conductivity mechanism of the above-mentioned materials. Mott notes that only electrons with energies in the same order of magnitude than k_BT below the Fermi energy have a significant probability of hopping. Moreover, the following assumptions are made:

- The Fermi energy lies in the hopping region, *i.e*. close to the localized states.
- k_BT is small compared with the band width and with E_F
- The states are strongly localized

Mott describes the jump frequency and therefore the conductivity behaving like [289]:

$$\ln \rho = A + B / T^{1/4} \qquad \textbf{(3-11)}$$

Which is the simplified notation of the above VRH equation. Such conduction mechanism is found in glasses containing transition metal ions as well as in semiconductors whose electrical conductivity at low temperatures is mainly determined by impurities, given the strong localization of the density of states at the impurity levels, as it has been pointed out by Mott [287,291]. In the former case, transition metal ions are randomly located across the amorphous glass matrix. In the latter case, impurities, which may originate from secondary phases forming a solid solution with the main phase, defects in the crystal structure or vacancies due to small variations in the chemical composition, are also randomly distributed across the semiconducting bulk phase. Hence, VRH is expected in impurity semiconductors at low temperatures as it has experimentally been observed in several metal oxides [292], the MGeTe narrow band gap materials studied in chapter 5 and also in the doped skutterudites $Co_{1-x}Ni_xSb_3$ [103]. Moreover, a VRH mechanism has been previously used to describe the conduction process at low temperature in the lightly doped ternary skutterudite $CoGe_{1.5}Se_{1.5}$ [293].

Table 3-11 Columns 2 and 3: Activation energies obtained from Arrhenius-type fittings at high and low temperature, respectively for the synthesized ternary skutterudites. Column 4: fitting range for the low-temperature Arrhenius fitting. Columns 5 to 7: Parameters extracted from variable-range-hopping fits.

Compound	High temp E_a / meV	Low temp E_a / meV	Low temp Fitting range / K	T_0 / x 10^5 K	ρ_0 / Ωcm	VRH Fitting range / K
$CoGe_{1.5}S_{1.5}$	91.4(5)	0.60(7)	79-125	0.45(4)	3.8(2)	79-140
$RhGe_{1.5}S_{1.5}$	36.2(4)	1.93(8)	81-130	0.11(4)	0.54(3)	81-146
$IrGe_{1.5}S_{1.5}$	22.9(2)	5.53(9)	77-160	0.63(6)	0.11(3)	77-232
$CoGe_{1.5}Te_{1.5}$	192(2)	63(2)	84-125	720(40)	9(4) x 10^{-6}	84-113
$IrGe_{1.5}Te_{1.5}$	92.9(8)	29.1(5)	81-125	89(2)	5.7(8) x 10^{-3}	81-147
$CoSn_{1.5}Te_{1.5}$	116.2(7)	27.4(4)	85-130	54(2)	2.1(2) x 10^{-2}	85-170
$RhSn_{1.5}Te_{1.5}$	9.88(6)	3.9(2)	86-240	0.490(6)	3.34(4) x 10^{-3}	86-340
$IrSn_{1.5}Te_{1.5}$	68.9(4)	18.3(4)	87-140	16.8(4)	5.4(4) x 10^{-3}	87-182

Nevertheless, with the present data, other low-mobility conduction mechanisms, such as polaron conduction, cannot be discarded [281]. Hopping conduction (variable or not) may be linked to the size of the band gap. As the temperature increases, the Fermi level moves away from the conduction band towards the gap centre. This shift seems to grow larger insofar as the size of the band gap does so. Hopping conduction ceases when the Fermi level moves far away enough from the impurity levels and the hopping activation energy becomes too large. Other conduction mechanisms are then expected to take over. Conversely, the smaller the band gap, the longer conduction electrons remain close to Fermi energy; whereby lingering the VRH process throughout a larger temperature range. The activation energy obtained at low temperatures (Table 3-11) is commonly associated with the charge carrier hopping activation energy and its absolute value is related to the width of the localized states through which the hopping process takes place [287].

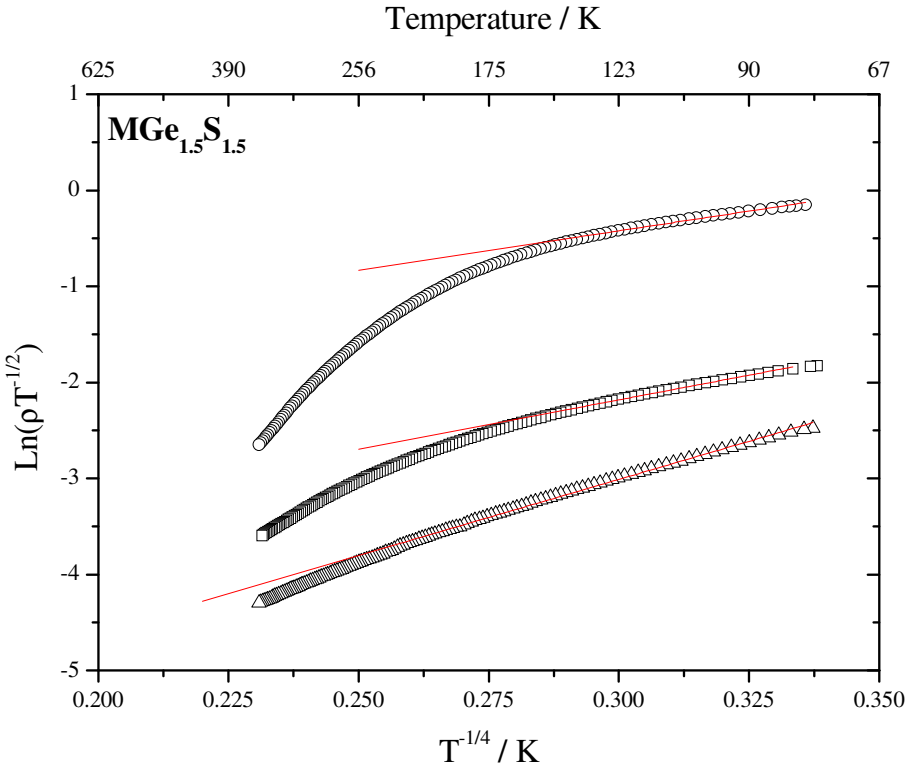

Figure 3-33 Variable-range-hopping fits to electrical resistivity data of the ternary skutterudites $MGe_{1.5}S_{1.5}$. M = Co (empty circles), Rh (empty squares) and Ir (empty circles).

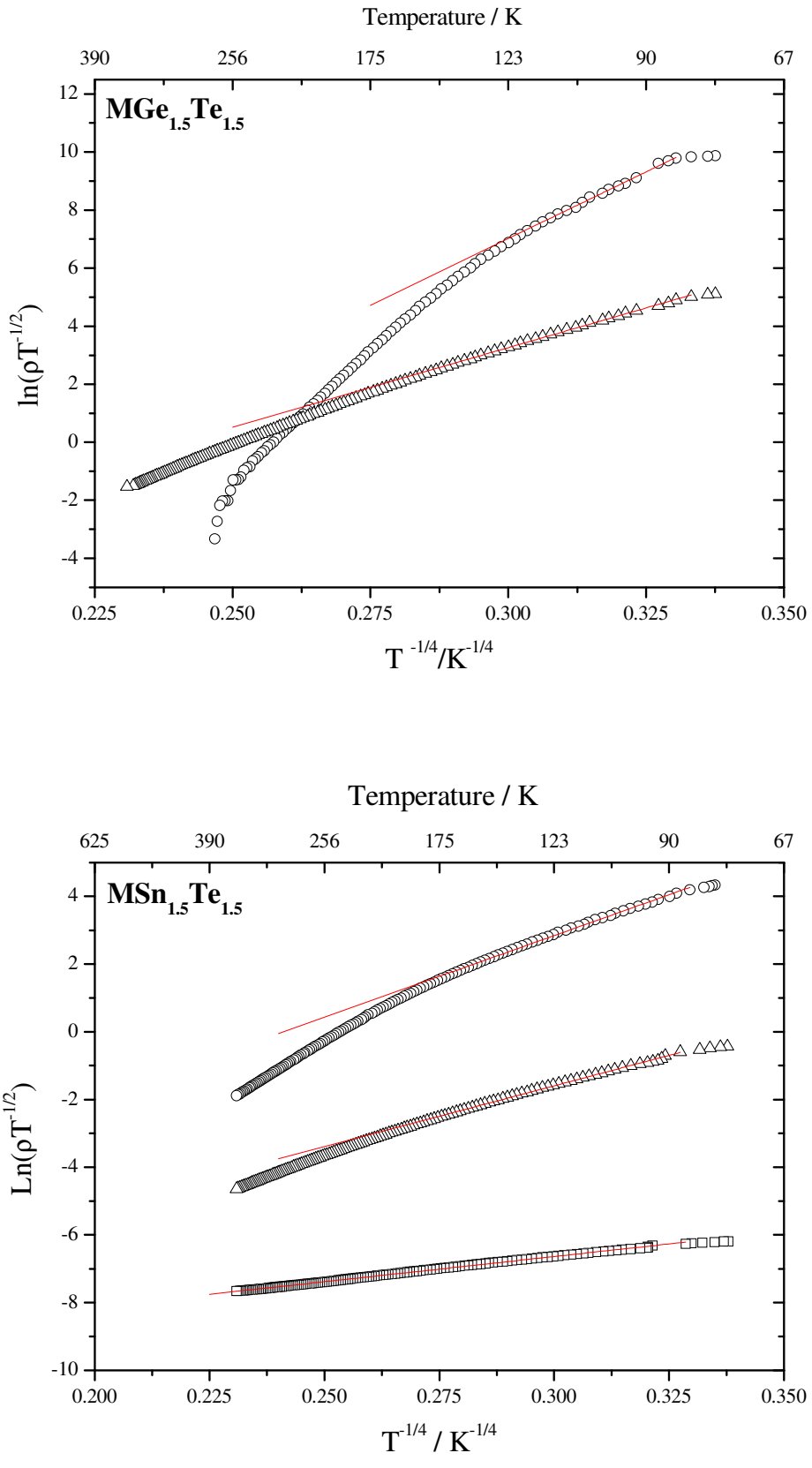

Figure 3-34 Variable-range-hopping fits to electrical resistivity data of the ternary skutterudites $MGe_{1.5}Te_{1.5}$ (top) and $MSn_{1.5}Te_{1.5}$ (bottom). M = Co (empty circles), Rh (empty squares) and Ir (empty circles).

The electrical resistivity datasets have been fitted to a VRH mechanism at low temperature (Figure 3-33 and Figure 3-34). It can be observed that as the group 9 metal varies from cobalt to iridium, a VRH law is able to fit larger temperature ranges at low temperature. In the case of $RhSn_{1.5}Te_{1.5}$ the agreement is optimal throughout the whole temperature range. This evidence correlates well with the value of the high-temperature activation energies within a family obtained by means of electrical conductivity measurements, becoming smaller as the metal varies down the group (Table 3-11). The smallest activation energy corresponds to $RhSn_{1.5}Te_{1.5}$; however, given the large amount of the impurity $RhTe_2$ found in this sample, it is highly unlikely that this value is particularly meaningful. The applicability of the VRH model is, according to its assumptions (*vide supra*), limited to low temperature. At higher temperature, the Fermi level shifts away from the impurity region, where conduction by hopping is the main mechanism, and the energy available allows for transitions from the localized impurity states to the conduction band that will give rise to lower resistivity values and a deviation from the linear dependence with $T^{-1/4}$. It is worth emphasizing the fact that the model also assumes strongly disordered systems, which is a plausible assumption in the narrow gap impurity semiconductors under investigation, where crystallographic faults and/or small amounts of impurities dissolved in the bulk phase may account for the randomness and localization necessary for the VRH mechanism to take place. Values

Moreover, it is known that the value of the pre-exponential factor ρ_0 in equation (5-3), when used to fit resistivity data above room temperature, indicates whether the conduction mechanism takes place through localized or delocalized states when $T \rightarrow 0$. Values of the pre-exponential factor between 10^{-3}-10^{-4} Ωcm is indicative of extended-state conduction. Higher values are a sign that conduction occurs by hopping between localized states [294].

Table 3-12 Values of the pre-exponential factor, ρ_0, obtained from the high-temperature fittings (Figure 3-30 and Figure 3-31) for the skutterudites under study.

Compound	ρ_0 / Ωcm
$CoGe_{1.5}S_{1.5}$	0.065
$RhGe_{1.5}S_{1.5}$	0.016
$IrGe_{1.5}S_{1.5}$	0.12
$CoGe_{1.5}Te_{1.5}$	0.00087
$IrGe_{1.5}Te_{1.5}$	0.21
$CoSn_{1.5}Te_{1.5}$	0.064
$RhSn_{1.5}Te_{1.5}$	0.0063
$IrSn_{1.5}Te_{1.5}$	0.019

The values obtained in Table 3-12 are higher than 10^{-3} Ωcm, except for $CoGe_{1.5}Te_{1.5}$ and $RhSn_{1.5}Te_{1.5}$. This evidence supports the validity of the VRH model to account for the electrical conduction at low temperature. The value obtained for $CoGe_{1.5}Te_{1.5}$ is small enough to indicate extended-state conduction. This is confirmed in the following paragraph through the analysis of the VRH parameters. The $RhSn_{1.5}Te_{1.5}$ value is also small; however, it is not regarded as meaningful, given the presence of large amounts of impurities in the sample.

As regards the fitting parameters of the $CoGe_{1.5}Te_{1.5}$ sample, it is clearly seen that they are out of range, indicating that VRH process does not occur at low temperatures (Table 3-11). Further, the linear relation existing between the temperature and the logarithm of the resistivity in $CoGe_{1.5}Te_{1.5}$ is surprising (Figure 3-30). In an attempt to find a model which is able to explain such behaviour, non-linear curve fitting has been used for the resistivity *vs.* temperature plot based on the expression of the resistivity of a pure semiconductor at low temperatures obtained from Boltzmann transport theory [295]:

$$\rho \propto T^{-\frac{3}{2}} e^{-\frac{\Delta E}{2k_B T}} \qquad \textbf{(3-12)}$$

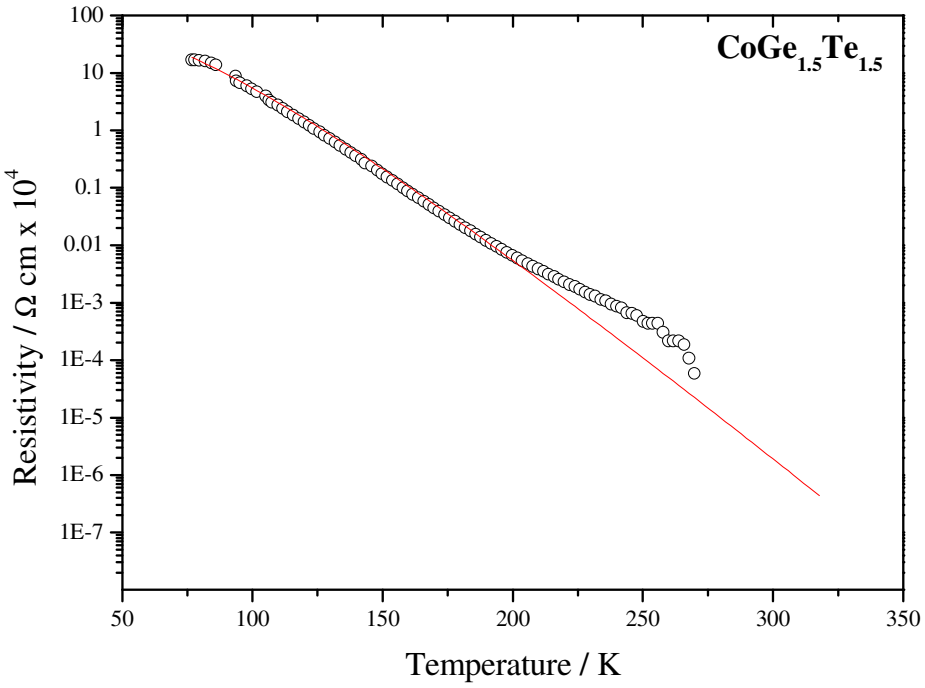

Figure 3-35 Non-linear curve fitting of the $CoGe_{1.5}Te_{1.5}$ electrical resistivity vs. temperature data to the equation (3-12).

The fitting formula used possesses a temperature factor in the exponential term, as observed experimentally in:

$$AT^{-\frac{3}{2}}e^{-yT} \qquad \textbf{(3-13)}$$

Being *A* and *y* refinable parameters whose self-consistent values are 2.5(3) x 10^9 Ωcm and 0.039(1) K^{-1}, respectively. Despite obtaining a good fit at low temperature (Figure 3-35), *i.e.* between 75-200 K, with an overall goodness-of-fit coefficient r = 0.982, the value of the band gap obtained, calculated as the reciprocal of the parameter *y*, was not consistent with that from the resistivity logarithm *vs*. inverse temperature plot at high temperature, indicating that this model is also flawed. Thus, the conduction mechanism of $CoGe_{1.5}Te_{1.5}$ at low temperature is not clear. The low-temperature activation energy obtained is the largest among the ternary skutterudites under study (Table 3-11), which is linked to little spread of the localized states [282]. It has been shown in Figure 3-30 that the slope of the ln ρ *vs*. 1/T plot tends to zero as $T \rightarrow 0$, which may be associated to a phonon-electron coupling caused by the Fermi level lying close enough to impurity levels.

This small polaron conduction mechanism cannot be confirmed by the data shown within this work. Hall mobility measurements would shed some light as to the conduction mechanism at low temperatures.

3.8 Seebeck coefficient

The Seebeck coefficient was measured between 77 K and 350 K (Figure 3-37). Regarding the sign of the Seebeck coefficient, the charge carriers of all the ternary skutterudites are holes (*p*-type), with the exception of $CoGe_{1.5}Te_{1.5}$ and $CoSn_{1.5}Te_{1.5}$ that possess negative Seebeck coefficient throughout the whole temperature range and therefore their charge carriers are electrons (*n*-type). The absolute values of the Seebeck coefficient correlate well with the band gap size both within the family of compounds and between them (Table 3-13). This is consistent with Welker´s rules, which state that the semiconductor with the largest ionic component of the bonding normally has the highest band gap and the lowest electron mobility [278]. This is reflected also in a larger effective mass of the charge carriers and a larger Seebeck coefficient thereof. The absolute values of the cobalt compounds $CoGe_{1.5}S_{1.5}$, $CoGe_{1.5}Te_{1.5}$ and $CoSn_{1.5}Te_{1.5}$ are larger than the $CoSb_3$ value, *i.e.* 225 μVK^{-1} at 300 K [296].

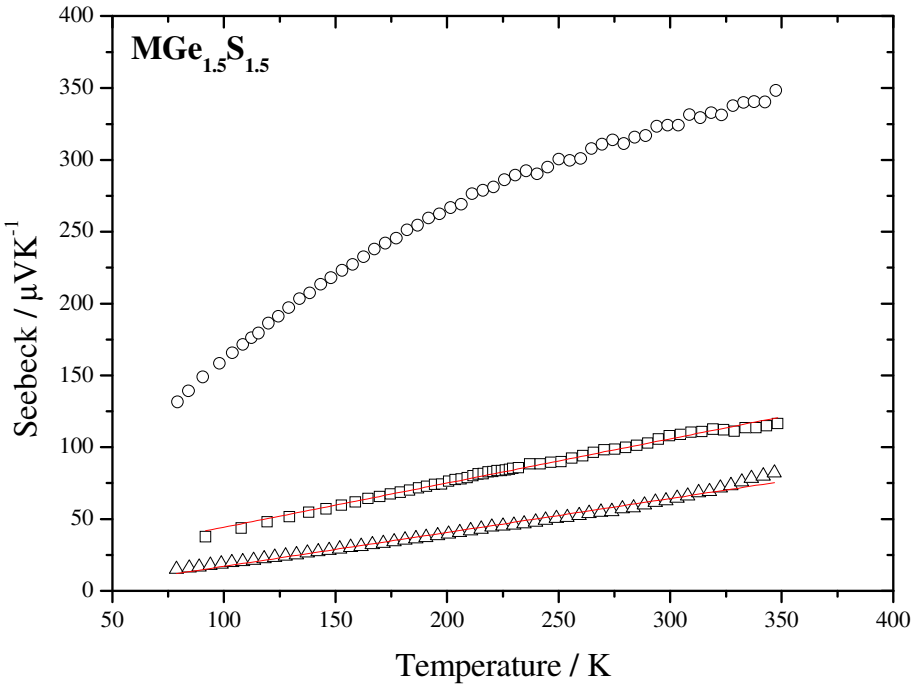

Figure 3-36 Seebeck *vs*. temperature of the ternary skutterudites $MGe_{1.5}S_{1.5}$. M = Co (empty circles), Rh (empty squares) and Ir (empty triangles). Red lines are least-square linear fits to those skutterudites that follow a metal-like Seebeck coefficient. $CoGe_{1.5}S_{1.5}$ Seebeck data is fitted to a low-impurity model in Figure 3-37.

It has been suggested that at low carrier concentration levels, impurity band conduction may play an important rôle in the electrical transport at low temperatures, and in doped $CoSb_3$ samples, the temperature dependence of the Seebeck coefficient has been accounted for using a two-band model consisting of the conduction band and an impurity band [103]. These values are expected to increase at higher temperatures, as the exhaustion region has not been reached yet. Two well-defined Seebeck *vs*. temperature trends are observed that account for the conduction mechanism: linear with respect to the temperature and linear with respect to the temperature logarithm.

Ternary skutterudites whose Seebeck coefficient matches the former trend have been fitted to a straight line, *i.e*. $RhGe_{1.5}S_{1.5}$, $IrGe_{1.5}S_{1.5}$, $CoSn_{1.5}Te_{1.5}$, $RhSn_{1.5}Te_{1.5}$ and $IrSn_{1.5}Te_{1.5}$. This behaviour is explained by the existence of a metallic impurity band, *i.e*. possessing a high degree of overlapping, near the Fermi energy that has the overall effect of reducing absolute value of the Seebeck coefficient and causing metal-like temperature dependence.

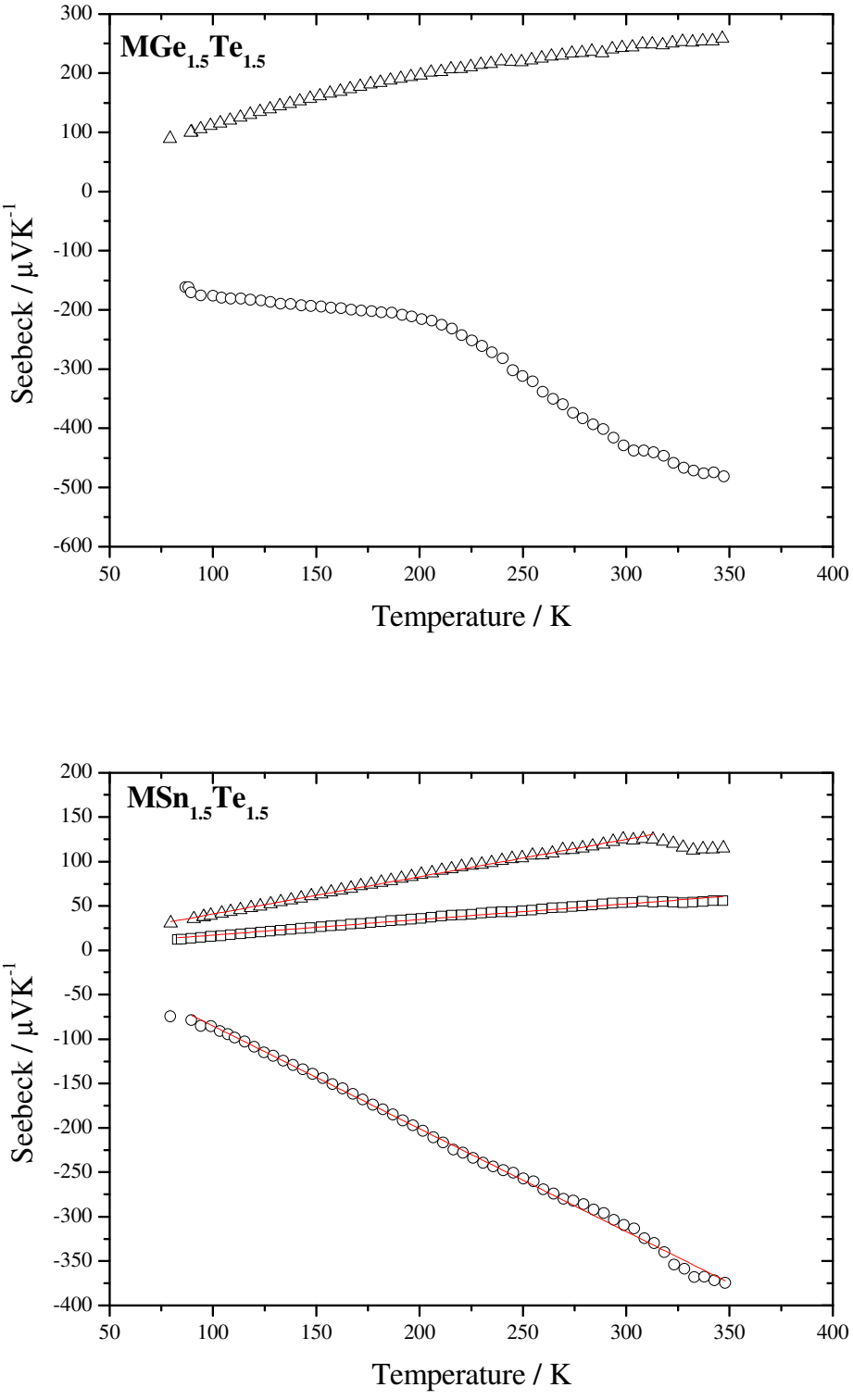

Figure 3-37 Seebeck *vs*. temperature of the ternary skutterudites $MGe_{1.5}Te_{1.5}$ (top) and $MSn_{1.5}Te_{1.5}$ (bottom). M = Co (empty circles), Rh (empty squares) and Ir (empty triangles). Red lines are least-square linear fits to those skutterudites that follow a metal-like Seebeck coefficient. $IrGe_{1.5}Te_{1.5}$ Seebeck data is fitted to a low-impurity model in Figure 3-37. $CoGe_{1.5}Te_{1.5}$ data does not follow any of the above-mentioned models.

Conversely, narrow impurity bands possessing low electron mobility and large effective masses will enhance the total Seebeck coefficient as seen in heavily doped *n*-type $CoSb_3$ [297]. Therefore, the same formula used to explain the Seebeck coefficient of metals can be used to describe the Seebeck coefficient of degenerate semiconductors with metallic impurity bands [291]:

$$S = \frac{\pi^2}{3}\frac{k_B^2 T}{e}\left\{\frac{d(\ln\sigma)}{dE}\right\}_{E=E_F} \qquad \textbf{(3-14)}$$

Where it is shown that the density of states is the predominating term. At this stage, the anomaly observed in the $RhSn_{1.5}Te_{1.5}$ compound can be explained in terms of a wide metallic impurity band that confers low electrical resistivity and low and metal-like Seebeck coefficient values. A wider impurity band will originate more electron delocalization and a smaller derivative value in equation (3-14), accounting for the low Seebeck observed for this compound. Thus, as the temperature rises, the Fermi energy will dwell longer close to the metal-like band, thereby extending the temperature rage at which VRH conduction may occur (Table 3-11).

Table 3-13 Comparison of Seebeck coefficient (μVK^{-1}) and band gap values (meV) extracted from electrical resistivity data at 350 K.

Compound	Seebeck	Band gap
$CoGe_{1.5}S_{1.5}$	350	183(1)
$RhGe_{1.5}S_{1.5}$	125	72.4(8)
$IrGe_{1.5}S_{1.5}$	80	45.8(4)
$CoGe_{1.5}Te_{1.5}$	-500	384(4)
$IrGe_{1.5}Te_{1.5}$	250	186(2)
$CoSn_{1.5}Te_{1.5}$	-380	232(1)
$RhSn_{1.5}Te_{1.5}$	50	9.88(6)
$IrSn_{1.5}Te_{1.5}$	125	137.8(8)

Moreover, Mott and Davis have indicated that the Seebeck coefficient should be proportional to T in the metallic range and of the form $A + BT$ in the hopping range (variable or not) of the conduction mechanism [291]. Supporting the existence of this wide metallic impurity band in $RhSn_{1.5}Te_{1.5}$ is the fact that the linear fit to the Seebeck data intercepts the y-axis at the origin.

Table 3-14 Y-intercepts (μVK^{-1}) of the metal-like ternary skutterudite linear fits.

Compound	Intercept
$RhGe_{1.5}S_{1.5}$	13.6(9)
$IrGe_{1.5}S_{1.5}$	-6.6(8)
$CoSn_{1.5}Te_{1.5}$	31(2)
$RhSn_{1.5}Te_{1.5}$	-0.5(7)
$IrSn_{1.5}Te_{1.5}$	-1.3(7)

The $IrSn_{1.5}Te_{1.5}$ y-axis intercept also includes the origin within three standard deviations, pointing at a similar conduction process in both compounds, whereas the rest of the skutterudites follow the $A + BT$ relation (Table 3-14).

On the other hand, $CoGe_{1.5}S_{1.5}$ and $IrGe_{1.5}Te_{1.5}$ adopt a linear relation with the temperature logarithm characteristic of non-degenerate semiconductors, evidencing the lower impurity concentration and therefore a lower electron concentration that places the Fermi energy away from the conduction band or wide impurity bands (Figure 3-38). The theoretical expression of the Seebeck coefficient for this type of semiconductors is [291]:

$$S = \frac{3}{2}\frac{k_B}{e}\ln T + \text{const.} \qquad \textbf{(3-15)}$$

The slopes of the $CoGe_{1.5}S_{1.5}$ and $IrGe_{1.5}Te_{1.5}$ linear fits correspond to 148.6(8) μVK^{-1} and 118.5(6) μVK^{-1}, respectively (Figure 3-38). These values are relatively close to the theoretical value predicted in equation (3-15) of 129.3 μVK^{-1}. Since the 3/2 factor originates from a parabolic band form, the difference with the experimental values is attributed to deviations from the parabolicity of the band [280].

Finally, the $CoGe_{1.5}Te_{1.5}$ compound is a source of conflict, yet again, with the above-mention models, as none of them adjusts its Seebeck data throughout the whole temperature range. Considering the problems encountered when fitting the $CoGe_{1.5}Te_{1.5}$ electrical conductivity data to both a VRH and a pure semiconductor conduction mechanism, the present mismatch was also expected. The increasing Seebeck coefficient as the temperature rises, as seen in the other compounds, confirms the existence of an undetermined number of acceptor impurity levels (*p*-type) close to the valence band. A slope change is observed at approximately 200 K, not seen in the resistivity *vs*. temperature plot. Regarding the fact that the Seebeck coefficient is a

means of probing the density of states near the Fermi level, if a change in the right term of equation (3-14) occurs and a sufficiently large number of electrons is involved in the conduction process, such change may easily be overlooked in the resistivity measurement.

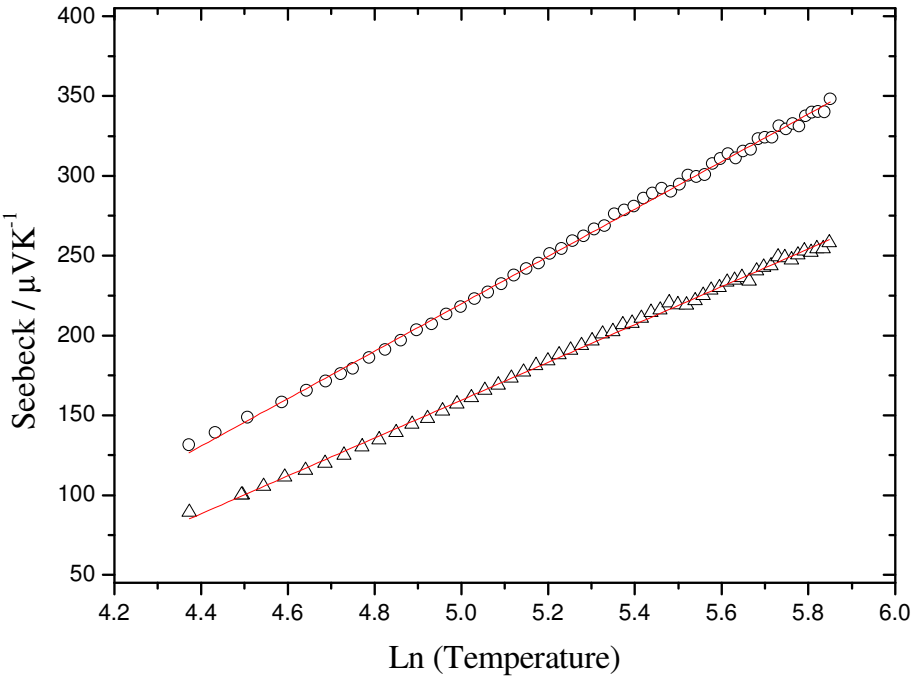

Figure 3-38 Seebeck *vs*. temperature logarithm of the ternary skutterudites $CoGe_{1.5}S_{1.5}$ (empty circles) and $IrGe_{1.5}Te_{1.5}$ (empty triangles).

3.9 Thermal conductivity

The thermal conductivity of the cobalt skutterudites $CoGe_{1.5}S_{1.5}$, $CoGe_{1.5}Te_{1.5}$, $CoSn_{1.5}Te_{1.5}$ has been measured between 300 K and 800 K in 25 K steps (Figure 3-39). 13 mm diameter pellets were cold pressed and sintered during 5 days at synthesis temperature until a 70%, 75% and 73% of the theoretical density was reached, respectively. $CoGe_{1.5}S_{1.5}$, $CoGe_{1.5}Te_{1.5}$ and $CoSn_{1.5}Te_{1.5}$ reach thermal conductivity values as low as 1.8, 1.5 and 0.8 $Wm^{-1}K^{-1}$, respectively, at 325 K (Figure 3-39). Porosity is known to cause a strong reduction in the thermal conductivity of materials. An estimation of the thermal conductivity for porous samples has been developed by Klemens that takes into account the porosity of the sample [298]:

$$\frac{\kappa_{\text{porous}}}{\kappa_{\text{dense}}} = 1 - \frac{4}{3}\phi \qquad \textbf{(3-16)}$$

Where ϕ is the porosity of the material defined as [100 – (% theoretical density)] / 100.

The modified experimental values are 3.0, 2.3 and 1.3 $Wm^{-1}K^{-1}$, respectively. They follow a decreasing trend with atomic weight, consistent with the fact that heavier atoms scatter phonons more efficiently. The minimum thermal conductivity in skutterudites has been calculated by C. Uher based on the shortest mean free path of phonons that can be achieved at any given temperature. The concept of minimum thermal conductivity developed by Slack assumed that such free path cannot be smaller than one phonon wavelength [299]. However, Cahill and Pohl, based on studies of heat transport in amorphous solids, developed an alternative approach, in which the thermal conductivity is viewed as a random walk of the thermal energy between neighbouring atoms vibrating with random phases [300]. The shortest mean free path that originates from this model is half the phonon wavelength, which, in turn, yields lower values of the minimum thermal conductivity [301].

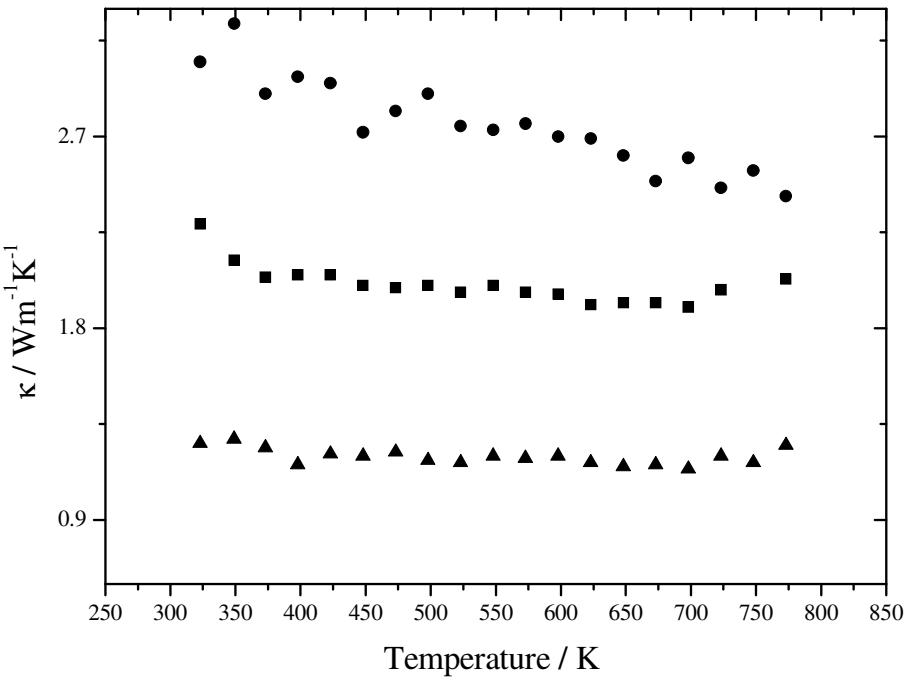

Figure 3-39 Thermal conductivity of the ternary skutterudites $CoGe_{1.5}S_{1.5}$ (black circles), $CoGe_{1.5}Te_{1.5}$ (black squares) and $CoSn_{1.5}Te_{1.5}$ (black triangles). Porosity-corrected values.

The value obtained using the latter model was 0.31 $Wm^{-1}K^{-1}$. When compared to the thermal conductivity of $CoSb_3$, *i.e.* 10 $Wm^{-1}K^{-1}$ [116], it provides an idea of the large extent to which thermal conductivity is reduced by anionic substitution, *i.e.* between 70-90 %. The smallest attainable value is 0.2 $Wm^{-1}K^{-1}$, which is of the same order as the values observed in non-porous insulating solids [14]. The differences in mass and volume of the anions involved in the isoelectronic substitution are too small to be the

main phonon scattering source. There exist other phonon scattering mechanisms seen in skutterudites, namely mixed valency in the compound $Ru_{0.5}Pd_{0.5}Sb_3$ [54]; however there is no evidence of mixed valency in anion-substituted ternary skutterudites under study. The ring distortion occurring when anion substitution takes place may then be responsible for such decrease in the thermal conductivity. Lutz *et al*. reported an increase of the lattice vibrations in the anion substituted ternary skutterudites $MGe_{1.5}Y_{1.5}$ (M = Co, Rh, Ir; Y = S, Se) when compared to the binary analogue $CoAs_3$ [56]. Therefore, the symmetry reduction from $Im\overline{3}$ to $R\overline{3}$ has a strong effect on the phonon scattering. Analysis of the calculated phonon DOS for $CoSb_3$ indicates that Co and Sb vibrations are mainly decoupled and that low frequency phonon modes involving the Sb_4^{4-} rings are heat carriers giving high contributions to the thermal conductivity [302,303]. Therefore, an important decrease in the lattice thermal conductivity is expected with substitution. Large reductions have also been observed less markedly in other anion-substituted skutterudites at 300 K such as $CoGe_{1.5}Se_{1.5}$ (8 $Wm^{-1}K^{-1}$), $CoSn_{1.5}Te_{1.5}$ (4 $Wm^{-1}K^{-1}$) and $IrSn_{1.5}Se_{1.5}$ (3 $Wm^{-1}K^{-1}$) [50,107,109]. Nevertheless, a 90 % reduction in the thermal conductivity is difficult to explain solely on the grounds of anion substitution. In spite of the fact that a porosity correction has been included, the values obtained are still too small when compared to existent literature values, *i.e*. 1.3 to 4 $Wm^{-1}K^{-1}$ in $CoSn_{1.5}Te_{1.5}$, which may indicate that porosity effects are not fully accounted for. Low values of thermal conductivity are also associated with poorly compacted or small grain size polycrystalline samples that are typically of no more than 70% the theoretical density [301]. Comparative studies carried out on $CoSb_3$ show that cold-pressed pellets with a 70% density possess nearly half the thermal conductivity of a hot-pressed pellet with a 97% density [102,304].

3.10 Power factors

Power factors ($S^2\sigma$) of all the ternary skutterudites under study have been calculated using the data obtained in the electrical resistivity and Seebeck measurements (Figure 3-41 and Figure 3-41). $RhSn_{1.5}Te_{1.5}$ compound possesses the most outstanding electronic properties, mostly due to the low value of the electrical resistivity at room temperature. The $RhSn_{1.5}Te_{1.5}$ Seebeck coefficient is half that of $IrSn_{1.5}Te_{1.5}$ at room temperature (Figure 3-37), but the overall effect is to enhance the power factor to such an extent that $RhSn_{1.5}Te_{1.5}$ turns out to be the ternary skutterudite under study with the best electronic properties for thermoelectric purposes. The improvement of

thermoelectric properties owing to the existence of impurity phases has already been reported in skutterudites for the case of $Ce_{2-x/3}Fe_6Co_2Sb_{24-x}Sn_x$ when $FeSb_2$ and Sb are also present [305].

$CoGe_{1.5}Te_{1.5}$ is the next compound in the series, whose power factor boosts at room temperature because the Seebeck coefficient steadily increases up to 350 K without reaching the exhaustion region. With a similar argument the rapid increase of $CoGe_{1.5}S_{1.5}$ can be justified, achieving comparable values. The power factor values of $RhGe_{1.5}S_{1.5}$, $IrGe_{1.5}S_{1.5}$, $IrGe_{1.5}Te_{1.5}$ and $IrSn_{1.5}Te_{1.5}$ remain low as neither the Seebeck coefficient nor the resistivity attain their optimal values of 200 μVK^{-1} and 10^{-3} Ωcm, respectively [14]. Surprisingly, $CoSn_{1.5}Te_{1.5}$ is found below $IrSn_{1.5}Te_{1.5}$ despite having the largest Seebeck coefficient at 350 K, being damped by an electrical resistivity which is nearly three orders of magnitude larger than that of $RhSn_{1.5}Te_{1.5}$. Power factors at the highest measured temperature are two orders of magnitude lower than the values that can be achieved by *n*-type or *p*-type $CoSb_3$, *i.e.* 2.5-3 x 10^{-3} $Wm^{-1}K^{-2}$ [50]. This fact evidences that the increase in the Seebeck coefficient is not enough in order to compensate for the deleterious effect of anion substitution upon the electrical resistivity. The values obtained, however, are larger than those measured for other anion-substituted ternary skutterudites at room temperature such as $CoGe_{1.5}Se_{1.5}$ (5.8 x 10^{-8} $Wm^{-1}K^{-2}$) or $CoSn_{1.5}Te_{1.5}$ (6.6 x 10^{-7} $Wm^{-1}K^{-2}$), and of the same order of magnitude as other samples of the same compounds, namely $CoGe_{1.5}Te_{1.5}$ (1 x 10^{-5} $Wm^{-1}K^{-2}$) [107,109,246]. Dimensionless figure-of-merit values at 350 K can be calculated for the cobalt-containing ternary skutterudites whose thermal conductivity has been measured, *i.e.* $CoGe_{1.5}S_{1.5}$, $CoGe_{1.5}Te_{1.5}$ and $CoSn_{1.5}Te_{1.5}$. The figures obtained are 0.0006, 0.001 and 0.002, respectively. These values are three orders of magnitude lower than those achieved in state-of-the-art thermoelectric materials such as Bi_2Te_3. Nevertheless, they are comparable to those reported for other ternary skutterudites [107,109].

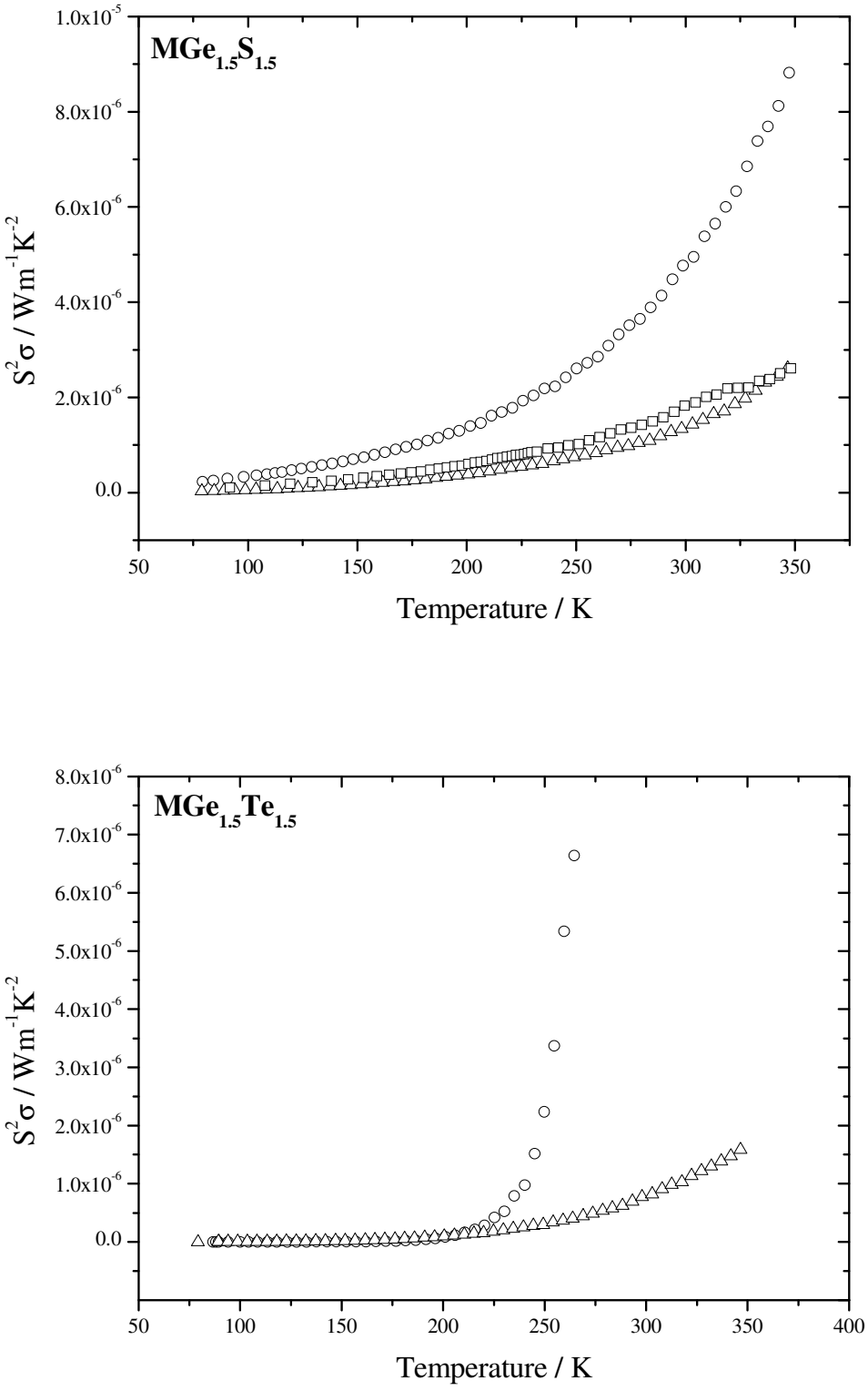

Figure 3-40 Power factors between 77 K and 350 K of the ternary skutterudites $MGe_{1.5}S_{1.5}$ (top) and $MGe_{1.5}Te_{1.5}$ (bottom). M = Co (empty circles), Rh (empty squares), Ir (empty triangles).

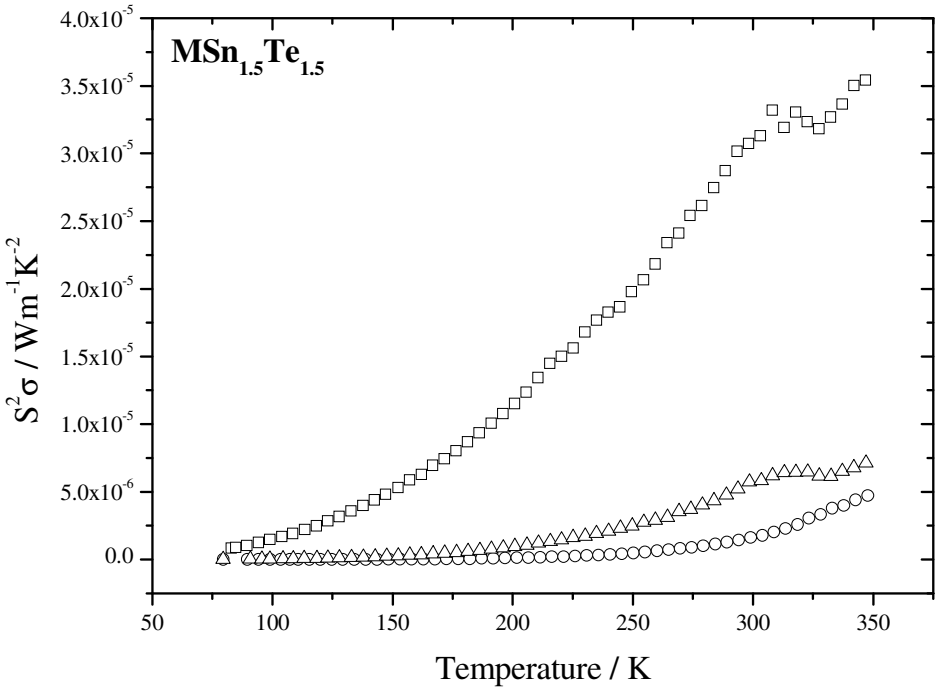

Figure 3-41 Power factors between 77 K and 350 K of the ternary skutterudites $MGe_{1.5}Te_{1.5}$ (previous page) and $MSn_{1.5}Te_{1.5}$ (above). M = Co (empty circles), Rh (empty squares), Ir (empty triangles).

Chapter 4

Filled ternary skutterudites

4.1 Introduction

Filling of skutterudites is a crucial step to reduce its thermal conductivity and make them suitable for thermoelectric applications. It has been demonstrated that, for a given host skutterudite structure, the lattice thermal conductivity decreases with filling fraction, reaching a minimum at approximately 30-40% of void occupancy [80]. Given the recent success in the synthesis of the filled skutterudite $LaFe_3CoSb_{12}$ by Sales *et al.* [71], the synthesis of the ternary filled skutterudite $LaFe_3CoGe_6Te_6$ has been attempted. Within this chapter, the synthetic approach as well as the theoretical backing of the results obtained are presented.

4.2 Synthetic approach

Each cubic unit cell possesses two cavities that can be represented as $\square_2Co_4Sb_{12}$ (section 1.2.1). In the ternary skutterudites $MY_{1.5}Q_{1.5}$ (M = Co, Rh, Ir; Y = Ge, Sn; Q = S, Te) under study, the centre of the cavity is surrounded by 20 atoms, where 6 Y atoms and 6 Q atoms form a 12-vertex distorted icosahedron and the M atoms a cube. These together form a distorted pentagon dodecahedron [41] (Figure 4-1).

In order to assess the capacity of the cavity to accommodate a guest atom, the volume of the 20-atom cavity in which host species may be inserted has been calculated for each of the ternary skutterudites under study, as well as the distance from the centre to each type of atom. For this purpose, the program VOLCAL [306] has been used in combination with the crystallographic information obtained for each of the phases during the course of this work. In order to obtain the standard deviations of the calculated volume, the cell variance-covariance matrix extracted from the Rietveld refinements was used and included in the input file (appended CD-ROM). They only data that the program requires are the unit-cell parameters and the atomic coordinates of the atoms forming the polyhedron. Any convex polyhedron composed n points is uniquely defined by its ν vertices. By definition, a point is a vertex if there exists a plane such that the point is contained in that plane and all the remaining points lie to one side of that plane. Collinear and coplanar points can be identified with vector tests and then eliminated from the initial array of n points. By permuting the n points, three at a time, the number R of unique triangular planes is given by $n!/3!(n-3)!$. The number T of exterior triangular faces that define the polyhedron is given by $2\nu-4$. Each exterior

triangular face *T* is the base of a tetrahedron whose apex can be any point *P* lying inside the polyhedron. *P* is the common apex of the *T* tetrahedra and also defines an origin for the polyhedron, so that the three vertices that define the face become the end points of three vectors denoted **A**, **B** and **C**, which outline a tetrahedron. Then, the volume of the tetrahedron is one-sixth of the volume of the parallelepiped defined by the same three vectors and is given by $1/6|\mathbf{A} \bullet \mathbf{B} \times \mathbf{C}|$. Summing the *T* tetrahedral volumes, the total volume is obtained [307,308].

The radius of the cavity was calculated as the averaged distance *d* from the centre of the void to the Y/Q atoms minus half of the averaged Y(1)-Q(1) distance, *r*(YQ), as follows [72]:

$$r(\text{void}) = d - r(\text{YQ}) \qquad \textbf{(4-1)}$$

The void radii are very similar to those calculated in partially filled skutterudites such as $Yb_{0.19}Co_4Sb_{12}$ (1.897 Å), $Y_{0.33}Fe_{0.7}Co_{3.3}Sb_{12}$ (1.904 Å), or $Ba_{0.6}Fe_{0.6}Co_{2.4}Sb_{12}$ (1.923 Å) [80]. *A priori*, all the ternary skutterudites synthesized present a suitable cavity for filling as seen in Table 4-1.

Table 4-1 Cavity volumes (Å^3), void radii (Å) and averaged distances (Å) from the centre of the cavity (O) for the ternary skutterudites $M_4Y_6Q_6$ (M = Co, Rh, Ir; Y = Ge, Sn; Q = S, Te).

Compound	O-M	O-Y	O-Q	Volume	*r*(void)
$Co_4Ge_6S_6$	3.490	2.939	3.003	96.4(4)	1.739
$Rh_4Ge_6S_6$	3.585	3.064	3.167	108.1(2)	1.897
$Ir_4Ge_6S_6$	3.595	3.045	3.139	107.7(3)	1.860
$Co_4Ge_6Te_6$	3.789	3.138	3.273	120.8(3)	1.779
$Ir_4Ge_6Te_6$	3.874	3.395	3.244	133.6(3)	1.918
$Co_4Sn_6Te_6$	3.967	3.283	3.411	137.6(3)	1.863
$Rh_4Sn_6Te_6$	4.047	3.360	3.509	148.8(3)	1.950
$Ir_4Sn_6Te_6$	4.033	3.431	3.508	149.5(2)	2.003

During the process of choosing a filler atom, there were several restraints that were taken into account. It has been shown that the thermal vibration amplitude and, therefore, the phonon scattering strongly depends on the size of the filler atom relative to that of the cage, so that smaller filler atoms decrease even further the thermal conductivity of skutterudites [117]. It is noteworthy that the study of variables affecting the filling fraction in Co_4Sb_{12}-based systems is paradigmatic, and its conclusions are very useful as to the understanding of the filling mechanism in other environments, namely, charge-compensated systems (section 1.2.3).

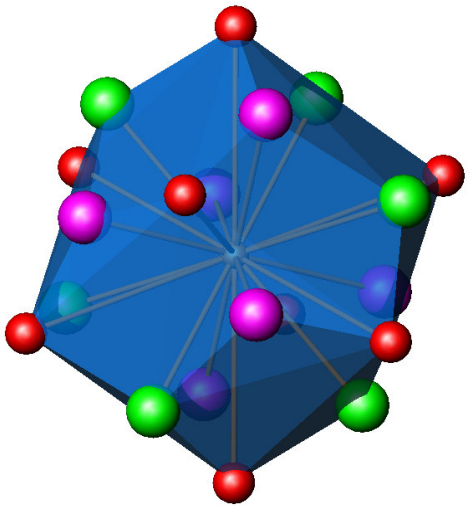

Figure 4-1 20-atom pentagon-dodecahedral cavity. Key: cobalt in red, germanium in pink and tellurium in green.

Nevertheless, a clear bottom threshold regarding the size of the filler atom has been experimentally observed. Rare-earth elements at the beginning of the period seem to possess the required characteristics of ionic radius, valence state and electronegativity of the filler atom to fit in the skutterudite voids, as many of these compounds have been already synthesized (Table 1-2). Contrarily, late period rare earth elements do not form filled skutterudites. According to the lanthanide contraction, as the atomic number of the rare-earth element increases, its size contracts and filled skutterudite structures do not form with the smallest rare-earth elements (Dy-Tm). This fact was rationalized by Sales as the impossibility for the smallest elements to form the necessary bonding with the cage atoms [69]. This explanation has also been backed by theoretical calculations, where it is shown that Gd, Tb, Dy, Tm and Lu cannot form stable filled skutterudites, as the formation energies of the corresponding secondary phases are lower than those of the filled compound [309]. In terms of filler and cage radii, Chen indicates that when the ratio r_{ion} / r_{cage} is lower than 0.6 the bonding is too loose to keep the filler atom in its equilibrium position. Ideally, a ratio value in the range $0.6 < r_{ion} / r_{cage} < 0.9$ establishes the stability range in which filled skutterudites can be formed [80].

Further, Shi *et al*. have suggested a simple selection rule for an impurity to be able to fill the voids in Co_4Sb_{12} systems in terms of the electronegativity difference between the filling atom and that of the neighbouring Sb atom [310]:

$$\Delta x = x_{Sb} - x_F \geq 0.8 \qquad \textbf{(4-2)}$$

It states that the difference between them has to be large enough, so that the rare-earth outer core electrons are handed over to the Sb framework and no covalent interactions occur between them. Finally, considering the valence state, it is also known that, in Co_4Sb_{12}-based systems, ions with low valence states enter much more easily the cavities than other high valence ions [80].

Hence, the selected element was lanthanum and $CoGe_{1.5}Te_{1.5}$ the ternary skutterudite framework in which it was to be inserted. Lanthanum was then the most suitable element according to the following criteria:

- Firstly, lanthanum fulfils all the numerical restraints that appear in the literature. The ratio $r_{ion} / r_{cage} = 0.76$ falls right in the middle of the allowed range. A radius of 1.36 Å is the largest within the lanthanides period and the electronegativity difference between La (1.1) and the averaged Ge (1.8) and Te (2.1) values also complies with the inequality imposed in (4-2).
- Secondly, La-filled skutterudites are one of the most studied systems, both experimentally and theoretically, owing to their outstanding thermoelectric properties at high temperatures [67,71,311].
- Thirdly, lanthanum is relative cheap, commercially available and one of the relatively less air-sensitive rare earths. The $CoGe_{1.5}Te_{1.5}$ framework was chosen owing to availability of chemicals and also because its structure has been studied in depth within this work [246].

The stoichiometric amount of filler was fixed at 1 in relation to the desired semiconducting properties of the target phase and the ideal VEC of 72 that confers a full valence band configuration. The phase $LaFe_4Sb_{12}$ is know to be a poor metal given that its electron count is equal to 71 (8 electrons from each Fe atom and 3 electrons from each Sb and La atom) and, accordingly, the Seebeck coefficient is relatively small, being the electrical conductivity dominated by holes [69]. It has been demonstrated that charge compensation is an effective means to increase the filler occupancy, being used successfully in the synthesis of completely filled skutterudites, such as $CeFe_{0.75}Co_{3.25}Sb_{12}$ [78]. More recently, Sales *et al.* managed to synthesize the completely filled lanthanum skutterudite $LaFe_3CoSb_{12}$ using also charge compensation [71]. This approach has been introduced in the experiment by replacing one iron atom by one cobalt atom, taking into account that each lanthanum atom enters the skutterudite voids donating three electrons, *i.e.* La^{3+}.

Prior to the phase exploration in order to find the target phase $LaFe_3CoGe_6Te_6$, initial attempts to synthesize phases such as $LaFe_4Ge_6S_6$, $LaFe_3CoGe_6S_6$ and $LaFe_4Ge_6Te_6$ were also attempted. They were carried out using prereacted commercial binary reactants, namely La_2S_3 (Strem Chemicals 99.9%) and La_2Te_3 (Alfa Aesar 99.9%), along with elemental iron (Alfa Aesar 99+%), cobalt (Alfa Aesar 99.5%) and germanium (Goodfellow 99.999%). The high melting point of La_2S_3 and La_2Te_3, *i.e.* ~ 1100 °C, suggested taking the reaction up to the highest possible temperature and then quenching the melt in an ice bath to freeze the reaction product. Subsequently, an annealing treatment at lower temperature would produce the desired crystallographic phase.

The reactants were ground together in an agate mortar and sealed into an evacuated silica tube (< 10^{-4} torr). Initially, the reaction mixture was heated up to 1150 °C at 0.5 °C min^{-1}, left at this temperature for 1 day and then quenched under an ice bath. The tube was immediately placed back into the chamber furnace at 500 °C for a period of 2 days. A second firing was carried out at 800 °C after sample grinding and it was let cool down to room temperature at 0.5 °C min^{-1}.

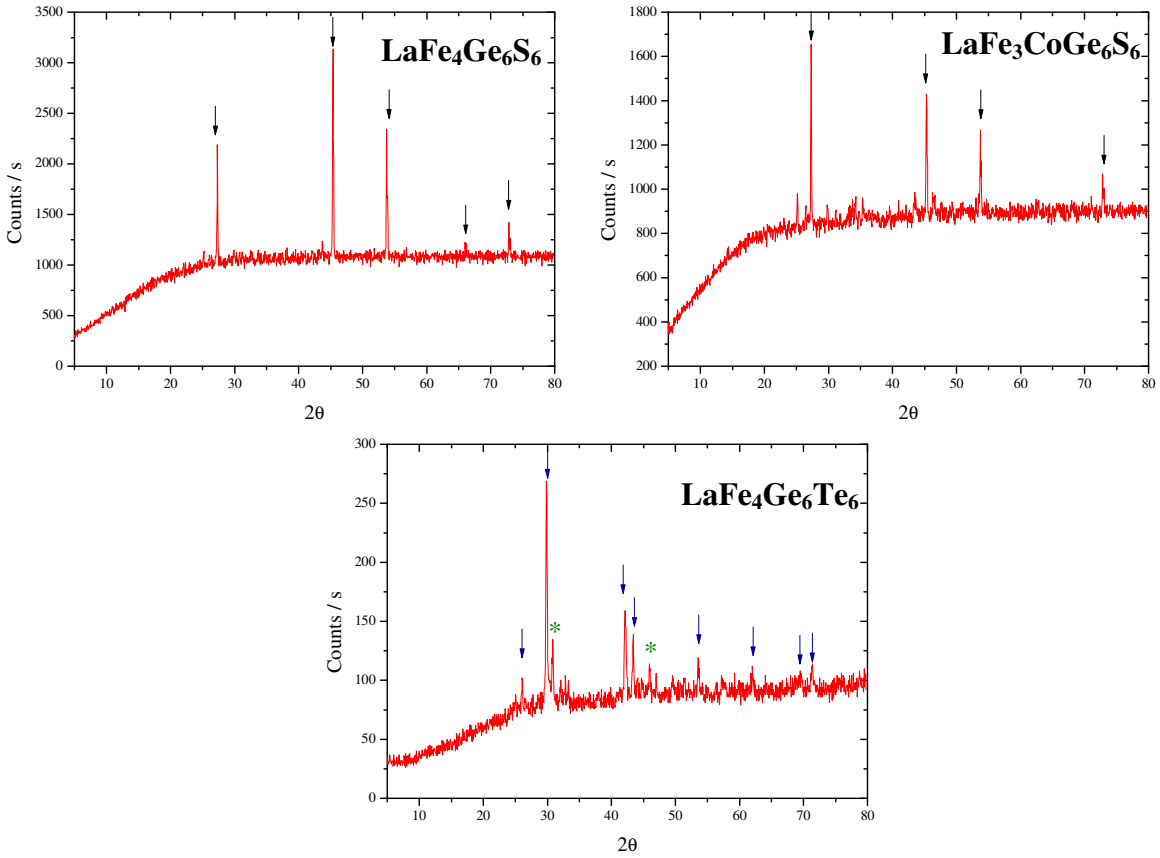

Figure 4-2 Laboratory X-ray diffraction patterns of reaction products. Top left: $LaFe_4Ge_6S_6$. Top right: $LaFe_3CoGe_6S_6$. Bottom: $LaFe_4Ge_6Te_6$. Key: black arrows point at Ge reflections; blue arrows at GeTe reflections and green stars at Fe_3Te_2 reflections.

Despite all efforts, mostly binary phases were obtained. In the sulphur-containing phases only germanium was identified as a crystalline reaction product, whereas all the other phases either were not crystalline enough or were blended in with the background (Figure 4-2).

In $LaFe_4Ge_6Te_6$, germanium telluride was the main product and the second main phase (marked with a green star) was identified as Fe_3Te_2 with the powder diffraction file (PDF) number 00-041-0759 (Figure 4-2, bottom). This phase cannot be found in the ICDS service, nor in the crystalweb database and there is no information regarding its space group, lattice parameters or atom positions available [312]. This phase belongs to the iron-rich binary telluride phases; which, in turn, all crystallize in the space group *P*4/*nmm*. FeTe, $Fe_{1.11}Te$ and $Fe_{1.125}Te$ are examples of such compounds. The presence of an extra iron atom in a special Wyckoff position (2*c*) with variable atomic occupancy accounts for the extra iron. Therefore, a plausible guess of the crystal structure of Fe_3Te_2 would be the same as the other iron-rich binary tellurides with half-occupied sites for the second iron atom. The powder pattern of $Fe_{1.25}Te$ agrees well with the relative intensity of the peaks experimentally observed, although the peak positions indicate a smaller unit cell (Figure 4-3).

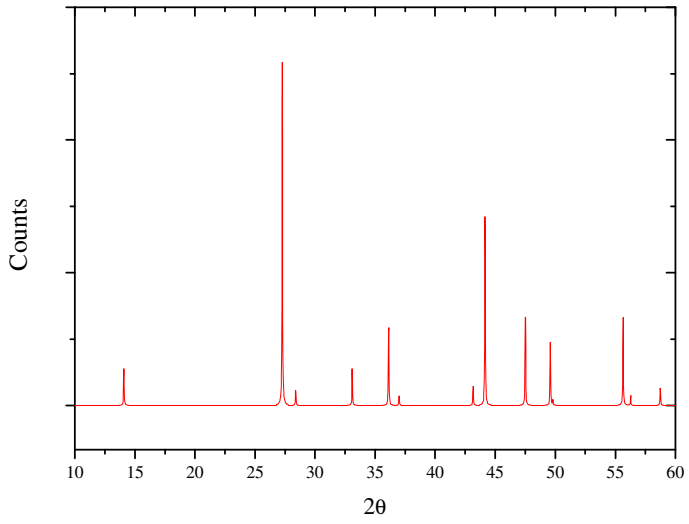

Figure 4-3 Powder pattern of $Fe_{1.125}Te$. The two most intense reflections along with their relative intensity and separation from each other match the two observed experimental reflections ascribed to Fe_3Te_2.

The simulation of the Fe_3Te_2 powder pattern is not shown, as the relative intensities strongly depend not only on the atomic occupancy of the second iron atom, but also on the value of its *z* coordinate, which is unknown.

The high melting temperature of the binary reactants was thought to be accountable for the failure to synthesize the above-mentioned phases and another synthetic route was attempted, starting directly from the elements. Sales *et al*. developed a simple and clean synthesis approach to the completely filled skutterudite $LaFe_3CoSb_{12}$ by a traditional metallurgical technique as follows [71]. They mixed stoichiometric amounts of the starting elements in an agate mortar and loaded them into a carbon-coated silica ampoule, which was sealed off under vacuum. The silica ampoule was heated to 600 °C at 2 °C/min, left at 600 °C for 3 h, and then slowly (0.5 °C/min) heated to 1050 °C and left for 20 h. The silica ampoule containing the molten liquid was removed from the furnace at temperature and quenched in a water bath. The same ampoule was then placed in a furnace and annealed at 700 °C for 30 h to form the correct crystallographic phase.

The target phase was then set to $LaFe_3CoGe_6Te_6$ and a comprehensive exploration of the phase space was carried out by means of 22 reactions following Sales' approach (Table 4-2 and Table 4-3). Lanthanum powder (Aldrich 99.9%) was used in the initial mixture and all the reactants were weighed out inside a glovebox under an argon atmosphere. In order to rule out impurity phases or unexpected reactions, the germanium underwent a previous reduction process to eliminate the presence of germanium oxide consisting of three or four five-hour heat treatments at 600 °C under a current of a hydrogen/nitrogen (5/95) mixture.

Table 4-2 Phase exploration between 400 °C and 1100 °C without temperature quench.

Sample	1st firing	2nd firing
1	400 °C 2 days	400 °C 2 days
2	450 °C 2 days	450 °C 2 days
3	500 °C 2 days	500 °C 2 days
4	550 °C 2 days	550 °C 2 days
5	600 °C 2 days	600 °C 2 days
6	650 °C 2 days	650 °C 2 days
7	700 °C 2 days	700 °C 2 days
8	750 °C 2 days	750 °C 2 days
9	800 °C 2 days	800 °C 2 days
10	850 °C 2 days	850 °C 2 days
11	900 °C 2 days	900 °C 2 days
12	950 °C 2 days	950 °C 2 days
13	1000 °C 2 days	1000 °C 2 days
14	1050 °C 2 days	1050 °C 2 days
15	1100 °C 2 days	1100 °C 2 days

The reduction completeness was monitored by X-ray diffraction. In the first firing, the silica tubes used were carbon coated by pyrolysis of acetone, whereas no coating was applied in the second firing. This was done on the grounds that in the second firing all the starting elements had already reacted and attack of the inner tube walls was unlikely. No chemical attack was observed in the silica ampoules after the second firing. The tubes were then baked in an oven at 150-200 °C overnight and placed immediately into the glovebox to eliminate any trace of moisture that might interfere with the target reaction.

Table 4-3 Phase exploration between 400 °C and 1100 °C with temperature quench.

Sample	1st firing		2nd firing
16	Heated at 1°C min^{-1} to 1150° Held for 12 hours Quenched in ice	400°C 2 days	400°C 2 days
17	Heated at 1°C min^{-1} to 1150° Held for 12 hours Quenched in ice	500°C 2 days	500°C 2 days
18	Heated at 1°C min^{-1} to 1150° Held for 12 hours Quenched in ice	600°C 2 days	600°C 2 days
19	Heated at 1°C min^{-1} to 1150° Held for 12 hours Quenched in ice	700°C 2 days	700°C 2 days
20	Heated at 1°C min^{-1} to 1150° Held for 12 hours Quenched in ice	800°C 2 days	800°C 2 days
21	Heated at 1°C min^{-1} to 1150° Held for 12 hours Quenched in ice	900°C 2 days	900°C 2 days
22	Heated at 1°C min^{-1} to 1150° Held for 12 hours Quenched in ice	1000°C 2 days	1000°C 2 days

Maximum care was also taken to assure that no trace of moisture was present in the glassware and funnels used to transfer the powder mixture from the mortar to the silica tube, as they were also baked. The contact between the reaction powder and the air was minimized by placing the powder into a sample bottle and stored in a desiccator immediately after the silica tube was opened and the X-ray diffraction pattern collected. Further firings were carried out at the same temperature when necessary until the intensity of the reflections remained constant.

4.3 Powder X-ray diffraction

All these efforts, however, did not lead to the targeted compound, *i.e.* $LaFe_3CoGe_6Te_6$, but to the binary phase GeTe between 700 °C and 1100 °C and to a mixture of phases between 450 °C and 650 °C as shown in Figure 4-4 and Table 4-4.

The mixture of phases is composed mainly by the ternary skutterudite $CoGe_{1.5}Te_{1.5}$, $LaTe_2$, GeTe, as well as Fe_3Te_2. The latter phase could not be found in any of the routine crystal structure databases and was identified using the latest PDF-2 database that accompanies the state-of-the-art X-ray powder diffractometer recently acquired in our research group. Fe_3Te_2 (PDF number 00-041-0759) also was found during the analysis of the $LaFe_4Ge_6Te_6$ diffraction pattern and is consistent with the need of finding an iron-containing phase to explain its high content in the nominal stoichiometry; given that none of the previously identified phases had iron in their respective unit cells. Whenever a sufficient number of reflections could be indexed, the lattice parameters of the phases were refined and compared with those available in the Inorganic Crystal Structure Database calculated with the program LAZY PULVERIX for the final phase assignment (Table 4-5) [313].

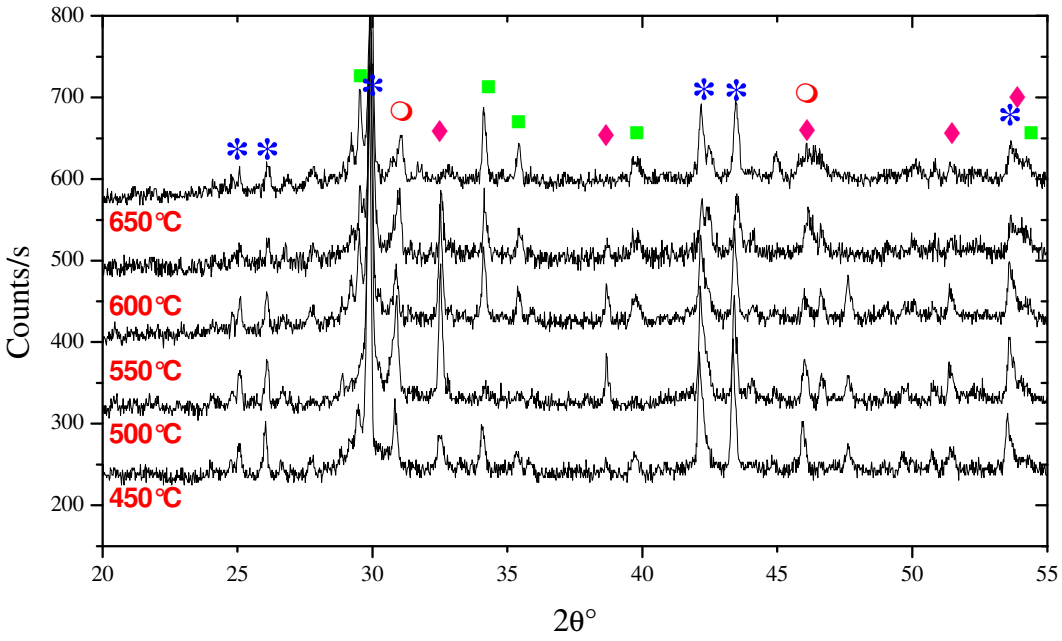

Figure 4-4 X-ray patterns and phase identification between the temperature range 450-650 °C for the stoichiometric mixture $LaFe_3CoGe_6Te_6$. Reflections belonging to the same phase have been marked with the same symbol: GeTe (blue stars), $LaTe_2$ (green squares), $CoGe_{1.5}Te_{1.5}$ (pink ovals) and Fe_3Te_2 (red empty circles).

The failure of the synthesis of the target compound $LaFe_3CoGe_6Te_6$ may be attributed to both a synthetic and a stability problem. It is well known that traditional solid-state synthesis results solely in thermodynamically stable products because of the high temperature needed to obtain a reasonable diffusion rate of the reactants.

Since there is little control over the reaction intermediates, it can be very difficult to prevent the formation of impurity phases [314,315]. It is also well known that metastable phases unattainable by means of traditional metallurgical methods have been synthesized by non-traditional synthetic methods such as the multilayer repeat or thin-film technique [84] or mechanical alloying [316].

Table 4-4 Temperature conditions and resulting phases obtained during the synthesis attempt of $LaFe_3CoGe_6Te_6$ (F = fast scan, S = slow scan).

Sample	File	Quench	Temp	firings	Identified phases	Scan
1	GS498	N	400 °C	3	GeTe	F
16	GS524	Y	400 °C	2	GeTe	F
2	GS523	N	450 °C	2	GeTe, $LaTe_2$, $CoGe_{1.5}Te_{1.5}$	S
3	GS544	N	500 °C	3	GeTe, $LaTe_2$, $CoGe_{1.5}Te_{1.5}$	S
17	GS545	Y	500 °C	4	GeTe, $LaTe_2$, $CoGe_{1.5}Te_{1.5}$	S
4	GS529	N	550 °C	3	GeTe, $LaTe_2$, $CoGe_{1.5}Te_{1.5}$	S
5	GS541	N	600 °C	4	GeTe, $LaTe_2$, $CoGe_{1.5}Te_{1.5}$	S
18	GS542	Y	600 °C	2	GeTe, $LaTe_2$, $CoGe_{1.5}Te_{1.5}$	S
6	GS550	N	650 °C	4	GeTe, $LaTe_2$, $CoGe_{1.5}Te_{1.5}$	S
7	GS533	N	700 °C	2	GeTe	F
19	GS534	Y	700 °C	2	GeTe	F
8	GS551	N	750 °C	3	GeTe	F
9	GS530	N	800 °C	2	GeTe	F
20	GS532	Y	800 °C	3	GeTe	F
10	GS552	N	850 °C	2	GeTe	F
11	GS525	N	900 °C	3	GeTe	F
21	GS528	Y	900 °C	2	GeTe	F
12	GS543	N	950 °C	2	GeTe	F
13	GS522	N	1000 °C	4	GeTe	F
22	GS552	Y	1000 °C	2	GeTe	F
14	GS546	N	1050 °C	3	GeTe	F
15	GS531	Y	1100 °C	3	GeTe	F

Even the synthesis of the filled skutterudite $La_{0.75}Fe_3CoSb_{12}$ has been reported by spark plasma sintering [317]. It is likely that full occupancy of the voids in ternary skutterudites is hindered by thermodynamics. Given the recent results on the filling of ternary skutterudites, where compounds such as $Yb_xCo_4Ge_6Te_6$, $La_xCo_4Ge_6Te_6$, synthesized by the group of Navrátil *et al.* [248,318], and $RE_xCo_4Ge_6Se_6$ (RE = Ce, Yb, Eu), synthesized by Lin *et al.*, all having $0 \leq x \leq 0.3$, several conclusions may be drawn

[59]. The fact that fully filled ternary skutterudites have not been yet reported (only partially filled systems) nor charge-compensated partially filled skutterudites, tell us about the difficulty of filling these systems; comparable to that found in synthesizing cerium-filled Co_4Sb_{12}-based skutterudites [78]. Attempts to synthesize fully filled $CeCo_4Ge_6Se_6$ as well as samples with high concentration of filler atom by means of both a traditional high temperature and a thin-film technique were carried out by Lin *et al*. without success [59]. This evidence may indicate that ternary uncompensated skutterudites behave analogously to Co_4Sb_{12}-based systems as to the type and amount of filler atom that can be inserted into the cavities (section 1.2.3).

Charge-compensation at the cation site has been attempted in the present work to facilitate the diffusion of lanthanum into the interstitial sites without success. Nevertheless, Lin *et al*. have found a correlation between the cerium filling fraction and the Ge / Se ratio [59]. They realized that increasing such ratio, *i.e*. increasing the electron-poorer anion and lowering the electron-richer anion concentration, led to an increment in the amount of cerium incorporated into the voids. This leaves a door open towards further improvement of the filling fraction limit in the near future.

Table 4-5 Refined lattice parameters of the identified phases in those X-ray patterns in which a sufficient number of reflections is observed.

		GeTe		$LaTe_2$		$CoGe_{1.5}Te_{1.5}$
Sample	**File**	***a***	***c***	***a***	***c***	***a***
1	GS498	4.1684(9)	10.635(9)	-	-	-
16	GS524	4.169(3)	10.62(3)	-	-	-
2	GS523	4.168(3)	10.65(3)	4.53(1)	9.20(6)	8.709(6)
3	GS544	4.171(2)	10.65(3)	-	-	8.714(3)
17	GS545	4.166(4)	10.57(4)	-	-	-
4	GS529	4.172(1)	10.670(9)	4.542(3)	9.15(1)	8.713(3)
5	GS541	4.152(8)	10.56(6)	4.536(4)	9.15(2)	8.704(2)
18	GS542	4.165(1)	10.65(1)	-	-	-
6	GS550	4.170(2)	10.68(1)	4.538(4)	9.16(2)	-
7	GS533	4.155(5)	10.55(3)	-	-	-
19	GS534	4.166(6)	10.64(6)	-	-	-
8	GS551	4.161(4)	10.64(3)	-	-	-
9	GS530	4.155(6)	10.68(4)	-	-	-
20	GS532	4.168(1)	10.72(2)	-	-	-
10	GS552	4.164(2)	10.62(2)	-	-	-
11	GS525	4.162(3)	10.66(3)	-	-	-
21	GS528	4.168(1)	10.688(9)	-	-	-
12	GS543	4.163(3)	10.65(1)	-	-	-
13	GS522	4.168(4)	10.62(3)	-	-	-
22	GS552	4.171(1)	10.670(7)	-	-	-
14	GS546	4.157(3)	10.67(3)	-	-	-
15	GS531	4.1740(6	10.65(5)	-	-	-

Lin *et al.* rationalized the synthetic failure of highly concentrated filled ternary skutterudites as the impossibility for the crystal lattice to expand any further [59]; which, in turn, is related to previous work carried out by Takizawa *et al*. on high-pressure filling of Co_4Sb_{12}-based skutterudites [319]. They attributed the low filling threshold to the inability of the Sb-Sb bonds to stretch while maintaining the crystal structure stability. On the other hand, the stability problem when high concentrations of filler atom are present has been studied theoretically by Zhang *et al*., who have demonstrated that the filling fraction limit of a skutterudite void is determined by the competition between the formation of filled skutterudites and secondary phases formed between the filler and the host atoms [320]. Thus, if the filling fraction exceeds the limit, the unit cell expands whereby destabilizing the filled skutterudite and leading to the collapse of the structure into thermodynamically more stable secondary phases. This may explain why a mixture of a partially filled ternary skutterudite and other phases is not obtained, but mostly binary phases and a small amount of the ternary skutterudite (Figure 4-4).

Chapter 5

Equiatomic ternary phases MGeTe M = Co, Rh

5.1 Introduction

Attempts to synthesize the ternary skutterudite $RhGe_{1.5}Te_{1.5}$ in powder form led to the identification of the new phase RhGeTe. The crystal growth of CoGeTe was successfully accomplished, whereas RhGeTe could only be synthesized in powder form. The occurrence of equiatomic ternary compounds whilst studying skutterudites has already been reported in the past by Wojciechowski *et al*. [104,321]. They identified the phase CoSbTe as an impurity while doping the skutterudite $CoSb_3$ with tellurium, which is isostructural to FeSbTe [322]. Navrátil *et al*. accidentally synthesized two different compounds during another investigation on a ternary skutterudite with nominal composition $CoGe_{1.5}Te_{1.5}$, owing to thermal gradients present during the reaction [108]. They determined the stoichiometry to be $CoGe_{1.70}Te_{1.47}$ and $CoGe_{1.15}Te_{1.05}$. The former compound was assigned the skutterudite structure, whereas the latter was indexed according to the orthorhombic space group P*mmm* with unit cell dimensions a = 11.134 Å, b = 6.233 Å and c = 6.194 Å. The powder pattern of $CoGe_{1.15}Te_{1.05}$ shown is very similar to that of CoGeTe (section 5.3). In this chapter, the structure determination by single-crystal X-ray diffraction of CoGeTe is presented as well as the structure of RhGeTe determined by powder X-ray diffraction making use of the single crystal model. Moreover, their thermoelectric and magnetic properties are measured and assessed in relation to other state-of-the-art thermoelectric materials.

5.2 Synthesis

CoGeTe single crystals were grown by the temperature gradient technique using iodine as transporter agent. A mixture of cobalt (Alfa Aesar, 99.8%), germanium (Alfa Aesar, 99.999%) and tellurium, (Alfa Aesar, 99.999%) was ground in an agate mortar and sealed into an evacuated ($< 10^{-4}$ Torr) silica ampoule. The tube in which crystals were grown had the same size as those used for synthesis in powder form, *i.e*. 12-13 cm long and 1 cm across. The tube was placed into a chamber furnace with the top end close to the door, where a small temperature gradient is known to exist (between 2-5 °C), for 6 days at 700 °C before cooling down to room temperature at natural rate. CoGeTe single crystals were found as aggregates along with the powder at the hot end of the tube and were characterized by single crystal X-ray diffraction (data collected by Ms Patricia Leyva).

CoGeTe and RhGeTe were synthesized in powder form following identical procedures for both of them. Stoichiometric amounts of the elements cobalt (Alfa Aesar, 99.5%), rhodium (Goodfellow, 99.9%), germanium (Aldrich, 99.99%) and tellurium (Aldrich, 99.997%) were ground in an agate mortar prior to sealing into an evacuated ($< 10^{-4}$ Torr) silica tube. Germanium powder was pretreated under a 5% H_2/N_2 reductive atmosphere at 600 °C for several hours to eliminate traces of germanium oxide. The tube inner walls were coated with a layer of pyrolitic carbon to avoid reactions with the silica. The mixture was placed directly into a furnace at 440 °C for 36 hours. The temperature was then increased slowly (0.5 °C min^{-1}) up to 580 °C and left for 10 days before the furnace was cooled down to room temperature at natural cooling rate. Following regrinding, the sample was placed into a second evacuated silica tube for refiring directly at 580 °C for 2 days, then it was slowly cooled down to room temperature at 0.5 °C min^{-1}. The resultant black powder was analysed by powder X-ray diffraction. The synthesis of IrGeTe was also attempted following an identical procedure; however, a mixture of phases consisting of the ternary skutterudite $IrGe_{1.5}Te_{1.5}$ and elemental iridium were obtained instead.

5.3 Structural characterization of MGeTe (M = Co, Rh)

The structure of CoGeTe was determined by single-crystal X-ray diffraction (section 2.2.2). Crystallographic information on the structure solution can be found in Table 5-1. The space group was determined to be P*bca*, with reflection conditions: $h = 0$, $k = 2n$; $k = 0$, $l = 2n$; $l = 0$, $h = 2n$. Such space group and the atom positions obtained were then used in the Rietveld refinement of both CoGeTe and RhGeTe X-ray powder diffraction data (Figure 5-3). Tabulated information of the atomic postions as well as relevent bond distances and angles extracted from the Rietveld refinements can be found in Table 5-3 and Table 5-4.

The most characteristic feature of this type of structure is the metallic bond between pairs of cobalt atoms oriented along the [011] and [$0\,\bar{1}\,1$] directions alternatively, whose centres form a fcc-type lattice elongated along *c* (Figure 5-1). From this point of view, the MGeTe structures can be regarded as formed by layers of dimers whose metal-metal bonds alternate in orientation. The asymmetric unit cell contains three atoms in general positions. From a polyhedral point of view, M atoms are octahedrally coordinated by

three germanium and three tellurium atoms in an antiprismatic configuration, sharing a germanium-germanium edge to form $[M_2Ge_4Te_6]$ dimers.

Table 5-1 Single crystal data for CoGeTe.

Formula	CoGeTe
M_w	259.14
Crystal system	Orthorhombic
Space group	P*bca*
a	6.1930(4)
b	6.2326(4)
c	11.1289(7)
Z	8
μ /mm^{-1}	34.55
Measured data	3381
Unique data	642
Observed data I>2σ(I)	599
R_{int}	0.033
Residual electron density (min, max) / eÅ^{-3}	(-5.51, 2.05)
R(F^2)	0.039
$_w$R(F^2)	0.031

Thus, each octahedron is coordinated to ten other octahedra by corner sharing and to one octahedron by edge sharing. The coordination between layers of metal atoms along the *c*-axis is alternatively pyrite type and marcasite type, analogously to α–$NiAs_2$ (section 1.3.2). The tellurium atoms maintain a pyrite-like packing arrangement, whereas germanium is packed in a marcasite environment (Figure 5-4).

CoGeTe and RhGeTe can then be regarded as a ternary ordered variant of the α-$NiAs_2$ structure. Anion disorder is highly unlikely as the smaller anions occupy the marcasite-type edge-sharing positions, allowing the metal-metal interaction to take place; whereas larger anions occupy pyrite-type positions instead. This behaviour is observed also in all the ternary α-$NiAs_2$-type compounds already known, where the smaller anion is always found in the marcasite-type environment and in the edge-sharing positions of the dimers (Table 1-10).

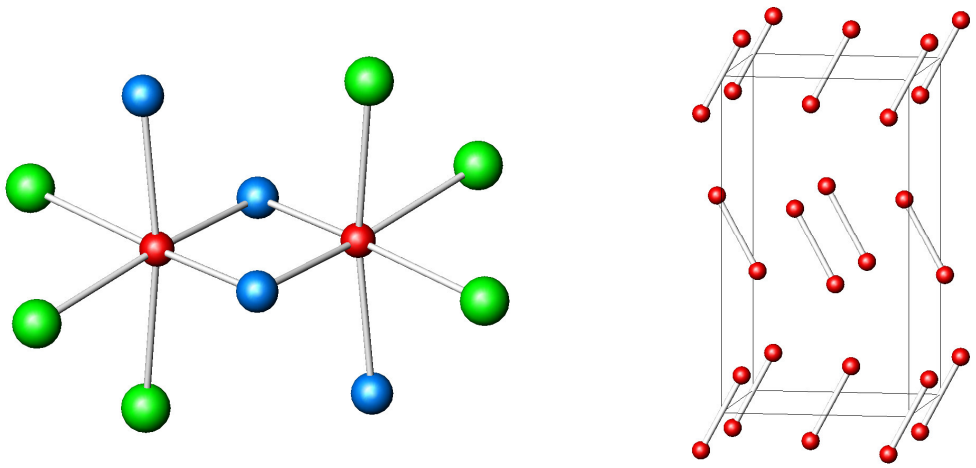

Figure 5-1 Left: $Co_2Ge_4Te_6$ dimer view. Right: fcc-type lattice formed by the centres of the Co-Co bonds. Key: cobalt in red, germanium in blue and tellurium in green.

Further, disorder would lead to an anomalously small and an anomalously large isotropic thermal parameter for the germanium and tellurium atoms, respectively, during the Rietveld refinement of the powder X-ray diffraction data. However, this evidence has not been observed experimentally. MGeTe phases are then formed by a stacking sequence of pyrite-marcasite blocks along the unit cell *c* axis (Figure 5-2). The coordination of both blocks along with their respective FeS_2-pyrite and FeS_2-marcasite archetypes is shown in Figure 5-4. The thickness of such blocks can be compared to obtain information as to the distortion of the structure (Table 5-2). Such thickness is calculated as the distance between cobalt atom layers along the *c*-axis delimiting either a pyrite or a marcasite block.

For the compounds CoSSb, PtSiTe, PtSiSb, CoSeAs, CoGeTe and RhGeTe the pyrite blocks are thicker than the marcasite blocks, whereas for the others, this trend is reversed. It is seen that the difference between the two types of blocks can be accounted for by size effects in CoSSb, PtSiTe and CoSeAs, being the latter compound less distorted given the smaller difference in anion size when compared to the former two. However, larger differences (~ 0.8 Å) are caused by an extra structural distortion, consisting of bond formation between the metal atoms as seen in PtSiSb [162]. The difference between the pyrite and the marcasite block for CoGeTe and RhGeTe is similar to that of CoSSb and PtSiTe (Table 5-2). Germanium is an element from the fourth period much closer to tellurium than third-row elements to argue exclusively anion size differences. Therefore, the smaller anion size difference is most likely offset by the metal-metal pairing distortion, having both phenomena additive effects as to the difference between pyrite and marcasite blocks.

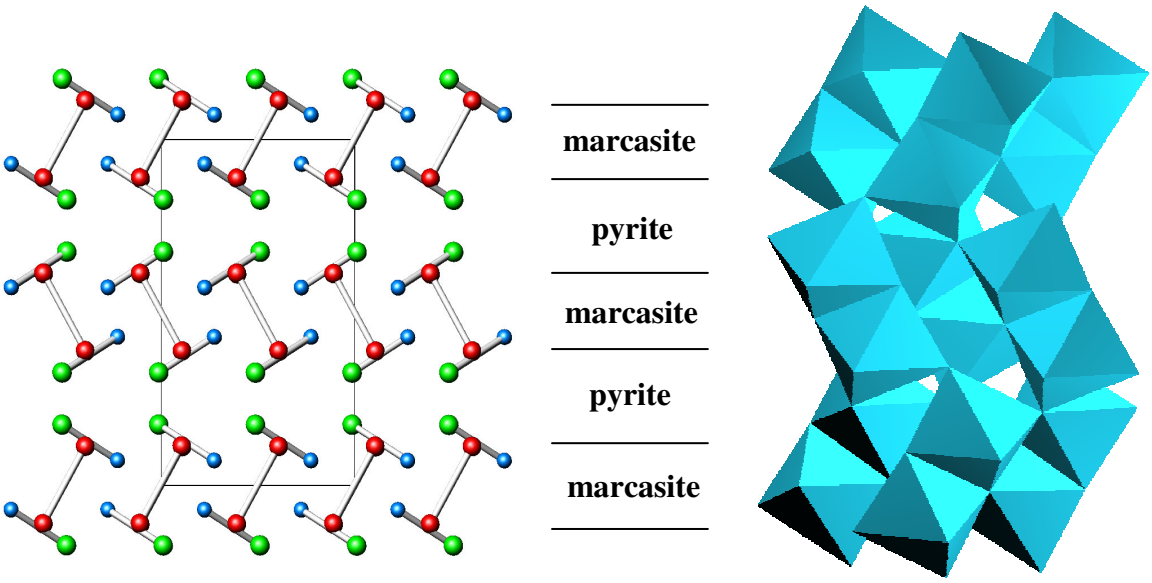

Figure 5-2 Left: View along the *a*-axis showing the anion-anion pairs and the metal-metal bonds in MGeTe (M = Co, Rh). Right: polyhedral representation of the same view. Marcasite and pyrite blocks are highlighted for clarity. Key: metal atom in red, germaniun in blue and tellurium in green.

Table 5-2 Thickness (Å) of pyrite and marcasite blocks in α–$NiAs_2$-type compounds and the difference (Δ) between them.

Compound	pyrite	marcasite	Δ	ref
α-$NiAs_2$	2.839	2.871	-0.032	[166]
PtSiTe	3.332	2.857	0.475	[165]
PtSiSb	3.250	2.448	0.802	[162]
CoSeAs	3.060	2.864	0.196	[166]
CoPSe	2.774	2.819	-0.045	[166]
CoSSb	3.165	2.653	0.512	[167]
IrPTe	-	-	-	[169]
$PtBi_2$	3.208	3.465	-0.257	[168]
CoGeTe	2.983	2.493	0.490	this work
RhGeTe	3.199	2.546	0.546	this work

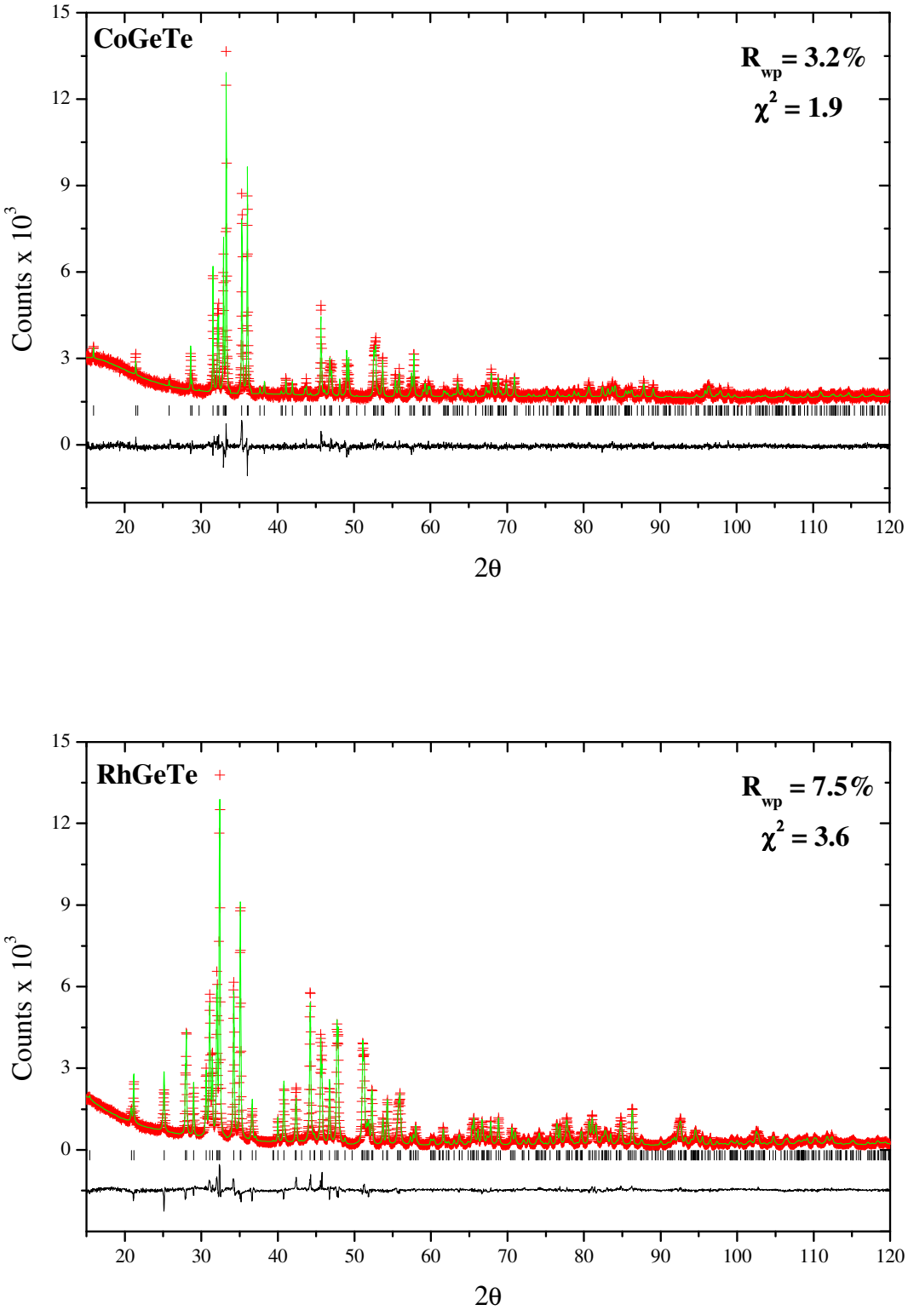

Figure 5-3 Rietveld refinement of powder X-ray diffraction data of the compound CoGeTe (top) and RhGeTe (bottom). Red crosses: experimental data. Green line: fitted model. Black bottom line: difference curve. Black markers correspond to MGeTe reflections. Space group P*bca*.

Table 5-3 Refined parameters for MGeTe (M = Co, Rh). Space group P*bca*. CoGeTe single-crystal data is included for comparison.

		$CoGeTe^S$	$CoGeTe^P$	RhGeTe
a	Å	6.1930(4)	6.1882(1)	6.3575(2)
b	Å	6.2326(4)	6.2302(1)	6.3875(2)
c	Å	11.1289(7)	11.1236(2)	11.4896(4)
M 8*c*	*x*	0.50163(9)	0.4951(7)	0.4974(3)
	y	0.60783(8)	0.6059(6)	0.6111(3)
	z	0.61125(4)	0.6096(4)	0.6108(2)
	B / Å^2	0.25(2)	1.3(1)	0.70(4)
Ge 8*c*	*x*	0.16410(8)	0.1622(5)	0.1536(3)
	y	0.77030(7)	0.7734(6)	0.7689(4)
	z	0.56936(3)	0.5714(3)	0.5728(2)
	B / Å^2	0.39(2)	0.51(5)*	0.58(3)*
Te 8*c*	*x*	0.61845(4)	0.6202(3)	0.6161(2)
	y	0.98830(4)	0.9884(4)	0.9965(2)
	z	0.67523(2)	0.6748(2)	0.6741(1)
	B / Å^2	0.29(2)	0.51(5)*	0.58(3)*
R_{wp}	%	3.1	3.2	7.5
χ^2		-	1.9	3.6

S Single crystal data
P Powder data
***Anion isotropic thermal parameters have been constrained to the same value.**

The Co-Ge-Co or Rh-Ge-Rh bridge angle is much smaller than in α–$NiAs_2$ (73.2° *vs.* 117.7°), being a measure of the metal-metal interaction strength, since the value of this angle is a compromise between the metal-metal bond and the structural integrity of the phase. As the two octahedra approach to fulfil the metal-metal bonding requirements, the axial ligands are pushed away owing to the steric repulsion causing the bridge Ge-Co(Rh)-axial Te angle to change from 88.0° to 100.6° (99.6°) (Table 5-4).

The Co-Ge distances are as short as those found in CoGe (2.35-2.62 Å) [323] and the Co-Te distances are very similar to those found in the marcasite-type $CoTe_2$ (2.58-2.60 Å) [324]. The [$CoGe_3Te_3$] octahedra share a Ge-Ge edge to form [$Co_2Ge_4Te_6$] dimers with a metal-metal distance of 2.830(9) Å (Table 5-4). This distance is 0.3 Å larger than that found in Co metal (2.52 Å). Nevertheless, it is much shorter than twice the Co van der Waals radius (2.00 Å) and it is regarded as bonding when compared to the second shortest Co-Co distance (4.380(7) Å) and to other Co compounds with similar metal-metal bonding distances, such as CoAs [325].

Table 5-4 Relevant angles (°) and bond distances (Å) in the compounds MXY (M = Co, Rh, Ni, Pt; X = Ge, Si, As_I; Y = Te, Sb, As_{II}).

	$CoGeTe^S$	$CoGeTe^P$	$RhGeTe^P$	$PtSiSb$[162]	α–$NiAs_2$[161]
M-M	2.818(1)	2.822(10)	2.916(3)	2.857	3.531
M-X	2.3726(7)	2.365(6)	2.427(3)	2.394	2.389
M-X	2.3690(7)	2.354(6)	2.446(3)	2.427	2.398
M-X	2.3867(7)	2.380(6)	2.455(3)	2.430	2.415
M-Y	2.5990(6)	2.581(5)	2.676(2)	2.696	2.354
M-Y	2.5686(6)	2.575(5)	2.665(2)	2.680	2.367
M-Y	2.5794(6)	2.600(5)	2.676(3)	2.685	2.347
X-Y	2.7458(6)	2.745(5)	2.706(3)	2.584	2.449
M-X-M	135.87(3)	136.4(3)	133.8(1)	130.8	124.5
M-X-M	132.67(2)	131.8(2)	130.1(1)	128.4	121.0
M-X-M	72.60(2)	73.2(2)	73.34(9)	72.1	97.0
M-X-Y	101.91(2)	103.0(2)	104.5(1)	107.2	102.9
M-X-Y	106.97(2)	106.6(2)	108.3(1)	108.2	104.4
M-X-Y	101.43(2)	101.5(2)	103.0(1)	105.8	97.5
X-M-X	87.64(2)	88.7(2)	89.16(8)	96.4	91.1
X-M-X	94.05(2)	94.7(2)	94.54(7)	90.7	85.9
X-M-X	107.40(2)	106.8(2)	106.66(9)	107.9	83.0
X-M-Y	84.77(2)	84.7(2)	85.49(8)	90.9	91.7
X-M-Y	94.05(2)	92.7(2)	92.10(9)	87.8	95.1
X-M-Y	101.09(2)	100.6(2)	99.60(9)	87.2	88.0
X-M-Y	86.52(2)	85.7(2)	86.98(8)	96.9	86.2
X-M-Y	78.63(2)	78.3(2)	79.24(8)	79.9	97.2
X-M-Y	79.66(2)	80.4(2)	80.34(8)	78.8	83.8
Y-M-Y	86.17(2)	85.7(2)	85.50(6)	84.5	95.9
Y-M-Y	85.73(2)	85.6(2)	85.33(6)	83.9	86.6
Y-M-Y	95.25(2)	95.4(2)	94.40(5)	93.5	96.4
M-Y-M	116.56(2)	117.1(2)	116.00(8)	115.2	121.0
M-Y-M	115.83(2)	115.7(1)	115.25(6)	114.7	124.5
M-Y-M	115.62(2)	115.3(2)	115.18(8)	116.3	97.0
M-Y-X	107.33(2)	107.1(2)	107.22(7)	107.6	109.1
M-Y-X	106.92(2)	106.2(1)	106.88(7)	105.7	102.1
M-Y-X	91.52(2)	91.1(2)	92.90(7)	93.9	101.0

^{S} Single-crystal data
^{P} Powder data

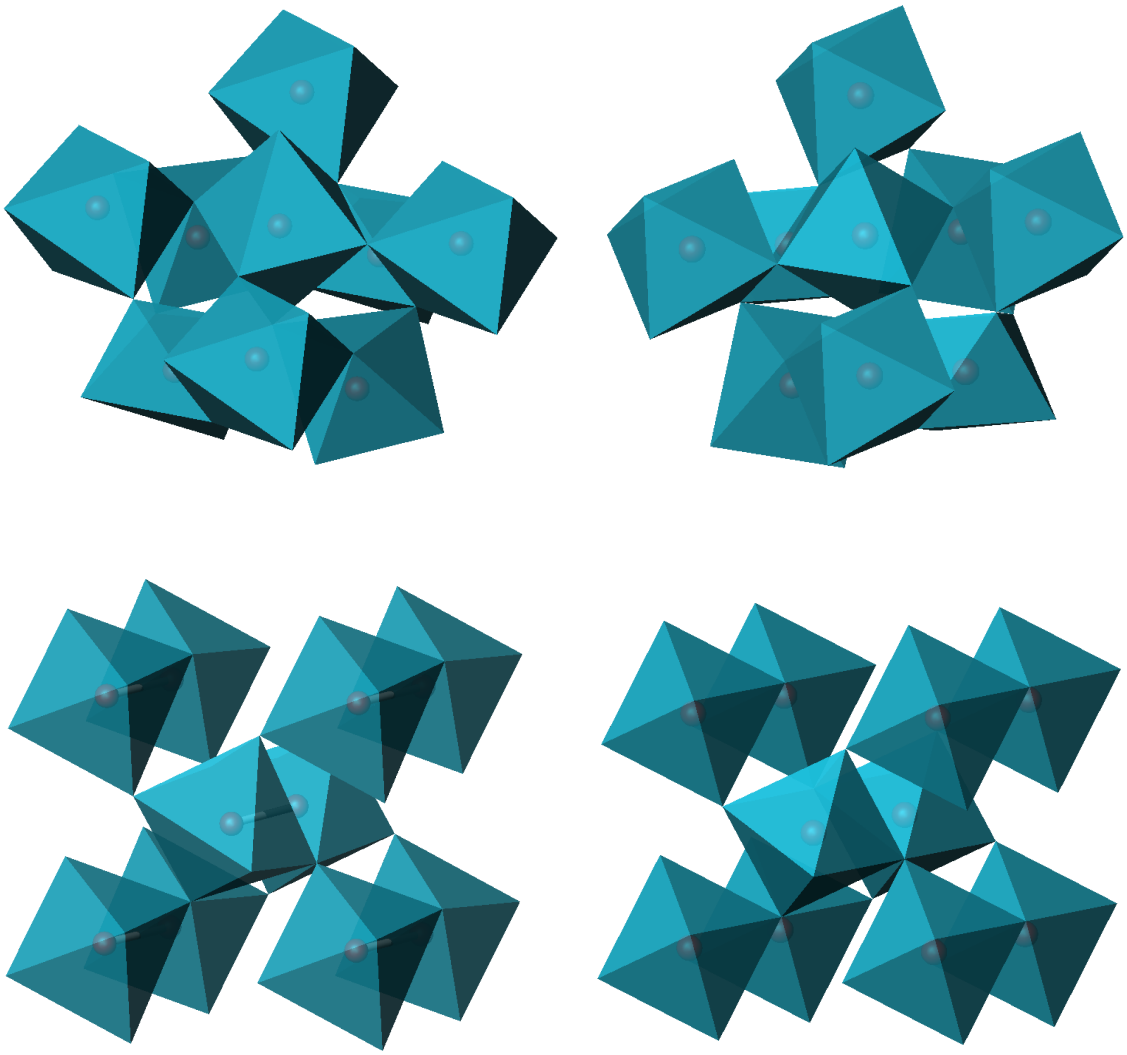

Figure 5-4 Top left: CoGeTe pyrite block coordination environment. Top right: FeS_2 pyrite coordination environment. Bottom left: CoGeTe marcasite block coordination. Bottom right: FeS_2 marcasite octahedra arrangement. Key: metal atoms in red.

The Rh-Rh distance is 2.916(3) Å, only 0.23 Å longer than that of the metal. The Rh-Ge distances are also shorter than those found in RhGe (2.92 Å) but comparable to those found in the metal-rich compound Rh_5Ge_3 (2.46-2.82 Å). The Rh-Te distances, however, are slightly larger than those of the pyrite-like compound $RhTe_2$ (2.676(2) and 2.665(2) Å *vs*. 2.659 Å). This fact can be linked to the shorter Ge-Te distance in RhGeTe (2.706(3) Å) than in CoGeTe (2.745(3) Å). The bonding interaction between the metal and the anions will result in depletion of the electron density on the anion-anion pairs and *vice versa*, as it was pointed out in a study of the bonding in pyrite, marcasite and arsenopyrite type structures [150].

From the anion point of view, Ge and Te are found in tetrahedral coordination to three Co atoms and one Te or Ge atom, respectively. The anion pairs are also characteristic of this structure type (section 1.3.2) and their bond length is shorter (2.70-2.75 Å) than Ge-Te distances seen in GeTe (2.842 Å). The analogy between pyrite and marcasite tetrahedra and As_I and As_{II} tetrahedral environments, respectively, in α–$NiAs_2$ has been highlighted elsewhere [166]. On the other hand, the CoGeTe pairing distortion affects the ideal tetrahedral coordination of the germanium atoms severely as seen in the value of the tetrahedral angle M-A-M (Table 5-4). Nevertheless, the Te coordination environment remains unaffected and resembles that observed around sulphur in pyrite, where the Fe-S-Fe angle amounts to 115.38°. Alternatively, the structure can be described by considering the undistorted tellurium-centred tetrahedra, which form layers of tetrahedra bound one another by Co-Co (Rh-Rh) bonds in alternate directions. These layers can be decomposed in chains of pyrite-like tetrahedra linked as in the marcasite structure which, in turn, are rotated 180° alternatively to form a 2D array of corner-sharing tetrahedra (Figure 5-5).

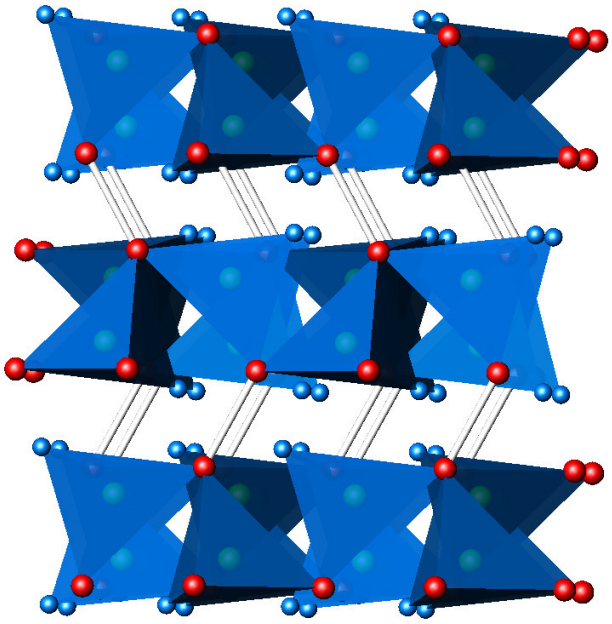

Figure 5-5 $TeCo_3Ge$ tetrahedra forming layers bound to each other by Co-Co bonds in alternate orientation. Key: Co in red, Ge in blue, Te in green.

α–$NiAs_2$-type structures usually undergo a phase transformation at high temperature (nearly 800 °C) to a marcasite-type structure. Such transformation is of reconstructive nature, owing to the change in the coordination number of the octahedra, and there is no group-subgroup relation between them.

This type of non-symmetry related phase transitions is common in nature [326]. It has been observed in CoAsSe and $NiAs_2$ and it has not been studied in depth yet for CoSSb and CoPSe, nor for any of the other related compounds.

Moreover, α–$NiAs_2$-type phases, under high pressure and high temperature, also undergo another reconstructive phase transition to a FeS_2-pyrite-type structure, either with complete anion disorder (space group $Pa\bar{3}$) or with anion ordering (space group $P2_13$) as seen in the ullmannite structure [166]. Reconstructive transformations follow a common pattern whenever pressure and/or temperature are present. High temperatures favour lower coordination numbers (marcasite-type octahedra *vs*. marcasite / pyrite-type octahedra) and high pressures favour higher coordination numbers (pyrite-type octahedra *vs*. marcasite or marcasite / pyrite-type octahedra) [327]. It is then not surprising that the same type of phase transitions occurs for the arsenopyrite-type compounds, owing to its close resemblance to the FeS_2-marcasite [166]. CoGeTe and RhGeTe may undergo the same type of phase transition leading to the marcasite orthorhombic space group P*nnm*. Likewise, at high pressure both phase will may also undergo a transformation to a pyrite-like phase, either anion-ordered or anion-disordered. Nevertheless, a recent publication about the CoGeTe structure shows differential thermal analysis data indicating the incongruent melting and decomposition into GeTe, CoGe and $CoTe_2$ at approximately 725 °C [328].

Nevertheless, the question as to why ternary MGeTe phases crystallize in the P*bca* space group is still unclear. It does not seem to be a simple relation based on the electron count. ZrSiS-type structures, possessing low valence electron counts, are formed by early transition metals, including lanthanides and actinides. Cobaltite-type structures possess the same number of valence electrons as pyrite and marcasite structures (20 e^- or 21 e^-); however they are exclusively formed by group 9 and group 10 transition metals with pnictogens and chalcogens. FeAsS-type compounds are mainly formed by group 8 transition metals (except IrAsSb), pnictogens and chalcogens; possess the same electron count as CoGeTe (19 e^-) and also show metal-metal pairing. Therefore, *a priori*, it should be natural to think that CoGeTe is formed by isoelectronic substitution at the anion site in $CoSb_2$, as it was first suggested by Navrátil *et al*. [108]. Instead, it crystallizes in the α–$NiAs_2$ group, whose members possess a 20 e^- count and occurs between transition metals from group 9 and group 10, pnictogens, chalcogens and, also group 14 main group elements.

There exists only one member with a 19 e^- count, PtSiSb, which is offset by metal-metal pairing in order to obtain a filled-shell configuration, in full analogy to the situation found in CoGeTe. Hence, cation pairing is ruled out to account for the stabilization of the α-$NiAs_2$ against the arsenopyrite structure, as it has also been ruled out to explain the stability of the arsenopyrite against the marcasite structure [329].

The problem bears a close resemblance to that of the arsenopyrite stabilization and the results can be extrapolated to our discussion owing to the evident similarities among the three compounds. Kjekshus *et al*. ascribe the difference between the marcasite and the arsenopyrite to variations in the bonding character of the metal-anion bonds [330]. The same reason has been argued to justify the existence of two different types of marcasite compounds, namely, the "anomalous" marcasite, possessing large *c/a* and *c/b* ratios, and the "Jahn-Teller" marcasites. They are grouped in two different values of the octahedral angle X-M-X which is intimately coupled to the length of the *c* axis [331].
The main structural difference between the α–$NiAs_2$-type and the arsenopyrite dimer is the dihedral angle formed by the plane containing the metal-metal bond along with the two germanium atoms and the plane containing the two equatorial tellurium atoms along with one cobalt atom (Table 5-5). There is a four-fold increase in the dihedral angle when compared to the ideal -180° coplanar value. This extra distortion in the α–$NiAs_2$ dimer may be linked to its stability with respect to the arsenopyrite.

Table 5-5 M-X-M-Y dihedral angle (°) in MXY compounds crystallizing in α–$NiAs_2$ and arsenopyrite structures.

α-$NiAs_2$-type	dihedral	$CoSb_2$-type	dihedral
α-$NiAs_2$	-172.8	$CoSb_2$	-178.1
PtSiTe	-164.2	FeSAs	-178.2
PtSiSb	-172.2	OsSAs	-178.4
CoAsSe	-173.5	RuSAs	-179.3
CoPSe	-173.6		
CoSSb	-167.8		
$PtBi_2$	-173.8		
CoGeTe	-172.3		
RhGeTe	-175.1		

Moreover, it is worth noticing that α-$NiAs_2$-type structures are packed so that heavy elements from groups 15 and 16 never occupy edge-sharing positions. They lie at the boundaries between pyrite and marcasite blocks at a distance from each other that resembles that of the elements (Figure 1-9). It turns out that As, Se, Sb, Te and Bi all

crystallize in layered rhombohedral structures and the Y-Y distances are very close to the interlayer distances found in the elements, emphasizing the extra anion-anion interaction that contributes to the stabilization of the phase (Table 5-6).

Table 5-6 B-B bond distance (Å) in MXY compounds with the α–$NiAs_2$ structure. Interlayer distance in the elements (Y) is also shown.

α-$NiAs_2$-type	Y-Y	element
α-$NiAs_2$	3.3	3.1
PtSiTe	3.5	3.5
PtSiSb	3.6	3.4
CoAsSe	3.2	3.4
CoPSe	3.1	3.4
CoSSb	3.3	3.4
$PtBi_2$	3.8	3.5
CoGeTe	3.5	3.5
RhGeTe	3.6	3.5

Bond-valence calculations have been attempted to find the oxidation state of the cobalt atom, taking advantage of the existing relation between bond strength and bond length. The concept of bond valence, *i.e*. the amount of valence associated with a particular bond, accounts for the fact that it is always possible to distribute the valence of an atom among the bonds it forms. Therefore, the total bond valence received by an atom is equal to its atomic valence, this is known as the *valence sum rule*. Moreover, there are two more rules, the *equal valence rule* and *the bond length-bond valence correlation* that conform the foundations of the bond valence model. The equal valence rule states that the sum of bond valences around any loop in the bond network, having regard to the direction of the bond, is zero. The first and second rules are equivalent to say that the valence of each atom is distributed as uniformly as possible among the bonds it forms [332]. The third rule is explained in the following paragraph.

The bond valence model assumes an ionic model of the crystal lattice, in which formal positive and negative charges can be assigned to cations and anions, respectively. In organic compounds the coordination number is often equal to the valence and sometimes the word valence is used as a synonym of coordination number. Most of the times, to describe de bonding in such compounds, a formalism based on single, double and triple bonds is enough.

It has been experimentally observed that bond valence correlates very well with bond length. These correlations have been studied for many different types of bonds by

examining large numbers of crystal structures, and they proved to be accurate to 0.05 valence units. Hence, the bond valence distribution can be accurately calculated through a determination of the crystal structure. Taking into account the above-mentioned assumptions, experimental bond valences can be used to identify elements with poor X-ray contrast or light elements difficult to locate by means of X-rays. Also, if several atoms have low valences, it may indicate that a molecule of solvent of crystallization has been missed during the structure determination or that significant bonds have been overlooked. The model has some limitations linked to the fact that it does not take into account non-bonding interactions. It works well in crystals where the assumption of two-body interactions is valid, *i.e*. in crystal structures where there are no delocalized bonds. However, the model cannot predict distortions caused by electronic effects, namely Jahn-Teller or sterically active lone pairs of electrons. Moreover, a network of valences is not enough to predict a whole crystal structure as information about the non-bonding interactions and the bond angles is also needed.

Bond-valence parameters have been tabulated for a series of metal-anion bonds from where the Co-Te and Rh-Te parameters (2.56 and 2.55) have been extracted [333].
Co-Ge and Rh-Ge bond-valence parameters are not tabulated and the equation provided by Brown *et al*. has been used to obtain an approximate value (1.605 and 1.790) [334]:

$$R_0 = r_C + Ar_A + P - D - F \qquad \textbf{(5-1)}$$

Where r_C and r_A are contributions of the cation and the anion, respectively, to the parameter R_0. A is a constant and P, D and F are contributions that depend on the number of non-bonding P, D and F electrons. The valence of the cation is then a contribution from each of the atoms it is bounded to, expressed by the equation:

$$V_i = \sum_j s_{ij} = \sum_j \exp\left(\frac{R_0 - r_{ij}}{B}\right) \qquad \textbf{(5-2)}$$

Where s_{ij} is the valence of the bond between atom i and atom j; r_{ij} is the interatomic distance between atom i and j and B is a constant which amounts to 0.37.
Within the CoGeTe structure, cobalt is bonded to three germanium and three tellurium atoms in octahedral coordination and to another cobalt atom forming a metal-metal bond. If momentarily the latter bond is not taken into account, the valence of the metal atoms, assuming an oxidation state of 2- for Te, would be:

$V_{Co} = 0.819 + 0.841 + 0.801 + 0.128 + 0.132 + 0.123 = 2.84$

$V_{Rh} = 0.711 + 0.733 + 0.711 + 0.179 + 0.170 + 0.166 = 2.67$

These values are close to three and the difference may be attributed to the numerical error existing when equation (4-1) is combined with equation (4-2), given that the latter contains and exponential term. On the grounds of what is known about the CoGeTe and RhGeTe structures, each metal atom shares one electron with another metal atom, forming a well-localized two-centre-two-electron single bond at the middle of the $M_2Ge_4Te_6$ dimer. The bond length is not that of the metal, but a compromise between bonding strength and octahedral distortion, which does not change the above-mentioned description. Provided that this description is correct and following the procedure for homoatomic bonds explained by O'Keeffe *et al*., the metal-metal bond can be assigned a valence of 1 [335]. This is consistent with the two-body-interaction assumption of the bond valence model as well as the second rule, stating that bonds between equal atoms have almost the same bond valence. The two metal atoms have exactly the same coordination environment, *i.e.* each metal atom is bonded to three germanium and three tellurium atoms and to one metal atom, and there is no metal-metal interaction other than the bond within the dimer. Therefore, assigning a bond valence value of 1 would be consistent with the observed transport and magnetic properties and also with the fact that the metal-metal bond length is close to that found in the metal (2.82 Å *vs*. 2.51 Å for Co, 2.92 Å vs. 2.69 Å for Rh). Overall, the cobalt atom in CoGeTe would possess a valence whose closest integer is 4+; which, as it will be seen later, is consistent with both the transport property and magnetic measurements.

5.4 Electrical resistivity

Electrical resistivity measurements were carried out between 77 K and 350 K (Figure 5-6). Both plots show how the resistivity decreases as the temperature rises, indicative of semiconducting behaviour. Plots of the resistivity logarithm against inverse temperature are also included in the insets to assess their agreement with an Arrhenius-type law:

$$\rho = \rho_0 e^{-\frac{Ea}{k_B T}} = \rho_0 e^{-\frac{\Delta E}{2k_B T}} \qquad \textbf{(5-3)}$$

Where ρ is the resistivity, ρ_0 the resistivity when $T \rightarrow \infty$ and E_a is the activation energy. Provided that intrinsic conduction is the only conduction mechanism present at high

temperature, the Fermi energy lies exactly in the middle of the band gap, ΔE, and amounts to twice the Arrhenius activation energy.

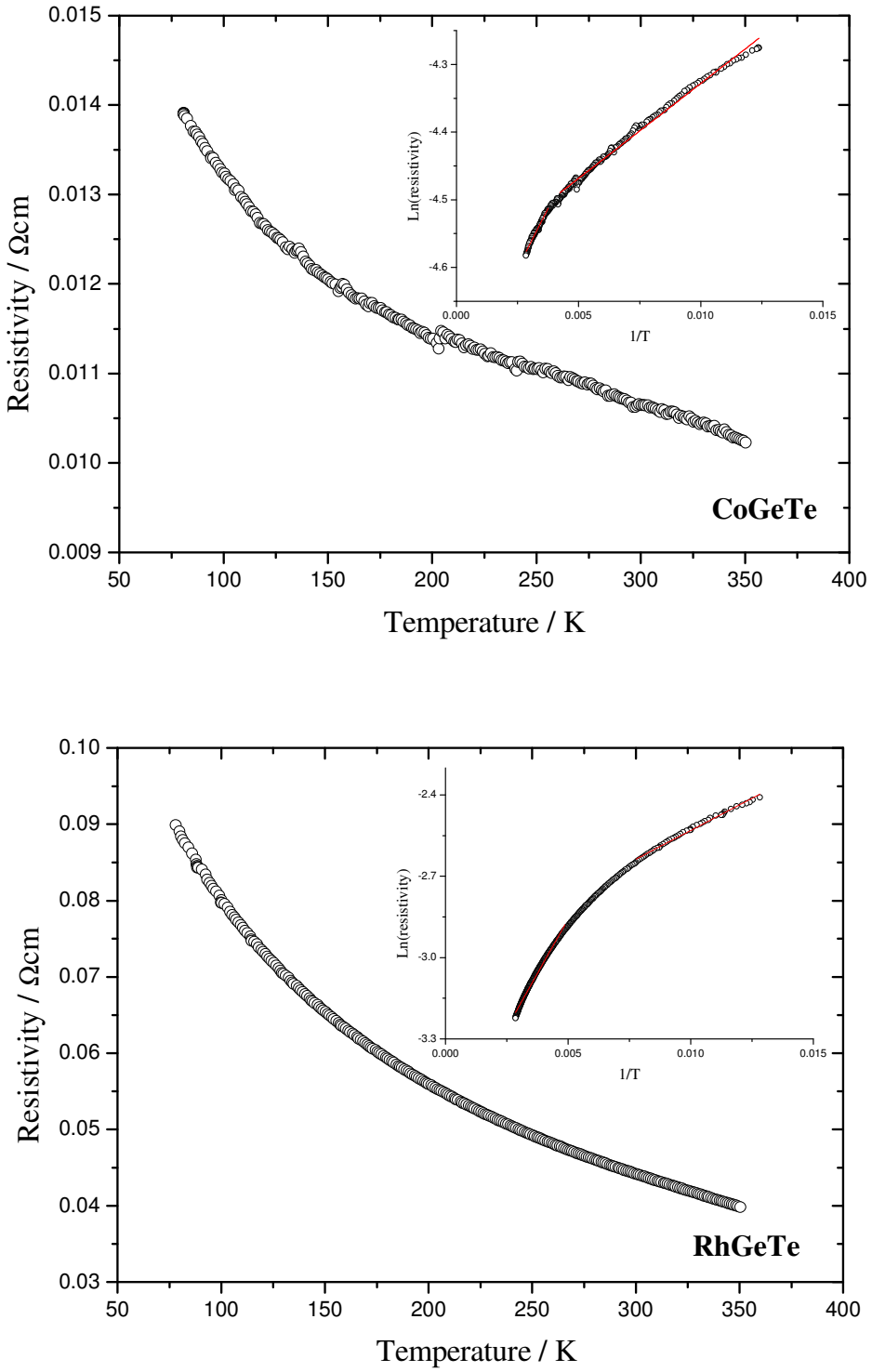

Figure 5-6 Resistivity vs. Temperature plots for CoGeTe (top) and RhGeTe (bottom). Insets: Natural logarithm of the resistivity vs. inverse temperature. Linear fittings at both ends of the curves are shown in red.

It is seen, however, that the data cannot be fitted to a single straight line throughout the whole temperature range, but to two linear fits at both the high-temperature and the low-temperature ends. This behaviour is typical of semiconductors with some degree of impurities.

These may originate from secondary phases forming a solid solution with the sample, defects in the crystal structure or vacancies due to small variations in the chemical composition. It has been shown that impurity levels as low as 20 ppm by weight can change dramatically the resistivity logarithm *vs*. inverse temperature plot from a straight line to a curve with two well-defined slopes in highly pure $NiO_{1+\delta}$ semiconducting samples [292]. Changes in the band structure originated by magnetic phase transitions may also cause a change in the slope of the Arrhenius plot, as seen in $NiCr_2S_4$ [288]. The resistivity is then best described by a sum of contributions taking into account the impurity conduction mechanism [336]:

$$\rho = \rho_1 e^{\frac{\Delta E}{2k_B T}} + \rho_2 e^{\frac{\Delta E_I}{2k_B T}} \qquad \textbf{(5-4)}$$

Where ΔE_I is the energy gap between the impurity electrons / holes and the conduction / valence band, and its value strongly depends on the electronegativity of the impurity.

At low temperature, the conduction mechanism will be governed by electrons originating from the impurities, whereas at high temperature, when the impurity electrons are exhausted, intrinsic conduction will take over as the main conduction mechanism. This type of conduction is analogue to that of glasses containing transition metal atoms, and has been studied in more detail by N. F. Mott [287]. Further, it has also been observed in other lightly doped semiconductors, such as $Li_xNi_{1-x}O$ [337].

Analogously to the ternary skutterudites studied in the previous chapter, MGeTe (M = Co, Rh) phases are narrow gap impurity semiconductors. Therefore, at low temperature the Fermi energy lies close to more or less delocalized impurity levels, which originates a VRH charge carrier conduction mechanism (section 3.7). As the temperature rises, the Fermi level shifts from the impurity states towards the centre of the band gap, all the more insofar as the band gap increases, thereby reducing the interaction with the conduction band. This mechanism has fitted successfully the resistivity data at low temperature (Figure 5-8 and Figure 5-9).

A resistivity value of approximately 0.018 Ωcm at 300 K for CoGeTe has been recently reported by Laufek *et al*. and is consistent with the measurement presented in this work, *i.e*. 0.011 Ωcm [328]. From the shape of the resistivity curve (Figure 5-6) and the straight line obtained in the Seebeck *vs.* temperature plot (Figure 5-10), these samples can be described as non-degenerated doped semiconductors with a low content of impurities, given that large quantities of impurity electrons available would originate an impurity-band conduction type characterized by an approximately temperature independent resistivity plot [338].

The semiconducting nature of CoGeTe and RhGeTe is also backed by their structure. It is well known that semiconductors possess a filled-shell configuration, are normal valence compounds and follow the octet rule. Such rule can easily be verified with equation (1-11) for MGeTe phases with the values $n_e = 19$, $b_A = 2$, $b_C = 1 + 4$, $n_A = 2$ per formula unit.In order to obtain further stabilization, MGeTe phases form yet another localized metal-metal bond by distorting the octahedral coordination and bonding the unpaired d^5 electron to another neighbouring d^5 unpaired electron, thereby achieving a 18-electron rare-gas configuration, should electrons around the cation be considered. Using a covalent electron counting scheme [155], each Ge atom in tetrahedral coordination is covalently bonded to a tellurium atom and is shared by three metal atoms. Therefore, it can only supply three out of four valence electrons to the cation electronic shell. Likewise, each tellurium atom contributes five out of six valence electrons, given the covalent bond to a germanium atom. Hence, if the total number of electrons around the cation is counted, we obtain:

Co in $CoGe_{3/3}Te_{3/3}$ neutral atom:	9 e^-
3/3 Ge atom in $GeCo_3Te$ units: 3/3 x 3	3 e^-
3/3 Te atom in $TeCo_3Ge$ units: 3/3 x 5	5 e^-
1 Co-Co bond:	1 e^-
Total:	18 e^-

Thus, the cation possesses the 18-electron-favoured rare-gas configuration typical of diamagnetic semiconductors as seen in, for instance, FeS_2 pyrite [339]. The metal-metal bond is necessary to achieve the 18-electron rare-gas configuration and, as long as these bonds remain isolated, the compound will preserve its diamagnetic and semiconducting properties. Isolated metal-metal bonds in semiconducting compounds

are observed in MnP_4, possessing the closely related arsenopyrite structure [340]. On the contrary, if infinite chains were present, then electron delocalization could lead to metallic properties, as seen in the transition-metal polyphosphides CrP_4 and VP_4 [153,341].

Regarding the Zintl-Klemm counting scheme for the anions [170], Ge and Te atoms obtain the filled-shell configuration only if the metal atom has a 4+ oxidation state. Whether or not the metal atom will obtain a closed-shell configuration, consistent with semiconducting properties, will strongly depend on the band structure around the metal d orbitals. It is not possible to assess quantitatively the heights and the widths of the bands; however, qualitative predictions can be postulated, considering certain factors [142].

It was mentioned earlier on (section 5.3) that MGeTe phases possess the α–$NiAs_2$ structure, which can be described as a stacking sequence of MGe_3Te_3 octahedra layers linked to one another alternatively in a pyrite or marcasite-like fashion. The essential difference between the pyrite and the marcasite band structures is the increased splitting in the t_{2g} orbitals existent in the marcasite structure (Figure 5-7) [339]. The rest of the band structure is analogous and may be extrapolated to the MGeTe. Ge and Te atoms are much more electronegative than cobalt or rhodium and their orbitals will form the valence band. The GeTe pairs present in the structure are equivalent to the S_2^{2-} units in FeS_2, having both 14 valence electrons available to completely fill the valence band [142]. Therefore, only cation d orbitals need to be considered.

It can be postulated then that the t_{2g} orbital splitting in the MGeTe phases is somewhere in between the pyrite splitting and the marcasite splitting, given the alternate sequence of pyrite and marcasite blocks (Figure 5-7, left). Therefore, the 4+ d^5 metal, either cobalt or rhodium, would fill completely the two lowest-lying t_{2g} orbitals with four electrons, while leaving one unpaired electron in the third t_{2g} orbital.

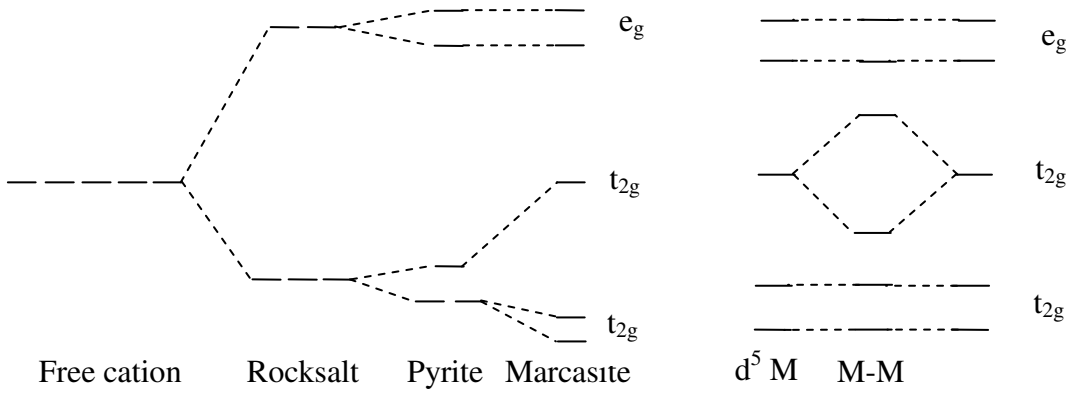

Figure 5-7 Left: crystal field splitting of d electrons in related pyrite-like structures. Right: Bond formation between neighbouring unpaired electrons in MGeTe phases (M = Co, Rh) [342].

The latter would pair up with a neighbouring metal atom to further stabilize the structure and also obtain a closed-shell configuration, as mentioned before (Figure 5-7, right). As regards the band gap values obtained at high temperature, they do not follow the expected trend had the structure been completely unknown. General structure-property relations in semiconductors indicate that more ionic compounds possess larger band gaps [278]. In our case, the band gap corresponds to the energy difference between filled t_{2g} and empty e_g bands. Despite having the same oxidation state, rhodium is expected to be less ionic owing to its larger size and polarizability. However, RhGeTe has a larger band gap (~ 28 meV) than CoGeTe (~ 12 meV) (Table 5-7).

This fact may be explained by comparing MGeTe metal-metal bond distances with those of the elements Co (2.50 Å) and Rh (2.69 Å). It is seen that the difference in the cobalt compound is approximately 0.32(1) Å, whereas in the rhodium compound the difference is smaller, approximately 0.227(3) Å. This evidence shows that the rhodium-rhodium metal bond in RhGeTe is stronger than the cobalt-cobalt metal bond in CoGeTe. Stronger bonds give rise to a larger splitting between bonding and antibonding orbitals, causing the fully occupied bonding orbital to lie deeper towards the already occupied t_{2g} bands, with the overall effect of increasing the effective band gap.

Table 5-7 Band gaps (meV) at high and low temperature obtained by means of Arrhenius-type fits. Temperature ranges (K) of the linear fits are also indicated.

Compound	High temperature	Range	Low temperature	Range
CoGeTe	12.2(2)	267-351	4.84(4)	81-238
RhGeTe	27.7(2)	210-338	8.4(1)	78-162

Overall, the values of 12.2(2) meV for CoGeTe and 27.7(2) meV for RhGeTe are small, and fall within the group of narrow band-gap semiconductors. It is possible to compare these values with those of chemically related compounds with a similar structure. For instance, the skutterudite $CoSb_3$ has the same cation as CoGeTe in a similar octahedral environment close to that of the rocksalt structure and an anion that is very close to tellurium and germanium in the periodic table. Moreover, it is also a narrow band gap semiconductor. $CoSb_3$ has a band gap of approximately 50 meV [283], which can be regarded as a good estimation of the energy gap between non-bonding electrons and the conduction band in our system if no metal-metal pairing takes place. The smaller band gap values of CoGeTe and RhGeTe can be understood in terms of a geometrical marcasite distortion, where metal-metal interaction occurs. The formation of a covalent metal-metal bond has the overall effect of bringing closer together valence electrons and antibonding orbitals, *i.e.* the conduction band, thereby decreasing the band gap value (Figure 5-7, right).

Nevertheless, it should be borne in mind that these band gap values are probably underestimated due to the short data range available at high temperature. Taking into account the fact that the Seebeck has not reach the exhaustion limit at the highest measured temperature, *i.e*. 350 K, it has to be concluded that conduction is still under an extrinsic regime and that these values are not real band gaps. Hence, resistivity measurements at high temperature, up to 500 K, are expected to give a more realistic figure. Further, these band gaps would imply that at room temperature, with a thermal energy of approximately k_BT (25 meV), the reduced Fermi energy, E_F^* , (section 1.1.2) would be close to zero, indicating a moderate degeneracy situation [13]. If that were the case, the temperature dependence of the conductivity would not be so strong, tending to a flat curve as it is observed in other moderately degenerate semiconductors, such as SnO_2 [343].

CoGeTe data can be fitted to a VRH mechanism throughout a wide temperature range, *i.e*. up to approximately 260 K, consistent with the slope change observed in the lnρ *vs*.

1/T plot at approximately the same temperature. The same correlation is seen in RhGeTe (Table 5-8 and Table 5-7). In turn, the correlation between the VRH maximum fitting temperature and the band gap size was already emphasized in the previous chapter. Therefore, the maximum fitting temperatures obtained for both compounds support the electrical resistivity data with regard to assigning a larger band gap to RhGeTe, instead of CoGeTe, as it would be expected.

Table 5-8 VRH Fitting parameters extracted from the resistivity vs. temperature data for the MGeTe (M = Co, Rh) compounds.

Compound	T_0 / K	ρ_0 / Ωcm	Range / K
CoGeTe	9148(37)	0.549(4)	81-258
RhGeTe	2039(48)	19.5(7)	80-184

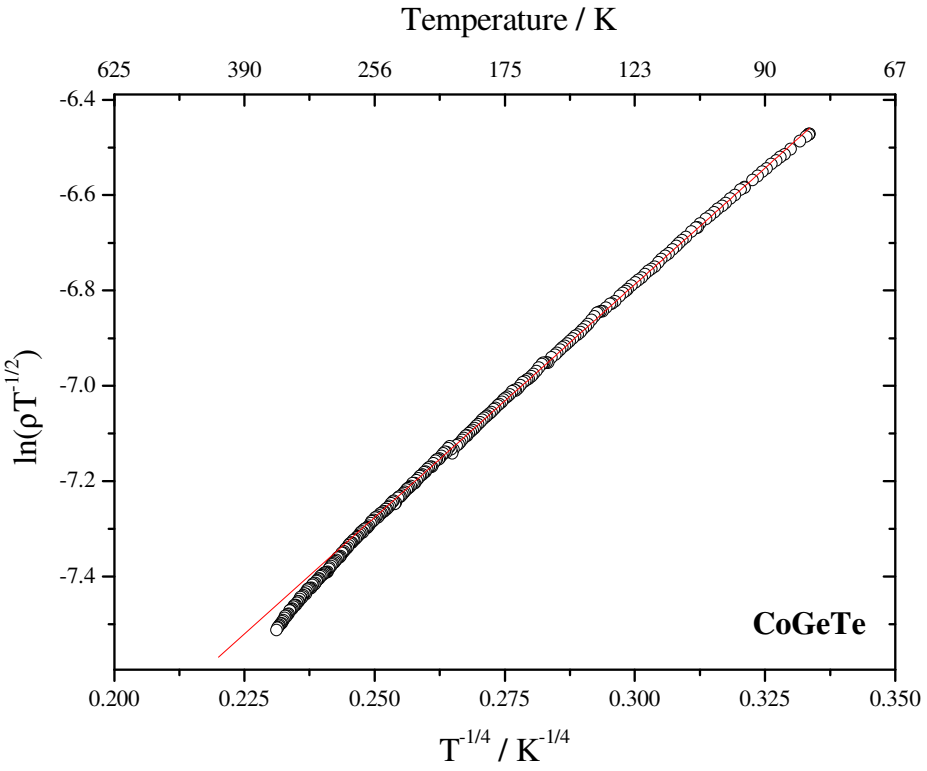

Figure 5-8 $T^{-1/4}$ dependence of the electrical resistivity logarithm for CoGeTe. The red lines of best fit correspond to the variable-range-hopping expression (3-4).

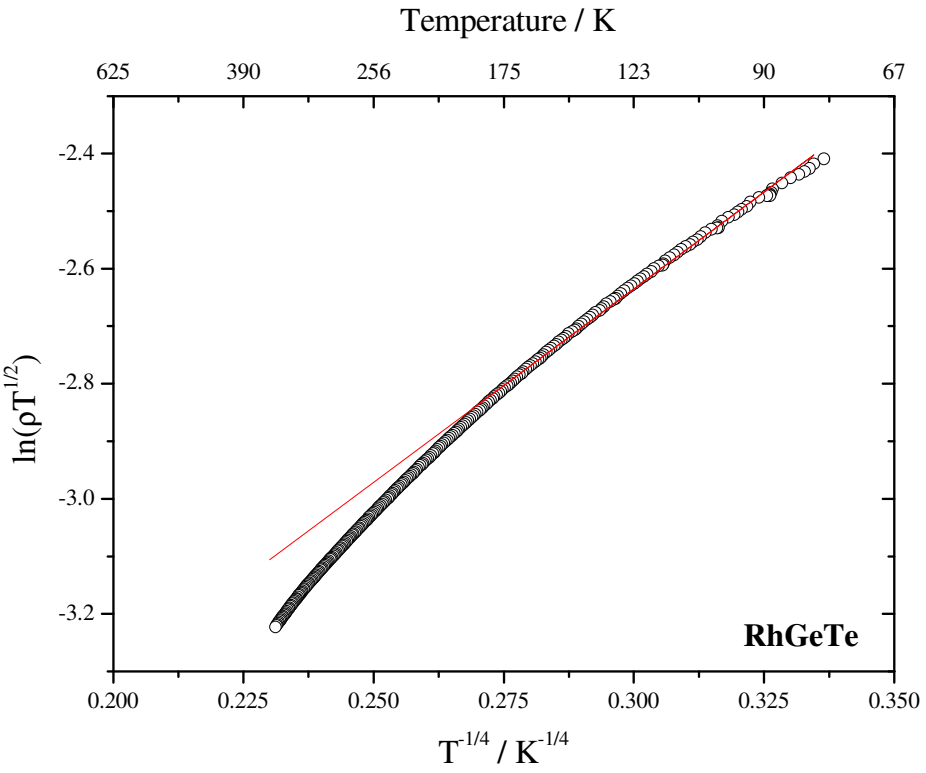

Figure 5-9 $T^{-1/4}$ dependence of the electrical resistivity logarithm for RhGeTe. The red lines of best fit correspond to the variable-range-hopping expression (3-4).

5.5 Seebeck coefficient

The Seebeck coefficient of CoGeTe and RhGeTe was measured between 25 K and 400 K and the data was collected by Mr. Fabien Guinet (Figure 5-10). They both show a negative Seebeck coefficient throughout the whole temperature range, indicating that electrons are the main charge carriers. Both Seebeck coefficients present many similarities. They possess similar slopes, similar magnitudes and also the same sign, consistent with similar band structures. Both plots show a linear increase with temperature above approximately 150 K, which can be accounted for by an impurity band close to the Fermi energy (section 3.7).

The Seebeck value at 325 K for RhGeTe (~ -180 μVK^{-1}) is larger than that of CoGeTe (~ -170 μVK^{-1}), which may be linked to the larger band gap size of RhGeTe (Table 5-7) (section 3.8). Further, they show a Seebeck coefficient-band gap ratio larger than other well-known semiconductors, namely silicon and germanium, and comparable to other compounds with potential thermoelectric applications owing to their enhanced Seebeck coefficient, such as $CoSb_3$ (Table 5-9). The anomalously large value found for CoGeTe

is most probably related to the underestimation of the band gap value obtained by means of electrical conductivity measurements.

Table 5-9 Band gap (eV) and Seebeck values (μVK^{-1}) for some doped semiconductors.

Semiconductor	Band gap	Seebeck	ratio	Reference
Si	1.12	500	446	[344]
Ge	0.66	300	454	[345]
$CoSb_3$	0.050	200	4000	[283]
CoGeTe	0.012	-170	14100	this work
RhGeTe	0.028	-180	6428	this work

None of the Seebeck plots indicate a Seebeck enhancement at low temperatures, thus phonon-drag effects are excluded. The onset of hole-driven conduction is not still observed at high temperatures, *i.e.* 325 K, therefore it is expected that the Seebeck coefficient of both compounds continues rising until exhaustion of electron donors is reached. There exist methods to calculate band gaps from the variation of the Seebeck coefficient with temperature; however it is essential to reach the exhaustion region, where the Seebeck acquires its maximum value [346].

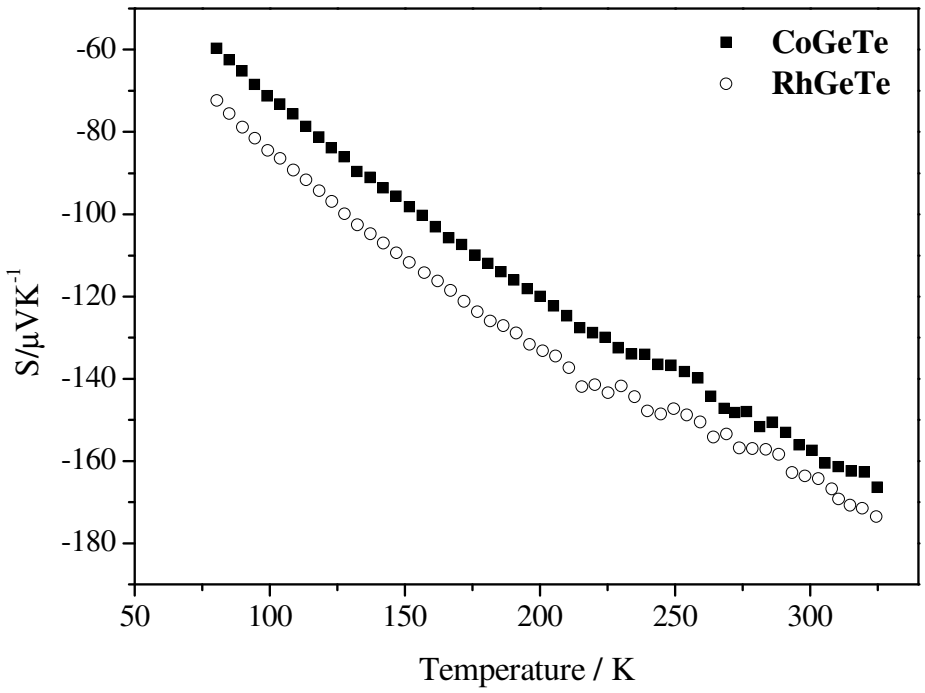

Figure 5-10 Seebeck coefficient *vs*. Temperature plots for CoGeTe (black squares) and RhGeTe (empty circles).

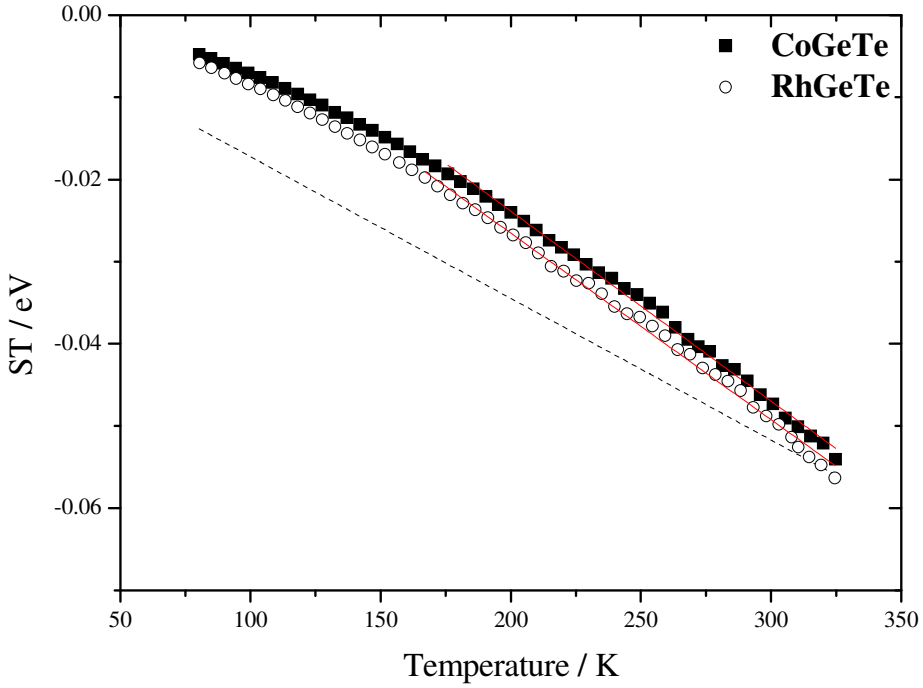

Figure 5-11 ST *vs*. Temperature plots for CoGeTe (black squares) and RhGeTe (empty circles). The dashed line corresponds to $2k_BT$. The red lines correspond to the best linear fit between 175 and 325 K.

ST plots are included to verify band gaps obtained by means of electrical conductivity measurements and to elucidate differences in carrier scattering mechanisms. They are based on the thermodynamic relation between the Peltier heat, π, and the Seebeck coefficient expressed as follows [347]:

$$\pi = ST = (E_C - E_F) + (r+2)k_BT \qquad \textbf{(5-5)}$$

The quantity ST is a measure of the energy flux relative to the Fermi energy carried through the thermoelectric circuit per charge carrier. The first term on the right amounts to the potential energy of the charge carrier relative to the Fermi energy, E_C-E_F, required to reach the energy of the conduction band, E_C. Its advantage is that, at high temperature, the Fermi energy can be read off the y-axis intercept. The second term is a measure of the kinetic energy of the charge carrier and is to be affected to some extent by different scattering mechanisms. It can be expressed in terms of a scattering parameter, *r* (section 1.1.2), which appears in the solution of the transport equation for a single parabolic band, taking different values depending on the different types of scattering mechanisms. Thus, the dashed line in Figure 5-11 accounts for the kinetic energy of a charge carrier in the conduction band obeying Boltzmann statistics, being

affected only by acoustic phonon scattering, *i.e.* $r = 0$, in a purely diffusive Seebeck coefficient [13].

Linear fits of both datasets between 175 and 325 K fit well the data, from which a Fermi energy of 22.4(7) and 18.9(6) meV is obtained for CoGeTe and RhGeTe, respectively (Figure 5-11). These correspond to band gap values of 45(1) and 38(1) meV, respectively. These values are higher than those obtained through electrical resistivity measurements and larger than the thermal energy threshold. Therefore, they can be regarded as more accurate but not precise enough, given the graphical method used in their obtention. Up to 175 K the slope of both curves is very close to $2k_B$, *i.e.* $r = 0$, where acoustic scattering would be the predominant charge carrier scattering mechanism. Over this temperature the slopes of both datasets increase to approximately the same value, *i.e.* -0.231(3) and -0.227(3) $meVK^{-1}$ for CoGeTe and RhGeTe, respectively, and the scattering parameter r obtained is 0.63(4). This is consistent with the onset of optical phonon scattering, whose r value amounts to 0.5. At high temperature, the interaction of charge carriers with phonons of higher energy (optical) is elastic, overlapping with acoustic phonon scattering at the same time [13].

5.6 Magnetic susceptibility

The magnetic susceptibility measurement was carried out under zero-field-cooled conditions between 5 K and 270 K in a 1000 Oe magnetic field (Figure 5-12). Measurements under field-cooled conditions were not carried out as the first run clearly revealed the nature of the system. The flat susceptibility as a function of temperature is reasonably consistent with the formal oxidation state description $Co^{4+}[Ge\text{-}Te]^{4-}$, by which both semiconducting and diamagnetic properties are explained.

There exist two well defined regions in Figure 5-12. Up to approximately 25 K there is a strong decrease in the magnetic susceptibility; whereas at higher temperature a slow but steady increase is observed. This behaviour has previously been observed in other semiconducting and diamagnetic systems, namely $CoSb_3$, and has been accounted for by the following expression [348]:

$$\chi = \chi_i + \chi_e + \chi_m = \chi_i + N_0 e^{-\frac{\Delta E}{2k_B T}} + \frac{C}{T} \qquad \textbf{(5-6)}$$

Where χ_i is the diamagnetic susceptibility of ion cores, χ_e is the paramagnetic susceptibility of conduction electrons and χ_m is the paramagnetic susceptibility of magnetic impurities. ΔE is the band gap value, N_0 is a constant and C is the Curie constant.

The steepest region can be attributed to the paramagnetic contribution of impurities at very low concentration (ppm), given that they follow a Curie law. As the temperature rises, the magnetic moments can no longer be aligned, giving rise to a rapid decrease of the magnetic susceptibility. Impurities may originate from the starting materials, *i.e.* Fe or Ni ppm in Co or trace amounts of impurity phases that cannot be seen in the X-ray pattern. They are diluted within the bulk phase and behave as non-interacting paramagnets. A Curie constant value of 2.8 emuKmol^{-1} has been determined from the inverse susceptibility *vs*. temperature plot up to 25 K. Had the impurities been identified and their effective magnetic moments known, it would be possible to calculate their respective concentrations in the sample.

At higher temperatures, the charge carriers jump to the non-localized conduction band in a thermally activated process. These conduction electrons originate then another paramagnetic contribution. The determination of the band gap seeking consistency with the value from the electrical conductivity measurement has been attempted; however unexpectedly low values were obtained (tenths of meV).

Diamagnetic systems show flat and negative magnetic susceptibility curves when plotted against temperature. However, the CoGeTe plot shows relatively large positive values throughout the whole temperature range (Figure 5-12). This may be explained by van Vleck paramagnetism, which is positive, small and temperature independent and offsets the small, negative and also temperature independent ion core diamagnetic contribution [237]. Ce-filled $Ce_xCo_4Sb_{12}$ displays the same steep decrease of the magnetic susceptibility at low temperature and the values are small and positive throughout the whole temperature range. However, the increase of the susceptibility as the temperature rises disappears, as it becomes masked by the paramagnetic effects of the dopants. This may indicate that the paramagnetism observed in Figure 5-12 is caused by trace impurities [78]. This evidence adds up to the semiconducting behaviour (section 5.4) and the metal-metal pairs (section 5.3) observed to support the filled-shell electronic configuration of the MGeTe (M = Co, Rh) phases.

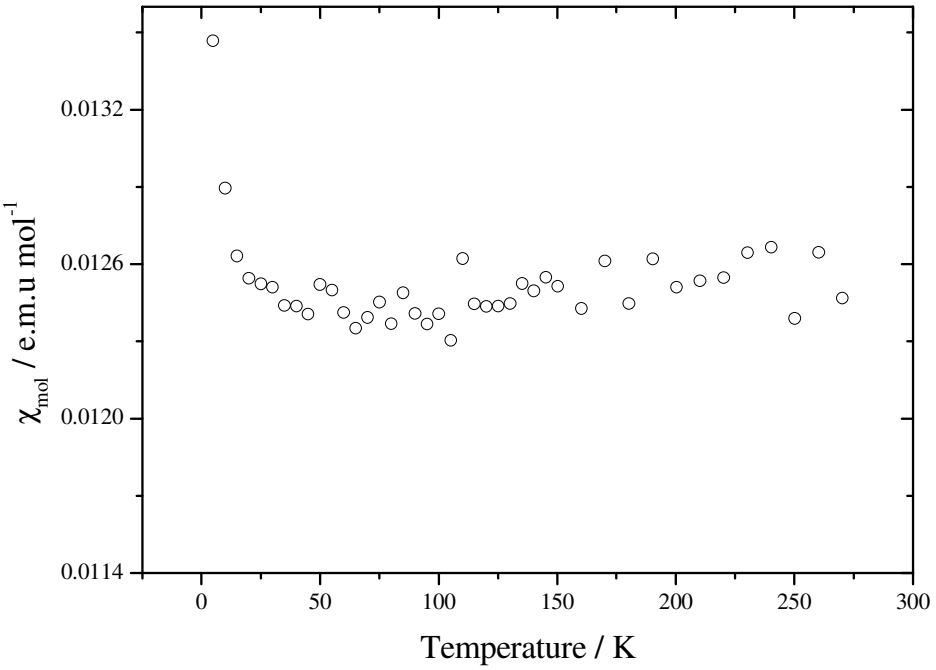

Figure 5-12 Magnetic susceptibility *vs*. Temperature plot for CoGeTe.

5.7 Thermal conductivity and power factors

The thermal conductivity has been measured between 300 K and 700 K in 50 K steps by Mr. Fabien Guinet. A 13 mm diameter pellet was used with an 87.4% of the theoretical density. The values obtained through this temperature range oscillate around a value of 1.4 $Wm^{-1}K^{-1}$ (Figure 5-13).

The porosity-corrected value of the thermal conductivity at 300 K would be close to 1.7 $Wm^{-1}K^{-1}$. The skutterudite $CoSb_3$ possesses a thermal conductivity of approximately 10 $Wm^{-1}K^{-1}$ at 300 K [116]. Filled skutterudites, which are known to scatter lattice phonons to a greater extent owing to the rattling motion of the filler atoms, possess thermal conductivities of 2.4 $Wm^{-1}K^{-1}$ at 300 K [349]. It is well known that isoelectronic anion substitution produces a decrease in the thermal conductivity. This fact is observed, for instance, when substituting antimony by germanium and tellurium in $CoSb_3$, which originates a ~ 60% reduction decreasing down to 4 $Wm^{-1}K^{-1}$ in $CoSn_{1.5}Te_{1.5}$ at 300 K [109]. Such reduction is increased even further when the mass difference between the anions is larger, as seen in $CoGe_{1.5}Te_{1.5}$, where a conductivity value of 1.5 $Wm^{-1}K^{-1}$ has been measured [350].

The lowest threshold for the thermal conductivity obtained in a material with potential thermoelectric applications has been found in the germanium clathrate $Sr_8Ga_{16}Ge_{30}$. The lattice thermal conductivity *vs*. temperature plot shows a truly glass-like behaviour in which values as low as 1 $Wm^{-1}K^{-1}$ at 250 K are observed [351]. Power factors of both CoGeTe and RhGeTe increase as the temperature rises, although the CoGeTe curve is steeper (Figure 5-13). A higher electrical resistivity in RhGeTe may be accounted for by a lower electron mobility originated by stronger metal-metal bonds and a larger band gap, according to Welker's rules [278]. The power factor for CoGeTe at 300 K amounts to 2.5 x 10^{-4} $Wm^{-1}K^{-2}$, which is an order of magnitude lower than the values typically found in state-of-the-art thermoelectric materials and also in doped cobalt triantimonide, *i.e*. 1 x 10^{-3} $Wm^{-1}K^{-2}$ [352]. CoGeTe thermal conductivity at room temperature (1.7 $Wm^{-1}K^{-1}$) is comparable to the thermal conductivity of state-of-the-art thermoelectric materials composed of Bi_2Te_3, *i.e*. 1.5 $Wm^{-1}K^{-1}$ [3], lying in the region of low thermal conductivity materials suitable for thermoelectric applications. A ZT value of 0.05 indicates that, at room temperature, the thermoelectric performance of CoGeTe is an order of magnitude lower than state-of-the-art thermoelectric materials with a ZT of approximately unity. Nevertheless, taking into account that the exhaustion region has not yet been observed in the Seebeck measurements, a better performance is expected at higher temperatures (Figure 5-13).

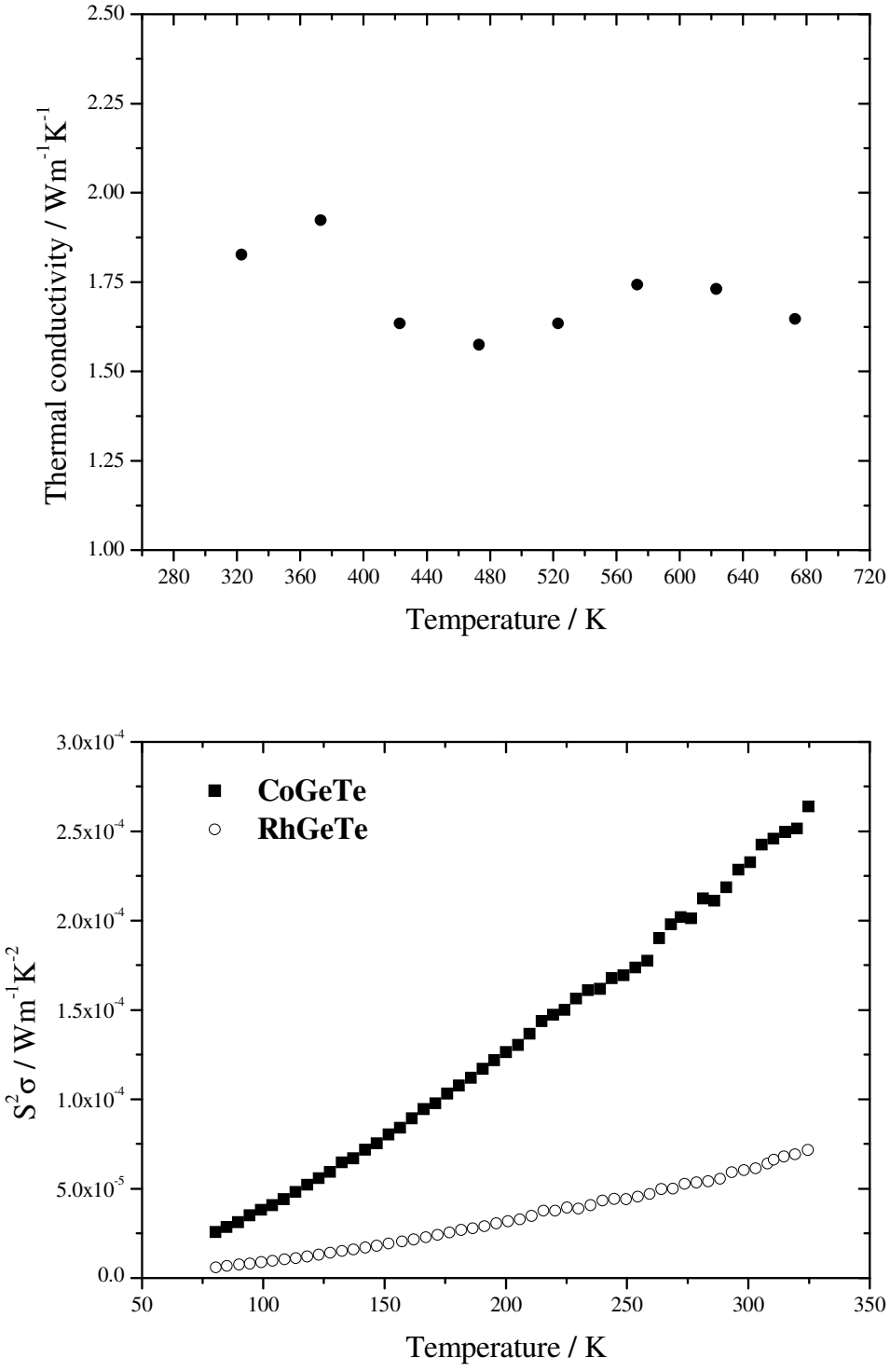

Figure 5-13 Top: Thermal conductivity *vs*. temperature plot for CoGeTe. Bottom: Power factor *vs*. temperature for both CoGeTe and RhGeTe.

Chapter 6

$Co_3Sn_2S_2$ Shandite

6.1 Introduction

While mapping out the ternary system Co-Sn-S the ternary metal chalcogenide $Co_3Sn_2S_2$ was identified. A comprehensive structure-property study has been carried out involving powder neutron diffraction, Seebeck coefficient, electrical resistivity and magnetic susceptibility measurements. An already reported anomaly in the resistivity *vs*. temperature at approximately 175 K motivated the high resolution powder diffraction experiment in order to elucidate whether such anomaly might be ascribed to a subtle crystallographic or electronic phase transition. Other magnetic and transport property measurements support the outcome of the experiment.

6.2 Synthesis

Sulphur was dried under vacuum and placed into a nitrogen glovebox prior to the synthesis. Stoichiometric amounts of cobalt (Alfa Aesar, 99.5%), tin (J. M. 99.8%) and sulphur (Aldrich) were ground together in an agate mortar inside a glovebox. The reaction mixture was placed into a silica tube and sealed under vacuum (10^{-4} torr) before being placed into a chamber furnace at 500 °C for 2 days. The contents of the tube were then ground and the products analyzed by X-ray powder diffraction. The procedure was then repeated at a temperature of 700 °C for 2 days, this time using a controlled cooling rate of 0.5 °C min^{-1} to achieve reaction completeness and high crystallinity. The final powder was rechecked by powder X-ray diffraction before the powder neutron diffraction experiment.

6.3 Thermogravimetric analysis

The composition of the sample was checked to verify it was the expected material. Thermogravimetric analysis of a $Co_3Sn_2S_2$ sample was carried out under a flow of O_2 and the temperature was raised up to 1000 °C at a 5 °C min^{-1} rate. Oxidation products were characterized by powder X-ray diffraction and assigned to SnO_2 and the spinel Co_2SnO_4. Figure 6-1 shows the weight change as a function of time, which represents the balance between counteracting weight on and weight off effects owing to oxidation and sublimation, respectively. The experimental weight change is 9.82%, whereas the theoretical weight change corresponds to 10.01%. Therefore, the experimental stoichiometry is $Co_3Sn_2S_{2.019(8)}$, consistent with the nominal $Co_3Sn_2S_2$ stoichiometry.

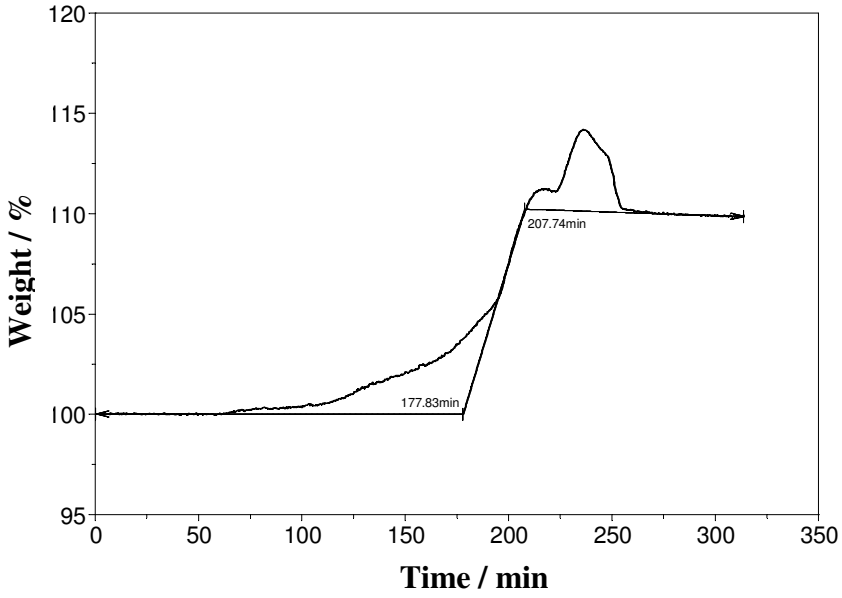

Figure 6-1 Weight change *vs*. time plot obtained from the thermogravimetric analysis of $Co_3Sn_2S_2$.

6.4 Powder neutron diffraction

Time-of-flight (TOF) powder neutron diffraction patterns were collected at ISIS in the high resolution powder diffractometer (HRPD) as described in section 2.2.5. A vanadium can, containing the sample in the form of friable powder, was attached to the end of a long rod fitted to a vanadium-walled cryostat in order to perform low-temperature time-of-flight neutron scattering experiments. A background data set was collected to be subtracted from raw datasets. Initial data manipulation and reduction was carried out using Genie spectrum manipulation software [249]. Neutron diffraction data from the highest resolution backscattering bank of detectors ($2\theta = 180°$) and from the mid-angle bank of detectors ($2\theta = 90°$) were summed and normalized for subsequent use in Rietveld refinements using the GSAS software package [250].

Neutron diffraction data were collected on a sample of $Co_3Sn_2S_2$ at 50 K, 110 K, 120 K, 180 K and room temperature (300 K). Given the similarity among patterns only those at room temperature and 50 K are shown (Figure 6-4 and Figure 6-5). An anomaly in the resistivity *vs*. temperature plot approximately at 115 K, that eventually turned out to be a spurious signal, led to the collection of two sets of data at both sides of the anomaly and one at room temperature for comparison purposes. Subsequent Rietveld refinements were carried out on data from both the backscattering and the 90° bank. Initially, only the backscattering data was treated and, once the analysis was completed, the 90° bank

data was added. The initial atom positions and the space group $R\bar{3}m$ for the refinement was taken from reference [353]. At an early stage of the refinement, the histogram scale, the lattice parameters and the background-fitting coefficients of a shifted Chebyshev function of the first type were allowed to vary. Once the convergence criterion was achieved, *i.e.* $\Sigma\,(\Delta x / \sigma_x) \leq 0.01$ (where Δx is the shift of the variable x and σ_x is its estimated standard deviation), the atomic positions as well as the thermal parameters were released. The thermal parameters of the tin atoms were constrained to a single value. Eventually, the profile coefficients of the exponential pseudovoigt function were allowed to vary until convergence was reached.

At a second stage of the refinement, the histogram scale and the lattice parameters of the backscattering bank were fixed and the 90° bank data added to the refinement. Likewise, the histogram scale and an identical number of variables in the background function were also refined. The diffractometer constants for the backscattering bank were kept fixed throughout the refinement given the high precision with which they are determined. The diffractometer constants of the second histogram were allowed to vary to accommodate the *d*-spacing *vs*. TOF of the backscattering bank. The last step was to fit the peak shape by releasing the variables of the profile function as described for the first histogram.

Excluded regions are found in the refinement wherever extra reflections from the vanadium can and the cryostat walls were likely to interfere in the normal development of the refinement. The weighed-profile agreement factor, R_{wp}, was found to be larger for the analysis at 110, 120 and 180 K and lower at 50 and 300 K owing to the fact that the statistical averaging, in terms of collection time, was larger for the data collections at 50 and 300 K. Two small unindexed peaks that have been assigned (Figure 6-7). The reflection at 1.752 Å corresponds to the maximum-intensity reflection of the cobalt pentlandite Co_9S_8, whereas the reflection at 1.764 Å might belong to either γ-Co_6S_5 or Co_4S_3 which both have maximum-intensity reflections at such *d*-spacing. Splitting of reflections at large *d*-spacing is observed as the temperature rises, evidencing the pseudosymmetry present in the system when it deviates from the ideal rhombohedral angle, *i.e.* 60 °, as shown in Table 6-2. By comparison with the powder pattern of the cubic aristotype $MgCo_3C$, the pseudocubic symmetry becomes readily evident [195]. The rhombohedral, α_{rh}, and the pseudocubic, α_{pc}, angles are then related by [354]:

$$90^\circ - \alpha_{pc} = \sqrt{\frac{3}{2}}(60^\circ - \alpha_{rh}) \qquad \textbf{(6-1)}$$

There is no evidence of extra magnetic peaks at low temperature and there is no additional intensity on the crystallographic reflections either. This is due to the fact that the value of the saturation magnetic moment is too small to cause any noticeable magnetic scattering in HRPD (section 6.5). The structural information extracted from the Rietveld refinements has been tabulated in Table 6-2 to Table 6-4. The lattice parameter as well as the bond distances and bond angles display a gradual contraction as the temperature decreases and no discontinuities or abnormal changes have been observed. The rhombohedral angle decreases with raising temperature (Figure 6-6). Cobalt and sulphur atoms occupy 9*d* and 6*c* Wyckoff positions, respectively; whereas tin atoms are split between 3*a,* Sn2, and 3*b*, Sn1, Wyckoff sites. Cobalt atoms form a 3636 Kagomé net. 3636 indicates the sequence of rings found around any of the cobalt atoms within the net, *i.e.* a triangle is followed by a hexagon, then another triangle and finally another hexagon. The $Co_3Sn_2S_2$ structure can be viewed as formed by a stacking sequence of these layers aligned perpendicularly to the *c*-axis, in which Sn2 atoms occupying 3*b* Wyckoff positions are centring the hexagons within the Kagomé net. Co and Sn2 atoms together form then a close packed hexagonal 3^6 net. Sn1 and S atoms are located in between the layers forming two distorted interwoven SnS 6^3 honeycomb lattices (Figure 6-3). Alternatively, $Co_3Sn_2S_2$ can be compared with the CoSn structure, with which bears a close resemblance [355]. Both structures possess tin-centred cobalt Kagomé lattices forming perpendicular layers to the *c*-axis, having CoSn a tin honeycomb lattice in between the layers.

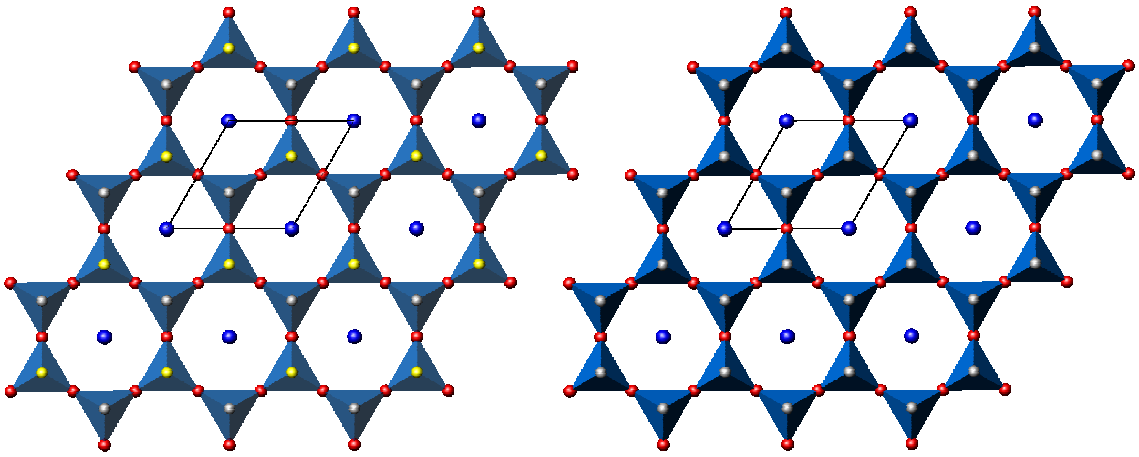

Figure 6-2 Left: View of the Kagomé lattice along the *c*-axis in $Co_3Sn_2S_2$. Right: analogous view in CoSn. Key: Co in red, Sn2 in blue, Sn1 in grey and S in yellow.

From a polyhedral point of view, CoSn is formed by layers of Co_3Sn_2 corner-linked trigonal bipyramids where cobalt and tin atoms occupy equatorial and axial positions, respectively. These layers are linked one another through axial tin atoms and possess a simple-hexagonal (AAA) stacking sequence (Figure 6-3). Analogously, $Co_3Sn_2S_2$ structure can be described as layers of corner-linked trigonal bipyramids with composition Co_3SnS, where cobalt atoms are found in equatorial positions and both tin and sulphur in axial positions. However, these layers are linked one another through tin atoms only, possessing a fcc-type (ABC) stacking sequence instead (Figure 6-3).

Coordination wise, cobalt atoms are octahedrally coordinated by two sulphur atoms and four tin atoms, forming layers of distorted face-sharing octahedra, where Co-S distances (~ 2.2 Å) are shorter than Co-Sn distances (~ 2.7 Å) (Table 6-3). These values are similar to those found in compounds such as Co_9S_8 (~ 2.3 Å) or CoS_2 (~ 2.32) [356] and CoSn (~ 2.6 Å) [355]. The A-S distances in the shandites $M_3A_2Ch_2$ (M = Co, Ni, Rh and Pd; A = In, Pb, Sn and Tl; Ch = S or Se) are closer to their respective binary sulphide distances as the main group metal changes from In to Pb. Thus, the shortest In-S distances are nearly 0.5 Å longer than those found in InS (2.58 Å), In_5S_4 (2.48 Å) or In_2S_3 (2.44 Å), whereas they are shorter (~ 0.2 Å) in the Sn compounds when compared to SnS (2.63 Å) and almost equal in the Pb compounds, considering the Pb-S galena distance (2.97 Å). It has also been shown by band structure calculations than the angle S-A(2)-S is of paramount importance as to the formation of a pseudoband gap when Sn is present [195].

S atoms capping equilateral triangles of M atoms show M-S distances slightly shorter (~ 0.5 Å) than those found in binary sulphides, indicating the presence of stronger bonding possibly due to extra π or δ bonding interactions between metal and S atoms. As a result, the pictorial view of the bonding in shandites regarding the interatomic distances is that of a tightly bound S-M-S network [M_3S_2] sharing some degree of covalency with the A atoms. Such description is envisaged in the alternative formulation of the cobalt shandite $Sn_2[Co_3S_2]$ [195].

Table 6-1 Sulphur z-coordinate (hexagonal setting) and relevant interatomic distances (Å) of some $M_3A_2S_2$ shandite compounds [195,198,201,353,357].

Shandite	z(S)	M-M	M-S	A-S	Metal	M-M
$Ni_3In_2S_2$	0.279	2.69	2.23	2.92	Ni	2.49
$Co_3In_2S_2$	0.279	2.66	2.17	2.92		
$Ni_3Sn_2S_2$	0.282	2.73	2.22	2.83	Co	2.50
$Co_3Sn_2S_2$	0.283	2.68	2.18	2.86		
$Ni_3Pb_2S_2$	0.285	2.80	2.28	2.92	Rh	2.69
$Rh_3Pb_2S_2$	0.285	2.74	2.28	2.98		

Further, each cobalt atom is coordinated to four other cobalt atoms at a distance of 2.68 Å, close to that found in cobalt metal, *i.e.* 2.51 Å. Sn2 atoms centring the Kagomé lattice are surrounded by six cobalt atoms and are bonded to two sulphur atoms at a distance of *ca.* 2.86 Å. Sn1 atoms are located between Kagomé layers and act as layer linkers. Thus, their coordination environment consists of a trigonal antiprism of cobalt atoms.

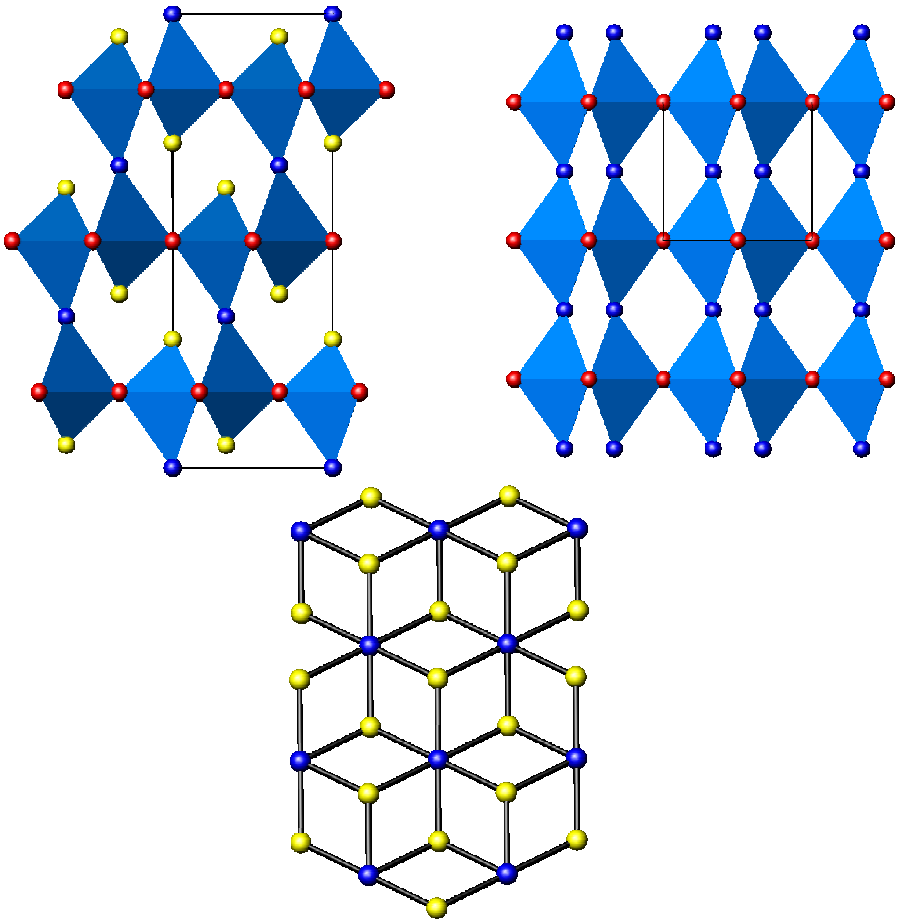

Figure 6-3 Top: View along the *a*-axis showing the bipyramidal units along with the linkage between them in $Co_3Sn_2S_2$ (left) and CoSn (right). Bottom: interwoven honeycomb SnS lattice. Key: Co in red, Sn1 in blue and S in yellow. For the sake of clarity Sn2 atoms are not shown.

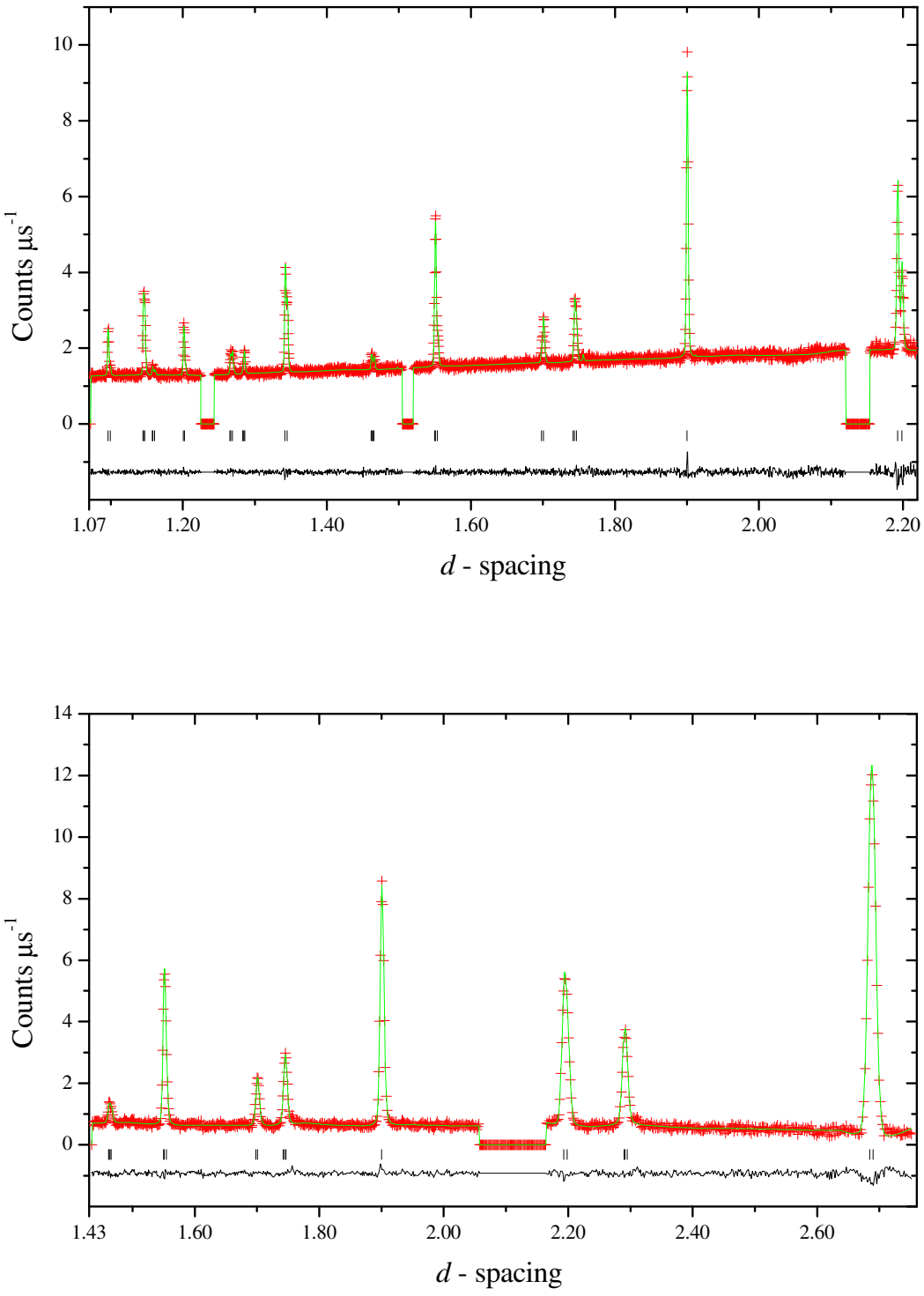

Figure 6-4 Rietveld refinement of neutron data at 300 K. Top: Backscattering bank. Bottom: 90° bank. Vanadium peaks have been excluded for simplicity. Key: experimental data (crosses), fitted model (full line), difference curve (lower full line). Reflections positions are shown as markers.

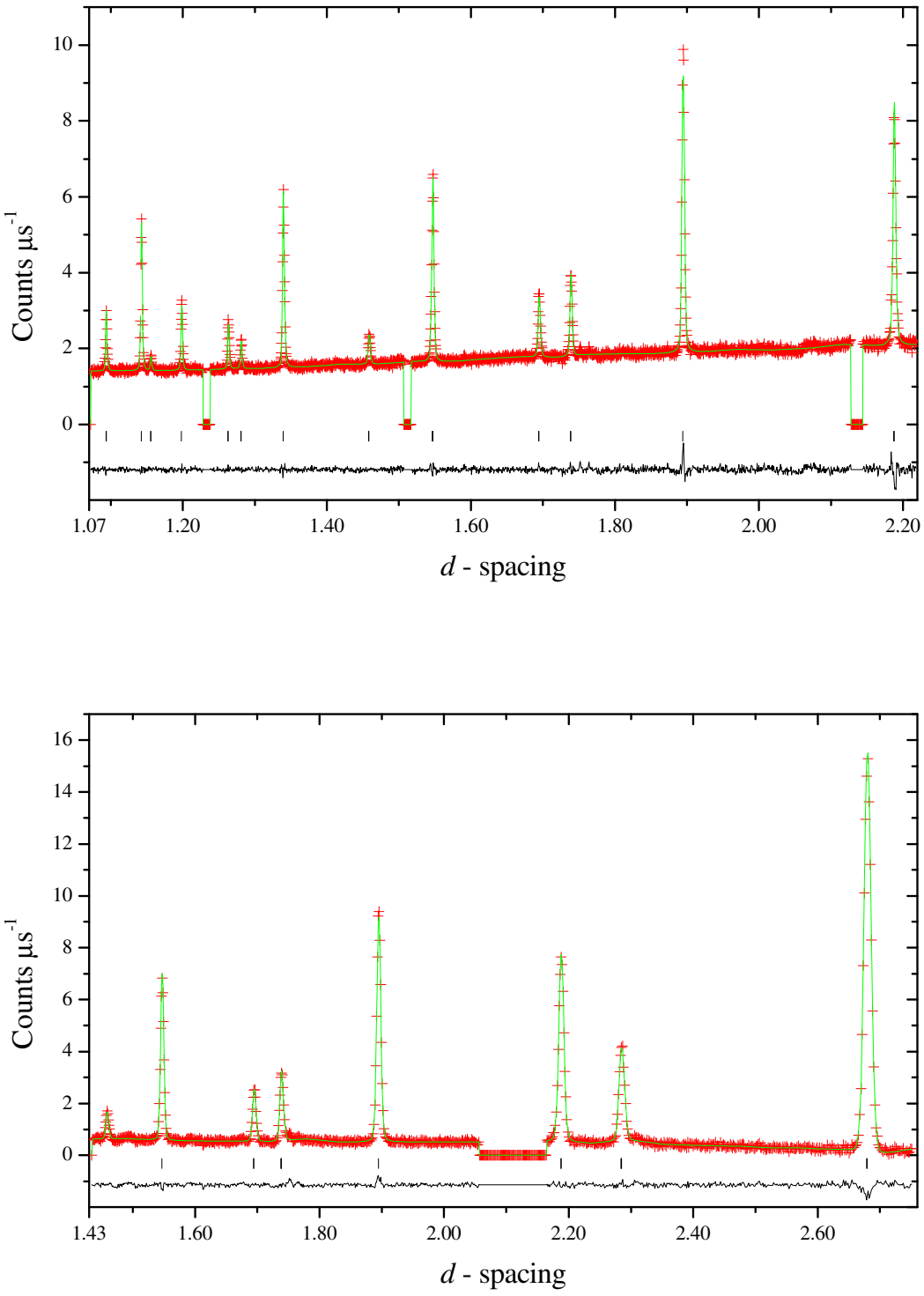

Figure 6-5 Rietveld refinement of neutron data at 50 K. Top: Backscattering bank. Bottom: 90° bank. Vanadium peaks have been excluded for simplicity. Key: experimental data (crosses), fitted model (full line), difference curve (lower full line). Reflections positions are shown as markers.

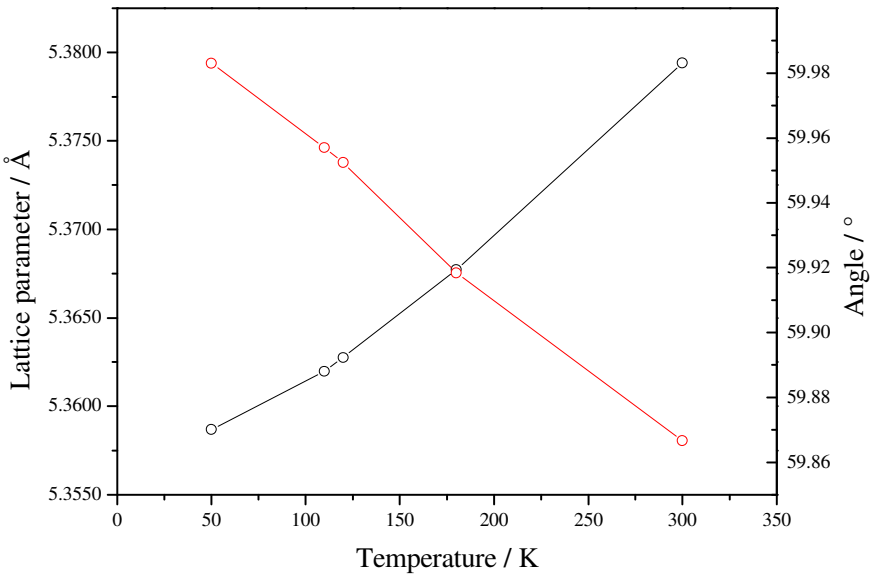

Figure 6-6 Lattice parameters vs. temperature plot across the temperature range 50-300 K for the shandite $Co_3Sn_2S_2$ in rhombohedral setting. The red line indicates the rhombohedral angle α.

Table 6-2 Refined parameters of $Co_3Sn_2S_2$ ($R\bar{3}m$) at different temperatures (hexagonal setting). Atom positions fixed by symmetry: Co (0.5,0,0.5); Sn(1) (0,0,0); Sn(2) (0,0,0.5); S (0,0,x). ADPs of the tin atoms have been constrained to the same value.

		50 K	110 K	120 K	180 K	300 K
a_h	Å	5.35734(8)	5.35854(8)	5.35895(7)	5.36116(6)	5.36860(4)
c_h	Å	13.1280(3)	13.1387(3)	13.1410(3)	13.1566(2)	13.1903(1)
a_r	Å	5.35866(6)	5.36197(6)	5.36275(6)	5.36773(5)	5.37941(4)
α	°	59.983(1)	59.957(1)	59.9524(9)	59.9184(7)	59.8666(5)
Co 9*d*	B / Å^2	0.02(5)	0.08(4)	0.09(4)	0.26(4)	0.61(5)
Sn(1) 3*a*		0.15(3)	0.19(2)	0.21(2)	0.29(2)	0.68(3)
Sn(2) 3*b*		0.15(3)	0.19(2)	0.21(2)	0.29(2)	0.68(3)
S 6*c*		0.4(1)	0.31(8)	0.17(8)	0.40(7)	0.51(7)
x(S)		0.7172(2)	0.7175(2)	0.7171(2)	0.7172(2)	0.7173(2)
$R_{wp}(H_1)$	%	2.9	10.4	10.7	10.8	3.4
$R_{wp}(H_2)$	%	6.1	6.7	6.5	6.7	6.5
χ^2		1.35	1.25	1.23	1.23	1.36

Table 6-3 Relevant interatomic distances (Å) in $Co_3Sn_2S_2$.

	50 K	110 K	120 K	180 K	300 K	
Co-Co	2.67864(5)	2.67924(5)	2.67945(5)	2.68056(4)	2.68428(3)	x 4
Co-Sn(1)	2.67933(3)	2.68098(3)	2.68138(3)	2.68387(2)	2.68970(2)	x 2
Co-Sn(2)	2.67864(5)	2.67923(5)	2.67945(4)	2.68056(3)	2.68428(2)	x 2
Co-S	2.172(2)	2.170(2)	2.174(2)	2.175(2)	2.178(2)	x 2
Sn(1)-S	3.1633(6)	3.1649(6)	3.1642(6)	3.1659(5)	3.1708(5)	x 6
Sn(2)-S	2.851(3)	2.857(3)	2.853(3)	2.858(3)	2.867(3)	x 2

Table 6-4 Relevant bond angles (°) in $Co_3Sn_2S_2$.

	50 K	110 K	120 K	180 K	300 K	
Sn(1)-Co-Sn(1)	180(0)	180(0)	180(0)	180(0)	180(0)	x 1
Sn(1)-Co-Sn(2)	90(0)	90(0)	90(0)	90(0)	90(0)	x 4
Sn(1)-Co-S	80.65(5)	80.70(5)	80.61(5)	80.59(5)	80.55(5)	x 2
Sn(1)-Co-S	99.35(5)	99.30(5)	99.39(5)	99.41(5)	99.45(5)	x 2
Sn(2)-Co-S	90.000(1)	90.000(1)	90.000(1)	90.000(1)	90(1)	x 4
S-Co-S	180	179.960	179.966	180	179.980	x 1
Co-Sn(1)-Co	59.983(1)	59.957(1)	59.952(1)	59.918(1)	59.867(1)	x 6
Co-Sn(1)-Co	120.017(1)	120.043(1)	120.048(1)	120.082(1)	120.133(1)	x 6
Co-Sn(2)-S	90.000(1)	90.000(1)	90(0)	90(0)	90(0)	x 6
S-Sn(2)-S	180(0)	180(0)	180(0)	180(0)	179.980(0)	x 1
Co-S-Co	76.14(8)	76.23(8)	76.10(8)	76.10(8)	76.09(7)	x 3
Co-S-Sn(2)	134.60(5)	134.54(5)	134.63(5)	134.63(5)	134.63(5)	x 3

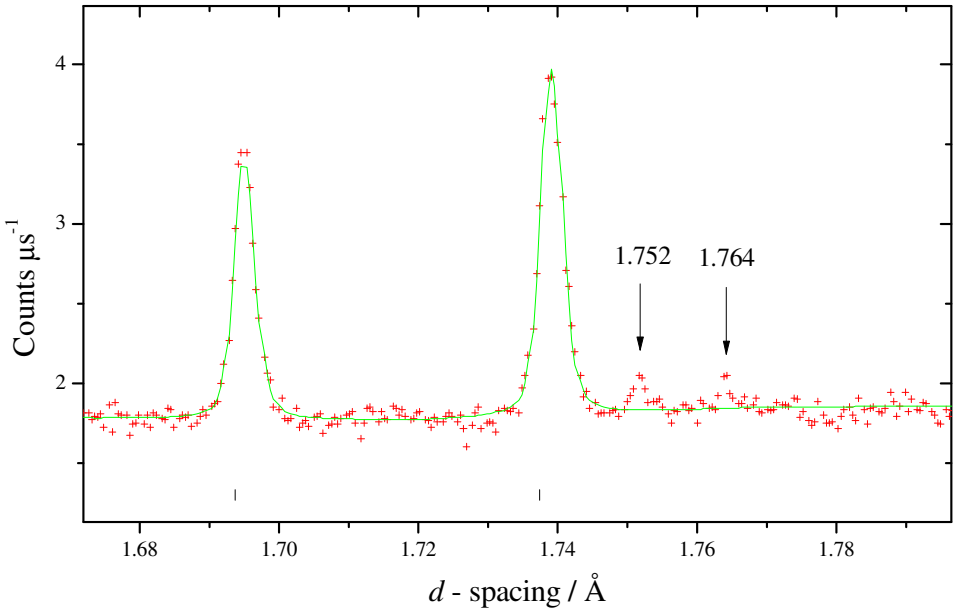

Figure 6-7 Zoom of the plot at 50 K showing unindexed reflections corresponding to impurity traces.

6.5 Magnetic measurements

The magnetic behaviour was studied using SQUID magnetometry as described in section 2.4.1. The magnetic susceptibility as a function of temperature has been measured under field-cooled (FC) and zero-field-cooled (ZFC) conditions at two different magnetic field strengths, namely 100 and 1000 Oe (Figure 6-10 and Figure 6-10). The magnetization has also been measured as a function of the magnetic field at 5 K to obtain the saturation magnetic moment (Figure 6-8).

Table 6-5 Magnetic properties for the shandite $Co_3Sn_2S_2$.

Magnetic property	$Co_3Sn_2S_2$
Curie temperature, T_C	170(4) K
Weiss constant, θ	172(2) K
Effective magnetic moment / ion, μ_{eff}	1.12(7) μ_B
Saturation magnetic moment / ion, μ_{sat}	0.29(1) μ_B

The magnetic properties of $Co_3Sn_2S_2$ have been summarized in Table 6-5. The Curie temperature has been determined as the maximum in the temperature variation of the $d\chi/dT$ at the lowest field, *i.e.* 100 Oe. This allows a more precise determination of T_C, as it has been shown in the Curie temperature determination for other ferromagnetic

spinel-type phases [358]. A clear paramagnetic-ferromagnetic phase transition is observed at approximately 175 K and the paramagnetic region has been fitted to a Curie-Weiss law with good agreement (Figure 6-10 and Figure 6-10 insets).
A positive Weiss constant indicates that the predominant magnetic interactions are ferromagnetic. A saturation magnetic moment of 0.29 μ_B per cobalt ion is obtained from the extrapolation of the magnetization *vs*. magnetic field plot at infinite field, which is in excellent agreement with a previously reported value of 0.29 μ_B [359].

DFT calculations performed on $Co_3Sn_2S_2$ indicate that it possesses a spin ½ type I_A half-metallic ground state, which should have an integral value of the saturation magnetic moment [195]. Non-integral values of the saturation magnetic moments are understood within the collective electron treatment for ferromagnetism, which takes into account s-d hybridization, and was first applied successfully in describing the magnetic properties of iron, cobalt and nickel [360]. Fe, Co and Ni are not half-metals despite the fact that they possess fully spin-polarized d bands, *i.e.* fully occupied ↑ d bands and partially occupied ↓ d bands. The s-d hybridization present at the Fermi energy destroys the polarization, thereby becoming normal ferromagnets. Hence, half-metals are binary or ternary compounds in which the s-d degeneracy is broken by different-strength covalent interactions among the forming elements [208].
Density functional theory (DFT) calculations have shown that this is indeed the case in $Co_3Sn_2S_2$, where spin split d bands are found close to the Fermi energy and a spin-polarized single electron occupies the conduction ↑ d band [195]. An overall magnetic moment of 0.87 μ_B per formula unit is close to the theoretical value of 1 μ_B that would be expected. The difference may be accounted for the high sensitivity of half-metallicity to crystallographic disorder and stoichiometry [213]. Coey *et al*. have proposed a classification of half-metals based on the conduction mechanism in both spin d bands [209]. The half-metals with metallic majority ↑ spin electrons and semiconducting minority ↓ spin electrons, namely $Co_3Sn_2S_2$, are defined as type-I_A (section 1.4.7).

Large differences between the FC and ZFC magnetic susceptibility plots are also observed. These are usually ascribed to spin-glass systems in which magnetic frustration occurs, such as Kagomé, pyrochlore, fcc and triangle lattices [361]. This phenomenon prevents the electronic configuration from reaching a single ground state, due to the inability to satisfy all the pair-wise interactions between neighbouring electronic spins. By and large, a criterion based on the magnitude of the Weiss constant,

θ, in relation to the onset temperature, T_c, of long-range magnetic ordering has been established in order to clearly distinguish frustrated magnetic systems [361]:

$$\frac{|\theta|}{T_c} > 10 \qquad \textbf{(6-2)}$$

In the system under study, this ratio amounts to 1.01, very close to one, and confirms the absence of frustration. This is characteristic of long-range ferromagnetic order, where strong deviations from the Curie-Weiss law are expected at temperatures close to the Curie temperature, *i.e.* $\theta \sim T_C$. The divergence between FC and ZFC curves may then be caused by magnetocrystalline anisotropy, which is known to determine the shape of FC-ZFC curves in ferromagnetic materials [362]. Such divergence is also related to the existence of a hysteresis loop and coercivity below the Curie temperature [362].

The value of the coercivity is a measure of the magnetic anisotropy present in a ferromagnetic system, which can be evaluated by the shape and absolute values of the FC-ZFC magnetic susceptibility plots. If the anisotropy of the sample is low, the ZFC maximum susceptibility value will be similar to the FC analogue and the FC curve will saturate quickly below the Curie temperature. By contrast, highly anisotropic samples will possess low values of the ZFC curve at low temperature and the FC curve will continue increasing well past the transition temperature. According to Figure 6-9 and Figure 6-10, the difference between the ZFC and the FC magnetic susceptibility values is large (66% and 87% at 100 and 1000 Oe, respectively), comparable to other known highly anisotropic ferromagnetic systems such as $SrRuO_3$ (89% at 100 Oe) and $La_{0.5}Sr_{0.5}CoO_3$ (88% at 50 Oe), opposed to other materials with low anisotropy such as $La_{0.7}Ca_{0.3}MnO_3$ (25% at 100 Oe) and $Ni_{0.8}Zn_{0.2}Fe_2O_4$ (29% at 50 Oe) [362]. Moreover, the FC curve continues rising well below the Curie temperature. Thus, we can conclude that $Co_3Sn_2S_2$ is also a highly anisotropic magnetic system. The existence of ferromagnetic domains, characteristic of ferromagnetic materials possessing large exchange energies, is consistent with large coercivity and, therefore, magnetic anisotropy. Typical FC-ZFC splitting attributed to magnetic domains has also been observed in other half-metallic compounds with similar small saturation magnetic moments, namely the alkali-filled skutterudites $NaFe_4Sb_{12}$ and KFe_4Sb_{12} [363].

As regards the magnitudes of the saturation and effective magnetic moments, the difference between them offers an insight into the conduction mechanism of the main charge carriers. It has been demonstrated that electrons confined in unfilled bands can be treated as free, *i.e*. their orbital angular momentum is not taken into account due to the equivalent of an internal field causing orbital momentum quenching [364].

In order to compare both values, Rhodes and Wohlfarth convert the saturation and effective magnetic moments into the equivalent amount of charge carriers that originate such moments, *i.e*. q_S and q_{eff}, respectively, considering the fact that each half-integer of spin corresponds to one electron [365]:

$$q_S = \frac{\mu_{Sat}}{\mu_B} = 2S \qquad \textbf{(6-3)}$$

$$\left.\begin{aligned} \mu_{eff} &= \sqrt{q_{eff}\,(q_{eff}+2)}\,\mu_B \\ q_{eff} &= 2S \end{aligned}\right\} \qquad \textbf{(6-4)}$$

The q_{eff} to q_S ratio can then be used to assess the extent of conduction electron delocalization. Systems with a high degree of electronic localization will possess a q_{eff} / q_S ratio very close to one, such as in $CrBr_3$ or EuO [365]; whereas highly delocalized systems will show large deviations from unity. For instance, large differences between effective and saturation magnetic moments are found in itinerant ferromagnets where electron delocalization describes best the conduction process, as in the semi-Heusler alloy CoVSb, with an effective and saturation magnetic moment of 1.04 and 0.11 μ_B, respectively and a ratio of 9.4 [366].

For the shandite $Co_3Sn_2S_2$, values of 0.5 and 0.29 are found for q_{eff} and q_S respectively, and a ratio of 1.7. Rhodes and Wohlfarth suggested a correlation between the q_{eff} / q_S ratio and the Curie temperature for a whole series of compounds (mainly transition metal alloys) whose q_{eff} / q_S ratio does not deviate largely from unity (between 1 and 8) [365].

These have been grouped in a family of compounds following an intermediate model where both delocalized and localized electron properties are found. The value of 1.7 for $Co_3Sn_2S_2$ does not match that of the correlation (a ratio of approximately 3 was expected for a compound with a Curie temperature of 176 K). Nonetheless, it is very close to that of CoS_2 (2.0), which is also an itinerant ferromagnet with a localized magnetic moment [367,368]. This fact evidences the analogous conduction mechanism and the similar extent of electron localization present in both compounds.

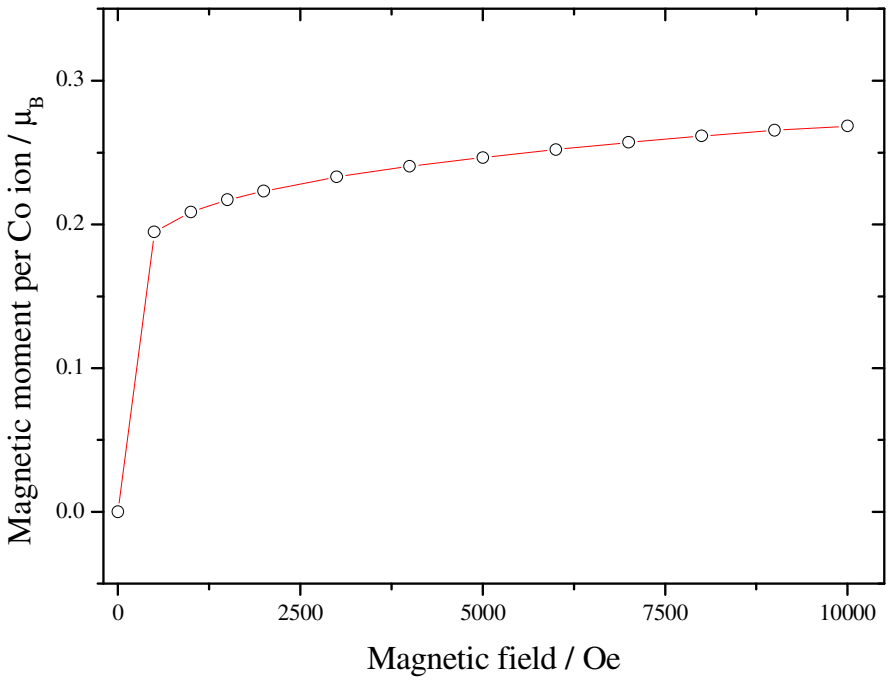

Figure 6-8 Magnetic moment per Co ion *vs*. magnetic field at 5 K. Cooled down in zero-field conditions.

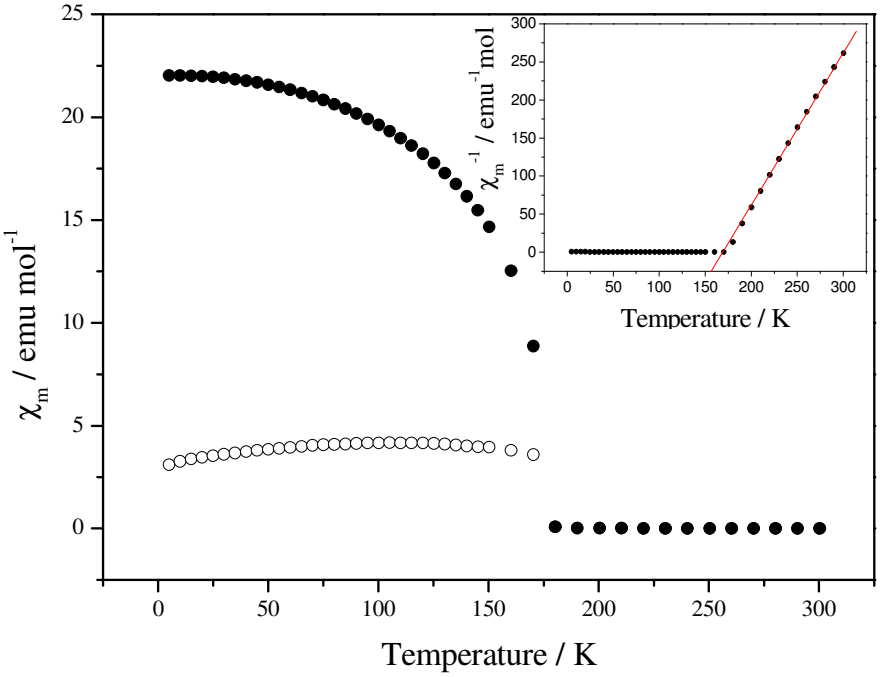

Figure 6-9 Magnetic susceptibility *vs*. Temperature for the shandite $Co_3Sn_2S_2$ in zero-field cooled (empty dots) and field-cooled (full dots) conditions. Inset: Curie-Weiss law fitting. Magnetic field set at 100 Oe.

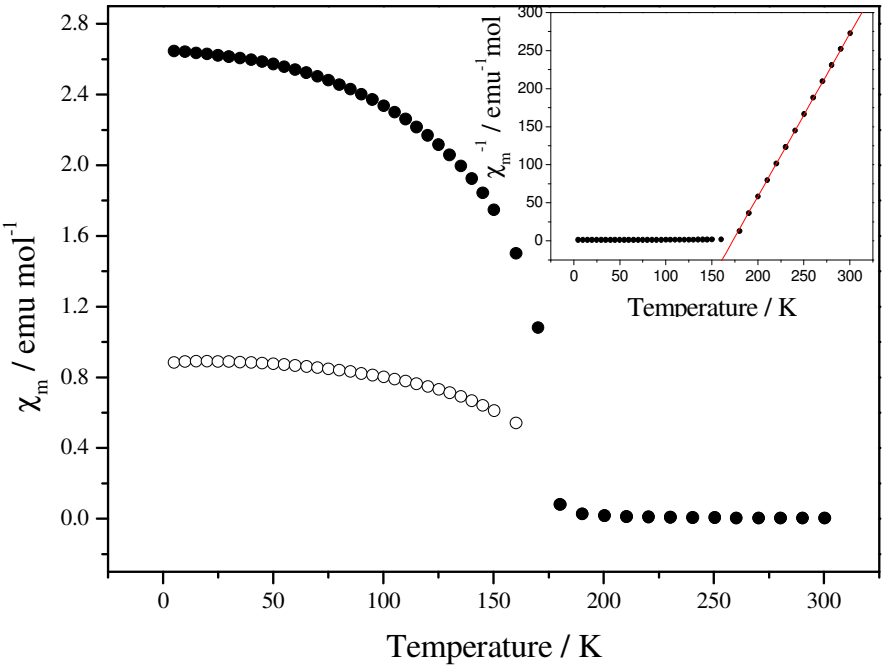

Figure 6-10 Magnetic susceptibility *vs*. Temperature for the shandite $Co_3Sn_2S_2$ in zero-field cooled (empty dots) and field-cooled (full dots) conditions. Inset: Curie-Weiss law fitting. Magnetic field set at 1000 Oe.

6.6 Electrical Resistivity

The measurement of the electrical resistivity was carried out between 77 and 350 K. The resistivity of the shandite $Co_3Sn_2S_2$ shows very small values as well as an increase in the resistivity as the temperature rises, consistent with metallic behaviour. A discontinuity consisting of a slope change approximately at 175 K is observed (Figure 6-11). Such anomaly was initially ascribed to a likely magnetic phase transition by Natarajan *et al*. [204] and it has been confirmed by magnetic measurements in the present study, corresponding to a paramagnetic-ferromagnetic transition (section 6.5). The resistivity values obtained are of the same order of magnitude as those measured by Natarajan *et al*. and Kubodera *et al*. [359]. The room temperature value is two orders of magnitude higher than that of cobalt metal (6×10^{-6} Ωcm) and similar to that of the pyrite-like CoS_2 (3×10^{-4} Ωcm) [369].

The only reported study dealing comprehensively with the physical properties (electrical resistivity, Hall coefficient and magnetic susceptibility) of shandite and parkerite phases is that of Michelet *et al*. (Table 1-13). $Ni_3Sn_2S_2$ possesses low values of electrical

resistivity, similar to those of Ni metal (7 x 10^{-5} Ωcm), whereas $Co_3Sn_2S_2$ deviates largely (two orders of magnitude) from the Co metal resistivity.
Such behaviour may be attributed to a narrow band present at the Fermi energy. Narrow bands do not allow the existence of largely delocalized electron wave functions, causing a decrease in the electron mobility as well as an increase in the electrical resistivity.

In order to explain the origin of the discontinuity observed in Figure 6-11, it is necessary to rely on itinerant-electron band models capable of describing properties belonging to both localized and delocalized electrons for the same particle. The Hubbard model for electron correlations in narrow energy bands describes best the magnetic properties of conduction *d* electrons exhibited by $Co_3Sn_2S_2$ [370]. Therein, the intra-atomic interactions allow the existence of an overall spin-up orientation of the electron being localized on the atom, despite the fact that band electrons are changing all the time. The spins of itinerant electrons are ferromagnetically coupled to the local moments through Hund rule coupling in what is called double exchange interaction, as in CrO_2 [371]. It is not surprising then that the resistivity *vs*. temperature plot is similar to that of CrO_2 [372]. Therefore, both localized-electron and band-electron properties coexist in the same material. The decreasing slope below the Curie temperature has its origin in the conservation of the spin alignment as electrons are transferred from atom to atom, which causes an increase in the kinetic energy of the charge carriers and a decrease in the electrical resistivity thereof [373].

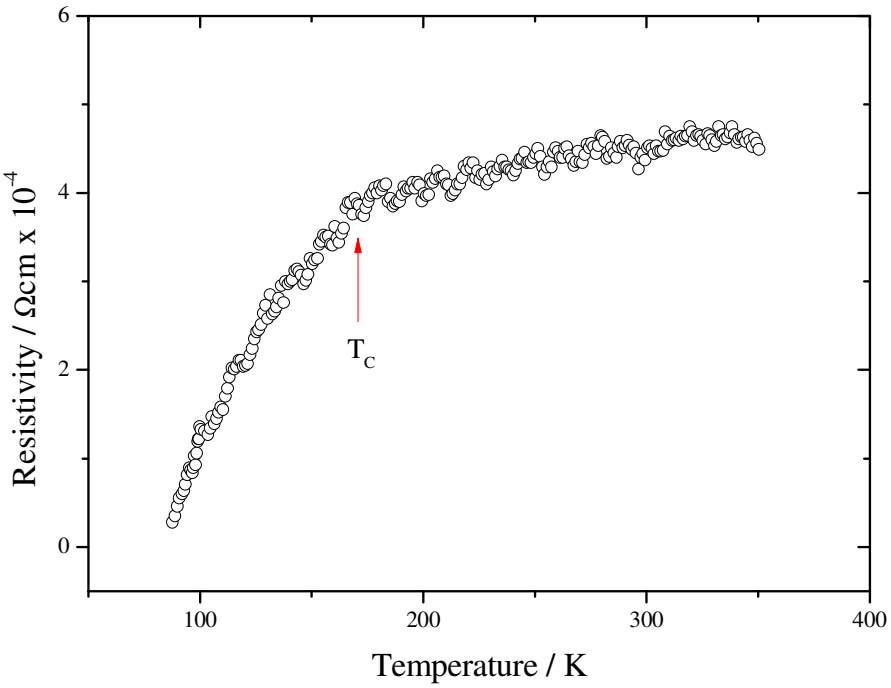

Figure 6-11 Resistivity *vs*. Temperature plot for the shandite $Co_3Sn_2S_2$. The Curie temperature has been marked with an arrow.

6.7 Seebeck coefficient

The Seebeck coefficient was measured between 77 and 350 K (Figure 6-12). The values obtained are larger than those of metals (a few μVK^{-1}) and are also larger than those of other shandite phases (Table 1-13). Nevertheless, they are lower than those measured in conventional semiconductors (200-300 μVK^{-1}). As the temperature rises, an increase in the Seebeck coefficient is observed, consistent with metallic behaviour. Moreover, the negative values indicate than electrons are the main charge carriers.

The measurement of the Seebeck coefficient is a good method to probe the density of states near the Fermi energy. The magnitude of the Seebeck for metals is small mainly because the Fermi energy is independent of the temperature. Thermal excitation gives rise to small changes in the energy of the electrons with respect to the Fermi energy, therefore the thermoelectric phenomena is much less pronounced. The expression describing the Seebeck coefficient as a function of temperature in metals is also used to describe the electron diffusion contribution to the Seebeck coefficient [240]:

$$S = \frac{\pi^2 k_B^2}{3eE_F} T \qquad \textbf{(6-5)}$$

Hence, the linear increase of the Seebeck coefficient in $Co_3Sn_2S_2$ above the Curie temperature may be explained by the typical metallic behaviour of conduction electrons in a paramagnetic state, according to equation (6-5). Further, an estimate of the Fermi energy has been obtained by fitting the paramagnetic region of the Seebeck *vs*. temperature plot to the same equation (Figure 6-12). A value of 216(8) meV is obtained, which is comparable to those of other shandites, such as $Rh_3Pb_2S_2$ (470 meV) and $Pd_3Pb_2Se_2$ (580 meV) obtained by Natarajan *et al*. using the same method [204].

DFT calculations have shown that the ↓ spin band is fully occupied and is separated from the conduction band by a gap, showing semiconducting characteristics below T_C. The intermediate values of the Seebeck coefficient, between those of a metal and a semiconductor, can also be accounted for a narrow band at the Fermi energy, where the DOS derivative with respect to the energy changes rapidly and originates and increase in the Seebeck value according to equation (3-14). The Seebeck data is also consistent with an additive behaviour of both metallic and semiconducting properties, which are accounted for the metallic ↑ spin band and the semiconducting ↓ spin band, respectively.

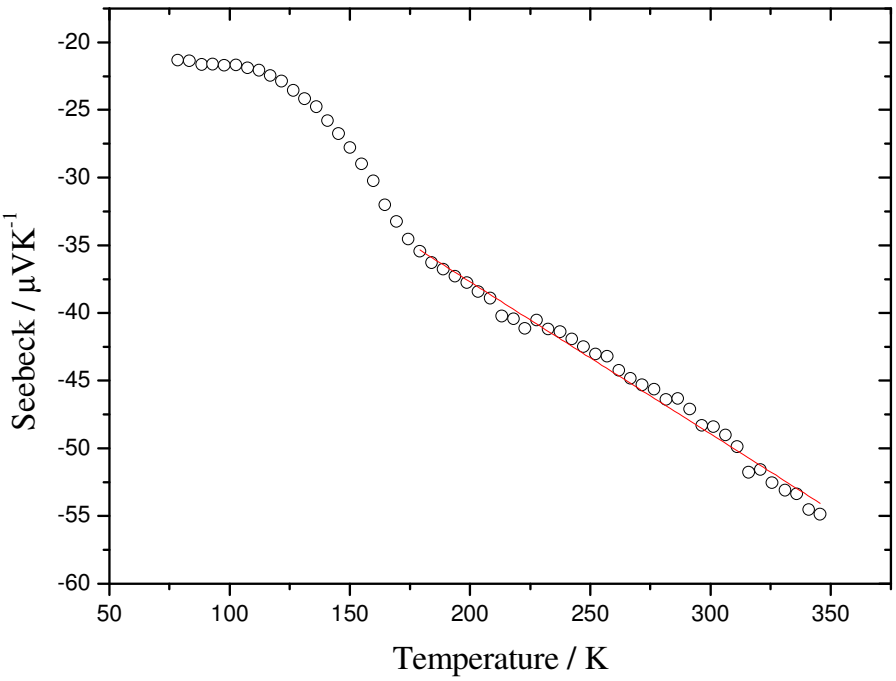

Figure 6-12 Seebeck coefficient *vs*. Temperature plot for the shandite $Co_3Sn_2S_2$. The paramagnetic region has been fitted linearly according to equation (6-5).

Chapter 7

Conclusions

7.1 Anion-substituted ternary skutterudites

Neutron powder diffraction data of the anion-substituted ternary skutterudite $CoGe_{1.5}Te_{1.5}$ showed unindexed reflections when modelled with the cubic space group $Im\overline{3}$ of the binary skutterudite $CoSb_3$. Previous studies reported a symmetry lowering from $Im\overline{3}$ to $R3$ when anion substitution occurred [56]; however Rietveld refinements with such space group resulted unstable and did not reach convergence. Group theoretical analysis revealed that there was an inversion centre missing in the model used and that the actual space group possessed higher symmetry, being identified as $R\overline{3}$, with which the refinements reached convergence. The 24*g* cubic Wyckoff position splits into four 18*f* positions and the four possible different anion configurations were used in consecutive refinements for comparison. The anion configuration with the lowest R_{wp} factor matched that of the model (associated to the irreducible representation H4+), corresponding to an antiprismatic anion configuration around the metal in which different anions are occupying opposite triangular faces. Such configuration originates alternate layers of anions along the [111] direction.

Rietveld refinements also revealed cubic pseudosymmetry, where metal atoms are shifted slightly from their cubic ideal positions. This is translated into a rhombohedral angle very close to 90° and it was possible to successfully refine the metal atom positions only at low temperature. The symmetry lowering gives rise to two crystallographically distinct anion square rings, in which the same type of anion occupies trans positions within the rings. Moreover, the fact that the irreducible representation H4+ consist of anion ordering without octahedra tilting is confirmed by a tilt angle experimental value of 32.5°, very close to the parent cubic $CoSb_3$ skutterudite, *i.e.* 32.8°.

Analysis of available crystallographic data of $CoGe_{1.5}S_{1.5}$ with the software package PLATON/ADDSYM also revealed a missing inversion centre in the assigned *R*3 space group. Rietveld refinements of neutron powder diffraction data of the sulphides $MGe_{1.5}S_{1.5}$ (M = Co, Rh, Ir) using the crystallographic model obtained for $CoGe_{1.5}Te_{1.5}$ showed good agreement. Anion disorder was modelled and the results show that it is present to a small extent, consistent with the high electronegativity difference between Ge and S (1.8 *vs*. 2.5). The tilt pattern is retained and the tilt angle is close to that of their binary antimony counterparts. The increase of the tilt angle as the metal varies down the group is consistent with results obtained by O'Keefe *et al*. in structures related to the cubic perovskite [260].

A resonant scattering synchrotron experiment was carried out on the tellurides $MQ_{1.5}Te_{1.5}$ (M = Co, Rh, Ir; Q = Ge, Sn) in order to find out whether or not the model obtained for $CoGe_{1.5}Te_{1.5}$ was applicable in all of them and also to determine the extent of anion disorder. Rietveld refinements using the rhombohedral space group $R\bar{3}$ always resulted in better agreement factors than the parent cubic space group $Im\bar{3}$. Moreover, modelling of anion disorder also resulted in better agreement factors by 1-2%. Within the telluride family under study, three factors affecting the anion disorder have been identified, namely the size of the anion Q and the polarizability of the cation M. For the same cation, tin-containing compounds show larger disorder than their germanium counterparts. Tin atomic radius (1.62 Å) is much closer to tellurium (1.60 Å) than germanium (1.37 Å), because both belong to the same period. Therefore, tin and tellurium are more likely to exchange positions than germanium and tellurium, given that it will originate smaller changes in the covalent interactions with the surrounding elements. Likewise, a larger disorder is observed as the metal atom changes down the group 9, keeping the same anion pair. This is attributed to the smaller charge-to-radius ratio, which is a measure of the cation polarizing power. According to Welker, bonding in heteroatomic semiconductors possesses an ionic as well as a covalent component. Resonance between the ionic and covalent structures originates an increase in the bond strength which, in turn, gives rise to larger band gaps [278]. Therefore, iridium is the least polarizing cation with the smallest ionic bonding component. Such decrease in the metal-anion bonding interaction may allow for a larger extent of disorder.

A relation between the extent of the disorder and the proximity of the metal atomic positions to those of the ideal parent cubic structure is also observed. The intensity and width of the extra reflections unaccounted for by the cubic $Im\bar{3}$ model change with the anion disorder. They reach the lowest intensity for $IrSn_{1.5}Te_{1.5}$, whose metal positions are the closest most to the parent cubic structure.

Furthermore, a correlation between the intraring and metal-anion distances is noticed thanks to the high collimation and brightness of the synchrotron source; which allows a more accurate determination of bond distances. Larger (and weaker) metal-anion distances have the effect of shortening (strengthening) intraring distances. Depletion of electron density in any of these two regions seems to cause stronger covalent interactions in the other. Such behaviour has already been seen in other transition metal semiconductors containing anion-anion bonds, such as those with the arsenopyrite or pyrite structure [150].

Resistivity measurements on all the ternary skutterudites under study show a decreasing resistivity as the temperature rises, characteristic of semiconductors. The expected relative values are Co > Rh > Ir, and for those compounds with the same metal S > Te and Ge > Sn, given that a more ionic bonding gives rise to lower electron mobilities and lower resistivity values. However, several anomalies are observed with respect to this trend. The $MGe_{1.5}S_{1.5}$ (M = Co, Rh, Ir) sulphides show unexpectedly low values of the absolute resistivity, which can be explained by sample degradation problems, this type of sulphides has proven to be highly sensitive to ageing. $RhSn_{1.5}Te_{1.5}$ shows a much lower resistivity than $IrSn_{1.5}Te_{1.5}$. Neutron diffraction data reveals a large content (~ 14%) of the impurity phase $RhTe_2$. Therefore, further analysis of $RhSn_{1.5}Te_{1.5}$ data is not believed to be meaningful.

A two-slope resistivity logarithm *vs*. inverse temperature is observed. This is consistent with impurity-driven conduction at low temperature. Narrow bands in the vicinity of the Fermi energy explain the thermally activated hopping electronic transport at low temperature, where the thermal energy is insufficient to promote charge carriers into the delocalized conduction band. The origin of the impurities is ascribed to secondary phases forming a solid solution within the main phase, defects in the crystal structure or small variations in the stoichiometry. Random distribution of such defects causes variable-range thermally activated conduction events. Moreover, variable-range hopping (VRH) conduction is expected in impurity semiconductors with strongly localized impurity levels, as indicated by Mott [291]. A VRH law has been fitted to low temperature resistivity data except for the telluride $CoGe_{1.5}Te_{1.5}$. The onset of the low-temperature conduction mechanism is linked to the onset of VRH conduction as their respective temperature fitting ranges are similar. Moreover, a correlation between the VRH temperature fitting range and the size of the band gap calculated from resistivity temperature at high temperature (~ 350 K) is observed, which is believed to be caused by the onset of electronic transitions from the impurity states into the conduction band. Somehow, the shallowness of such states seems to be linked to the expected relative band gap size (*vide infra*), which might indicate faults in the anion crystallographic sites, given their larger electronegativity.

High temperature (up to 350 K) resistivity data has been used to extract an estimated band gap value for all the ternary skutterudites under study. Fleurial *et al*. estimated the band gap values for anion-substituted ternary skutterudites, such as $CoGe_{1.5}Se_{1.5}$,

$IrGe_{1.5}Se_{1.5}$ and $IrSn_{1.5}Te_{1.5}$, to be approximately between 1.5 and 2.5 eV. Measurements of the electrical resistivity up to 900 K are also reported [50]. The values obtained within this work are approximately between 0.05 and 0.3 eV, which are clearly one order of magnitude lower than expected. Such values are hypothesized to correspond to the activation energy of electrons needed to promote from impurity states to the conduction band. Therefore, the intrinsic regime has not been reached at 350 K. The expected band gap size for the ternary skutterudites under study follows the same trend as the resistivity (*vide supra*) and is directly correlated to the ionic component of the bonding. The relative band gap sizes obtained in our measurements up to 350 K are those expected for the actual high-temperature band gaps, showing the same anomalies as those seen in the resistivity data, which can be accounted for analogously.

Seebeck measurements reveal that electrons are the main charge carriers (*n*-type) in the cobalt-containing tellurides, whereas they are holes (*p*-type) for the rest of the compounds. The absolute values of the Seebeck coefficient at 350 K correlate well with the band gap values obtained with resistivity data up to 350 K and with the expected high-temperature band gaps, taking into account the anomalies already accounted for. This supports the previous hypothesis as to the relation between impurity shallowness and the ionic component of the bonding. Seebeck curves follow two well-defined trends, namely a linear relation with the temperature or a linear relation with the temperature logarithm. The latter relation is followed by $CoGe_{1.5}S_{1.5}$ and $IrGe_{1.5}Te_{1.5}$ and is characteristic of extrinsic semiconductors with an undetermined number of localized impurity states. Conversely, the linear temperature dependence is followed by $RhGe_{1.5}S_{1.5}$, $IrGe_{1.5}S_{1.5}$, $CoSn_{1.5}Te_{1.5}$, $RhSn_{1.5}Te_{1.5}$ and $IrSn_{1.5}Te_{1.5}$ and is consistent with metal-like behaviour typical of semiconductors with broader impurity bands. Such bands overlap to a greater extent and electronic conduction takes place not only by hopping, but also by means of tunnelling. $CoGe_{1.5}Te_{1.5}$ Seebeck does not follow any of the above trends, nor does the resistivity, being the conduction mechanism in the measured sample still unknown, which may be explained by sample decomposition problems. At 350 K the exhaustion region has not been reached by any of the compounds under study, thus the extrinsic regime dominates the conduction mechanism up to this temperature. The intrinsic regime is predicted to take over at approximately 500 K, as seen, for instance, in a high-temperature resistivity measurement on $CoSn_{1.5}Te_{1.5}$ [109].

According to the transport property measurements presented, $CoGe_{1.5}S_{1.5}$ and $IrGe_{1.5}Te_{1.5}$ are non-degenerate extrinsic semiconductors with localized impurity states, whereas $RhGe_{1.5}S_{1.5}$ and $CoSn_{1.5}Te_{1.5}$ are non-degenerate extrinsic semiconductors possessing broader impurity bands. $IrGe_{1.5}S_{1.5}$, $RhSn_{1.5}Te_{1.5}$ and $IrSn_{1.5}Te_{1.5}$ show a weak temperature dependence in the resistivity plots as well as low values of the Seebeck coefficient characteristic of strongly degenerate semiconductors. Nevertheless, considering the fact that the latter compounds contain non-negligible amounts of impurities, this conclusion should be taken with caution. The ionic formula that best describes these properties is $M_4^{3+}[Y_2(Q^{2-})_2]_3$, in which the electropositive atom acquires a filled-shell d^6 electron configuration by giving up three electrons to the main-group element framework. These six electrons fill the d_{xy}, d_{xz} and d_{yz} t_{2g} non-bonding and localized orbitals in the transition metal (*cf.* section 7.3). The electronic charge in the heteroatomic four-membered ring is occupying molecular orbitals localized mainly on the chalcogen atom, because of its larger electronegativity [264]. This ionic Zintl-type view of the bonding, however, has been questioned, as group 9 elements turn out to be more electronegative than those of group 14 and, in the case of Ir and Rh, even more than Te. Semiempirical band structure calculations indicate that metal d orbtals lie below anion p orbitals, giving rise to e_g antibonding orbitals energetically more stable than anion-localized electrons. These situation favours a charge transfer from such anions towards the $d_{x^2-y^2}$ and d_{z^2} metal orbitals, thereby filling them completely and becoming a d^{10} system [155,264].

Porosity-corrected thermal conductivity values of 3.0, 2.3 and 1.3 $Wm^{-1}K^{-1}$ have been measured for the cobalt-containing ternary skutterudites $CoGe_{1.5}S_{1.5}$, $CoGe_{1.5}Te_{1.5}$ and $CoSn_{1.5}Te_{1.5}$, respectively. Such low values when compared to the binary skutterudite $CoSb_3$, *i.e.* 10 $Wm^{-1}K^{-1}$, are explained on the grounds of anion ring distortion. Theoretical studies show that the four-membered antimony rings contribute extensively to the thermal conductivity of the bulk phase. Their distortion is responsible for the large increase in phonon scattering. Literature values for $CoSn_{1.5}Te_{1.5}$ of 4 $Wm^{-1}K^{-1}$ may indicate that porosity is not fully accounted for with the correction used.

The highest power factor ($S^2\sigma$) is attained by $CoGe_{1.5}Te_{1.5}$, although it still is two orders of magnitude lower than that found in state-of-the-art thermoelectric materials. The thermoelectric figure of merit for the cobalt-containing compounds has been calculated and values that are approximately three orders of magnitude lower than commercially

available materials are obtained. When compared to the binary skutterudite with the best thermoelectric properties, *i.e*. $CoSb_3$, it is clearly seen than anion substitution causes a deleterious effect on the electrical conductivity. Ring distortion and the different electronegativity of the elements forming the four-membered ring have a direct effect on the electron mobilities, decreasing them as the bands become narrower. This is partially offset by an important decrease in the thermal conductivity as well as an increase in the Seebeck coefficient; however this is not enough and the overall thermoelectric performance decreases notably.

7.2 Filled ternary skutterudites

Attempts to synthesize the fully filled anion-substituted ternary skutterudite $LaFe_3CoGe_6Te_6$ may indicate that filling this type of system is analogous to Co_4Sb_{12}-based skutterudites in terms of the amount and type of filler atom that can diffuse into the interstitial sites. Despite fulfilling all the requirements for a filler atom to form filled phases, lanthanum does not form the target phase. Charge compensation in the cation site may have deleterious effects as to the formation of such phase, given that it introduces an extra cation with which the isoelectronically substituted anion site may form more stable secondary binary phases. A recent publication indicates that the amount of filler atom in partially filled (up to 30%) anion-substituted ternary skutterudites may be increased by varying the anion-anion ratio, instead [59].

7.3 Equiatomic ternary phases MGeTe (M = Co, Rh)

The new compounds CoGeTe and RhGeTe crystallize in the α–$NiAs_2$ structure and are regarded as a ternary ordered variant of such archetype. The metal atom is octahedrally coordinated by three germanium and three tellurium atoms in an antiprismatic configuration occupying opposite triangular faces. Octahedra share the equatorial germanium-germanium edge forming dimers that allow metal atoms to shift and form metal-metal single bonds. The metal pairs are oriented along the [011] and $[0\,\bar{1}\,1]$ directions alternatively, and their centres conform a fcc-type lattice with an elongated *c* axis. Ge-Te pairs are oriented alternatively in a pyrite and marcasite fashion, being this structure understood in terms of a stacking sequence of pyrite and marcasite blocks. The relative thickness of such blocks is determined by the anion size difference and the existence of metal-metal pairing, causing both a contraction of the marcasite block. The

approximately 0.5 Å difference found in the MGeTe compounds is ascribed to the metal pair formation, since anions from adjacent periods originate a smaller difference, *i.e.* ~ 0.2 Å. Further, as a result of the metal pairing, the tetrahedral coordination of the germanium atoms is severely distorted (M-X-M ~ 134-136 °), whereas that of tellurium remains undistorted (M-Y-M ~ 116-117 °), resembling the ideal pyrite value, *i.e.* (115.4 °). Anion disorder is highly unfavourable from a crystallographic point of view, given that the smallest anion is always found in edge-sharing positions, whereby occupying an independent 8*c* Wyckoff site. Disorder is not observed experimentally either.

The reason why MGeTe crystallizes in the α–$NiAs_2$ structure instead of the arsenopyrite structure is not straightforward. The filled shell configuration obtained by a 20 VEC acts as a driving force with respect to other compounds with similar VECs, thereby distorting and even forming extra metal pairs in order to achieve such configuration.

Table 7-1 Correlation between VEC and structure for equiatomic compounds with the formula MXY (M = Group 8-10 transition metal; X and Y = Group 14-16 main group element).

	18 e⁻	**19 e⁻**	**20 e⁻**	**21 e⁻**
Marcasite (*Pnnm*)	**Binary** Group 8 + 15 (*e.g.* $FeAs_2$)			
Arsenopyrite ($P2_1c$)		**Ternary** Group 8 + 15 + 16 (*e.g.* FeSAs)		
α-$NiAs_2$ (*Pbca*)		**Ternary** Group 9 + 14 + 16 (*e.g.* CoGeTe) Group 10 + 14 +15 (*e.g.* PtSiSb)	**Binary** Group 10 + 15 (*e.g.* $PtBi_2$) **Ternary** Co + group 15 + 16 (*e.g.* CoSeAs) Group 10 + 14 +16 (*e.g.* PtSiTe)	
Pyrite ($Pa\bar{3}$)		**Binary** (*e.g.* MnS_2)	**Binary** Group 8 + 16 (*e.g.* FeS_2)	**Binary** (*e.g.* CoS_2)
Cobaltite ($Pca2_1$)			**Ternary** Rh & Ir + 15 + 16 (+ CoSAs) Group 10 + 14 + 16 (*e.g.* PtSiSe)	
Ullmannite ($P2_13$)				**Ternary** Group 10 + 15 + 14 (*e.g.* NiSAs)

As a result, all of them can be described in relation to the pyrite structure, possessing similar band structures with differences in the width and degeneracy of the metal d orbitals [147].

Its wide occurrence in transition metal dichalcogenides and dipnictides points at the large stability of this structure [374]. Thus, a correlation between structure and electron count can be drawn, revealing all the interrelated structures (Table 7-1). Marcasite compounds form linear chains of metals atoms, whereas arsenopyrite and some α–$NiAs_2$ compounds form metal pairs instead to achieve the full band configuration, sharing two and one electrons per metal atom, respectively.

Most of the α–$NiAs_2$-type compounds possess a VEC of 20, where no metal pairing occurs as the distance between metal centres is ≥ 3.5 Å; whereas those with a VEC of 19 form metal-metal pairs. It is also seen that 20 e^- compounds formed by group 15 and 16 anions, such as AsSe, PSe and SSb, crystallize in the α–$NiAs_2$ for the first-row transition metal cobalt; whereas, in the presence of rhodium and iridium, crystallize in the cobaltite structure instead. Regarding the larger charge-to-radius ratio of 3d transition metals, this may indicate that a certain degree of ionicity is required to stabilize the α–$NiAs_2$ structure. The 5d metal Platinum is found in the same structure when silicon is present, however is the 4d metal palladium when silicon changes to the more polarizable tin [162,164]. Bond valence calculations result in a 4+ oxidation state for Co and Rh, which is high and relatively rare, supporting the high charge / radius ratio assumption.

As regards α–$NiAs_2$-type 19 e^- compounds, those formed by group 8 metals with group 15 and 16 anions have not been synthesized hitherto. It seems then that group 8 metals crystallize only in the arsenopyrite structure (Table 1-9). Nevertheless, they form by combination of group 9 and 10 metals with group 15 and 16 anions and with group 14 and 15 anions, respectively (Table 7-1).Pair-forming α–$NiAs_2$ compounds with a 19 e^- VEC possess an anomalously large dihedral angle between equatorial ligands when dimers from both structures are compared. Whilst in arsenopyrite the dimer dihedral angle deviates a maximum of 2°, in α–$NiAs_2$ this value reaches 16 ° with respect to the ideal 180° coplanar value (Table 5-5). These evidences indicate that stability differences may be attributed to variations in the metal-anion covalent interaction; which, in turn, has also been argued as the main factor determining the stability between the marcasite and the arsenopyrite structures [330].

Resistivity measurements decrease with temperature in both compounds, consistent with semiconducting behaviour. The CoGeTe resistivity agrees well with recently published data on this compound [328]. The data obtained cannot be fitted to a single Arrhenius-type thermally activated behaviour throughout the whole temperature range. Two Arrhenius-type laws are able to fit the data at high and low temperature instead, characteristic of impurity semiconductors. The low temperature fit accounts for the thermally activated hopping conduction process in the impurity region. Charge carrier hopping and polaron hopping are both low-mobility conduction mechanisms that may occur at low temperature in impurity semiconductors. However, with the existent data, none of them can be ruled out. The high temperature fit explains the thermally activated conduction across the band gap, when the Fermi energy lies at the middle of the band gap and a two-band (electrons in the conduction band and holes in the valence band) conduction mechanism accounts for the resistivity values observed. Nonetheless, it is seen from the inverse temperature plots that the measurement is cut off at the onset of the transition regime. Therefore, the band gap values obtained from such plots are unrealistically small and unreliable (a few tens of meV). Extended Hückel calculations carried out on the isotypic 19 e^- compound PtSiSb reveal a band gap of 0.6 eV and a band gap of 1.6 eV for the 20 e^- PtSiTe [162] and also an experimentally determined band gap of 0.11 eV has been measured in CoSbS [163]. In spite of this fact, the justification of the larger band gap obtained for RhGeTe than for CoGeTe has been attempted in terms of the metal-metal bond strength.

Bonding within the octahedra in the α–$NiAs_2$ structure can be regarded as analogous to that of the pyrite octahedra, for which there exist well established models. One tetrahedral sp^3 hybrid orbital from each of the six anions forms six σ-bonds with d^2sp^3 hybrid orbitals of the transition metal. These transition metal hybrid orbitals consist of the two e_g orbitals ($d_{x^2-y^2}$ and d_{z^2}), one 4*s* orbital and three 4*p* orbitals and the three transition metal t_{2g} orbitals (d_{xy}, d_{yz}, d_{xz}) remain non-bonding [142]. In the rocksalt structure these non-bonding orbitals are degenerate; in the pyrite only two of them are degenerate; whereas the degeneracy is completely broken in the marcasite structure and the three orbitals have different energies [147]. The non-bonding orbital splitting in α–$NiAs_2$ may be assumed to be in between that of the pyrite and the marcasite, given alternate sequence of pyrite and marcasite blocks that constitute its structure, *i.e.* completely broken degeneracy. The 19e^- VEC completely fills the valence band and two non-bonding orbitals, leaving one unpaired electron in the non-bonding orbital with the

highest energy, which will pair up with a neighbouring metal unpaired electron to form the metal-metal bond. Owing to the fact that, at high temperature, the conduction event will not consist on a carrier excitation from the valence band to the empty antibonding e_g band, but from the highest occupied and localized band to the empty band, then the highest-energy non-bonding orbital is believed to critically determine the effective band gap. Therefore, the extent of the bonding interaction between metal centres will determine the splitting of the highest-energy non-bonding orbital and the band gap thereof. RhGeTe may possess a larger band gap than CoGeTe on the grounds of the metal-metal distances observed when compared with those found in the metal. Thus, differences of 0.32(1) Å and 0.227(3) Å are observed in CoGeTe and RhGeTe, respectively; which points at a stronger bond in rhodium than in cobalt. The larger binding energy of rhodium (~ 550 $KJmol^{-1}$) with respect to cobalt (~ 450 $KJmol^{-1}$) may explain such difference [375]. Moreover, the resistivity of RhGeTe is approximately three times larger than that of CoGeTe (the same band gap ratio is seen from flawed high-temperature data), which is also consistent with the lower electron mobility found among compounds with similar structure but possessing larger band gaps, according to Welker's rules [278]. At this point is worth noticing the similarity between the anion ordering in the octahedra that form the building blocks of the anion-substituted ternary skutterudites and the α–$NiAs_2$ structure. Despite having a completely different linkage among them, anions in both structures are found around the metal atom forming a trigonal antiprismatic configuration, in which anions are occupying opposite triangular faces.

The presence of localized impurity states suggests a VRH conduction mechanism at low temperature, given the random distribution of impurities over the crystal lattice. The temperature range of such mechanism is believed to be correlated with the band gap size. Thus, the RhGeTe VRH temperature range is 1/3 shorter than the CoGeTe range. The VRH and the low-temperature Arrhenius law temperature ranges are approximately the same in CoGeTe and also in RhGeTe. The onset of a different conduction mechanism at low temperature may then be explained by the variable-range hopping mechanism. The Seebeck coefficient of both compounds is negative, indicating that electrons are the main charge carriers, and increases with temperature showing a metal-like behaviour characteristic of impurity states. At 325 K the exhaustion region has not been reached yet and confirms that band gaps obtained from resistivity data at the same

temperature are not real. From ST plots, a change in the charge carrier scattering mechanism has been determined to occur at 175 K.

The scattering parameter *r* changes from 0 to approximately 0.5, consistent with the onset of optical phonon scattering, in addition to the acoustic phonon scattering. The RhGeTe absolute values are approximately 10 μVK^{-1} larger than those of CoGeTe, which is consistent with the larger resistivity and the lower electron mobility of RhGeTe predicted based on the band gap difference. The Seebeck coefficients follow a metal-like temperature dependence indicating the existence of broad impurity bands with some degree of localization. From these transport property measurements it can be concluded that both CoGeTe and RhGeTe are non-degenerate extrinsic semiconductors with broad impurity bands. The ionic formula describing these properties would be $M^{4+}Ge^{3-}Te^{-}$, where the metal atom acquires a d^6 configuration and the d electrons fill the non-bonding t_{2g} orbitals. This formula, however, enters in contradiction with the respective element electronegativities. The metal is not the most electropositive atom, nor is Ge the most electronegative. As seen also in the ternary skutterudites formed by elements from the same groups, group 9 d orbitals possess lower energy than main group p orbitals, giving rise to a charge transfer from the latter orbitals to the antibonding e_g orbitals. Both t_{2g} and e_g orbitals become completely full and the transition metal achieves a d^{10} configuration. This has been confirmed by band structure calculations on PtSiSb, which also crystallizes in the α–$NiAs_2$ structure and shows metal-metal paring [162].

Magnetic susceptibility measurements on CoGeTe reveal that it is a diamagnetic and semiconducting system with trace amounts of paramagnetic impurities. The thermal conductivity corrected for porosity has been determined to be 1.6 $Wm^{-1}K^{-1}$, which is comparable to other state-of-the-art thermoelectric materials (*i.e.* 1.6 $Wm^{-1}K^{-1}$ Bi_2Te_3). The power factor ($S^2\sigma$) of CoGeTe is larger than that of RhGeTe; however, at the highest temperature measured, *i.e.* 325 K, it is an order of magnitude lower than typical values for thermoelectric materials, e.g. 1 x 10^{-3} $Wm^{-1}K^{-2}$. Nevertheless, the power factor is expected to increase with temperature given that neither the Seebeck coefficient has reached its maximum, nor the electrical conductivity. The exhaustion region is reached in the binary skutterudite $CoSb_3$ at approximately 600 K, whereas in other ternary skutterudites, namely $CoSn_{1.5}Te_{1.5}$ or $IrSn_{1.5}Te_{1.5}$, occurs at 500 K of even higher temperatures [50,109]. Therefore, we can conclude that CoGeTe is a potential thermoelectric material for mid-temperature applications.

7.4 $Co_3Sn_2S_2$ shandite

The powder neutron diffraction experiment evidences that $Co_3Sn_2S_2$ retains the shandite structure, *i.e*. space group $R\bar{3}m$, between 50 and 300 K. As the temperature rises, the rhombohedral angle deviates further from the ideal 60° value; giving rise to a peak splitting that is more noticeable at low *d*-spacing (Figure 6-4 and Figure 6-5). This is consistent with pseudocubic symmetry, previously reported by Weihrich *et al*., when compared with the parent structure of the superconductor $MgCo_3C$, which crystallizes in the cubic space group $Pm\bar{3}m$ [195].

No extra magnetic reflections are observed at low temperature, nor any significant change in the intensities when datasets at 50 and 300 K are compared. Taking into account that $Co_3Sn_2S_2$ is ferromagnetic at low temperature (*vide infra*), this indicates that the magnetic and the crystallographic unit cells are coincident as expected and that the saturation magnetization is small enough to not to cause appreciable scattering.

The rhombohedral lattice parameter increases with temperature and no discontinuities are noticed at any point of the temperature interval nor in any bond distance or bond angle; thereby observed changes are ascribed to those expected in a progressive temperature variation. The $Co_3Sn_2S_2$ structure can be described as alternate layers of cobalt Kagomé lattices and distorted interwoven SnS honeycomb lattices, where hexagons in the Kagomé lattice are centred by Sn2 atoms occupying 3*b* Wyckoff positions. The shorter Co-S distances when compared with other binary sulphides indicate a tightly bound cobalt-sulphur framework best described by the alternative formula $Sn_2[Co_3S_2]$.

Magnetic measurements reveal that $Co_3Sn_2S_2$ is a ferromagnet with a Curie temperature of 176 K and an effective magnetic moment in the paramagnetic region of 1.12 μ_B. The positive Weiss constant obtained, albeit relatively small, confirms the presence of ferromagnetic correlations among unpaired electrons. A saturation magnetic moment, measured at 5 K and extrapolated to infinite field, of 0.29 μ_B is also obtained. Both the splitting and shape of ZFC-FC magnetic susceptibility *vs*. temperature plots indicate that $Co_3Sn_2S_2$ is a highly anisotropic magnetic system, which supports the existence of magnetic domains with large exchange energies as well as large values of the coercivity. Both characteristics are consistent with ferromagnetism. The occurrence of magnetic frustration owing to the presence of the cobalt Kagomé lattice has been discarded, since

the Weiss constant and the Curie temperature possess similar values and their ratio is very close to one.

The electrical resistivity *vs*. temperature plot is consistent with metallic behaviour and presents a clear discontinuity at approximately 175 K, consistent with the onset of a ferromagnetic phase transition. The steep decrease in the resistivity as the temperature drops beyond the Curie temperature is linked to an increase of the kinetic energy of charge carriers caused by the conservation of the spin alignment. The absolute resistivity values obtained are two orders of magnitude higher than other broadband metals (~ 10^{-6} Ωcm) and one order of magnitude higher than $Ni_3Sn_2S_2$ shandite (Table 1-13), which possesses exactly the same structure. This anomaly can be explained by both the width and density of states available at the Fermi energy. Band calculations performed on $Ni_3Sn_2S_2$ indicate that the DOS available at the Fermi energy is too low and wide to sustain magnetic interactions, thereby showing a Pauli-type magnetic susceptibility typical of metals [200,203]. On the contrary, the DOS in $Co_3Sn_2S_2$ is narrow enough for the existence of long-range magnetic ordering which, in turn, explains the lower mobilities reflected in large values of the resistivity [201]. CoS_2-$CoSe_2$ is a completely analogue binary system where the bandwidth at the Fermi energy explains the ferromagnetism and the high resistivity of CoS_2 when compared to the Pauli magnetic susceptibility and lower resistivity of $CoSe_2$ [376,377].

The negative Seebeck coefficient throughout the whole temperature range shows that electrons are the main charge carriers and the observed increasing values with temperature are consistent with metallic character. The absolute values are one order of magnitude larger than expected for broad-band metals, *i.e*. a few μVK^{-1}, which can be explained by the larger derivative term in expression (3-7), characteristic of a narrow conduction band. Thus, the conduction model that is able to explain magnetic properties of localized unpaired electrons (ferromagnetism) and electron delocalization (metallic character) is that of an itinerant electron model. Hubbard developed a specific model for electron correlations in narrow energy bands that accounts for the properties seen in $Co_3Sn_2S_2$ [370].

Spin polarized calculations indicate that there is a difference of one electron in the occupation of the up and down channels of $Co_3Sn_2S_2$, where the minority spin channel shows a band gap, hence constituting a half-metal of the type I_A [195]. The saturation magnetization at low temperature should be an integer value for this type of materials; however a value of 0.87 μ_B per formula unit is obtained. Such divergence has been

ascribed to the high sensitivity of half-metallicity to crystallographic disorder and small variations in the stoichiometry [213].

Finally it is noteworthy to emphasize the striking similarity between the transport and magnetic properties of $Co_3Sn_2S_2$ and those of CoS_2. Despite CoS_2 crystallizing in the pyrite structure (section 1.3.2), it exemplifies the well-known fact that the band structure at the Fermi energy critically determines the properties of a material. CoS_2 has also been described as an itinerant electron ferromagnet with a Curie temperature of 124 K [376]. The degree of electronic delocalization, indicated by the q_{eff} / q_S ratio as described by Rhodes and Wolfarth [365], is very similar to $Co_3Sn_2S_2$ (2.0 *vs.* 1.7) with exactly the same saturation magnetic moment per cobalt atom, *i.e.* 0.87 μ_B [368]. Moreover, CoS_2 has also been predicted to be a half-metal by band structure calculations [378]. It has been already mentioned that s-d hybridisation is an antagonist of half-metallicity in first-row transition metal ferromagnetic elements, *i.e.* Fe, Co and Ni [208]. Thus, only binary and ternary compounds are expected to be half-metallic. Furthermore, it has been demonstrated that strong hybridization between cobalt 3d bands and sulphur 3p bands are an essential ingredient for highly polarized half-metals in pyrite-type transition metal materials, such as CoS_2 [379]. It turns out that the highest occupied bands in $Co_3Sn_2S_2$ are also formed by a strong mixing of cobalt 3d states and sulphur 3p states, as indicated by DFT calculations [201].

Nevertheless, the predicted half-metallicity of $Co_3Sn_2S_2$ is doubtful. Hitherto, CrO_2 is the only unambiguously determined half-metal by Andréev reflection and tunnelling with a 100% spin polarization [211,368]. The actual half-metallicity of CoS_2, previously classified as a half-metallic ferromagnet, has been questioned owing to the fact that its saturation magnetic moment is 0.87 and not the expected 1 μ_B. Polarized neutron diffraction experiments have determined the presence of unpaired electrons in both spin bands, which breaks the half-metallicity condition [367]. A similar result has been obtained for the Heusler alloy Co_2MnSi, another theoretical half-metal [380]. Therefore, the actual half-metallicity of $Co_3Sn_2S_2$ should be put on hold until further experimental confirmation.

7.5 Summary

In this thesis, the symmetry inconsistencies regarding the anion-substituted ternary skutterudites have been settled. Such results have also clarified a relatively obscure area within a family of materials with exceptional properties for thermoelectric applications,

namely the binary skutterudites. Moreover, the thermoelectric properties of these skutterudite-type ternary sulphides and tellurides have been studied and reported. They shed some light on a scarcely studied field, something striking given the importance of their binary counterparts. On the whole, it is seen that the distortion of the nearly square rings of the binary skutterudites occurring upon anion substitution has a clear deleterious effect on the thermoelectric properties, mainly observed in the dramatic increase of the electrical resistivity. Nevertheless, such substitution enhances the Seebeck coefficient and decreases the thermal conductivity down to values of state-of-the-art materials, but not enough to offset the electrical resistivity increase.

The two novel narrow-band semiconductors CoGeTe and RhGeTe have been discovered, their structure reported and their thermoelectric properties measured. They crystallize in a ternary ordered variant of the α-$NiAs_2$ structure. The properties of CoGeTe are promising for mid-temperature applications, *i.e*. between 500 and 700 K.

Finally, a neutron powder diffraction experiment of the shandite phase $Co_3Sn_2S_2$ has clarified the origin of their anomalous electrical and magnetic properties at low temperature and further measurements of these properties have confirmed the existing data.

7.6 Further work

High-temperature measurements of resistivity and Seebeck are necessary to assess the real performance of the anion-substituted ternary skutterudites at their optimal temperature, *i.e*. approximately 500 K. Doping both at the cation and anion site in $CoGe_{1.5}Te_{1.5}$ would give an optimal view as to the limits attainable by this type of material. Partially filled anion-substituted ternary skutterudites without charge compensation seems to be feasible up to 30% with already reported filler atoms. This might also be attempted. Given the few α-$NiAs_2$-type phases reported hitherto, it is certain that further research on this area will uncover new phases. By means of Table 7-1 it is possible to work out easily all the possible combinations that could be attempted. Doping as well as high-temperature transport property measurements could be carried out to assess their thermoelectric performance at optimal temperature. The study of the metal-metal bond evolution with either cation or anion progressive substitution is also suggested.

References

[1] Mahan G. D., Thermionic refrigeration, *J. Appl. Phys.*, **76**, 4362-4366 (1994).

[2] DiSalvo F. J., Thermoelectric cooling and power generation, *Science*, **285**, 703-706 (1999).

[3] Stockholm J. G., Current state of Peltier cooling, *XVI International Conference on Thermoelectrics*, 37-46 (1997).

[4] Ikoma K., Munekiyo M., Furuya K., Kobayashi M., Izumi T., Shinohara K., Thermoelectric module and generator for gasoline engine vehicles, *XVII International Conference on Thermoelectrics*, 464-467 (1998).

[5] Bell L. E., Crane D. T., High capacity thermoelectric temperature control systems, *XXV International Conference on Thermoelectrics*, 193-197 (2006).

[6] Altenkirch E., Electrotehrmische kalteerzeugung und reversible elektrische Heizung, *Physikalische Zeitschrift*, **12**, 920-924 (1911).

[7] Ioffe A. F., *Semiconductor Thermoelements, and Thermoelectric Cooling*, (Infosearch, ltd, 1957).

[8] Sherman B., Heikes R. R., Ure R. W., Calculation of efficiency of thermoelectric devices, *J. Appl. Phys.*, **31**, 1-16 (1960).

[9] Nolas G. S., Sharp J., Goldsmid H. J., *Thermoelectrics: basic principles and new materials developments*, (Springer, 2001).

[10] Slack G. A., Hussain M. A., The maximum possible conversion efficiency of silicon-germanium thermoelectric generators, *J. Appl. Phys.*, **70**, 2694 (1991).

[11] Harman T. C., Special techniques for measurement of thermoelectric properties, *J. Appl. Phys.*, **29**, 1373-1374 (1958).

[12] Chasmar R. P., Stratton R., The thermoelectric figure of merit and its relation to thermoelectric generators, *Int. J. Electron.*, **7** (1), 52-72 (1959).

[13] Fistul V. I., *Heavily Doped Semiconductors*, (Nauka, Moscow, 1967).

[14] Goldsmith H. J., *Electronic Refrigeration*, (Pion, London, 1986).

[15] Morelli D. T., Potential applications of advanced thermoelectrics in the automobile industry, *XV International Conference on Thermoelectrics*, 383-386 (1996).

[16] Littman H., Davidson B., Theoretical bound on the thermoelectric figure of merit from irreversible thermodynamics, *J. Appl. Phys.*, **32**, 217-219 (1961).

[17] Simon R., Thermoelectric figure of merit of two-band semiconductors, *J. Appl. Phys.*, **33**, 1830-1841 (1962).

[18] Mahan G. D., Figure of merit for thermoelectrics, *J. Appl. Phys.*, **65**, 1578-1583 (1989).

[19] Rittner E. S., Neumark G. F., Theoretical bound on the thermoelectric figure of merit of two-band semiconductors, *J. Appl. Phys.*, **34**, 2071-2077 (1963).

[20] Wood C., Materials for thermoelectric energy conversion, *Rep. Progr. Phys.*, **51**, 459-539 (1988).

[21] Mahan G., Sales B., Sharp J., Thermoelectric materials: new approaches to an old problem, *Phys. Today*, **50** (3), 42-47 (1997).

[22] Chung D. Y., Hogan T., Brazis P., Rocci-Lane M., Kannewurf C., Bastea M., Uher C., Kanatzidis M. G., $CsBi_4Te_6$: A high-performance thermoelectric material for low-temperature applications, *Science*, **287** (5455), 1024-1027 (2000).

[23] Nolas G. S., Poon J., Kanatzidis M., Recent developments in bulk thermoelectric materials, *MRS Bulletin*, **31**, 199-205 (2006).

[24] Brown S. R., Kauzlarich S. M., Gascoin F., Snyder G. J., $Yb_{14}MnSb_{11}$. New high efficiency thermoelectric material for power generation, *Chem. Mater.*, **18** (7), 1873-1877 (2006).

[25] Snyder G. J., Christensen M., Nishibori E., Caillat T., Iversen B. B., Disordered zinc in Zn_4Sb_3 with phonon-glass and electron-crystal thermoelectric properties, *Nat. Mater.*, **3**, 458-463 (2004).

[26] Kauzlarich S. M., Brown S. R., Snyder G. J., Zintl phases for thermoelectric devices, *Dalton Trans.*, **2007** (21), 2099-2107 (2007).

[27] Terasaki I., Sasago Y., Uchinokura K., Large thermoelectric power in $NaCo_2O_4$ single crystals, *Phys. Rev. B*, **56** (20), 12685-12687 (1997).

[28] Shikano M., Funahashi R., Electrical and thermal properties of single-crystalline $(Ca_2CoO_3)_{0.7}CoO_2$ with a $Ca_3Co_4O_9$ structure, *Appl. Phys. Lett.*, **82** (12), 1851-1853 (2003).

[29] Littleton Iv R. T., Tritt T. M., Kolis J. W., Ketchum D. R., Transition-metal pentatellurides as potential low-temperature thermoelectric refrigeration materials, *Phys. Rev. B*, **60** (19), 13453-13457 (1999).

[30] Hsu K. F., Loo S., Guo F., Chen W., Dyck J. S., Uher C., Hogan T., Polychroniadis E. K., Kanatzidis M. G., Cubic $AgPb_mSbTe_{2+m}$: bulk thermoelectric materials with high figure of merit, *Science*, **303** (5659), 818-821 (2004).

[31] Hicks L. D., Dresselhaus M. S., Effect of quantum-well structures on the thermoelectric figure of merit, *Phys. Rev. B*, **47** (19), 12727-12731 (1993).

[32] Dresselhaus M. S., Koga T., Sun X., Cronin S. B., Wang K. L., Chen G., Low dimensional thermoelectrics, *XVI International Conference on Thermoelectrics*, 12-20 (1997).

[33] Hicks L. D., Harman T. C., Dresselhaus M. S., Use of quantum-well superlattices to obtain a high figure of merit from nonconventional thermoelectric materials, *Appl. Phys. Lett.*, **63**, 3230-3232 (1993).

[34] Venkatasubramanian R., Siivola E., Colpitts T., O'Quinn B., Thin-film thermoelectric devices with high room-temperature figures of merit, *Nature*, **413**, 597-602 (2001).

[35] Slack G. A., *CRC Handbook of Thermoelectrics*, (Chemical Rubber, Boca Raton, FL, 1995).

[36] Kuznetsov V. L., Kuznetsova L. A., Kaliazin A. E., Rowe D. M., Preparation and thermoelectric properties of $A_8(II)B_{16}(III)B_{30}(IV)$ clathrate compounds, *J. Appl. Phys.*, **87** (11), 7871-7875 (2000).

[37] Tritt T. M., Subramanian M. A., Thermoelectric materials, phenomena, and applications: A bird's eye view, *MRS bulletin*, **31** (3), 188-194 (2006).

[38] Kjekshus A., Nicholson D. O., Rakke T., Compounds with the skutteradite type crystal slracture. I On Ofledal's relation, *Acta Chem. Scand.*, **27**, 1307-1314 (1973).

[39] Llunell M., Alvarez S., Alemany P., Skutterudite *vs*. ReO_3 structures for MX_3 solids: electronic requirements, *Dalton Trans.*, **1998** (7), 1195-1200 (1998).

[40] Oftedal I., Die Kristallstruktur von Skutterudit and Speiskobalt-chloanthit, *Z. Kristallogr.*, **A66**, 517-546 (1928).

[41] Kaiser J. W., Jeitschko W., The antimony-rich parts of the ternary systems calcium, strontium, barium and cerium with iron and antimony; structure refinements of the $LaFe_4Sb_{12}$-type compounds $SrFe_4Sb_{12}$ and $CeFe_4Sb_{12}$; the new compounds $CaOs_4Sb_{12}$ and $YbOs_4Sb_{12}$, *J. Alloys Compd.*, **291** (1-2), 66-72 (1999).

[42] Jeitschko W., Braun D., $LaFe_4P_{12}$ with filled $CoAs_3$-type structure and isotypic lanthanoid-transition metal polyphosphides, *Acta Crystallogr., Sect. B: Struct. Sci.*, **33** (11), 3401-3406 (1977).

[43] King R. B., Chemical bonding topology of binary and ternary transition-metal polyphosphides, *Inorg. Chem.*, **28** (15), 3048-3051 (1989).

[44] Müller U., *Inorganic structural chemistry*, (John Wiley and Sons, New york, 1993).

[45] Hulliger F., Halbleitende Verbindungen mit Skutterudit-Struktur, *Helv. Phys. Acta*, **34**, 782-786 (1961).

[46] Rundqvist S., Phosphides of the Platinum Metals, *Nature*, **185** (4705), 31-32 (1960).

[47] Grytsiv A., Rogl P., Berger S., Paul C., Bauer E., Godart C., Ni B., Abd-Elmeguid M. M., Saccone A., Ferro R., Structure and physical properties of the thermoelectric skutterudites $Eu_yFe_{4-x}Co_xSb_{12}$, *Phys. Rev. B*, **66** (9), 94411 (2002).

[48] Tang X. F., Chen L. D., Goto T., Hirai T., Yuan R. Z., Synthesis and thermoelectric properties of filled skutterudite compounds $Ce_yFe_xCo_{4-x}Sb_{12}$ by solid state reaction, *J. Mater. Sci.*, **36** (22), 5435-5439 (2001).

[49] Bauer E., Grytsiv A., Chen X. Q., Melnychenko-Koblyuk N., Hischer G., Kaldarar H., Michor H., Royanian E., Rotter M., Podloucky R., Rogl P., $BaPt_4Ge_{12}$: A skutterudite based entirely on a ge framework, *Adv. Mater.*, **20** (7), 1325-1328 (2008).

[50] Fleurial J. P., Caillat T., Borshchevsky A., Skutterudites: an update, *XVI International Conference on Thermoelectrics*, 1-11 (1997).

[51] Bauer E., Berger S., Mea M. D., Hilscher G., Michor H., Paul C., Grytsiv A., Rogl P., Scheidt E. W., Godart C., Filled skutterudites: formation, ground state properties and thermoelectric features, *Acta Phys. Pol. B*, **34** (2), 595-608 (2003).

[52] Grytsiv A., Rogl P., St B., Paul C., Michor H., Bauer E., Hilscher G., Godart C., Knoll P., Musso M., Lottermoser W., Saccone A., Ferro R., Roisnel T., Noel H., A novel skutterudite phase in the Ni-Sb-Sn system: phase equilibria and physical properties, *J. Phys. Condens. Matter*, **14** (29), 7071-7090 (2002).

[53] Lyons A., Gruska R. P., Case C., Subbarao S. N., Wold A., Preparation and characterization of some skutterudite related compounds, *Mater. Res. Bull.*, **13** (2), 125-128 (1978).

[54] Caillat T., Kulleck J., Borshchevsky A., Fleurial J. P., Preparation and thermoelectric properties of the skutterudite-related phase $Ru_{0.5}Pd_{0.5}Sb_3$, *J. Appl. Phys.*, **79** (11), 8419-8426 (1996).

[55] Partik M., Kringe C., Lutz H. D., X-ray structure determination of pseudomerohedrally twinned $CoGe_{1.5}S_{1.5}$ and $CoGe_{1.5}Se_{1.5}$, absorption correction, *Z. Kristallogr.*, **211** (5), 304-312 (1996).

[56] Lutz H. D., Kliche G., Lattice vibration spectra. XXVI. Far-infared spectra of the ternary skutterudites $CoP_{3-x}As_x$, $CoAs_{3-x}Sb_x$, and $MGe_{1.5}Y_{1.5}$ (M= Co, Rh, Ir; Y= S, Se), *J. Solid State Chem.*, **40** (1), 64-68 (1981).

[57] Bos J. W. G., Cava R. J., Synthesis, crystal structure and thermoelectric properties of $IrSn_{1.5}Te_{1.5}$-based skutterudites, *Solid State Commun.*, **141** (1), 38-41 (2007).

[58] Laufek F., Navratil J., Golias V., Synthesis and Rietveld refinement of skutterudite-related phase $CoSn_{1.5}Te_{1.5}$, *Powder Diffr.*, **23** (1), 15-19 (2008).

[59] Lin Q., Smalley A. L. E., Johnson D. C., Martin J., Nolas G. S., Synthesis and properties of $Ce_xCo_4Ge_6Se_6$, *Chem. Mater.*, **19** (26), 6615-6620 (2007).

[60] Nolas G. S., Fowler G., Yang J., Assessing the role of filler atoms on the thermal conductivity of filled skutterudites, *J. Appl. Phys.*, **100**, 043705 (2006).

[61] Braun D. J., Jeitschko W., Preparation and structural investigations of antimonides with the $LaFe_4P_{12}$ structure., *J. Less Common Met.*, **72** (1), 147-156 (1980).

[62] Meisner G. P., UFe_4P_{12} and $CeFe_4P_{12}$: Nonmetallic isotypes of superconducting LaF_4P_{12}, *J. Appl. Phys.*, **57** (8), 3073 (1985).

[63] Braun D., Jeitschko W., Ternary arsenides with $LaFe_4P_{12}$-type structure, *J. Solid State Chem.*, **32**, 357-363 (1980).

[64] Grandjean E., Gerard A., Braun D. J., Jeitschko W., Some physical properties of $LaFe_4P_{12}$-type compounds, *J. Phys. Chem. Solids*, **45** (8-9), 877-886 (1984).

[65] Tritt T. M., Low-temperature transport properties of the filled and unfilled $IrSb_3$ skutterudite system, *J. Appl. Phys.*, **79** (11), 8412-8418 (1996).

[66] Chen B. X., Xu J. H., Uher C., Morelli D. T., Meisner G. P., Fleurial J. P., Caillat T., Borshchevsky A., Low-temperature transport properties of the filled skutterudites $CeFe_{4-x}Co_xSb_{12}$, *Phys. Rev. B*, **55** (3), 1476-1480 (1997).

[67] Sales B. C., Mandrus D., Williams R. K., Filled skutterudite antimonides: A new class of thermoelectric materials, *Science*, **272** (5266), 1325-1328 (1996).

[68] Chapon L., Ravot D., Tedenac J. C., Nickel-substituted skutterudites: synthesis, structural and electrical properties, *J. Alloys Compd.*, **282** (1-2), 58-63 (1999).

[69] Sales B. C., *Handbook on the Physics and Chemistry of the Rare Earths, Vol. 33*, (Elsevier, 2003).

[70] Fukuoka H., Yamanaka S., High-pressure synthesis and structure of new filled skutterudite compounds with Ge-substituted host network; $LnRh_4Sb_9Ge_3$, Ln = La, Ce, Pr, and Nd, *J. Alloys Compd.*, **461** (1-2), 547-550 (2008).

[71] Sales B. C., Mandrus D., Chakoumakos B. C., Keppens V., Thompson J. R., Filled skutterudite antimonides: Electron crystals and phonon glasses, *Phys. Rev. B*, **56** (23), 15081-15089 (1997).

[72] Nolas G. S., Slack G. A., Morelli D. T., Tritt T. M., Ehrlich A. C., The effect of rare-earth filling on the lattice thermal conductivity of skutterudites, *J. Appl. Phys.*, **79** (8), 4002-4008 (1996).

[73] Fleurial J. P., Borshchevsky A., Caillat T., Morelli D. T., Meisner G. P., Ieee, High figure of merit in Ce-filled skutterudites, *XV International Conference on Thermoelectrics*, 91-95 (1996).

[74] Meisner G. P., Morelli D. T., Hu S., Yang J., Uher C., Structure and lattice thermal conductivity of fractionally filled skutterudites: Solid solutions of fully filled and unfilled end members, *Phys. Rev. Lett.*, **80** (16), 3551-3554 (1998).

[75] Nolas G. S., Fowler G., Partial filling of skutterudites: Optimization for thermoelectric applications, *J. Mater. Res.*, **20** (12), 3234-3237 (2005).

[76] Chen L. D., Tang X. F., Kawahara T., Dyck J. S., Chen W., Uher C., Goto T., Hirai T., Multi-filling approach for the improvement of thermoelectric properties of skutterudites, *XX International Conference on Thermoelectrics*, 57-60 (2001).

[77] Nolas G. S., Cohn J. L., Slack G. A., Effect of partial void filling on the lattice thermal conductivity of skutterudites, *Phys. Rev. B*, **58** (1), 164-170 (1998).

[78] Morelli D. T., Meisner G. P., Chen B., Hu S., Uher C., Cerium filling and doping of cobalt triantimonide, *Phys. Rev. B*, **56** (12), 7376-7383 (1997).

[79] Arita Y., Ogawa T., Kobayashi H., Iwasaki K., Matsui T., Nagasaki T., Thermoelectric properties of uranium filled skutterudites $U_y(Fe_xCo_{4-x})Sb_{12}$, *J. Nucl. Mater.*, **344** (1-3), 79-83 (2005).

[80] Chen L., Recent advances in filled skutterudite systems, *XXI International Conference on Thermoelectrics*, 42-47 (2002).

[81] Chen L., Tang X., Goto T., Hirai T., Synthesis of filled skutterudite compounds: $Ba_yFe_xCo_{4-x}Sb_{12}$, *J. Mater. Res.*, **15** (11), 2276-2279 (2000).

[82] Chakoumakos B. C., Sales B. C., Skutterudites: Their structural response to filling, *J. Alloys Compd.*, **407** (1-2), 87-93 (2006).

[83] Chapon L. C., Girard L., Haidoux A., Smith R. I., Ravot D., Structural changes induced by Ce filling in partially filled skutterudites, *J. Phys. Condens. Matter*, **17** (23), 3525-3535 (2005).

[84] Sellinschegg H., Johnson D. C., The effect of various filler atoms on the thermoelectric properties of ternary skutterudites, *XVIII International Conference on Thermoelectrics*, 19-22 (1999).

[85] Sellinschegg H., A. S., G. Y., Johnson D. C., Synthesis of filled skutterudite compounds with varied degree of filling, *XVIII International Conference on Thermoelectrics,* , 338-341 (1998).

[86] Kuznetsov V. L., Kuznetsova L. A., Rowe D. M., Effect of partial void filling on the transport properties of $Nd_xCo_4Sb_{12}$ skutterudites, *J. Phys. Condens. Matter*, **15** (29), 5035-5048 (2003).

[87] Lamberton G. A., Bhattacharya S., Littleton R. T., Kaeser M. A., Tedstrom R. H., Tritt T. M., Yang J., Nolas G. S., High figure of merit in Eu-filled $CoSb_3$-based skutterudites, *Appl. Phys. Lett.*, **80** (4), 598-600 (2002).

[88] Nolas G. S., Kaeser M., Littleton R. T., Tritt T. M., High figure of merit in partially filled ytterbium skutterudite materials, *Appl. Phys. Lett.*, **77** (12), 1855-1857 (2000).

[89] Pei Y. Z., Bai S. Q., Zhao X. Y., Li X. Y., Zhang W., Chen L. D., Synthesis and thermodynamics properties of alkaline metals filled $CoSb_3$ skutterudites, *XXVI International Conference on Thermoelectrics*, 181-183 (2008).

[90] Pei Y. Z., Chen L. D., Zhang W., Shi X., Bai S. Q., Zhao X. Y., Mei Z. G., Li X. Y., Synthesis and thermoelectric properties of $K_yCo_4Sb_{12}$, *Appl. Phys. Lett.*, **89** (22) (2006).

[91] Puyet M., Lenoir B., Dauscher A., Dehmas M., Stiewe C., Muller E., High temperature transport properties of partially filled $Ca_xCo_4Sb_{12}$ skutterudites, *J. Appl. Phys.*, **95** (9), 4852-4855 (2004).

[92] Zhao X. Y., Shi X., Chen L. D., Zhang W. Q., Zhang W. B., Pei Y. Z., Synthesis and thermoelectric properties of Sr-filled skutterudite $Sr_yCo_4Sb_{12}$, *J. Appl. Phys.*, **99** (5) (2006).

[93] Chen L. D., Kawahara T., Tang X. F., Goto T., Hirai T., Dyck J. S., Chen W., Uher C., Anomalous barium filling fraction and n-type thermoelectric performance of $Ba_yCo_4Sb_{12}$, *J. Appl. Phys.*, **90** (4), 1864-1868 (2001).

[94] He T., Chen J. Z., Rosenfeld H. D., Subramanian M. A., Thermoelectric properties of indium-filled skutterudites, *Chem. Mater.*, **18** (3), 759-762 (2006).

[95] Sales B. C., Chakoumakos B. C., Mandrus D., Thermoelectric properties of thallium-filled skutterudites, *Phys. Rev. B*, **61** (4), 2475-2481 (2000).

[96] Nolas G. S., Yang J., Takizawa H., Transport properties of germanium-filled $CoSb_3$, *Appl. Phys. Lett.*, **84** (25), 5210-5212 (2004).

[97] Nolas G. S., Takizawa H., Endo T., Sellinschegg H., Johnson D. C., Thermoelectric properties of Sn-filled skutterudites, *Appl. Phys. Lett.*, **77** (1), 52-54 (2000).

[98] Takizawa H., Miura K., Ito M., Suzuki T., Endo T., Atom insertion into the $CoSb_3$ skutterudite host lattice under high pressure, *J. Alloys Compd.*, **282** (1-2), 79-83 (1999).

[99] Zemni S., Tranqui D., Chaudouet P., Madar R., Senateur J. P., Synthesis and crystal structure of a new series of ternary phosphides in the systems Tr-Co-P (Tr: rare earth), *J. Solid State Chem.*, **65**, 1-5 (1986).

[100] Tang X. F., Zhang Q. J., Chen L. D., Goto T., Hirai T., Synthesis and thermoelectric properties of p-type- and n-type-filled skutterudite $R_yM_xCo_{4-x}Sb_{12}$(R : Ce,Ba,Y; M : Fe,Ni), *J. Appl. Phys.*, **97**, 093712 (2005).

[101] Caillat T., Fleurial J. P., Borshchevsky A., Bridgman-solution crystal growth and characterization of the skutterudite compounds $CoSb_3$ and $RhSb_3$, *J. Cryst. Growth*, **166** (1-4), 722-726 (1996).

[102] Katsuyama S., Shichijo Y., Ito M., Majima K., Nagai H., Thermoelectric properties of the skutterudite $Co_{1-x}Fe_xSb_3$ system, *J. Appl. Phys.*, **84**, 6708-6712 (1998).

[103] Dyck J. S., Chen W., Yang J., Meisner G. P., Uher C., Effect of Ni on the transport and magnetic properties of $Co_{1-x}Ni_xSb_3$, *Phys. Rev. B*, **65** (11), 115204 (2002).

[104] Wojciechowski K. T., Effect of tellurium doping on the thermoelectric properties of $CoSb_3$, *Mater. Res. Bull.*, **37** (12), 2023-2033 (2002).

[105] Kim I. H., Park K. H., Ur S. C., Thermoelectric properties of Sn-doped $CoSb_3$ prepared by encapsulated induction melting, *J. Alloys Compd.*, **442** (1-2), 351-354 (2007).

[106] Korenstein R., Soled S., Wold A., Collin G., Preparation and characterization of skutterudite-related phases $CoGe_{1.5}S_{1.5}$ and $CoGe_{1.5}Se_{1.5}$, *Inorg. Chem.*, **16** (9), 2344-2346 (1977).

[107] Nolas G. S., Yang J., Ertenberg R. W., Transport properties of $CoGe_{1.5}Se_{1.5}$, *Phys. Rev. B*, **68**, 193206 (2003).

[108] Navrátil J., Plechácek T., Beneš L., Vlcek M., Some transport properties of $CoGe_{1.5}Te_{1.5}$, *J. Optoelectron. Adv. Mater.*, **6** (3), 787-790 (2004).

[109] Nagamoto Y., Tanaka K., Koyanagi T., Thermoelectric properties of the skutterudite-related phase $CoSn_{1.5}Te_{1.5}$, *XVI International Conference on Thermoelectrics*, 330-333 (1997).

[110] Vaqueiro P., Sobany G. G., Stindl M., Structure and electrical transport properties of the ordered skutterudites $MGe_{1.5}S_{1.5}$ (M= Co, Rh, Ir), *J. Solid State Chem.*, **181** (4), 768-776 (2008).

[111] Kjekshus A., Rakke T., Compounds with skutterudite type crystal-structure III. Structural data for arsenides and antimonides, *Acta Chem. Scand.*, **A 28** (1), 99-103 (1974).

[112] Pleass C. M., Heyding R. D., Arsenides of the transition metals VI. Electrical and magnetic properties of the triarsenides, *Can. J. Chem.*, **40** (4), 590-600 (1962).

[113] Bahn S., Gödecke T., Schubert K., Konstitution einiger mischungen des platins mit b-elementen (B = Sn, Sb, Te), *J. Less Common Met.*, **19**, 121-140 (1969).

[114] Caillat T., Preparation and thermoelectric properties of some arsenopyrite phases based on $RuSb_{2-2x}Te_{2x}$ and $RuSb_{2-2x}Se_{2x}$ solid solutions, *J. Phys. Chem. Solids*, **59** (1), 61-67 (1998).

[115] Watcharapasorn A., DeMattei R. C., Feigelson R. S., Caillat T., Borshchevsky A., Snyder G. J., Fleurial J. P., Thermoelectric properties of some cobalt phosphide-arsenide compounds, *Mater. Res. Soc. Symp. Proc.*, **626**, Z1.4.1-5 (2001).

[116] Caillat T., Borshchevsky A., Fleurial J. P., Properties of single crystalline semiconducting $CoSb_3$, *J. Appl. Phys.*, **80**, 4442-4449 (1996).

[117] Watcharapasorn A., DeMattei R. C., Feigelson R. S., Caillat T., Borshchevsky A., Snyder G. J., Fleurial J. P., Preparation and thermoelectric properties of some phosphide skutterudite compounds, *J. Appl. Phys.*, **86**, 6213-6217 (1999).

[118] Wojciechowski K. T., Study of transport properties of the $Co_{1-x}Rh_xSb_3$, *J. Alloys Compd.*, **439** (1-2), 18-24 (2007).

[119] Nolas G. S., Harris V. G., Tritt T. M., Slack G. A., Low-temperature transport properties of the mixed-valence semiconductor $Ru_{0.5}Pd_{0.5}Sb_3$, *J. Appl. Phys.*, **80** (11), 6304-6308 (1996).

[120] Galván D. H., Dilley N. R., Maple M. B., Posada-Amarillas A., Reyes-Serrato A., Samaniego Reyna J. C., Extended Huckel tight-binding calculations of the electronic structure of $YbFe_4Sb_{12}$, UFe_4P_{12}, and $ThFe_4P_{12}$, *Phys. Rev. B*, **68** (11), 115110 (2003).

[121] Falicov L. M., Hanke W., Maple M. B., *Valence Fluctuations in Solids*, (Amsterdam: North-Holland, 1981).

[122] Sato H., Abe Y., Okada H., Matsuda T. D., Abe K., Sugawara H., Aoki Y., Anomalous transport properties of RFe_4P_{12} (R= La, Ce, Pr, and Nd), *Phys. Rev. B*, **62** (22), 15125-15130 (2000).

[123] Takeda N., Ishikawa M., Anomalous magnetic properties of $CeRu_4Sb_{12}$, *Phys. B Condens. Matter*, **259**, 92-93 (1999).

[124] Bauer E. D., Frederick N. A., Ho P. C., Zapf V. S., Maple M. B., Superconductivity and heavy fermion behavior in $PrOs_4Sb_{12}$, *Phys. Rev. B*, **65** (10), 100506 (2002).

[125] Shirotani I., Uchiumi T., Ohno K., Sekine C., Nakazawa Y., Kanoda K., Todo S., Yagi T., Superconductivity of filled skutterudites $LaRu_4As_{12}$ and $PrRu_4As_{12}$, *Phys. Rev. B*, **56** (13), 7866-7869 (1997).

[126] Meisner G. P., Superconductivity and magnetic order in ternary rare earth transition metal phosphides, *Physica B+C*, 763-764 (1981).

[127] Jung D., Whangbo M. H., Alvarez S., Importance of the X_4 ring orbitals for the semiconducting, metallic, or superconducting properties of skutterudites MX_3 and RM_4X_{12}, *Inorg. Chem.*, **29** (12), 2252-2255 (1990).

[128] Llunell M., Alemany P., Alvarez S., Zhukov V. P., Vernes A., Electronic structure and bonding in skutterudite-type phosphides, *Phys. Rev. B*, **53** (16), 10605-10609 (1996).

[129] Uchiumi T., Shirotani I., Sekine C., Todo S., Yagi T., Nakazawa Y., Kanoda K., Superconductivity of $LaRu_4X_{12}$ (X= P, As and Sb) with skutterudite structure, *J. Phys. Chem. Solids*, **60** (5), 689-695 (1999).

[130] Nuss J., Wedig U., Jansen M., Geometric variations and electron localizations in intermetallics: PbFCl type compounds, *Z. Kristallogr.*, **221**, 554-562 (2006).

[131] haj Hassan F. E., Akbarzadeh H., Hashemifar S. J., Mokhtari A., Structural and electronic properties of matlockite MFX (MSr, Ba, Pb; XCl, Br, I) compounds, *J. Phys. Chem. Solids*, **65** (11), 1871-1878 (2004).

[132] Hulliger F., GdPS and related new rare earth compounds, *Nature*, **219** (5152), 373-374 (1968).

[133] Klein Haneveld A. J., Jellinek F., Zirconium silicide and germanide chalcogenides preparation and crystal structures, *Recl. Trav. Chim. Pays-Bas*, **83**, 776-783 (1964).

[134] Wang C., Hughbanks T., Main group element size and substitution effects on the structural dimensionality of zirconium tellurides of the ZrSiS type, *Inorg. Chem.*, **34** (22), 5524-5529 (1995).

[135] Lam R., Mar A., New ternary zirconium antimonides, Zr $Si_{0.7}Sb_{1.3}$, ZrGeSb, and $ZrSn_{0.4}Sb_{1.6}$: a family containing Zr Si S - type and β−(Zr Sb_2)-type compounds, *J. Solid State Chem.*, **134**, 388-394 (1997).

[136] Klein Haneveld A. J., Jellinek F., Some ternary uranium chalcogenides, *J. Less Common Met.*, **18**, 123-129 (1969).

[137] Kaczorowski D., Noel H., Potel M., Zygmunt A., Crystal structure, magnetic and electrical transport properties of UPS single crystals, *J. Phys. Chem. Solids*, **55** (11), 1363-1367 (1994).

[138] Johnson V., Jeitschko W., PbFCl-type pnictides of niobium with silicon or germanium, *J. Solid State Chem.*, **6** (2), 306-309 (1973).

[139] Wang Y. C., Poduska K. M., Hoffmann R., DiSalvo F. J., Structure and physical properties of CeSbTe, *J. Alloys Compd.*, **314** (1-2), 132-139 (2001).

[140] Payne A. C., Sprauve A. E., Holm A. P., Olmstead M. M., Kauzlarich S. M., Klavins P., EuSnP: a novel antiferromagnet with two-dimensional, corrugated Sn sheets, *J. Alloys Compd.*, **338**, 229-234 (2002).

[141] Levy F., *Structural chemistry of layer-type phases*, (Reidel, 1976).

[142] Bither T. A., Bouchard R. J., Cloud W. H., Donohue P. C., Siemons W. J., Transition metal pyrite dichalcogenides. High-pressure synthesis and correlation of properties, *Inorg. Chem.*, **7** (11), 2208-2220 (1968).

[143] Goodenough J. B., Energy bands in TX_2 compounds with pyrite, marcasite, and arsenopyrite structures, *J. Solid State Chem.*, **5** (1), 144-152 (1972).

[144] Pratt J. L., Bayliss P., Crystal structure refinement of a cobaltian ullmannite, *Am. Mineral.*, **65** (1-2), 154-156 (1980).

[145] Foecker A. J., Jeitschko W., The atomic order of the pnictogen and chalcogen atoms in equiatomic ternary compounds TPnCh (T= Ni, Pd; Pn= P, As, Sb; Ch= S, Se, Te), *J. Solid State Chem.*, **162** (1), 69-78 (2001).

[146] Bayliss P., Crystal chemistry and crystallography of some minerals within the pyrite group, *Am. Mineral.*, **74** (9-10), 1168-1176 (1989).

[147] Hulliger F., Mooser E., Semiconductivity in pyrite, marcasite and arsenopyrite phases, *J. Phys. Chem. Solids*, **26**, 429–433 (1965).

[148] Hulliger F., New compounds with cobaltite structure, *Nature*, **198** (4878), 382-383 (1963).

[149] Entner P., Parthé E., PtGeSe with cobaltite structure, a ternary variant of the pyrite structure, *Acta Crystallogr. B: Struct. Crystallogr. Cryst. Chem.*, **29** (8), 1557-1560 (1973).

[150] Kjekshus A., Nicholson D. G., Significance of π Back-bonding in compounds with pyrite, marcasite and arsenopyrite type structures, *Acta Chem. Scand.*, **25** (3), 866-876 (1971).

[151] Davies S. C., Smith M. C., Evans D. J., 1,2-Bis(diphenylthioarsinoyl)ethane, *Acta Crystallogr. E*, **60**, M771-M772 (2004).

[152] Stassen W. N., Heyding R. D., Crystal structures of $RuSe_2$, $OsSe_2$, $PtAs_2$, and α-$NiAs_2$, *Can. J. Chem.*, **46**, 2159-2163 (1968).

[153] Jeitschko W., Flörke U., Scholz U. D., Ambient pressure synthesis, properties, and structure refinements of VP_4 and CoP_2, *J. Solid State Chem.*, **52** (3), 320-326 (1984).

[154] Papoian G. A., Hoffmann R., Hypervalent bonding in one, two, and three dimensions: Extending the Zintl-Klemm concept to nonclassical electron-rich networks, *Angew. Chem., Int. Ed.*, **39**, 2408-2448 (2000).

[155] Lee K. S., Koo H. J., Dai D., Ren J., Whangbo M. H., Electron counting scheme relevant for late transition metal compounds with weakly electronegative ligands. Electronic band structure study of phosphosilicides $PtSi_3P_2$ and $NiSi_2P_3$, *Inorg. Chem.*, **38** (2), 340-345 (1999).

[156] Hulliger F., Semiconductivity in $CoSb_2$-type compounds, *Physics Letters*, **4** (5), 282-283 (1963).

[157] Hulliger F., New semiconducting arsenopyrite-type compounds, *Nature*, **201** (4917), 381-382 (1964).

[158] Wijeyesekera S. D., Hoffmann R., Marcasite and arsenopyrite: structure, bonding, and electrical properties, *Inorg. Chem.*, **22** (22), 3287-3300 (1983).

[159] Kjekshus A., Peterzons P. G., Rakke T., Andresen A. F., Compounds with the marcasite type crystal structure. XIII. Structural and magnetic properties of $Cr_xFe_{1-x}As_2$, $CrxFe_{1-x}Sb_2$, $Fe_{1-x}Ni_xAs_2$ and $Fe_{1-x}Ni_xSb_2$, *Acta Chem. Scand.*, **33**, 469-480 (1979).

[160] Hyde B., O'Keeffe M., Marcasite and pyrite (FeS_2), *Aust. J. Chem.*, **49**, 867-872 (1996).

[161] Fleet M. E., The crystal structure of pararammelsbergite ($NiAs_2$), *Am. Mineral.*, **57**, 1–9 (1972).

[162] Wang M., Morgan M. G., Mar A., Platinum silicon antimonide (PtSiSb), *J. Solid State Chem.*, **175** (2), 231-236 (2003).

[163] Nahigian H., Steger J., McKinzie H. L., Arnott R. J., Wold A., Preparation and characterization of some cobalt phosphorus, cobalt arsenic, cobalt antimony sulfide or selenide compounds, *Inorg. Chem.*, **13** (6), 1498-1503 (1974).
[164] Laufek F., Vymazalová A., Navrátil J., Drábek M., Plášil J., Plechácek T., Synthesis and crystal structure of PdSnTe, *J. Alloys Compd.*, (in press) (2008).
[165] Mansuetto M. F., Ibers J. A., Crystal structure of platinum silicon telluride, PtSiTe, *Z. Kristallogr.*, **209**, 708-708 (1994).
[166] Kjekshus A., Rakke T., Structural transformations in $Co_tNi_{1-t}As_2$, $NiAs_{2-x}S_x$, Ni $As_{2-x}Se_x$, and Co $As_{1-x}Se_{1+x}$, *Acta Chem. Scand.*, **33**, 609-615 (1979).
[167] Cabri L. J., Harris D. C., Stewart J. M., Paracostibite (CoSbS) and nisbite ($NiSb_2$), new minerals from the Red Lake area, Ontario, Canada, *Can. Mineral.*, **10** (2), 232-246 (1970).
[168] Bhatt Y. C., Schubert K., Kristallstruktur von $PtBi_2$, *Z. Metallkd.*, **71**, 581-583 (1980).
[169] Kliche G., Iridiumphosphidtellurid, IrPTe, *Z. Naturforsch., B: Chem. Sci.*, **41** (1), 130-131 (1986).
[170] Schafer H., On the problem of polar intermetallic compounds: The stimulation of E. Zintl's work for the modern chemistry of intermetallics, *Annu. Rev. Mater. Sci.*, **15** (1), 1-42 (1985).
[171] Li B., Xie Y., Huang J., Su H., Qian Y., Synthesis and characterization of ternary chalcogenides Ag_8SnE_6 (E= S, Se), *J. Solid State Chem.*, **149** (2), 338-340 (2000).
[172] Lancaster J. R., *The bioinorganic chemistry of nickel*, (VCH, 1988).
[173] Fleet M. E., Structure of godlevskite, Ni_9S_8, *Acta Crystallogr., Sect. C: Cryst. Struct. Commun.*, **43**, 2255-2257 (1987).
[174] Groenvold F., Kjekshus A., Raaum F., The crystal structure of Ti_5Te_4, *Acta Crystallogr.*, **14** (9), 930-934 (1961).
[175] Maggard P. A., Corbett J. D., Sc_9Te_2: A two-dimensional distortion wave in the scandium-richest telluride, *J. Am. Chem. Soc.*, **122** (5), 838-843 (2000).
[176] Maggard P. A., Corbett J. D., Sc_6MTe_2 (M= Mn, Fe, Co, Ni): Members of the flexible Zr_6CoAl_2-type family of compounds, *Inorg. Chem*, **39** (18), 4143-4146 (2000).
[177] Gautier R., Furet E., Halet J. F., Lin Z., Saillard J. Y., Xu Z., Electronic structures of electron-rich octahedrally condensed transition-metal chalcogenide clusters, *Inorg. Chem*, **41** (4), 796-804 (2002).
[178] Mingos D. M. P., David J., *Introduction to cluster chemistry Prentice Hall advanced reference series Prentice Hall inorganic and organometallic chemistry series*, (Prentice Hall, 1990).
[179] Pauling L., *The Nature of the Chemical Bond*, (Ithaca: Cornell Univ. Press, 1960).
[180] Corbett J. D., Correlation of metal-metal bonding in halides and chalcides of the early transition elements with that in the metals, *J. Solid State Chem.*, **37** (3), 335-351 (1981).
[181] Maggard P. A., Corbett J. D., The synthesis, structure, and bonding of Sc_8Te_3 and Y_8Te_3. Cooperative matrix and bonding effects in the solid state, *Inorg. Chem.*, **37** (4), 814-820 (1998).
[182] Simon A., Condensed metal clusters, *Angew. Chem., Int. Ed. Engl.*, **20** (1), 1-22 (1981).
[183] Simon A., Clusters of valence electron poor Metals—structure, bonding, and properties, *Angew. Chem., Int. Ed. Engl.*, **27** (1), 159-183 (1988).
[184] Sheldrick W. S., Wachhold M., Solventothermal synthesis of solid-state chalcogenidometalates, *Angew. Chem., Int. Ed. Engl.*, **36** (3), 206-224 (1997).

[185] Schaefer H., Eisenmann B., Mueller W., Zintl phases: Transitions between metallic and ionic bonding, *Angew. Chem., Int. Ed. Engl.*, **12** (9), 694-712 (1973).

[186] Elder S. H., Jobic S., Brec R., Gelabert M., DiSalvo F. J., Structural and electronic properties of $K_2Ni_3S_4$, a pseudo-two dimensional compound with a honeycomb-like arrangement, *J. Alloys Compd.*, **235** (2), 135-142 (1996).

[187] Brewer L., Wengert P. R., Transition metal alloys of extraordinary stability; An example of generalized Lewis-acid-base interactions in metallic systems, *Metall. Mater. Trans. B*, **4** (1), 83-104 (1973).

[188] Chen L., Corbett J. D., Synthesis, structure, and bonding of $Lu_7Z_2Te_2$ (Z= Ni, Pd, Ru). Linking typical tricapped trigonal prisms in metal-rich compounds, *Inorg. Chem.*, **43** (11), 3371-3376 (2004).

[189] Lee C. S., Kleinke H., Synthesis, structure, and thermoelectric properties of the new antimonide sulfide $MoSb_2S$, *Eur. J. Inorg. Chem.*, **2002** (3), 591-596 (2002).

[190] Baranov A. I., Isaeva A. A., Kloo L., Popovkin B. A., New metal-rich sulfides Ni_6SnS_2 and $Ni_9Sn_2S_2$ with a 2D metal framework: synthesis, crystal structure, and bonding, *Inorg. Chem.*, **42** (21), 6667-6672 (2003).

[191] Baranov A. I., Isaeva A. A., Kloo L., Kulbachinskii V. A., Lunin R. A., Nikiforov V. N., Popovkin B. A., 2D metal slabs in new nickel–tin chalcogenides $Ni_{7-\delta}SnQ_2$ (Q= Se, Te): average crystal and electronic structures, chemical bonding and physical properties, *J. Solid State Chem.*, **177** (10), 3616-3625 (2004).

[192] Peacock M. A., McAndrew J., On parkerite and shandite, and the crystal structure of $Ni_3Pb_2S_2$, *Am. Mineral.*, **35**, 425-439 (1950).

[193] Zabel M., Wandinger S., Range K. J., Ternary chalcogenides $M_3M'_2X_2$ with shandite-type structure *Zeitschrift Fur Naturforschung Section B-a Journal of Chemical Sciences*, **34** (2), 238-241 (1979).

[194] Brower W. S., Parker H. S., Roth R. S., Reexamination of synthetic parkerite and shandite, *Am. Mineral.*, **59**, 296-301 (1974).

[195] Weihrich R., Anusca I., Half-Antiperovskites. III. Crystallographic and electronic structure effects in $Sn_{2-x}In_xCo_3S_2$, *Z. Anorg. Allg. Chem.*, **632** (8-9), 1531 (2006).

[196] Scholtz D. L., The magnetic nickeliferous ore deposits of east Griqualand and Pondoland, *Trans. Geol. Soc. South Africa*, **39**, 81-210 (1936).

[197] Fleet M. E., The crystal structure of parkerite ($Ni_3Bi_2S_2$), *Am. Mineral.*, **58**, 435-439 (1973).

[198] Weihrich R., Matar S. F., Eyert V., Rau F., Zabel M., Andratschke M., Anusca I., Bernert T., Structure, ordering, and bonding of half antiperovskites: $PbNi_{3/2}S$ and $BiPd_{3/2}S$, *Prog. Solid State Chem.*, **35** (2-4), 309-327 (2007).

[199] Weihrich R., Anusca I., Halfantiperovskites II: on the crystal structure of $Pd_3Bi_2S_2$, *Z. Anorg. Allg. Chem.*, **632** (2), 335-342 (2006).

[200] Gutlich P., Range K. J., Felser C., Schultz-Munzenberg C., Tremel W., Walcher D., Waldeck M., The valence states of nickel, tin, and sulfur in the ternary chalcogenide $Ni_3Sn_2S_2$ XPS, 61 Ni ans 119 Sn Mossbauer investigations and band structure calculation, *Angew. Chem., Int. Ed.*, **38** (16), 2381-2384 (1999).

[201] Weihrich R., Anusca I., Zabel M., Half-antiperovskites: Structure and type-antitype relations of shandites $M_{3/2}AS$ (M = Co, Ni; A = In, Sn), *Z. Anorg. Allg. Chem.*, **631** (8), 1463-1470 (2005).

[202] Hughbanks T., Exploring the metal-rich chemistry of the early transition elements, *J. Alloys Compd.*, **229** (1), 40-53 (1995).

[203] Michelet A., Collin G., Gorochov O., Study of some physical properties of $Ni_3B_2S_2$ (B = Pb, Tl, Bi, Sn) and $Ni_3Pb_2Se_2$ phases, *J. Less Common Met.*, **97**, 73-78 (1984).

[204] Natarajan S., Subba Rao G. V., Baskaran R., Radhakrishnan T. S., Synthesis and electrical properties of shandite-parkerite phases, $A_2M_3Ch_2$, *J. Less Common Met.*, **138** (2), 215-224 (1988).
[205] Sakamoto T., Wakeshima M., Hinatsu Y., Matsuhira K., Charge-density-wave superconductor $Bi_2Rh_3Se_2$, *Phys. Rev. B*, **75** (6), 60503 (2007).
[206] Sakamoto T., Wakeshima M., Hinatsu Y., Superconductivity in ternary chalcogenides $Bi_2Ni_3X_2$ (X= S, Se), *J. Phys. Condens. Matter*, **18** (17), 4417-4426 (2006).
[207] de Groot R. A., Mueller F. M., Engen P. G., Buschow K. H. J., New class of materials: half-metallic ferromagnets, *Phys. Rev. Lett.*, **50** (25), 2024-2027 (1983).
[208] Venkatesan M., *Handbook of magnetism and advanced magnetic materials*, (Chichester: John Wiley and Sons Limited, 2007).
[209] Coey J. M. D., Sanvito S., Magnetic semiconductors and half-metals, *J. Phys. D: Appl. Phys.*, **37** (7), 988-993 (2004).
[210] Hanssen K., Mijnarends P. E., Positron-annihilation study of the half-metallic ferromagnet NiMbSb, *Phys. Rev. B*, **34** (8), 5009-5016 (1986).
[211] Kämper K. P., Schmitt W., Güntherodt G., Gambino R. J., Ruf R., CrO_2. A new half-metallic ferromagnet?, *Phys. Rev. Lett.*, **59** (24), 2788-2791 (1987).
[212] Wolf S. A., Awschalom D. D., Buhrman R. A., Daughton J. M., von Molnar S., Roukes M. L., Chtchelkanova A. Y., Treger D. M., Spintronics: A spin-based electronics vision for the future, *Science*, **294**, 1488-1495 (2001).
[213] Felser C., Fecher G. H., Balke B., Spintronics: A challenge for materials science and solid-state chemistry, *Angew. Chem., Int. Ed.*, **46** (5), 668-699 (2007).
[214] Zutic I., Fabian J., Das Sarma S., Spintronics: Fundamentals and applications, *Rev. Mod. Phys.*, **76** (2), 323-410 (2004).
[215] Schäfer H., Jacob H., Etzel K., Die Verwendung der Zerfallsgleichgewichte der Eisen-(II)-und Nickel-(II)-halogenide zum Metalltransport im Temperaturgefälle, *Z. Anorg. Allg. Chem.*, **286**, 42-55 (1956).
[216] Nitsche R., The growth of single crystals of binary and ternary chalcogenides by chemical transport reactions, *J. Phys. Chem. Solids*, **17** (1-2), 163-165 (1960).
[217] Bruker-AXS, Apex-2 Software (Madison, Wisconsin, USA, 2004).
[218] Altomare A., Cascarano G., Giacovazzo C., Guagliardi A., Burla M. C., Polidori G., Camalli M., SIR92 - a program for automatic solution of crystal structures by direct methods, *J. Appl. Crystallogr.*, **27** (3), 435 (1994).
[219] Watkin D. J., Prout C. K., Carruthers J. R., Betteridge P. W., CRYSTALS. Issue 10. Chemical Crystallography Laboratory (Oxford, England, 1996).
[220] Fitch A. N., The high resolution powder diffraction beam line at ESRF, *J. Res. Natl. Inst. Stan.*, **109** (1), 133-142 (2004).
[221] Elder F. R., Gurewitsch A. M., Langmuir R. V., Pollock H. C., Radiation from electrons in a synchrotron, *Phys. Rev.*, **71** (11), 829-830 (1947).
[222] Suortti P., Hastings J. B., Cox D. E., Powder diffraction with synchrotron radiation. II. Dispersion factors of Ni, *Acta Crystallogr. A*, **41**, 417-420 (1985).
[223] Hodeau J. L., Favre-Nicolin V., Bos S., Renevier H., Lorenzo E., Berar J. F., Resonant diffraction, *Chem. Rev.*, **101** (6), 1843-1867 (2001).
[224] Cromer D. T., Calculation of anomalous scattering factors at arbitrary wavelengths, *J. Appl. Crystallogr.*, **16**, 437-437 (1983).
[225] www.isis.rl.ac.uk, (2008).
[226] Von Dreele R. B., Neutron powder diffraction, *Rev. Mineral. Geochem.*, **20** (1), 333-369 (1989).

[227] David W. I. F., Johnson M. W., Knowles K. J., Moreton-Smith C. M., Crisbie G. D., Campbell E. P., Graham S. P., Lyall J. S., *Rutherford Appleton Lab.[Rep.] RAL, 1986*, (RAL–86–102).

[228] Stokes H. T., Hatch D. M., *ISOTROPY*, (Department of Physics and Astronomy, Bringham Young University, Provo, USA, 1998).

[229] Howard C. J., Stokes H. T., Structures and phase transitions in perovskites-a group-theoretical approach, *Acta Crystallogr.*, **61** (Part 1), 93-111 (2005).

[230] Hammond C., *Introduction to crystallography*, (Oxford University Press, USA, 1992).

[231] Boultif A., Louer D., Indexing of powder diffraction patterns for low-symmetry lattices by the successive dichotomy method *J. Appl. Crystallogr.*, **24**, 987-993 (1991).

[232] Rietveld H., A profile refinement method for nuclear and magnetic structures, *J. Appl. Crystallogr.*, **2**, 65-71 (1969).

[233] McCusker L. B., Von Dreele R. B., Cox D. E., Louer D., Scardi P., Rietveld refinement guidelines, *J. Appl. Crystallogr.*, **32**, 36-50 (1999).

[234] Duval C., *Inorganic Thermogravimetric Analysis*, (Elsevier, New York, 1963).

[235] Birks L. S., *Electron probe microanalysis*, (John Wiley and Sons, New York, 1971).

[236] Spiller T., Clark T., SQUIDS - Macroscopic quantum objects, *New Scientist*, **112** (1537), 36-40 (1986).

[237] Blundell S., *Magnetism in condensed matter*, (Oxford University Press, Oxford, 2001).

[238] MacDonald D. K. C., *Thermoelectricity: An Introduction to the Principles*, (Wiley, New York, 1962).

[239] Gibson A. F., Aigrain P., Burgess R. E., Morgenstern O., Progress in Semiconductors, Vol. 1, *J. Electrochem. Soc.*, **104**, 133C (1957).

[240] Barnard R. D., *Thermoelectricity in metals and alloys*, (Taylor & Francis, 1972).

[241] Mott N. F., Jones H., *The Theory of the Properties of Metals and Alloys*, (Courier Dover Publications, 1958).

[242] Burkov A. T., Heinrich A., Konstantinov P. P., Nakama T., Yagasaki K., Experimental set-up for thermopower and resistivity measurements at 100-1300 K, *Meas. Sci. Technol.*, **12** (3), 264-272 (2001).

[243] Roberts R. B., The absolute scale of thermoelectricity II, *Philos. Mag. B*, **43** (6), 1125 - 1135 (1981).

[244] Berman R., *Thermal conduction in solids*, (Clarendon Press, 1976).

[245] Parker W. J., Jenkins R. J., Butler C. P., Abbott G. L., Flash Method of Determining Thermal Diffusivity, Specific Heat and Thermal Conductivity, *J. Appl. Phys.*, **32** (9), 1679-1684 (1961).

[246] Vaqueiro P., Sobany G. G., Powell A. V., Knight K. S., Structure and thermoelectric properties of the ordered skutterudite $CoGe_{1.5}Te_{1.5}$, *J. Solid State Chem.*, **179** (7), 2047-2053 (2006).

[247] Goldstein J. I., Newbury D. E., Echlin P., Joy D. C., Romig A. D., Lyman C. E., Fiori C., Lifshin E., *Scanning electron microscopy and X-ray microanalysis: a text for biologists, materials scientists, and geologists*, (Plenum Press. New York. US, 1992).

[248] Navratil J., Plechacek T., Drasar C., Vlcek M., Beneš L., Laufek F., Effect of partial La filling of $Co_4Ge_6Te_6$ ternary skutterudite on their thermoelectric properties, *VI European Conference on Thermoelectrics*, 1-4 P1-24 (2008).

[249] David W. I. F., Johnson M. W., Knowles K. J., Moreton-Smith G. M., Crosbie G. D., Graham S. P., Lyall J. S., *Punch GENIE manual, version 2.5, SERC, Rutherford Appleton Laboratory*, (RAL-86-102, Chilton, Oxfordshire, 1986).

[250] Larson A. C., Von Dreele R. B., General Structure Analysis System (GSAS), *Los Alamos National Laboratory Report LAUR*, **86**, 748 (2000).
[251] Stokes H. T., Hatch D. M., Campbell B. J., ISOTROPY Tutorial, (2002).
[252] Glazer A., The classification of tilted octahedra in perovskites, *Acta Crystallogr. B*, **28**, 3384-3392 (1972).
[253] Mitchell R. H., *Perovskites: modern and ancient*, (Almaz Press, Thunder Bay, Ont., 2002).
[254] Toledano J. C., Toledano P., *The Landau theory of phase transitions*, (World scientific Teaneck, NJ, 1987).
[255] Stokes H. T., Hatch D. M., Kim J. S., Images of physically irreducible representations of the 230 space groups, *Acta Crystallogr. A*, **43** (1), 81-84 (1987).
[256] Lampis N., Sciau P., Geddo Lehmann A., Rietveld refinements of the paraelectric and ferroelectric structures of $PbFe_{0.5}Ta_{0.5}O_3$, *J. Phys.: Condens. Matter*, **12**, 2367-2378 (2000).
[257] Bondi A., Van der Waals volumes and radii, *J. Phys. Chem.*, **68** (3), 441-451 (1964).
[258] Lefebvre-Devos I., Lassalle M., Wallart X., Olivier-Fourcade J., Monconduit L., Jumas J. C., Bonding in skutterudites: Combined experimental and theoretical characterization of $CoSb_3$, *Phys. Rev. B*, **63** (12), 125110 (2001).
[259] Schmidt T., Kliche G., Lutz H. D., Structure refinement of skutterudite-type cobalt triantimonide, $CoSb_3$, *Acta Crystallogr. C*, **43** (9), 1678-1679 (1987).
[260] O'Keeffe M., Hyde B. G., Some structures topologically related to cubic perovskite ($E2_1$), ReO_3 ($D0_9$) and Cu_3Au ($L1_2$), *Acta Crystallogr. B*, **33** (12), 3802-3813 (1977).
[261] Spek A. L., PLATON, A Multipurpose Crystallographic Tool, 2003, Utrecht University, Utrecht, The Netherlands; AL Spek, *J. Appl. Cryst*, **36**, 7-13 (2003).
[262] Spek A. L., LEPAGE-an MS-DOS program for the determination of the metrical symmetry of a translation lattice, *J. Appl. Cryst.*, **21** (5), 578-579 (1988).
[263] Attfield J. P., Determination of valence and cation distributions by resonant powder X-ray diffraction, *Nature*, **343** (6253), 46-49 (1990).
[264] Partik M., Lutz H. D., Semiempirical band structure calculations on skutterudite-type compounds, *Phys. Chem. Miner.*, **27** (1), 41-46 (1999).
[265] Kjekshus A., Nicholson D. G., Rakke T., Compounds with the skutterudite type crystal structure II. The ^{121}Sb Mössbauer effect in $CoSb_3$, $Fe_{0.5}Ni_{0.5}Sb_3$, $RhSb_3$ and $IrSb_3$., *Acta Chem. Scand.*, **27** (4), 1315-1320 (1973).
[266] Shannon R. D., Revised effective ionic radii in halides and chalcogenides, *Acta Crystallogr. A*, **32**, 751-767 (1976).
[267] Evans G., Pettifer R. F., CHOOCH: a program for deriving anomalous-scattering factors from X-ray fluorescence spectra, *J. Appl. Crystallogr.*, **34**, 82-86 (2001).
[268] Cromer D. T., Liberman D., Anomalous dispersion calculations near to and on the long-wavelength side of an absorption edge, *Acta Cryst*, **37**, 267-268 (1981).
[269] Zhang Y., Wilkinson A. P., Nolas G. S., Lee P. L., Hodges J. P., Strategies for solving neighboring-element problems: a case study using resonant X-ray diffraction and pulsed neutron diffraction to examine $Sr_8Ga_{16}Ge_{30}$, *J. Appl. Crystallogr.*, **36**, 1182-1189 (2003).
[270] Wilkinson A. P., Lind C., Young R. A., Shastri S. D., Lee P. L., Nolas G. S., Preparation, transport properties, and structure analysis by resonant X-ray scattering of the type I clathrate $Cs_8Cd_4Sn_{42}$, *Chem. Mater.*, **14** (3), 1300-1305 (2002).
[271] Wilkinson A. P., Cox D. E., Cheetham A. K., Some aspects of the collection and analysis of powder diffraction data near X-ray absorption edges: resonant

diffraction studies of the garnets $Y_3Fe_5O_{12}$ and $Y_3Ga_5O_{12}$, *J. Phys. Chem. Solids*, **52** (10), 1257-1266 (1991).

[272] Hastings J. B., Thomlinson W., Cox D. E., Synchrotron X-ray powder diffraction, *J. Appl. Crystallogr.*, **17**, 85-95 (1984).

[273] Finger L. W., Cox D. E., Jephcoat A. P., A correction for powder diffraction peak asymmetry due to axial divergence, *J. Appl. Crystallogr.*, **27** (6), 892-900 (1994).

[274] Aranda M. A. G., Losilla E. R., Cabeza A., Bruque S., Effective correction of peak asymmetry: Rietveld refinement of high-resolution synchrotron powder data of $Li_{1.8}(Hf_{1.2}Fe_{0.8})(PO_4)_3$, *J. Appl. Crystallogr.*, **31**, 16-21 (1998).

[275] Hill R. J., Cranswick L. M. D., International Union of Crystallography. Comission on powder diffraction. Rietveld refinement round robin II. Analysis of monoclinic ZrO_2, *J. Appl. Crystallogr.*, **27**, 802-844 (1994).

[276] Ahtee M., Nurmela M., Suortti P., Järvinen M., Correction for preferred orientation in Rietveld refinement, *J. Appl. Crystallogr.*, **22**, 261-268 (1989).

[277] McCusker L. B., Von Dreele R. B., Cox D. E., Louër D., Scardi P., Rietveld refinement guidelines, *J. Appl. Crystallogr.*, **32**, 36-50 (1999).

[278] Mooser E., Pearson W. B., *Progress in Semiconductors V*, (Butterworth, London, 1956).

[279] Matsubara K., Sakakibara T., Notohara Y., Anno H., Shimizu H., Koyanagi T., Electronic transport properties of the skutterudite $CoSb_3$ and mixed alloys, *XV International Conference on Thermoelectrics*, 96-99 (1996).

[280] Mott N. F., Electrons in disordered structures, *Adv. Phys.*, **50** (7), 865-945 (2001).

[281] O'Dwyer J. J., *The theory of electrical conduction and breakdown in solid dielectrics*, (Clarendon Press, Oxford, 1973).

[282] El-Shazly O., Ramadan T., El-Hawary M., El-Anany N., Motaweh H. A., El-Wahidy E. F., Low-temperature electrical conductivity of ternary chalcogenide glasses in the system Se-S, *Can. J. Phys.*, **80** (5), 599-604 (2002).

[283] Mandrus D., Migliori A., Darling T. W., Hundley M. F., Peterson E. J., Thompson J. D., Electronic transport in lightly doped $CoSb_3$, *Phys. Rev. B*, **52** (7), 4926-4931 (1995).

[284] Mott N. F., Electrons in disordered solids I, *Adv. Phys.*, **16**, 49-144 (1967).

[285] Adler D., Feinleib J., Electrical and optical properties of narrow-band materials, *Phys. Rev. B*, **2** (8), 3112-3134 (1970).

[286] Böttger H., Bryksin V. V., *Hopping conduction in solids*, (Akademie-Verlag, Berlin, 1985).

[287] Mott N. F., Conduction in glasses containing transition metal ions, *J. Non-Cryst. Solids*, **1** (1), 1-17 (1968).

[288] Vaqueiro P., Bold M., Powell A. V., Ritter C., Structural, magnetic, and electronic properties of vanadium-substituted nickel chromium sulfide, *Chem. Mater.*, **12** (4), 1034-1041 (2000).

[289] Mott N. F., Conduction in non-crystalline materials, *Philos. Mag.*, **19** (160), 835-852 (1969).

[290] Miller A., Abrahams E., Impurity conduction at low concentrations, *Phys. Rev.*, **120** (3), 745-755 (1960).

[291] Mott N. F., Davis E. A., *Electronic Processes in Non-Crystalline Solids*, (Clarendon, Oxford, 1971).

[292] Honig J. M., Localized and itinerant electrons in oxides, *IBM J. Res. Dev.*, **14** (3), 232-244 (1970).

[293] Nolas G. S., Beekman M., Ertenberg R. W., Yang J., Low temperature transport properties of Ni-doped $CoGe_{1.5}Se_{1.5}$, *J. Appl. Phys.*, **100**, 036101 (2006).

[294] Mott N., Conductivity in non-crystalline systems. IV. Anderson localization in a disordered lattice, *Phil. Mag*, **22**, 7-29 (1970).

[295] Lovett D. R., *Semimetals & narrow-bandgap semiconductors*, (London: Pion, 1977).

[296] Morelli D. T., Caillat T., Fleurial J. P., Borshchevsky A., Vandersande J., Chen B., Uher C., Low-temperature transport properties of p-type $CoSb_3$, *Phys. Rev. B*, **51** (15), 9622-9628 (1995).

[297] Nagamoto Y., Tanaka K., Koyanagi T., Ieee, Transport properties of heavily doped N-type $CoSb_3$, *XVII International Conference on Thermoelectrics*, 302-305 (1998).

[298] Kennedy C. A., White M. A., Wilkinson A. P., Varga T., Low thermal conductivity of the negative thermal expansion material, $HfMo_2O_8$, *Appl. Phys. Lett.*, **90**, 151906 (2007).

[299] Slack G. A., The thermal conductivity of nonmetallic crystals, *Solid State Phys.*, **34**, 1-71 (1979).

[300] Cahill D. G., Watson S. K., Pohl R. O., Lower limit to the thermal conductivity of disordered crystals, *Phys. Rev. B*, **46** (10), 6131-6140 (1992).

[301] Tritt T. M., *Recent Trends in Thermoelectric Materials Research I, in Semiconductors and Semimetals Vol. 69*, (Academic Press, London, 2001).

[302] Ghosez P., Veithen M., First-principles study of filled and unfilled antimony skutterudites, *J. Phys. Condens. Matter*, **19** (9), 096002 (2007).

[303] Bertini L., Stiewe C., Toprak M., Williams S., Platzek D., Mrotzek A., Zhang Y., Gatti C., Müller E., Muhammed M., Nanostructured $Co_{1-x}Ni_xSb_3$ skutterudites: Synthesis, thermoelectric properties, and theoretical modeling, *J. Appl. Phys.*, **93**, 438-447 (2002).

[304] Sharp J. W., Jones E. C., Williams R. K., Martin P. M., Sales B. C., Thermoelectric properties of $CoSb_3$ and related alloys, *J. Appl. Phys.*, **78**, 1013-1018 (1995).

[305] Hasaka M., Morimura T., Nakashima H., Tsuji T., Ieee, Thermoelectric properties of the filled skutterudite in the Ce-Fe-Co-Sb-Sn system, *XXV International Conference on Thermoelectrics*, 627-630 (2006).

[306] Finger L., VOLCAL a program to calculate polyhedral volumes and distortion parameters (1971). Modified by Ohashi, Y. (1973), Finger, L. W. (1979), Light, M.E. (1997).

[307] Hazen R. M., Finger L. W., The crystal structures and compressibilities of layer minerals at high pressure; II, phlogopite and chlorite, *Am. Mineral.*, **63** (3-4), 293-296 (1978).

[308] Swanson D. K., Peterson R. C., Polyhedral volume calculations, *Can. Mineral.*, **18** (2), 153 (1980).

[309] Mei Z. G., Zhang W., Chen L. D., Yang J., Filling fraction limits for rare-earth atoms in $CoSb_3$: An *ab-initio* approach, *Phys. Rev. B*, **74** (15), 153202 (2006).

[310] Shi X., Zhang W., Chen L. D., Yang J., Filling fraction limit for intrinsic voids in crystals: doping in skutterudites, *Phys. Rev. Lett.*, **95** (18), 185503 (2005).

[311] Singh D. J., Mazin, II, Calculated thermoelectric properties of La-filled skutterudites, *Phys. Rev. B*, **56** (4), 1650-1653 (1997).

[312] Chaudhuri M. K., Haas A., Rosenberg M., Velicescu M., Welcman N., Mass spectrometry, DTA and TG methods for studying the iron carbonil chalcogenides $Fe_2(CO)_6X_2$ (X = S,Se) and $Fe_3(CO)_9X'_2$ (X' = S,Se,Te), *J. Organomet. Chem.*, **124** (1), 37-47 (1977).

[313] Yvon K., Jeitschko W., Parthe E., LAZY PULVERIX, a computer program, for calculating X-ray and neutron diffraction powder patterns, *J. Appl. Crystallogr.*, **10** (1), 73-74 (1977).

[314] Sellinschegg H., Johnson D. C., Nolas G. S., Slack G. A., Schujman S. B., Mohammed F., Tritt T., Nelson E., A novel approach to thermoelectrics materials research of skutterudites, *XVII International Conference on Thermoelectrics*, 338-341 (1998).

[315] Disalvo F. J., Solid state chemistry, *Solid State Commun.*, **102** (2-3), 76-85 (1997).

[316] Bao S., Yang J., Zhu W., Fan X., Duan X., Peng J., Preparation and thermoelectric properties of La filled skutterudites by mechanical alloying and hot pressing, *Mater. Lett.*, **60** (16), 2029-2032 (2006).

[317] Yang L., Wu J. S., Zhang L. T., Synthesis of filled skutterudite compound $La_{0.75}Fe_3CoSb_{12}$ by spark plasma sintering and effect of porosity on thermoelectric properties, *J. Alloys Compd.*, **364** (1-2), 83-88 (2004).

[318] Navratil J., Plechacek T., Beneš L., Vlcek M., Laufek F., Transport properties of partially filled $Yb_xCo_4Ge_6Te_6$-based skutterudites, presented at the European Conference on Thermoelectrics, 2007 (unpublished).

[319] Takizawa H., Okazaki K., Uheda K., Endo T., Nolas G. S., High Pressure Synthesis of New Filled Skutterudites, *Mater. Res. Soc. Symp. Proc.*, **691**, 37-48 (2002).

[320] Zhang W., Shi X., Mei Z. G., Xu Y., Chen L. D., Yang J., Meisner G. P., Predication of an ultrahigh filling fraction for K in $CoSb_3$, *Appl. Phys. Lett.*, **89**, 112105 (2006).

[321] Wojciechowski K. T., Tobola J., Leszczynski J., Thermoelectric properties and electronic structure of $CoSb_3$ doped with Se and Te, *J. Alloys Compd.*, **361** (1-2), 19-27 (2003).

[322] Petrova L. I., Abrikosov N. K., Dudkin L. D., Sokolova V. M., Musaelyan V. V., electrophysical properties of alloys in the system $FeSb_2$-$FeTe_2$, *Inorg. Mater.*, **26** (6), 1023-1027 (1990).

[323] Bhan S., Schubert K., Zum aufbau der systeme kobalt-germanium, rhodium-silizium sowie einiger verwandter legierungen, *Z. Metallkd.*, **51**, 327-339 (1960).

[324] Brostigen G., Kjekshus A., Compounds with the marcasite type crystal structure. V. Crystal structures of FeS_2, $FeTe_2$, and $CoTe_2$, *Acta Chem. Scand.*, **24**, 1925-1940 (1970).

[325] Lyman P. S., Prewitt C. T., Room- and high-pressure crystal chemistry of CoAs and FeAs, *Acta Crystallogr. B*, **40**, 14-20 (1984).

[326] Tolédano P., Dmitriev V., *Reconstructive phase transitions in crystals and quasicrystals*, (World Scientific Pub Co Inc, 1996).

[327] Borchardt-Ott W., *Crystallography*, (Springer, 1993).

[328] Laufek F., Navratil J., Plasil J., Plechacek T., Crystal structure determination of CoGeTe from powder diffraction data, *J. Alloys Compd.*, **460** (1), 155-159 (2008).

[329] Kjekshus A., Rakke T., Compounds with the marcasite-type crystal structure. X. ^{57}Fe Mössbauer studies of some ternary pnictides., *Acta Chem. Scand.*, **A 28** (9), 1001-1010 (1974).

[330] Kjekshus A., High temperature studies of marcasite and arsenopyrite type compounds, *act. Chem. Scand. Phys. Inorg. Chem.*, **31**, 517-529 (1977).

[331] Kjekshus A., Rakke T., Andersen A. F., Compounds with the marcasite-type crystal structure. XII. Structural data for RuP_2, $RuAs_2$, $RuSb_2$, OsP_2, $OsAs_2$ and $OsSb_2$, *Acta Chem. Scand.*, **31**, 253-259 (1977).

[332] Brown I. D., *The Chemical Bond in Inorganic Chemistry: The Bond Valence Model*, (Oxford University Press, 2002).

[333] Brese N. E., O'Keeffe M., Bond-valence parameters for solids, *Acta Crystallogr. B*, **47** (2), 192-197 (1991).

[334] Brown I. D., Altermatt D., Bond-valence parameters obtained from a systematic analysis of the Inorganic Crystal Structure Database, *Acta Crystallogr. B*, **41** (4), 244-247 (1985).
[335] O'Keeffe M., Brese N. E., Bond-valence parameters for anion-anion bonds in solids, *Acta Crystallogr. B*, **48** (2), 152-154 (1992).
[336] Ioffe A. F., *Physics of Semiconductors*, (Academic Press, New York, 1960).
[337] Springthorpe A., Hopping conduction in $Li_xNi_{1-x}O$ crystals at low temperatures, *Solid State Commun.*, **3**, 143-146 (1965).
[338] Blatt F. J., *Physics of Electronic Conduction in Solids*, (McGraw-Hill Education, 1968).
[339] Bullett D. W., Electronic structure of 3d pyrite and marcasite-type sulphides, *J. Phys. C: Solid State Phys.*, **15** (30), 6163-6174 (1982).
[340] Jeitschko W., Donohue P. C., High-pressure MnP_4, a polyphosphide with Mn-Mn pairs, *Acta Crystallogr. B: Struct. Crystallogr. Cryst. Chem.*, **31** (2), 574-580 (1975).
[341] Alvarez S., Fontcuberta J., Whangbo M. H., Importance of metal-metal interactions through the phosphorus-phosphorus bonds for the multidimensional electrical properties of MP_4 (M= vanadium, chromium, molybdenum), *Inorg. Chem.*, **27** (15), 2702-2706 (1988).
[342] Nickel E. H., Structural stability of minerals with the pyrite, marcasite, arsenopyrite and lollingite structures, *Can. Mineral.*, **9** (3), 311-321 (1968).
[343] Prins M. W. J., Grosse-Holz K. O., Cillessen J. F. M., Feiner L. F., Grain-boundary-limited transport in semiconducting SnO thin films: Model and experiments, *J. Appl. Phys.*, **83**, 888-893 (1998).
[344] Geballe T. H., Hull G. W., Seebeck Effect in Silicon, *Phys. Rev.*, **98** (4), 940-947 (1955).
[345] Johnson V. A., Lark-Horovitz K., Theory of Thermoelectric Power in Semiconductors with Applications to Germanium, *Phys. Rev.*, **92** (2), 226-232 (1953).
[346] Goldsmid H. J., Sharp J. W., Estimation of the thermal band gap of a semiconductor from seebeck measurements, *J. Electron. Mater.*, **28** (7), 869-872 (1999).
[347] Garrett C. G. B., Hannay N. B., *Semiconductors*, (Rheinhold, New York, 1959).
[348] Anno H., Hatada K., Shimizu H., Matsubara K., Notohara Y., Sakakibara T., Tashiro H., Motoya K., Structural and electronic transport properties of polycrystalline p-type $CoSb_3$, *J. Appl. Phys.*, **83** (10), 5270-5276 (1998).
[349] Nolas G. S., Morelli D. T., Tritt T. M., Skutterudites: A Phonon-Glass-Electron Crystal Approach to Advanced Thermoelectric Energy Conversion Applications, *Annu. Rev. Mater. Sci.*, **29** (1), 89-116 (1999).
[350] Vaqueiro P., Sobany G. G., Ternary Skutterudites: Anion Ordering and Thermoelectric Properties, *Mater. Res. Soc. Symp. Proc.*, **1044**, 1044-U1005-1008 (2008).
[351] Keppens Bc Sales D Mandrus B V., When does a crystal conduct heat like a glass?, *Philos. Mag. Lett.*, **80** (12), 807-812 (2000).
[352] Uher C., In search of efficient *n*-type skutterudite thermoelectrics, *XXI International Conference on Thermoelectrics*, 35-41 (2002).
[353] Range K. J., Rau F., Zabel M., Paulus H., Crystal structure of nickel tin sulfide $Ni_3Sn_2S_2$, *Z. Kristallogr.*, **212** (1), 50-50 (1997).
[354] Megaw H. D., Darlington C. N. W., Geometrical and structural relations in rhombohedral perovskites, *Acta Crystallogr. A*, **31**, 161-173 (1975).

[355] Larsson A. K., Haeberlein M., Lidin S., Schwarz U., Single crystal structure refinement and high-pressure properties of CoSn, *J. Alloys Compd.*, **240** (1-2), 79-84 (1996).

[356] Rajamani V., Prewitt C. T., Refinement of the Structure of Co_9S_8, *Can. Mineral.*, **13**, 75-78 (1975).

[357] Zabel M., Wandinger S., Range K. J., Ternary Chalcogenides $M_3M'_2X_2$ with Shadite-Type Structure, *Z. Naturforsch., B: Chem. Sci.*, **34** (2), 238-241 (1979).

[358] Suzuyama T., Awaka J., Yamamoto H., Ebisu S., Ito M., Suzuki T., Nakama T., Yagasaki K., Nagata S., Ferromagnetic-phase transition in the spinel-type $CuCr_2Te_4$, *J. Solid State Chem.*, **179** (1), 140-144 (2006).

[359] Kubodera T., Okabe H., Kamihara Y., Matoba M., Ni substitution effect on magnetic and transport properties in metallic ferromagnet $Co_3Sn_2S_2$, *Phys. B Condens. Matter*, **378**, 1142-1143 (2006).

[360] Stoner E. C., Atomic moments in ferromagnetic metals and alloys with nonferromagnetic elements, *Philos. Mag.*, **15**, 1018–1034 (1933).

[361] Greedan J. E., Geometrically frustrated magnetic materials, *J. Mater. Chem.*, **11** (1), 37-53 (2001).

[362] Kumar P. S. A., Joy P. A., Date S. K., Origin of the cluster-glass-like magnetic properties of the ferromagnetic system $La_{0.5}Sr_{0.5}CoO_3$, *J. Phys.: Condens. Matter*, **10**, L487-L493 (1998).

[363] Leithe-Jasper A., Schnelle W., Rosner H., Baenitz M., Rabis A., Gippius A. A., Morozova E. N., Borrmann H., Burkhardt U., Ramlau R., Weak itinerant ferromagnetism and electronic and crystal structures of alkali-metal iron antimonides: $NaFe_4Sb_{12}$ and KFe_4Sb_{12}, *Phys. Rev. B*, **70** (21), 214418 (2004).

[364] Stoner E. C., Collective electron specific heat and spin paramagnetism in metals, *Proc. R. Soc. London, A*, **154** (883), 656-678 (1936).

[365] Rhodes P., Wohlfarth E. P., The effective Curie-Weiss constant of ferromagnetic metals and alloys, *Proc. R. Soc. London, A*, **273** (1353), 247-258 (1963).

[366] Kaczmarska K., Pierre J., Beille J., Tobola J., Skolozdra R. V., Melnik G. A., Physical properties of the weak itinerant ferromagnet CoVSb and related semi-Heusler compounds, *J. Magn. Magn. Mater.*, **187** (2), 210-220 (1998).

[367] Brown P. J., Neumann K. U., Simon A., Ueno F., Ziebeck K. R. A., Magnetization distribution in CoS_2; is it a half metallic ferromagnet?, *J. Phys. Condens. Matter*, **17** (10), 1583-1592 (2005).

[368] Wang L., Chen T. Y., Leighton C., Spin-dependent band structure effects and measurement of the spin polarization in the candidate half-metal CoS_2, *Phys. Rev. B*, **69** (2004).

[369] Harada T., Kanomata T., Kaneko T., Transport properties of $CoS_{2-x}As_x$ ($0< x<1$), *Phys. B Condens. Matter*, **237**, 172-173 (1997).

[370] Hubbard J., Electron correlations in narrow energy bands, *Proc. R. Soc. London, Ser. A*, **277**, 238-257 (1964).

[371] Schlottmann P., Double-exchange mechanism for CrO_2, *Phys. Rev. B*, **67** (17), 174419 (2003).

[372] Ranno L., Barry A., Coey J. M. D., Production and magnetotransport properties of CrO films, *J. Appl. Phys.*, **81**, 5774-5776 (1997).

[373] Tsuda N., *Electronic Conduction in Oxides*, (Springer, 1991).

[374] Vaughan D. J., Craig J. R., *Mineral chemistry of metal sulfides*, (Cambridge University Press Cambridge, 1978).

[375] Adams D. M., *Inorganic solids*, (John Wiley, London, 1974).

[376] Adachi K., Matsui M., Kawai M., Further investigations on magnetic properties of $Co(S_xSe_{1-x})_2$, ($0 < x < 1$), *J. Phys. Soc. Jpn.*, **46** (5), 1474-1482 (1979).

[377] Yamada H., Terao K., Aoki M., Electronic structure and magnetic properties of CoS_2, *J. Magn. Magn. Mater.*, **177**, 607-608 (1998).

[378] Shishidou T., Freeman A. J., Asahi R., Effect of GGA on the half-metallicity of the itinerant ferromagnet CoS_2, *Phys. Rev. B*, **64**, 180401 (2001).

[379] Wu N., Losovyj Y. B., Wisbey D., Belashchenko K., Manno M., Wang L., Leighton C., Dowben P. A., The electronic band structure of CoS_2, *J. Phys. Condens. Matter*, **19**, 156224 (2007).

[380] Brown P. J., Neumann K. U., Webster P. J., Ziebeck K. R. A., The magnetization distributions in some Heusler alloys proposed as half-metallic ferromagnets, *J. Phys. Condens. Matter*, **12** (8), 1827-1835 (2000).